Doctoral Thesis

Orchestrated Mass Transport for Quantitative Liquid-Phase Transmission Electron Microscopy

Stefan Merkens
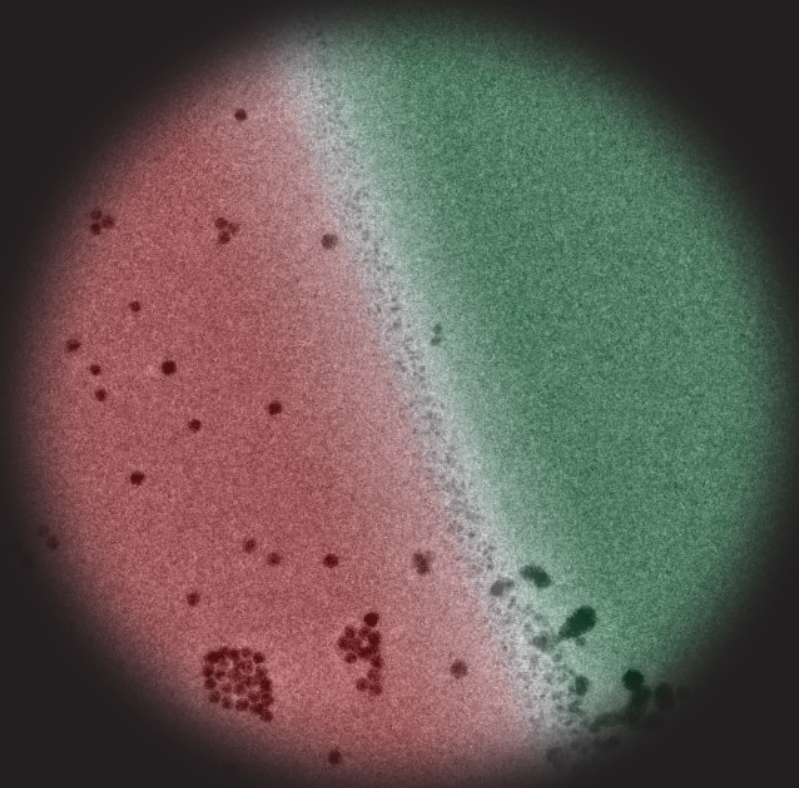
Donostia
2023

Doctoral Thesis by Published Papers

Orchestrated Mass Transport for Quantitative Liquid-Phase Transmission Electron Microscopy

submitted to

the Department of Polymers and Advanced Materials: Physics, Chemistry and Technology

of the University of the Basque Country/Euskal Herriko Unibertsitatea

by

Stefan Merkens

to obtain the degree

Doctor of Philosophy

supervised by

Andrey Chuvilin & Marek Grzelczak

Donostia - San Sebastián

2023

Universidad
del País Vasco / Euskal Herriko
Unibertsitatea

CIC nanoGUNE
MEMBER OF BASQUE RESEARCH & TECHNOLOGY ALLIANCE

"An electron is like an able guerilla leader who
occupies a wide area with rumours of his presence,
but when he strikes, he strikes with his whole force."

George P. Thompson, *Nature*, **1932**.

Acknowledgements

This thesis is a huge personal achievement which I could never have accomplished without the support of other people - and their money. Therefore, I would like to begin by expressing my gratitude for the financial support provided by the Basque Government under the *Programa Predoctoral de Formación de Personal Investigador No Doctor*.

I would like to further express my gratitude to my thesis supervisors Prof. Dr. Andrey Chuvilin, leader of the Electron Microcopy group at CIC nanoGUNE BRTA, and Dr. Marek Grzelczak, leader of the Colloidal Systems Chemistry group at the Center for Materials Research, for giving me the opportunity to develop this research project, for their lasting support and productive discussions. I learned a lot about how to think science, and myself, from two genuinely passionate scientists, each in their own way.

I want to extend my gratitude to all members of the Electron Microscopy and the Colloidal Systems Chemistry group for not only providing an intellectually stimulating environment but also for endless supply of lab equipment - and coffee. My biggest appreciation goes to my fellow PhD students, Dr. Joscha Kruse and Dr. 2b. Giuseppe De Salvo, for pushing through all the little challenges together knowing that the days of success & enlightenment would arrive. I also want to particularly thank Evegnii, Bente, Liza, Maria, Ana and of course Chris - the best technician in the history of nanoGUNE.

I want to thank all my colleagues at nanoGUNE for sharing coffee and lunch breaks. Not only have you patiently endured and shared complaints about science on an almost daily basis, but you have also engaged in stimulating conversations about the outside world which has been indispensable for refocusing the perspective on daily frustrations.

I am grateful for the various collaborators who provided ongoing support allowing me to pursue my ideas: John, Madeleine and Nynke from Protochips, Robin from Elveflow, the Mechnical and Industrial production department of Mondragon University. I am particularly grateful for having spent an incredibly hot summer at IIT in Torino growing beyond my field of expertise - grazie Kasia, Angelica e Marco.

It is of my particular concern to acknowledge all the people who I have met beyond

Summary

Liquid-phase transmission electron microscopy (LP-TEM) represents a cutting-edge experimental technique for characterizing samples in a liquid environment. In addition to sample morphology, which can already be resolved by cryogenic electron microscopy (cryo-EM) in frozen media, LP-TEM promises insights into nanoscale dynamics under *native* conditions. The recent burgeoning of LP-TEM is rooted in the invention of liquid cells (LCs), sealed enclosures of sub-micrometer liquid layers between electron beam-transparent membranes that protect the sample from the harsh conditions in an electron microscope. To date, LP-TEM has advanced research in areas ranging from materials to life sciences; however, access to quantitative data remains limited, primarily due to the challenges associated with controlling processes in the LC and the numerous experimental parameters that influence imaging. The implementation of quantitative methods, including the calibration of the applied stimuli and the control of radiation-induced artefacts, is pivotal for the future success of the technique.

LP-TEM flow reactors posses the potential to contribute to this development by enabling liquid exchange in the LC, thus facilitating control over the composition of the confined reaction solution. The manufacturing of LP-TEM flow reactors was propelled by micro-fabrication technologies, allowing the complex design criteria for building microfluidic devices that are compatible with an electron microscope to be satisfied. To fully harness the potential of LP-TEM flow reactors for the diverse samples investigated, several challenges still need to be overcome, including the understanding and the control of the dynamics of mass transport and radiation-induced chemistry.

Microfluidics is the research field that explores fluid behavior in small channels, usually less than a millimeter in size. Microfluidics has numerous advantages over *classical* batch chemistry, including low sample consumption, well-defined mixing dynamics and the integratability of numerous *in situ* sample characterization techniques. These have advanced the basic understanding of mass transport in flow reactors and established microfluidics in multiple research fields comprising bio- and nanotechnology. Moreover, excellent control over mass transport in diverse flow scenarios has been achieved through rational design of channel geometries and standardized experimental procedures. In other words, many of the knowledge gaps in LP-TEM have been effectively filled in the field of microfluidics.

This doctoral thesis was realized at the frontier between LP-TEM and microfluidics. Its main goal is to elevate LP-TEM into a quantitative technique for studying nanoscale dynamics in *native* liquid environment by applying concepts established in microfluidics research.

This thesis achieved a deep understanding of mass transport in LP-TEM flow reactors. Therefore, a bimodal approach combining numeric models & flow experiments was developed to investigate convective & diffusive transport in *realistic* 3D channel geometries. The approach revealed crucial structural elements of microfluidic LP-TEM reactors which define either convection or diffusion as the dominant mass transport mechanism. Additionally, characteristic hydrodynamic parameters were established as a quantitative basis for comparison of different flow reactors. Thereby, the potential and, more importantly, limitations of different setups for flow experiments were evaluated.

This thesis further contributes substantially to the understanding of radiation-induced artefacts in flow scenarios. When liquids are exposed to ionizing radiation like electron beams, they undergo a process called radiolysis, which, in brief, describes the generation of numerous chemical species, many of them highly reactive. These species are likely to react with the sample under investigation interfering with the applied stimulus. In this thesis, an established numeric reaction diffusion model was extended with the physics of flow in LP-TEM reactors to evaluate the effect of convective transport on the unfolding radiolysis reaction network. The response of the reaction network was found to be highly nonlinear: while only some species are efficiently removed, the concentration of other highly reactive species, *i.e.*, $H^{\cdot}$ and e_h^-, grows. Experimental parameters, such as the flow velocity and the composition of influent solution, were found to alter the response of the radiolysis reaction network, eventually providing control over the composition of the irradiated solution, at least to some extent. Finally, the results were discussed in the context of mass transport in *realistic* LP-TEM setups.

Based on the above findings, novel LP-TEM flow systems were developed that lack the drawbacks of existing systems and improve solute exchange dynamics by > 2 orders of magnitude. For numerous LP-TEM applications, diffusion is the preferred mass transport mechanism because there is less risk of the sample being flushed out of the limited imaging area (IA) than with convection. Consequently, *diffusion cell* systems were developed in

which diffusion is the dominant transport mechanism in the IA. Virtual and physical proto-types of *diffusion cells* were fabricated in a rapid prototyping procedure and their working principle was successfully demonstrated through the established bimodal approach. The long list of advantages of the novel *diffusion cell* concept includes efficient renewal and fast mixing (replacement within seconds) in the IA while ensuring compatibility with a broad range of samples and existing sample holder setups. To demonstrate the benefits of the novel reactor design, model experiments were conducted: 1) fast solution replacement was demonstrated by solvent-induced dynamics of metallic nanoparticles and 2) superior solution renewal was proven during in-operando studies of nano-catalysts under challenging electro-chemical conditions largely exceeding previous limitations.

In conclusion, the theoretical and experimental methods developed in this doctoral the-sis provide access to quantitative knowledge on mass transport processes in microfluidic LP-TEM reactors. The infrastructure established further facilitates the development of tai-lored flow reactors and improved experimental methods for a broad range of use cases. On this basis, this manuscript provides guidelines for the selection of LP-TEM setups to ensure appropriate experimental conditions for a broad variety of samples and processes. It further emphasizes the capability of calibrated mass transport and disentanglement of beam effects to extend the limits of LP-TEM in both established and novel sub-fields. In a broader con-text, the results presented contribute to LP-TEM becoming more quantitative, paving the way to valuable *in situ* and in-operando observations.

Resumen

La microscopía electrónica de transmisión en fase líquida (LP-TEM) es una técnica experimental emergente con alto potencial para caracterizar muestras en medio líquido. Junto con la morfología de las muestras, un parámetro que ya se puede resolver mediante criomicroscopía electrónica (cryo-EM) en medios congelados, la LP-TEM es capaz de revelar las dinámicas a nanoescala en su estado *natural*. El desarrollo de celdas líquidas (LCs), recintos sellados de capas líquidas finas sub-micrométricas, ha sido crucial para el desarollo de la LP-TEM, ya que se puede proteger la muestra de las exigentes condiciones de un microscopio electrónico, impulsando campos de investigación que van desde las ciencias de los materiales hasta las de la vida. Sin embargo, la información accesible ha estado limitado a observaciones cualitativas en la gran mayoria de los casos, ya que los procesos en la LC son difíciles de controlar y muchos parámetros experimentales influyen en la obtención de imágenes. Por lo tanto, la introducción de métodos cuantitativos, incluida la calibración de los estímulos aplicados y el control de los artefactos causados por la irradiación de electrones, es fundamental para el éxito futuro de la LP-TEM.

Los reactores de flujo LP-TEM se han mostrado como montajes prometedores para contribuir a este desarrollo, ya que permiten el intercambio de fluidos en la LC y, por tanto, el control de la composición de la solución de reacción encerrada. Su fabricación se ha visto impulsada por las tecnologías de micro-fabricación, que han permitido cumplir los complejos criterios de diseño de los dispositivos microfluídicos compatibles con un microscopio electrónico. No obstante, para aprovechar todo su potencial, hay que afrontar varios retos, como comprender y controlar la dinámica del transporte de masas y la química inducida por radiación, lo que permite satisfacer los requisitos individuales de las diversas muestras estudiadas.

La microfluídica es el campo de investigación que explora el comportamiento de los fluidos en canales pequeños, normalmente de menos de un milímetro de tamaño. La microfluídica tiene numerosas ventajas frente a la química por lotes, como el bajo consumo de muestras, una dinámica de mezcla bien definida y la integrabilidad de los métodos de caracterización de muestras. Estas ventajas han impulsado el entendimiento básico del transporte de masas en reactores de flujo y han implantado la microfluídica en múltiples campos de investigación, como la bio- y la nanotecnología. Además, el diseño racional de las geometrías de los canales y los procedimientos experimentales estandarizados han permitido lograr un excelente con-

trol del transporte de masa en diversos escenarios de flujo. En otras palabras, muchas de las carencias de conocimiento en LP-TEM se han logrado subsanar eficazmente en el campo de la microfluídica.

Esta tesis doctoral se desarrolla en la frontera entre la LP-TEM y la microfluídica. Su principal objetivo es elevar la LP-TEM a una técnica cuantitativa para el estudio de la dinámica a nanoescala en medio líquido *natural*. Para ello, se aplican conceptos establecidos en microfluídica a reactores de flujo LP-TEM.

Esta tesis ha logrado una comprensión profunda del transporte de masa en reactores de flujo LP-TEM. Se ha desarrollado un método bimodal que combina modelos numéricos con experimentos de flujo para estudiar la convección y la difusión en geometrías de canal 3D *realistas*. Dicho método permitió revelar elementos estructurales cruciales de los reactores microfluídicos LP-TEM que son cruciales para definir la convección o la difusión como mecanismo dominante de transporte de masa. Se establecieron parámetros hidrodinámicos característicos como base cuantitativa para la comparación de dichos reactores de flujo. Asi mismo, se evaluó el potencial y, lo que es más importante, las limitaciones de las diferentes configuraciones para los experimentos de flujo.

Además, esta tesis contribuye a mejorar la comprensión de los artefactos inducidos por haces de electrones en escenarios de flujo. Cuando los líquidos se exponen a radiaciones ionizantes como los haces de electrones sufren un proceso denominado radiólisis que, brevemente, describe la generación de numerosas especies químicas, muchas de ellas altamente reactivas. Por lo que es probable que estas especies acaben reaccionando con la muestra investigada interfiriendo con el estímulo aplicado. Se amplió un modelo numérico de difusión y reacciones establecido con la física del flujo en reactores LP-TEM para evaluar el efecto del flujo en la red de reacciones de radiólisis que se despliega. La respuesta de la red de reacción resultó ser altamente no lineal: mientras que unas especies se eliminan eficientemente, la concentración de otras especies de gran relevancia (H^- & e_h^-) crece. Los parámetros experimentales, como la velocidad de flujo y la composición de la solución, alteran la respuesta de la red de reacción de la radiólisis y pueden permitir controlar la composición de la solución irradiada, al menos hasta cierto punto. Finalmente, los resultados se analizaron en el contexto del transporte de masas en geometrías de canales *realistas*.

El conocimiento adquirido hasta este punto se aplicó para desarrollar nuevos reactores de flujo LP-TEM que careciesen de los inconvenientes mencionados y por tanto mejoran la dinámica de intercambio de solutos en > 2 órdenes de magnitud. En numerosas aplicaciones LP-TEM occure que la difusión es el mecanismo de transporte de masa preferido frente a la convección, ya que hay menos riesgo de que la muestra sea expulsada fuera del área de visión limitada. En consecuencia, se han desarrollado *diffusion cells* (celdas de diffusion) en los que la difusión es el mecanismo de transporte dominante. Se fabricaron prototipos virtuales y físicos de *diffusion cells* mediante un procedimiento de creación rápida de prototipos. El principio de funcionamiento de *diffusion cells* se demostró con éxito mediante el método bimodal establecido que indica su versatilidad para los reactores de flujo LP-TEM. El novedoso diseño de la *diffusion cell* garantiza una renovación eficaz y una mezcla rápida (sustitución en cuestión de segundos) en el área de visualización (IA), al tiempo que asegura la compatibilidad con una amplia gama de muestras y configuraciones de portamuestras existentes. Se realizaron modelos validados por experimentos para demostrar las ventajas del nuevo diseño: 1) la rápida sustitución de la solución se demostró mediante la dinámica de nanopartículas metálicas inducida por disolventes, mientras que 2) la renovación superior de la solución se demostró durante estudios in-operando de nano-catalizadores en condiciones electroquímicas exigentes, superando ampliamente las limitaciones anteriores.

En conclusión, los métodos teóricos y experimentales desarrollados en esta tesis doctoral han permitido acceder al conocimiento cuantitativo de los procesos de transporte de masas en reactores microfluídicos LP-TEM. La infraestructura establecida se ha demostrado eficaz para el desarrollo de reactores de flujo a medida y la mejora de métodos experimentales mejorados para una amplia gama de casos de uso. La tesis proporciona recomendaciones para la selección de reactores LP-TEM que garanticen unas condiciones experimentales adecuadas para una gran variedad de muestras y procesos. Se ha conseguido mostrar la contribución del transporte de masa calibrado y el desenredo de los efectos del haz para ampliar los límites del LP-TEM tanto en subcampos existentes como en subcampos nuevos. Los resultados presentados en este trabajo contribuyen a que la LP-TEM sea más cuantitativo, abriendo el camino a valiosas observaciones *in situ* e in-operando.

Zusammenfassung

Die Flüssigphasen-Transmissionselektronenmikroskopie (LP-TEM) ist eine aufkommende Technik zur Charakterisierung von Proben in flüssiger Umgebung. Zusätzlich zur Probenmorphologie, die bereits mit der Kryo-Elektronenmikroskopie (cryo-EM) in gefrorenen Medien sichtbar gemacht werden kann, verspricht LP-TEM Einblicke in die Dynamik im Nanometerbereich unter *nativen* Bedingungen. Die Entwicklung von Flüssigkeitszellen (LCs), versiegelten Einschlüssen von sub-mikrometerdünnen Flüssigkeitsschichten, war entscheidend für den Schutz der Probe vor den harschen Bedingungen in einem Elektronenmikroskop und hat Forschungsbereiche von Material- bis hin zu Biowissenschaften vorangetrieben. Die zugänglichen Informationen beschränkten sich jedoch weitgehend auf qualitative Beobachtungen, da die Prozesse in der LC schwer zu kontrollieren sind und viele experimentelle Parameter die Messung beeinflussen. Die Einführung quantitativer Methoden, einschließlich der Kalibrierung der angewandten Stimuli und der Kontrolle der durch die Elektronenbestrahlung verursachten Artefakte, ist entscheidend für den zukünftigen Erfolg der Technik.

LP-TEM-Durchflussreaktoren sind vielversprechende Vorrichtungen, um zu dieser Entwicklung beizutragen, da sie einen Flüssigkeitsaustausch in der LC und damit die Kontrolle über die Zusammensetzung der eingeschlossenen Reaktionslösung ermöglichen. Ihre Herstellung wurde durch Mikrofabrikationstechnologien vorangetrieben, die es ermöglichten, die komplexen Designkriterien für mikrofluidische Geräte zu erfüllen, die mit dem Aufbau eines Elektronenmikroskops kompatibel sind. Um ihr Potenzial für die Vielzahl von Proben voll auszuschöpfen, müssen verschiedene Herausforderungen bewältigt werden, darunter das Verständnis und die Kontrolle von Massentransportdynamiken und strahleninduzierter Chemie.

Die Mikrofluidik ist ein Forschungsgebiet, das das Verhalten von Flüssigkeiten in kleinen Kanälen untersucht, die in der Regel weniger als einen Millimeter groß sind. Ihre zahlreichen Vorteile gegenüber *klassischer* Batch-Chemie, einschließlich des geringen Probenverbrauchs, der gut definierten Mischungsdynamik und der Integrierbarkeit von Methoden zur Probencharakterisierung, haben das grundlegende Verständnis des Stofftransports in Strömungsreaktoren vorangetrieben und die Mikrofluidik in zahlreichen Forschungsbereichen wie beispielsweise der Bio- und Nanotechnologie etabliert. Durch die rationelle Gestaltung von Kanalgeometrien und standardisierten experimentellen Verfahren konnte eine hervorragende Kontrolle über den Stofftransport in verschiedenen Strömungsszenarien erreicht werden. Mit anderen Worten: Viele der Wissenslücken in der LP-TEM wurden auf dem Gebiet der

Mikrofluidik effektiv geschlossen.

Diese Doktorarbeit bewegt sich an der Grenze zwischen LP-TEM und Mikrofluidik. Ihr Hauptziel ist es, LP-TEM in eine quantitativen Technik für die Untersuchung von nanoskaligen Dynamiken in *nativer* flüssiger Umgebung zu entwickeln. Dazu werden die in der Mikrofluidik etablierten Konzepte auf LP-TEM-Durchflussreaktoren angewendet.

In dieser Arbeit wurde ein tiefes Verständnis des Stofftransports in LP-TEM-Durchflussreaktoren erreicht. HIerzu wurde ein bimodaler Ansatz entwickelt, der numerische Modelle mit Strömungsexperimenten kombiniert um für Konvektions- und Diffusionstransport in realistischen 3D-Kanalgeometrien zu studieren. Der Ansatz ermöglichte es, entscheidende Strukturelemente von mikrofluidischen LP-TEM-Reaktoren aufzudecken, die entweder Konvektion oder Diffusion als dominanten Stofftransportmechanismus definieren. Zusätzlich wurden charakteristische hydrodynamische Parameter ermittelt und als quantitative Grundlage für den Vergleich verschiedener Strömungsreaktoren etabliert. Die Möglichkeiten und vor allem die Grenzen der verschiedenen Systeme für Strömungsexperimente wurden bewertet.

Desweiteren leistet diese Arbeit einen wichtgen Beitrag zum Verständnis von strahleninduzierten Artefakten in Strömungsszenarien. Wenn Flüssigkeiten ionisierender Strahlung wie Elektronenstrahlen ausgesetzt werden, unterliegen sie einem Prozess, der Radiolyse genannt wird. Kurz gesagt, beschreibt Radiolyse die Entstehung zahlreicher chemischer Spezies, von denen viele sehr reaktiv sind. Diese Spezies reagieren mitunter mit der zu untersuchten Probe und überlagern mit dem angelegten Stimulus. Ein etabliertes numerisches Reaktionsdiffusionsmodell wurde um die Strömungsphysik in LP-TEM-Reaktoren erweitert, um dessen Auswirkungen auf das sich entfaltende Radiolyse-Reaktionsnetzwerk zu bewerten. Die Antwort des Reaktionsnetzwerks erwies sich als stark nichtlinear: Während einige Spezies effizient entfernt werden, steigt die Konzentration anderer weitgehend relevanter Spezies ($H^.$ & e_h^-) an. Es wurde festgestellt, dass experimentelle Parameter wie die Fließgeschwindigkeit und die Zusammensetzung der einströmenden Lösung die Antwort des Radiolyse-Reaktionsnetzwerks verändern und gegebenen Falls verwendet werden können um die Zusammensetzung der bestrahlten Lösung zumindest bis zu einem gewissen Grad zu kontrollieren. Schließlich wurden die Ergebnisse im Zusammenhang mit Stofftransport in realistischen Kanalgeometrien diskutiert.

Die oben gewonnenen Erkenntnisse wurden zur Entwicklung neuartiger LP-TEM-Durchfluss-systeme eingesetzt, die die Nachteile der bestehenden Systeme nicht aufweisen und die Dynamik des Lösungsaustauschs um mehr als zwei Größenordnungen verbessern. Für zahlreiche LP-TEM-Anwendungen ist die Diffusion der bevorzugte Massentransportmechanismus, da die Gefahr, dass die Probe aus dem begrenzten Sichtbereich herausgespült wird, geringer ist als bei Konvektion. Es wurden *diffusion cells* (Diffusionszellen) entwickelt, bei denen die Diffusion der dominierende Transportmechanismus ist. Virtuelle und physische Prototypen von *diffusion cells* wurden in einem Schnellverfahren (Rapid Prototyping) hergestellt. Das Funktionsprinzip der *diffusion cells* wurde erfolgreich durch den zuvor etablierten bimodalen Ansatz demonstriert, der seine Vielseitigkeit für LP-TEM-Durchflussreaktoren beweist. Das neuartige Design der *diffusion cells* gewährleistet eine effiziente Erneuerung und eine schnelle Durchmischung (Austausch innerhalb von Sekunden) im Sichtbereich, während gleichzeitig die Kompatibilität mit einer Vielzahl von Proben und bestehenden Probenhaltern gewährleistet ist. Um die Vorteile des neuen Designs zu demonstrieren, wurden Modellexperimente durchgeführt: 1) Die schnelle Erneuerung der Lösung wurde durch die lösungsmittelbedingte Dynamik metallischer Nanopartikel demonstriert und 2) die überlegene Erneuerung der Lösung wurde durch in-operando-Studien von Nanokatalysatoren unter schwierigen elektrochemischen Bedingungen nachgewiesen, die weit über die bisherigen Grenzen hinausgehen.

Zusammenfassend lässt sich feststellen, dass die in dieser Dissertation entwickelten theoretischen und experimentellen Methoden Zugang zu quantitativen Erkenntnissen über Massentransportprozesse in mikrofluidischen LP-TEM-Systemen bieten. Die geschaffene Infrastruktur ermöglicht die Entwicklung von gezielt konzipierten Durchflussreaktoren und verbesserten experimentellen Methoden für ein breites Anwendungsfeld. In dieser Arbeit werden weiterhin Leitlinien für die Auswahl von LP-TEM-Systemen diskutiert, um geeignete Versuchsbedingungen für eine Vielzahl von Proben und Prozessen zu gewährleisten. Es wird außerdem gezeigt, welchen Beitrag kalibrierter Massentransport und die Entkopplung von Strahleffekten zur Erweiterung der Grenzen von LP-TEM sowohl in bestehenden als auch in neuen Teilbereichen leisten. In einem breiteren Kontext tragen die in dieser Arbeit vorgestellten Ergebnisse dazu bei, dass LP-TEM quantitativer wird und wertvolle *in situ* und in-operando Beobachtungen möglich werden.

List of Dissemination

Peer-reviewed Publications as First Author

- <u>S. Merkens</u>, G. De Salvo, J. Kruse, E. Modin, C. Tollan; M. Grzelczak, A. Chuvilin, Quantification of reagent mixing in liquid flow cells for Liquid Phase-TEM, *Ultramicroscopy*, 245, 113654 (2023).

- <u>S. Merkens</u>, G. De Salvo, A. Chuvilin, The Effect of Flow on Radiolysis in Liquid Phase-TEM flow cells., *Nano Express*, 3 (4), 045006, (2023).

- <u>S. Merkens</u>, C. Tollan, G. De Salvo, K. Bejtka, M. Fontana, A. Chiodoni, M. Grzelczak, A. Seifert, A. Chuvilin, Towards sub-second Solution Exchange Dynamics in Liquid-Phase TEM Flow Reactors, *Nature Communications*, *in review*.

Further Publications

- J. Kruse, <u>S. Merkens</u>, A. Chuvilin, M. Grzelczak, Kinetic and Thermodynamic Hysteresis in Clustering of Gold Nanoparticles: Implications for Nanotransducers and Information Storage in Dynamic Systems, *ACS Appl. Nano Mater.*, 3, 9, 9520–9527 (2020).

- S. A. Mezzasalma, J. Kruse, <u>S. Merkens</u>, E. Lopez, A. Seifert, R. Morandotti, M. Grzelczak, Light-driven Self-Oscillation of Thermoplasmonic Nanocolloids, *Applied Materials*, 2302987 (2023).

- Y.Yao, J. Feijóo, V. Briega Martos, Q. Li, M. Krumov, <u>S. Merkens</u>, G. De Salvo, A. Chuvilin, J. Jin, H. Huang, C. J. Pollock, M. B. Salmeron, C. Wang, D. A. Muller, H. D. Abruña, P. Yang, Operando Methods: A New Era of Electrochemistry, *Current Opinion in Electrochemistry*, *accepted*.

- K. Bejtka, M. Fontana, C. Gho, <u>S. Merkens</u>, A. Chuvilin, A. Chiodoni, Electrochemical liquid phase TEM in aqueous electrolytes for energy applications: the role of liquid flow configuration, *Nature Communications*, *in submission*.

- J.Kruse, <u>S. Merkens</u>, M. Grzelczak, Making Sense of the Fourth Dimension in the Dynamic Self-Assembly of Nanoparticles, *in preparation*.

- (<u>S. Merkens</u>, G. De Salvo, J. Kruse, M. Dukes, E. Modin, C. Tollan, M. Grzelczak, A. Chuvilin, Fluidic liquid-phase TEM - Towards flow-controlled composition of reaction media, *Wiley Analytical Science*, 4, 28-31 (2020).)

Previous Publications

- <u>S. Merkens</u>, M.Vakili, A. Sánchez-Iglesias, L. Litti, Y. Gao, P. V. Gwozdz, L. Sharpnack, R. H. Blick, L. M. Liz-Marzán, M. Grzelczak, M. Trebbin, Time-Resolved Analysis of the Structural Dynamics of Assembling Gold Nanoparticles, *ACS nano*, 13 (6), 6596-6604 (2019).

- M. Vakili, <u>S. Merkens</u>, Yunyun Gao, Paul V. Gwozdz, Ramakrishna Vasireddi, Lewis Sharpnack, Andreas Meyer, Robert H. Blick, Martin Trebbin, 3D Micromachined Polyimide Mixing Devices for in Situ X-ray Imaging of Solution-Based Block Copolymer Phase Transitions, *Langmuir*, 35, 32, 10435–10445 (2019).

Glossary

ADF annular dark field.

AFM atomic force microscopy.

AuNP gold nanoparticle.

BF bright field.

BP bypass.

BSPP bis(p-sulfonatophenyl) phenylphosphine.

C&D convection & diffusion.

CA chronoamperometry.

CAD computer-aided design.

CE counter electrode.

cryo-EM cryogenic electron microscopy.

CV cyclic voltammetry.

EC electrochemistry.

EC-LC electrochemical liquid cell.

EELS electron energy loss spectroscopy.

EM electron microscopy.

FE finite element.

FIB focused ion beam.

GLC graphene liquid cell.

IA imaging area.

IP interface point.

LC liquid cell.

LFC liquid flow cell.

LP-TEM liquid-phase transmission electron microscopy.

MEMS micro-electromechanical systems.

MP mixing point.

NC nanochannel.

PTA phosphotungstic acid.

R&F radiolysis & flow.

RE reference electrode.

SAXS small-angle X-ray scattering.

SiN silicon nitride.

STED stimulated emission depletion microscopy.

STEM scanning transmission electron microscopy.

TEM transmission electron microscopy.

UV-vis ultraviolet-visible.

WE working electrode.

Contents

Chapter 1

General Introduction

An ancient english proverb says that "seeing is believing" reflecting the importance that anglophone societies have assigned to optical sensations.[1] As other senses as well, the sense of sight can be tricked easily. Such *artefacts* are commonly referred to as optical illusions. Not without reason, a widespread wisdom that tutors teach their students in academia phrases "Do *not* believe what you are seeing!". Yet, the historical relevance of sight in natural sciences resonates in the term *observable*, which describes a physical quantity that can be measured to characterize a sample.[2]

The fraction of the world that is directly perceivable through the *scientist´s eye* is restricted to a few hundreds of micrometers.[3] However, macroscopic material properties are typically determined at the microscopic level, *i.e.,* in the range of micrometers and smaller - far below the *natural* resolution limit. The development of magnifying tools thus became a necessity to satisfy the ongoing seek for knowledge and technological evolution in modern societies. Microscopes are laboratory instruments to examine objects below the resolution limit of the blank eye.[4] One of many crucial breakthroughs in microscopy was the invention of electron microscopes by Ruska and Knoll in 1931.[5] Electron-based imaging allowed for atomic resolution leading to new insights which have revolutionized numerous domains ranging from materials to life science.[6]

One research field that largely benefited from advances in microscopy is nanotechnology. Nanotechnology aims at understanding and controlling the morphology of matter in the order of one billionth of a meter - the nanoscale (10^{-9} m).[7] At this scale, materials

tend to exhibit new properties, such as optical or catalytic, varying drastically from those of the bulk material.[8, 9] Controlling the morphology of nanomaterials implies controlling their functionality eventually leading to technological innovation. Nanotechnology impacts fields comprising energy storage & conversion, catalysis, information technology and nanobiomedicine.[10]

A significant number of nanomaterials are either fabricated or operating in liquid environment.[11, 12] Unfortunately, liquid samples are poorly compatible with the requirements posed by conventional electron microscopy (EM) which relies on high vacuum inside the microscope's column. Thus, characterizing the *real* morphology and gaining insights into dynamic processes, *e.g.,* movement, formation and function, of nanomaterials in *native* liquid environment have been challenging ever since.

As illustrated in **Fig. 1.1**, expanding the capabilities of EM has always been crucial to keep up with experimental requirements. For that reason, new sample preparation and imaging routines have continuously been developed. The most trivial way to deal with liquid samples is to image it in its dry/dried state. Therefore, tiny amounts of sample solution are drop-casted on a beam-transparent support material. Once dried, the material is inserted into the microscope and imaged at high resolution. In this way, EM propelled research related to samples whose properties are largely independent of their hydration state. A typical example is the morphological and compositional characterization of inorganic nanomaterials with atomic resolution.[13, 14, 15] Despite its advantages, the approach is strongly limited, as hydrated structures and dynamics remain inaccessible. Moreover, artefacts often arise during the sample preparation process causing ambiguities in the image interpretation.

Cryogenic electron microscopy (cryo-EM) aims to overcome some of the discussed limitations by cooling the sample to cryogenic temperatures and/or embed them in vitreous water.[17] This allows for *in situ* structural characterization of nanoscale objects in their hydrated yet frozen state. Cryo-EM had large success for samples whose properties, both morphology & functionality, strongly depend on the presence of a hydration layer.[18] In biology and (bio-)chemistry, it contributed to the structure revelation of numerous (bio-)organic molecules (*e.g.*, enzymes) or engineered compound materials. The main limitations of the technique is the drastically reduced sample mobility at low operating temperatures as freezing the liquid largely prevents *realistic* observation of nanoscale dynamics.

Liquid-phase transmission electron microscopy (LP-TEM) is a recent EM technique
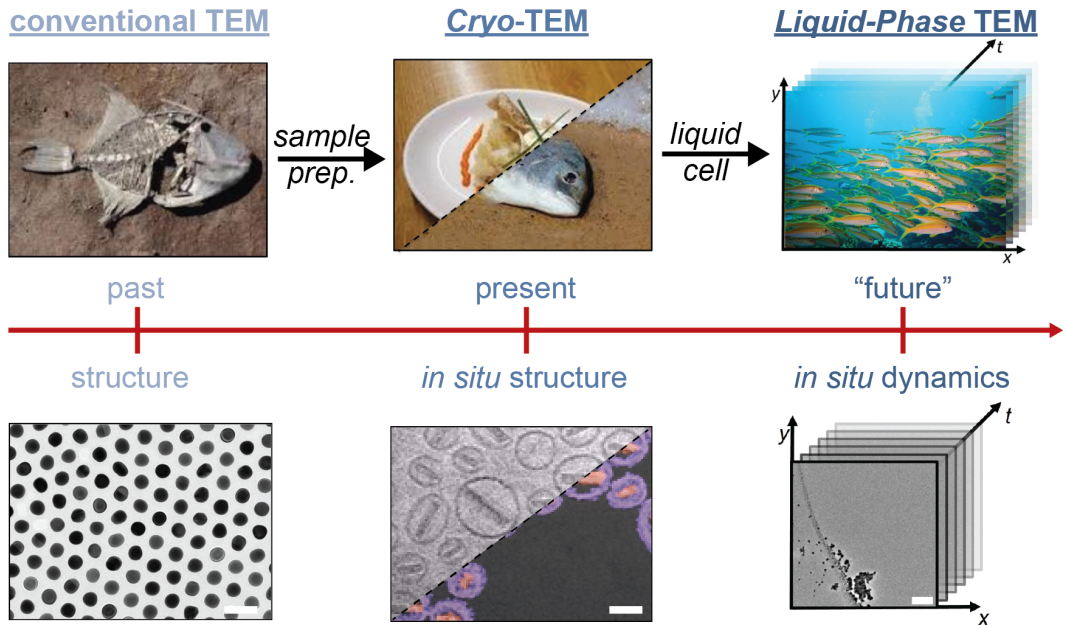
Figure 1.1: The Evolution of Electron Microscopy. Liquid samples are incompatible with the high vacuum in the microscope's column. New sample preparation methods provide increasingly realistic experimental conditions. The figure was compiled from refs. [16] & [17] (scale bars: 100 nm) and copyright-free stock images.

promising to overcome the aforementioned challenges and thus to image nanoscale samples and processes in *native* liquid environment.[19, 20, 21, 22] LP-TEM relies on liquid cells (LCs), sealed enclosures of tiny amounts of liquid solution between two ultrathin electron-transparent membranes, which separate the liquid from the microscope column's vacuum, while ensuring transparency for the electron beam.[23] **Fig. 1.2** shows a LC assembly which is typically integrated into customized sample holders.[22, 24] As also illustrated in **Fig. 1.2**, such setups were successfully used to image *samples & processes* in liquid sample environment with nanometer resolution despite the *inherent issues* associated with the technique.[22] *In situ* structural characterization of various samples extended the boundaries in research areas comprising energy storage, (electro-) catalysis and virology.[25, 26, 27] Many of these observations benefited from confinement effects; the enhanced interaction of the sample with the membrane surface drastically reduces the movement of the sample and enables imaging.[28, 29] Even more intriguing than structural characterization is the study of nanoscale dynamics. One intrinsic challenge when studying dynamics is that, apart from thermal motion, processes need to be triggered by applying a stimulus inside the

LC Historically, the electron beam itself has widely served to induce nanoscale dynamics mediated through a process called radiolysis.[30, 31] In brief, radiolysis describes the generation of highly reactive chemical species by irradiating liquids with ionizing radiation.[32] These beam-mediated experiments have mostly provided qualitative observations of processes like the formation, growth and self-assembly of nanoparticles.[30, 33] However, recent meta studies highlighted the strong dependence of observed phenomena on the imaging conditions.[31] This has prohibited correlating the results of LP-TEM experiments to those of *ex situ* scenarios.[34] In many cases, the beam-mediated stimulus differed from that used *ex situ*, leading to altered observations prone to miss-interpretation.[35]

In response to these shortcomings, the LP-TEM community identified two main challenges for advancing the field: 1) the understanding and mitigation of beam effects, foremost radiolysis, and 2) the integration of *external stimuli* into the LC setup.[36, 37] Considerations on radiation-induced artefacts have recently gained importance in the interpretation of LP-TEM experiments. Theoretical understanding was propelled by the development of numerical reaction kinetic models describing the reaction network unfolding between radiolytic species by adapting knowledge from nuclear reactor research dating back to the beginning of the 20th century.[37, 38] In parallel, strategies to mitigate the effect of radiolytic species were pursued. The principal mitigation strategy involves using chemical scavenger molecules added to the reaction solution, which ideally react selectively with those species that might interfere with the sample/process of interest.[39] Despite promising initial achievements, both approaches are still in their beginnings and need to be further elaborated.

Advances regarding the integration of *external stimuli* were propelled by high precision fabrication such as micro-electromechanical systems (MEMS) technology. Stimuli that were incorporated (alongside) in LP-TEM setups comprise heating, electric biasing, electromagnetic radiation as well as changing the composition of the enclosed liquid (compare **Fig. 1.2**).[26, 40, 41, 42] Within this comprehensive list, controlling the solution composition is a distinctive feature because historically it is presumably the most fundamental stimulus for processes in liquid media. However, it places significant demands on the LP-TEM setup, as the enclosed sample must be connected to liquid reservoirs outside the microscope. A broad variety of customized and commercial flow reactor designs have been developed enabling exchange of the solution inside the LC.[43, 44, 45, 46, 47] Notably, as with the other stimuli, solution exchange dynamics are still poorly calibrated, so that studies remain limited to
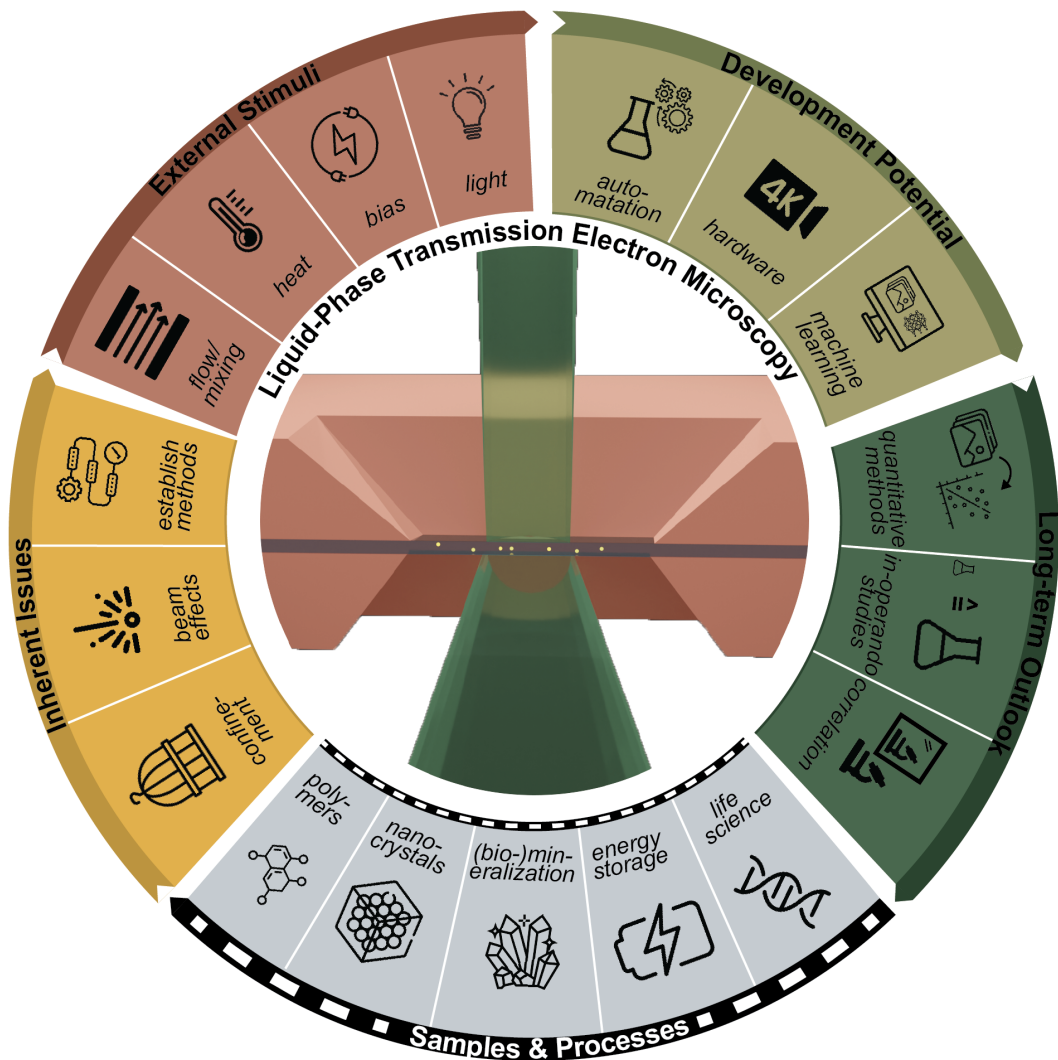
Figure 1.2: Liquid-Phase Transmission Electron Microscopy (LP-TEM). LP-TEM relies on liquid cells (LCs) forming thin enclosures of sample solution which are transparent to the electron beam. The technique's inherent issues, available external stimuli, development potential and long-term perspective are illustrated.

qualitative insights. For instance, self-organization of bio- and inorganic matter as well as degradation dynamics of energy storage and catalytic materials were tracked at near-atomic scale highlighting the potential of *in situ* LP-TEM.[48] Thus, the perception in the community is growing that accurate calibration of integrated stimuli is essential for acquiring reliable experimental data as it would ensure correct attribution of the observed dynamics

to the applied stimulus while superimposed beam effects could be excluded without doubt.

In the context of the two opening quotes of this manuscript (p. 1), the current state of LP-TEM can be described as scientific pubescence. Impetuously acquired qualitative observations are increasingly scrutinized while the *potential* to develop LP-TEM into a quantitative technique is increasingly recognized. The *long-term outlook* of LP-TEM can be envisioned as generating quantitative data under precisely controlled experimental conditions resembling those of conventional laboratory-scale experiments, thus ensuring correlatability with other characterization techniques (compare **Fig. 1.2**). This development is hampered by two bottlenecks, namely 1) the limited understanding of mass transport dynamics in the LC and 2) the lack of standardized procedures for time-resolved experiments and image data analysis.[49] These vacancies are particularly surprising given that most have already been addressed successfully in other research fields such as optical microscopy, data science & machine learning as well as microfluidics (compare **Fig. 1.2**).[16, 31, 50]

Microfluidics can be regarded as a platform technology which discusses the behavior, precise control and manipulation of fluids in micrometer-sized channels.[51, 52] Profound understanding of mass transport mechanisms within complex flow reactor setups has been acquired.[53, 54] Together with standardized experimental methods, this enabled precisely controlled reaction environments.[55, 56] These laboratory-like conditions gave rise to numerous *lab-on-a-chip* applications in the scope of highly interdisciplinary studies involving biology, chemistry, physics and medicine.[57, 58] Concerning nanotechnology, microfluidics contributed to improvements in the fabrication as well as characterization of nanomaterials and their processes in *native* liquid environment.[59] Microfluidic mixing reactors further facilitated the synthesis of well-defined nanoparticles and their assemblies.[60] In addition, the integration of time-resolved characterization techniques, *e.g.*, small-angle X-ray scattering (SAXS) and ultraviolet-visible (UV-vis) spectroscopy, revealed structural dynamics with temporal and spatial resolution in the microsecond and nanometer range.[16, 61]

As mentioned above, an increasing amount of LP-TEM systems are being designed as microfluidic reactors which enables the advantages associated with microfluidics to be transferred to the context of LP-TEM.[62] In conclusion, the knowledge on basic physics and flow reactor design gained in related microfluidics areas has the potential to propel the development of LP-TEM into a quantitative characterization technique (*lab-in-the-microscope*).

Chapter 2

Scope & Objectives

Microfluidics and electron microscopy are, taken individually, two research fields with proven track record when it comes to controlling and observing dynamic processes at the nanoscale. LP-TEM is an emerging EM technique which has shown significant advantages for sample characterization in *native* liquid environment. LP-TEM systems are increasingly set up as microfluidic reactors, enabling a wide range of experiments under flow conditions. However, due to the limited expertise in the community, LP-TEM is currently at a critical stage of development where it can greatly benefit from the knowledge established in the field of microfluidics.

The branch of LP-TEM which is based on flow experiments is experiencing a turbulent phase because of the extremely diverse experimental requirements. On one side, research questions related to material engineering, such as nucleation, growth and self-assembly, require well defined and rapid mixing dynamics; on the other side, electrochemical experiments often rely on the efficient flushing of species to maintain stable imaging conditions. Nevertheless, convenient methods for flow experiments are barely established, although a variety of microfluidic devices, both customized and commercial, are available. However, their mass transport characteristics are largely unavailable; either unknown, or not made accessible by commercial providers on purpose. Thus, choosing the adequate LP-TEM flow reactor and operation conditions for each use case is nearly impossible due to the lack of reliable calibration data. The continuous creation of reactive species under irradiation, *i.e.,* radiolysis, further adds to the complexity. In many cases, insufficiently calibrated stimuli and the poor understanding of beam effects are thus limiting success and credibility of the technique. To

strengthen LP-TEM as a powerful characterization technique in fields comprising materials, bio- and (electro-)chemical research, the introduction of quantitative methods and the development of calibrated setups are essential.

This doctoral thesis presents major advances in LP-TEM methodology by applying microfluidic concepts to understand and control mass transport in microfluidic LP-TEM reactors. In this context, the overall goals of this thesis are to 1) develop general methods to understand and quantify mass transport phenomena in LP-TEM flow reactors, 2) understand and control the effect of electron beam irradiation in realistic experimental scenarios, 3) apply the acquired knowledge to develop quantitative methods and optimize setups for LP-TEM experiments and 4) demonstrate their benefits in purposefully executed experiments.

This work combines experimental and theoretical methods. The core experimental work was conducted using multi-inlet LP-TEM flow reactors. Experimental concepts to calibrate solution exchange dynamics of the flow devices and to control nanoscale processes were largely adapted from microfluidics. The theoretic methods used primarily comprised numerical modelling. Various finite element models were implemented to describe the mass transport in *realistic* flow channel geometries and to investigate the effect of liquid flow on the radiolytic reaction network. Validated mass transport models further played an important role in the prototyping of flow devices with customized solution exchange characteristics.

The major part of this doctoral thesis, *i.e.,* LP-TEM experiments and numerical simulations, was performed in the Electron Microscopy group of the Collaborative Research Center (CIC) nanoGUNE BRTA (San Sebastian, Spain). Collaborations established with internal and external groups had indispensable impact on the thesis: Additional experiments were conducted in the Colloidal Systems Chemistry group of the Material Physics Center (CFM; San Sebastian, Spain) and the Advanced Materials for Sustainable Future Technologies group of the Istituto Italiano di Tecnologiá (IIT, Torino, Italy). Industrial partners contributed to the prototyping of new flow channel setups (Mechanics and Industrial Production department at Mondragon University, Mondragon, Spain) and provided scientific equipment such as LP-TEM sample holders & chips (Protochips Inc., Morisville, USA) and pumping systems (Elveflow, by Elvesys, Paris, France).

The doctoral project has led to valuable outcome, which was published in different sci-

entific articles and presented at international conferences. A full list of achievements is provided in the List of Dissemination (p. XIV). Therein, three of the manuscript are first author publications, which according to Chapter XI of the *Regulations Governing the Management of Doctoral Studies* of the University of the Basque Country (UPV/EHU), qualifies for presenting a *thesis by published papers* (*tésis por compendio de publicaciones*).[1] Thus, the presented thesis follows the structure outlined below, which diverges from the format of a *traditional* doctoral thesis.

Chapter 3 provides the theoretical framework for this thesis. It describes the fundamental aspects of conventional & liquid-phase electron microscopy as well as microfluidics. **Chapter 4** outlines the methods and materials underlying the conducted work addressing both experimental methods and numerical modelling approaches. **Chapter 5** summarizes the outcome of the thesis. The first part is dedicated to the calibration of mass transport mechanisms in LP-TEM flow reactors, and the development of prototypes with customized solution exchange properties. The benefits of the improved properties are illustrated in several model experiments with relevance in material engineering, energy storage and catalysis. The second part focuses on the effect of convective transport on the radiolysis reaction network under continuous electron beam irradiation. Where appropriate, the reader is referred directly to the corresponding articles to provide deeper understanding. The three central research articles are appended at the end of this manuscript (Appendix A, p. 125 ff.). **Chapter 6** finally presents the general conclusions of the thesis. Therein, the acquired knowledge on and control over mass transport in LP-TEM flow reactors are highlighted and the implication of developed methods are discussed based on various use cases. Finally, a concise outlook on the evolution of LP-TEM into a quantitative and correlative experimental technique is presented.

---

[1]S. Merkens *et al.*, *Nature Communications*, *in review* is a pre-print and had not yet been accepted for publication on the day this thesis was presented. However, the *Regulations Governing the Management of Doctoral Studies* allows a *thesis by published paper* on the basis of two accepted manuscripts if the student can count with two additional research articles published in line with the scope of the thesis within five years prior to the enrolment in the doctoral program (https://www.ehu.eus/en/web/doktoregoa/doctoral-thesis/thesis-by-published-papers, accessed 31.05.2023). The articles S. Merkens, *et al.*, *Langmuir*, 2019 and M. Vakili, S. Merkens, *et al.*, *ACS nano*, 2019 comply with said requirements (refer to p. XIV; *Previous Publications*).

Chapter 3

Fundamentals

3.1 Electron Microscopy - A concise Introduction

3.1.1 From Light to Electron Microscopes

The term *microscope* was coined by Giovanni Faber in 1629 to describe scientific instruments for observing (*scope*) objects smaller than the resolution limit of the unaided human eye (*i.e., microscale*).[4] The first microscopes were simple arrangements of two glass lenses that allowed for magnification of up to 10x by using visible light for imaging. During the following four centuries, the capabilities of light microscopes were greatly enhanced, mainly due to advances in glass lens fabrication technology. Magnification of up to 1000x was achieved, which revolutionized scientific research, foremost biology, as even individual particles of some hundreds of nanometers could be resolved.[4, 63]

Already in 1873, however, Ernst Abbe revealed that the resolution of light microscopes, as with all wave-based methods, would be limited by the diffraction of the imaging beam.[64] This limitation is formulated in the Abbe criterion (Eq. 3.1):

$$d = \frac{\lambda}{2 \cdot NA},$$

(3.1)

where λ and NA are the wavelength of the light used for imaging and the numerical aperture of the objective lens. According to Eq. 3.1, the minimum distance, d, for two adjacent objects to be distinguishable in a projected image is proportional to λ and $1/NA$. For optimized microscope setups (*e.g.*, immersion objectives: $NA \approx 1.4$), the Abbe limit is about $\lambda/2.8$, *i.e.*,

$d \approx 0.2$ µm, determined by the relatively large wavelength of visible light ($\lambda \geq 400$ nm).[4]

Numerous approaches aimed at increasing the resolution of light microscopes, but their success has been limited. One approach was to further reduce the imaging wavelength using X-rays.[63] Given the shorter wavelength, X-rays posses higher energy than visible light which caused challenges in the development of X-ray microscopes, including the fabrication of (diffraction-based) lens systems and increased sample damage due to ionization.[63] Recent X-ray microscopes could demonstrate nanometer-scale resolution, but the complexity and cost of the equipment required, comprising X-ray sources, lenses and detectors, are still damping their success.[63] Other approach to improve resolution rely on novel methods to generate image contrast.[4] For instance, stimulated emission depletion microscopy (STED) uses fluorescent dyes to emit light when selectively excited under electromagnetic irradiation.[65] This has enabled image resolution as low as $d \approx 20$ nm. Despite the intriguing insights obtained into biological samples, a fundamental drawback of STED imaging is its limitation to samples compatible with fluorescent staining.[4] This option is ruled out in the majority of research areas. Moreover, many structural phenomena occur at even smaller (sub-)nanometer scale.[63]

In the late 19th century, a revolutionary approach to overcome the diffraction limit of wave-based microscopes emerged: using particles for imaging.[6] Shortly after the discovery of the first elementary particle, the electron, efforts began to build such a device. A decisive advancement was the invention of electromagnetic lenses by Busch in 1926 which enabled the path of electron beams to be manipulated (in good analogy to glass lenses for a light beam).[66] Finally, in 1931, the first working electron microscope was presented by Ruska and Knoll.[5] With 17x, its magnification was only slightly higher than that of the first light microscopes 300 years earlier, but still far from the theoretic Abbe limit assigned to them.[6] This crucial benchmark was surpassed shortly after, in 1933, when Knoll showcased an updated prototype, with magnification up to 12000x, far exceeding the resolution limit of light microscopes (at that time).[63] In 1938, the first commercial prototype was announced by Siemens company (Germany) with reported spatial resolution of 10 nm.[63]

However, the enthusiasm of the nascent EM community was dampened when becoming aware of the work of De Broglie, in which particles, such as the electron, were assigned wave properties (Eq. 3.2):[67]

$$\lambda_{\mathrm{B}} = \frac{h}{p}. \tag{3.2}$$

In Eq. 3.2, λ_B is the wavelength assigned to a particle with momentum p; h denotes Planck's constant. The momentum, and thus the wavelength, of accelerated electrons can be calculated from their energy (Eq. 3.3):[63]

$$p = \sqrt{2m_0 e V_{acc}\left(1 + \frac{eV_{acc}}{2m_0 c^2}\right)}. \tag{3.3}$$

In Eq. 3.3, V_{acc}, m_0, e and c denote the acceleration voltage, the electron's rest mass, the elementary charge and the constant speed of light, respectively. The *intimidating* conclusion from Eq. 3.2 was that the resolution of electron microscopes might also be limited by diffraction.[68] As Ruska recalled during his Nobel lecture in 1987,[69] it was not until the wavelength of accelerated electrons was calculated that the true potential of electron microscopy was realized. According to Eq. 3.2 & 3.3, acceleration voltages $V_{acc} \leq 300$ keV typically used in modern electron microscopes correspond to $\lambda_B \approx 2$ pm. This wavelength is 5 orders of magnitude shorter than that of visible light and nearly 80% of its speed, theoretically short enough to enable *sub-atomic* resolution.[70]

In practice, however, the resolution of electron microscopes, and thus their success, remained limited to much higher values ($\sim$2 Å) for decades after their invention.[71] The limitation was due to imperfections of the electron optics, including chromatic (C_c) and spherical (C_s) aberration which led to blurring and distortion of the acquired images.[72] The development of correction systems has been pivotal in improving resolution approaching the theoretic limit. In 2009, Sawada and co-workers achieved sub-50 pm resolution with a C_s-corrected transmission electron microscope operated at $V_{acc} = 300$ keV, which was crucial for three-dimensional imaging of atomic structure.[71, 73] Recently, in 2020, aberration-corrected setups were reported to enable reconstruction of cryo-EM images at atomic resolution (1.22 Å was achieved for mouse apoferritin).[18] These latest developments finally established EM as powerful and versatile imaging technique. Efforts to further improve the imaging capabilities of electron microscopes are continuing.[74]

3.1.2   Imaging Modes in (Electron) Microscopy

Microscopes generate enlarged representations of objects in a process called imaging. Different modes can be employed for imaging comprising continuous irradiation and scanning probe mode.[4, 72] In the continuous irradiation mode, magnifying lenses project the ob-

ject plane in the imaging plane. An image can be acquired by placing a detector screen in the image plane. Geometric (using ray diagrams) and physical (using wave description) optics were developed to describe the formation of an image, and related artefacts.[68] The image magnification depends on the power of the objective lens. In the scanning mode, a focused probe is rastered across the sample to excite it on well-defined locations.[75] A variety of different signals is generated, depending on the microscope type, which can be detected with adequate detectors.[63] The time-dependent signal can thereby be associated with spatial information on the sample. In the scanning mode, the magnification is defined by the size of the raster. Both imaging modes can be applied in modern EMs, making them dual-mode (TEM/STEM) instruments.[63] **Fig. 3.1** illustrates conventional transmission electron microscopy (TEM) and scanning transmission electron microscopy (STEM) setups.

Conventional and scanning TEM are characterized by numerous differences including sample requirements, contrast formation and achievable image resolution.[63] In the context of this thesis, the most relevant difference is the spatio-temporal deposition of electron dose across the sample as illustrated in **Fig. 3.2**. In TEM mode, electrons are distributed stochastically but in average, *i.e.*, over long timescales, homogeneously across a large region (μm^2). In STEM mode, the beam is focused to spot sizes of a few square-Ångström ($Å^2$) resulting in a much higher local dose that is directed to ever changing locations across the sample. In conclusion, at the same accumulated dose, *i.e.*, dose rate integrated over time, the spatio-temporal electron bombardment experienced by a sample varies drastically between TEM and STEM irradiation. This aspect becomes particularly relevant in the context of radiation damage (compare Ch. 3.1.3.3).

3.1.3   Beam Sample Interaction

Image formation in microscopy relies on the interaction between the probe beam and the atoms of the sample. While in (transmitted) light microscopy this interaction is predominantly the absorption of photons; electron scattering is the underlying mechanism in electron microscopy. Scattering occurs either elastically or inelastically. In elastic events, the momentum of the incident electron is changed while its kinetic energy is conserved (see Ch. 3.1.3.1); whereas in inelastic events, neither momentum nor energy are conserved (Ch. 3.1.3.2). These different types of interaction provide a rich variety of mechanisms to generate signals suitable for image formation (Ch. 3.1.3.4). However, scattering events with substantial energy transfer can damage the irradiated sample (Ch. 3.1.3.3).
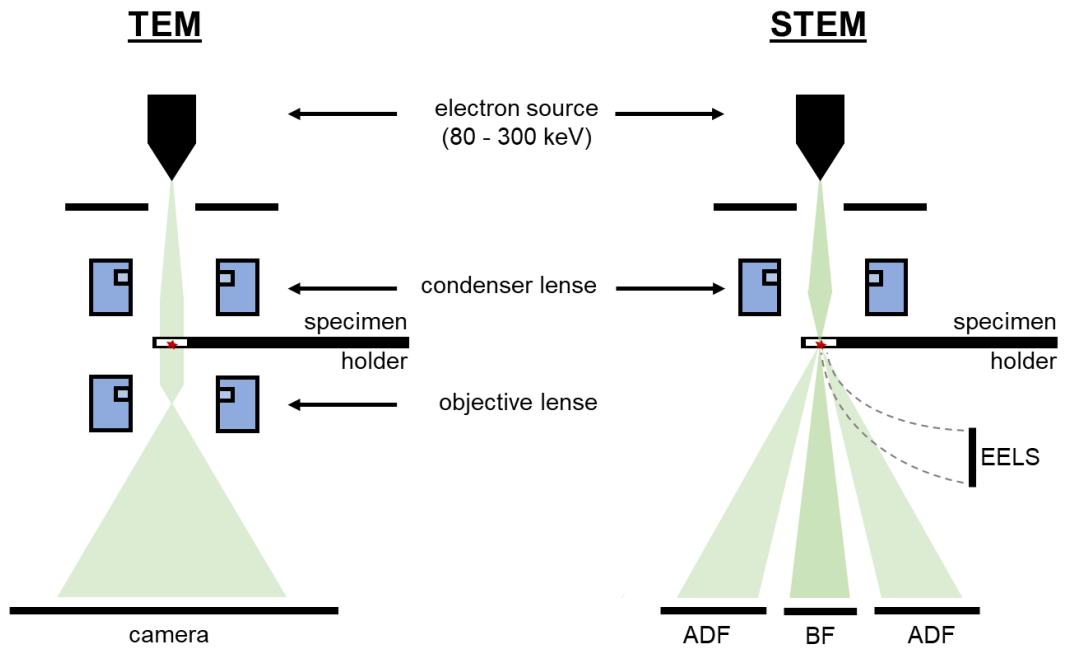
Figure 3.1: Imaging Principles of a Transmission Electron Microscope. In TEM mode, the sample is uniformly irradiated by an electron beam over a larger area. In STEM mode, the sample is irradiated locally by a focused electron beam. The possibility to detect various signals in STEM is illustrated by detectors for annular dark field (ADF) & bright field (BF) imaging and electron energy loss spectroscopy (EELS).
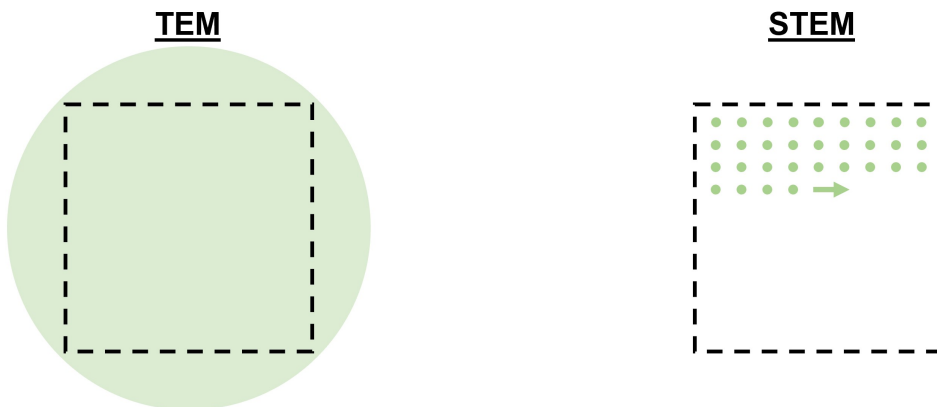
Figure 3.2: Continuous Irradiation (TEM) and Scanning (STEM) Imaging Mode. *Green areas/black dashed frames* indicate the irradiated/projected fraction of the sample under continuous/scanning mode irradiation, respectively.

3.1.3.1 Elastic Scattering

In elastic scattering, only the momentum of the incident electron changes resulting in the deviation from its initial path. The scattering occurs at the gradient of the electrostatic potential of the sample's atom(s) which is highest near the nuclei where the entire positive charge is localized. Nuclei therefore scatter to significantly higher angles compared to the electron cloud, typically up to a few degree, but scattering angles up to $\sim 180^{\text{o}}$ are possible (backscattering). The probability for scattering events to occur is expressed in the corresponding (differential) scattering cross-section which depends on various parameters, *e.g.*, the atomic number. The relevant parameters are excessively discussed in standard textbooks;[63, 75] however, more noteworthy in this context is the fact that elastically scattered electrons stay coherent, *i.e.*, they keep a constant phase relation (with themselves). This is advantageous to obtain sharp interference patterns which is typically exploited to generate diffraction contrast during high-resolution imaging (compare Ch. 3.1.3.4).[63, 72, 76, 77]

3.1.3.2 Inelastic Excitations

In inelastic scattering, in addition to deviation of its path, the electron transfers substantial energy to the sample exciting electronic or vibrational degrees of freedom. In contrast to elastic scattering, inelastically scattered electrons loose coherence. Various inelastic interaction mechanisms exist whose corresponding cross sections depend on the sample properties,[76] but generally decrease with increasing transferred energy: Scattering from phonon modes in crystalline solids leads to energy losses in the sub-electronvolt range. Electronic intra- & interband transitions, cathodoluminescence and valence ionization involve the transfer of a few electronvolts, while plasmon excitations occur at up to a few tens of electronvolts. Several tens of electronvolts are also transferred during knock-on displacement of bulk atoms. Even higher amounts of energy of a few hundreds of electronvolts are required for atomic core-level ionization.[63, 75]

Excited states resulting from the outlined interaction mechanisms tend to release energy in relaxation processes. These processes comprise the emission of particles, *e.g.,* secondary & Auger electrons, or electro-magnetic radiation, *e.g.,* X-rays, and enable additional analytic STEM imaging routines as illustrated in **Fig. 3.1** (*e.g.,* EELS).[72, 77]

3.1.3.3   Radiation Damage

If the energy transfer from the electron of the incident beam to the sample and its consequences cannot be compensated for, radiation damage occurs. The electron threshold above which the sample undergoes (irreversible) changes depends on the material properties defining the dominant damage mechanism. In conductive samples, knock-on damage is most relevant. Knock-on damage describes the displacement of atoms within the sample (or their ejection from the surface) as a result of high-angle scattering. Other damage mechanisms are suppressed due to the high density of delocalized electrons in conductive samples. In non-conductive solids, the most relevant mechanisms are ionization and bond breaking/rearranging resulting from inelastic scattering at the electron cloud. This is due to the poor capability to compensate for charge accumulation and to dissipate energy. In liquids, particularly water, ionization processes initiate secondary chemical reactions, which affect the sample much longer than the initial scattering event.[78] The spatio-temporal progression of this damage mechanism is decisively influenced by the diffusion of the beam-generated species. While diffusive expansion is largely contained in cryo-EM, the radiolytic species are more mobile in liquid media affecting a much larger volume. Given its relevance for LP-TEM, a separate chapter provides detailed information thereon (see Ch. 3.2.3 on radiolysis). Radiation damage may be reduced by adjusting irradiation conditions, such as acceleration voltage & imaging mode (see above), and sample properties (compare Ch. 3.1.4 on sample preparation).[63, 72, 75, 77]

3.1.3.4   Image Contrast

TEM/STEM images are generated based on electrons (or radiation) reaching a detector (screen) after interacting with the sample. The mechanisms of contrast formation are based on the interactions discussed in Ch. 3.1.3.1 & 3.1.3.2 and described in detail in textbooks.[63, 72, 75] Typically, a differentiation is made between phase and amplitude contrast, where the latter either arises due to coherent, *i.e.,* diffraction contrast, or incoherent scattering, *i.e.,* mass-thickness contrast.

Phase contrast is suited to resolve small-scale features in the sample based on interference phenomena. The phase of an electron wave cannot be measured directly, but phase differences between waves originating from different parts of the sample interfere which leads to contrast in slightly defocused TEM images. To achieve reasonable phase contrast in an image, a precise microscope setup is needed. Phase contrast has been beneficial to resolve

atomic lattices and interfaces within them, *i.e.,* grain boundaries, at high magnifications (>500.000x).[63, 72, 75]

Diffraction contrast is crucial for the imaging of crystalline samples. Diffraction can be understood through Bragg's law in analogy to X-ray diffraction: constructive interference between scattered electrons only arises under certain angles with respect to the incident direction where it results in Bragg peaks. The location of the peaks depends on the wavelength of the incident beam and the spacing between the atomic layers acting as diffracting planes. While poly-crystalline samples generate ring diffraction patterns, spot diffraction patterns are recorded for single crystals. Either the undiffracted (bright field image) or the diffracted (dark field) beam can be used to generate image contrast by selecting the appropriate objective aperture; under ideal conditions, *i.e.,* all scattered electrons can be collected, the two images are complementary. Diffraction contrast has been of outstanding importance for the study of crystalline materials comprising lattice orientation, defects and grain boundaries.[63, 72, 75]

Mass-thickness contrast is the most fundamental contrast mechanism and most relevant in non-crystalline samples with varying thickness and composition. Parts of a sample that are relatively thick and/or comprise, on average, higher atomic number lead to stronger scattering compared to parts that are thinner and/or posses a lower *effective* atomic number. Image contrast is achieved by *cutting* the scattered beam with an objective aperture resulting in thick/dense parts appearing darker than electronically less dense regions. Mass-thickness contrast does not rely on coherence of the beam and therefore provides good contrast for amorphous materials. If the thickness is constant, mass-thickness contrast is quantitative regarding the composition of the sample,[63, 72, 75] which is highly relevant for this thesis.

A convenient quantitative definition of contrast, C, is based on the difference in transmitted intensity, ΔI, between two adjacent regions, #1 and #2 with intensity $I_{T,1}$ and $I_{T,2}$, in an image. Eq. 3.4 denotes the definition of contrast according to Weber.[75]

$$C = \frac{I_{T,2} - I_{T,1}}{I_{T,1}} = \frac{\Delta I}{I_{T,1}} \tag{3.4}$$

In the general case, the transmitted intensity, I_T, which is detected at a given location on the screen corresponds to a fraction (I_T/I_0) of the intensity, I_0, of the incident beam:

$$\frac{I_T}{I_0} = exp(-\rho_s z).\tag{3.5}$$

In Eq. 3.5, ρ_s and z are the combined elastic & inelastic scattering power and the thickness of the irradiated sample, with $\rho_s = 1/\lambda_{mfp}$ and λ_{mfp} being the mean free path. ρ_s depends primarily on the imaging conditions and the composition of the material.[72, 75] While the dependence on imaging conditions requires calibration, the latter allows tracking of compositional changes, for instance *via* solution replacement in LP-TEM flow experiments (compare Ch. 3.3.3.3).

3.1.4 Sample Preparation

An electron microscope setup poses a set of prerequisites that have to be fulfilled by the sample to ensure high-quality imaging. The most relevant prerequisites are 1) compatibility with the high vacuum inside the column, 2) low sample thickness to ensure transmission of the electron probe, 3) minimum resilience under high-energy electron bombardment, and 4) conductivity of the sample to avoid charging effects.[63, 72, 75] Intrinsically, most samples are incompatible with these aspects when in *native* state urging for adequate sample preparation.

Much of the success of EM has been due to tedious sample preparation strategies which were developed to improve the compatibility of an ever increasing number of samples.[63, 72, 75] For instance, the excision of thin lamella *via* focused ion beam (FIB) cutting enabled the preparation of cross-sections of a variety of macroscopic samples. Moreover, depositing ultra thin layers of conductive materials through sputter coating is conveniently applied to avoid charging of non-conductive solid samples. A suitable strategy to increase compatibility of aqueous samples is cryogenic freezing. In cryo-EM, samples are maintained at low temperatures enabling for structural characterization of various biological samples in *realistic* environment. Dealing with samples in liquid state is tremendously more challenging; however, the expected benefits of imaging nanoscale dynamics have motivated a new generation of scientists to develop preparation techniques for liquid samples.[22] Ch. 3.2 aims at providing profound information thereon.

3.2   TEM in Liquid Phase

A large number of materials exists and undergoes processes in liquid media. Their characterization in *native* environment *via* EM imaging is a long-standing desire in materials science which is complicated by three main issues: 1) the poor compatibility of liquids with the high vacuum inside an electron microscope, 2) poor image contrast and limited electron transmission through solvent layers thicker than a few hundred of nanometers and 3) ionization and following beam damage upon high-energy electron irradiation of solvent molecules.[22] Efforts to overcome these fundamental problems have shaped the current state of *in situ* EM techniques for liquid phase processes. By today, the field of LP-TEM has become the most relevant technique for a broad range of samples and processes (see Ch. 3.2.4).[22] This evolution was thanks to the invention of the LC concept (Ch. 3.2.1) and despite issues resulting from sample confinement (Ch. 3.2.2) and beam-induced artefacts (Ch. 3.2.3).

3.2.1   The Liquid Cell (LC) Concept

Handling liquids inside the vacuum of an electron microscope is crucial to achieve information under *native* conditions. Early approaches relied on differential pumping, which creates pressure gradients inside the microscope's column providing moderate vapour pressures in proximity to the sample.[79, 80] Imaging techniques relying on this concept are usually referred to as environmental or wet-(S)TEM. Due to very specific sample requirements, *i.e.*, high effective vapour pressures, only a limited number of samples has been successfully imaged. Reported examples include biological cells or wet surfaces as well as ionic liquids and hydrogels.[80, 81, 82] Beyond that, environmental and wet-(S)TEM lack generalizibility to resolve challenges related to aqueous samples such as *in situ* structural characterization of biological samples, nucleation, growth and self-assembly of nanoparticles as well as electrochemistry and catalysis.[83]

In 1944, a more general concept was introduced: the liquid cell (LC).[84] In LCs, tiny amounts (picoliter) of sample solution are enclosed between two electron beam-transparent membranes forming a liquid layer thin enough to provide sufficient contrast during TEM imaging. An easy and cheap way to fabricate LCs is by sandwiching two graphene sheets resulting in enclosed droplets of typically a few tens of nanometers in thickness (compare **Fig. 3.3a**).[85, 86, 87] Thus, static graphene liquid cells (GLCs) are particularly interesting for high (near atomic) resolution imaging of nanoscale samples and beam-induced dynamics.
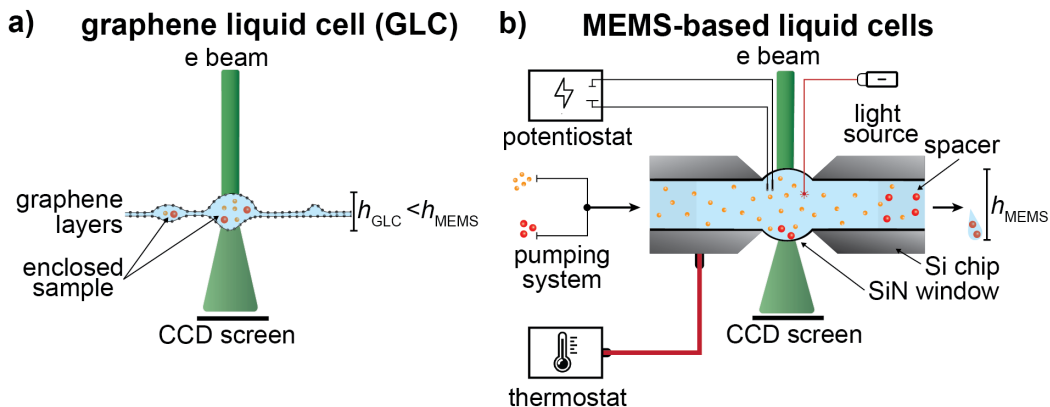
Figure 3.3: The Liquid Cell (LC) Concept. Picoliter droplets of sample solution are enclosed between beam transparent windows to avoid evaporation inside the high vacuum of the microscope. **a)** GLCs enable for high resolution imaging of primarily beam-induced dynamics due to ultra-thin liquid layers ($10 < h_{\text{GLC}} < 100$ nm). **b)** MEMS-based technology improved reproducibility of LC fabrication and enabled integration of stimuli, comprising heating, biasing, solution exchange and electro-magnetic radiation ($50 < h_{\text{MEMS}} < 1000$ nm).

Beyond that, the use of GLCs is limited by distinct drawbacks comprising poor controlability and large polydispersity of the created enclosures as well as limited integratability of external stimuli.[88]

Based on recent advances in MEMS-based fabrication techniques, another LC concept was introduced in which two MEMS-chips are assembled in the tip of modified TEM sample holders. In 2003, Ross and co-workers presented chips that were equipped with ceramic thin films, *i.e.,* silicon nitride (SiN), as window materials and separated by spacers.[89] Spacers provide control over the liquid layer thickness, typically between several tens to hundreds of nanometers.[62] Pressure differences between the enclosed liquid and the microscope's vacuum can lead to additional bulging of the thin film membranes resulting in effective liquid thickness of up to 1 µm in the center of the IA.[90]

The main advantage of MEMS-based systems is the flexibility regarding the LC design. For instance, microelectronics elements can be integrated during additional fabrication steps to make external stimuli available. Setups comprising metal electrodes for electric biasing as well as heating elements were reported.[89] Another highly relevant aspect is solution exchange, as it is used to control a broad range of chemical processes in *classical/ex situ*

mixing and electrochemistry experiments. Realizing solution exchange in LP-TEM setups is challenging as it requires *external* liquid to enter the supposedly sealed (static) LCs.[62]

A broad variety of LC concepts for controlled solution exchange were reported. Static mixing setups are a conceptual extension of GLCs.[91] They combine two liquid reservoirs separated by a sacrificing layer which is perforated by high intensity beam irradiation and thus allows intermixing of solutions from the adjacent reservoirs. This approach is conceptually limited due to the poor reliability & reproducibility in LC formation and non-reversibility of the solution mixing/exchange process. To date, relevant application examples of static mixing cells barely exist.[91]

Flow setups represent a more versatile approach for solution exchange. These systems consist of MEMS-based liquid flow cells (LFCs) which are located in customized microfluidic LP-TEM sample holders. The liquid inside the LFC is connected to liquid reservoirs outside the electron microscope through a tubing system integrated in the sample holder (compare **Fig. 3.3b**). External flow control units provide control over the mass transport through the microfluidic system. A variety of customized and commercial flow systems are available:[43, 44, 45, 46, 47] While, single-inlet designs permit supply[26, 92, 93] or renewal[19, 94] of reaction solutions only, multi-inlet setups additionally enable for replacement or *in situ* mixing.[95] The internal channel geometry of available flow systems is remarkably diverse. Besides very simple theoretic considerations, little knowledge is available about the mass transport in LP-TEM flow systems.[62]

Driven by the success of graphene- and MEMS-based LCs, efforts have urged to combine the advantages of both designs leading to ever more sophisticated designs.[87, 88, 96] LCs of the latest generation combine different external stimuli at controlled liquid thickness, thereby enabling atomic resolution imaging under experimental conditions reflecting the diverse *ex situ* scenarios.[90, 97]

3.2.2 Confinement Effects

Samples are significantly confined inside LCs. In MEMS-based LCs (**Fig. 3.3b**), confinement occurs along the vertical direction parallel to the beam path. To effectively detect the sample, the liquid layer thickness should not exceed a few micrometers at most, however, only a few hundred nanometers are preferable for reasonable image contrast. On the lower end, the liquid thickness may be reduced for high resolution applications, but the size of the sample itself represents an intrinsic limitation.[22]

Due to confinement, the surface-to-volume ratio of the liquid sample is drastically increased in the LC in comparison to macroscopic setups. Therefore dispersed nanoparticles are more likely to approach and interact with the surface charges present at the LC membrane. These interactions can appear both attractive and repulsive depending on the properties of the sample and membrane material, respectively.[98] Interactions with the membrane surface were widely described to alter the movement of the sample leading to non-classical diffusion dynamics, both sub- and super-diffusive.[29, 99] Examples of suppressed sample movement were reported more frequently.[100, 101, 102, 103] Experimental parameters such as the beam properties, *e.g.*, dose rate & irradiation mode, and liquid flow can further alter sample mobility.[104]

Confinement effects are further discussed to impact the mass transport of smaller solutes to and/or away from the IA. Kröger & Verch reported the depletion of precursor during the beam-induced precipitation of calcium carbonate nanoparticles from supersaturated solution in MEMS-based LC setups.[28] Another widespread phenomenon is the nucleation of bubbles upon accumulation of gaseous species, *i.e.*, O_2 and H_2. These species can either be generated in radiolytic or electrochemical processes. Independently, their re-dissolution is drastically aggravated due to confinement in the LC.[105]

3.2.3   Radiation Damage in LP-TEM

Ch. 3.1 demonstrated that the assumption that the electron beam would not damage the sample is a credulous simplification, yet often made in (early) LP-TEM literature.[22] During their passage through a LC setup, beam electrons interact with the sample, the liquid media and the LC membranes. Interactions with the liquid media result in the most relevant damage mechanism through a process called radiolysis. A detailed discussion of radiolysis is provided in Ch. 3.2.3.1 and 3.2.3.2. Further, beam-induced heating of the liquid media is generally considered insignificant.[106, 107] With respect to the membranes, knock-on damage was discussed to potentially alter the surface chemistry of thin films.[91, 108] These effects were discussed to induce electric fields and to affect the surface chemistry of the window surface, respectively, both altering the interaction with confined samples (see Ch. 3.2.2).[106] Moreover, interface processes play a role. For instance, secondary electron emission from the thin film membranes and the sample was discussed to affect the adjacent liquid media.[109]

3.2.3.1 Radiolysis of Water

Radiolysis describes the scission of molecules, most importantly water, upon high-energy ionizing irradiation resulting in the generation of molecular, ionic and radical species.[110] Deep understanding of radiolysis was acquired in the context of nuclear reactor engineering during the first half of the 20th century.[32] The radiolytic processes that are initiated upon the initial interaction (at $t = 0$ s) between a single irradiating electron and water can be separated in three stages which are referred to as the physical, physico-chemical and chemical stage based on the character of the dominant mechanisms.[38, 78, 110] The stages are illustrated in **Fig. 3.4**.

The physical stage ($t < 10^{-15}$ s) describes the energy deposition during the initial beam-molecule interaction when a high-energy electron is traveling through the solvent. The energy is deposited locally in space resulting in the formation of either exited water molecule (H_2O^*, *i.e.*, excitation) or ionized water molecules (H_2O^+, *i.e.*, ionization) and electrons - all highly reactive species.[78]

The physico-chemical stage ($10^{-15} < t < 10^{-12}$ s) is determined by numerous rapid processes. These processes include the dissociation, relaxation, auto-ionization of excited states, hydration of electrons, ion-molecule reactions as well as hole diffusion. All together they cause a reaction network of chemical species with increasing complexity to unfold. The chemical species of the network are heterogeneously distributed in a diffuse cloud with a diameter of ~1.2 nm around their point of generation. The term *spur* was introduced to describe this phenomenon.[111]

With proceeding time, the reaction network is increasingly affected by reactions including less reactive species, as emphasized by the terminology chemical stage ($t > 10^{-12}$ s), and diffusion. Diffusion of the radiolytic species leads to the expansion of the spur while the concentrations of the species within it decrease. Under continuous irradiation, spurs are continuously created. Diffusion acts to distribute all radiolytic species homogeneously across the entire irradiation volume within $t \sim 10^{-6}$ s. Thereafter, typically within a few milliseconds, the concentrations of species eventually reach steady-state.[78] The details of the dynamics depend strongly on the spatio-temporal specifications of the irradiation scenario (compare Ch. 3.1), as well as confinement and composition of the liquid.

Chemically the most relevant species that are generated during radiolysis of pristine water encompass hydrogen ($H^.$) and hydroxide radicals ($OH^.$), hydroxide and hydronium ions (OH^- & H^+), hydrogen peroxide (H_2O_2) as well as molecular hydrogen (H_2) and oxy-
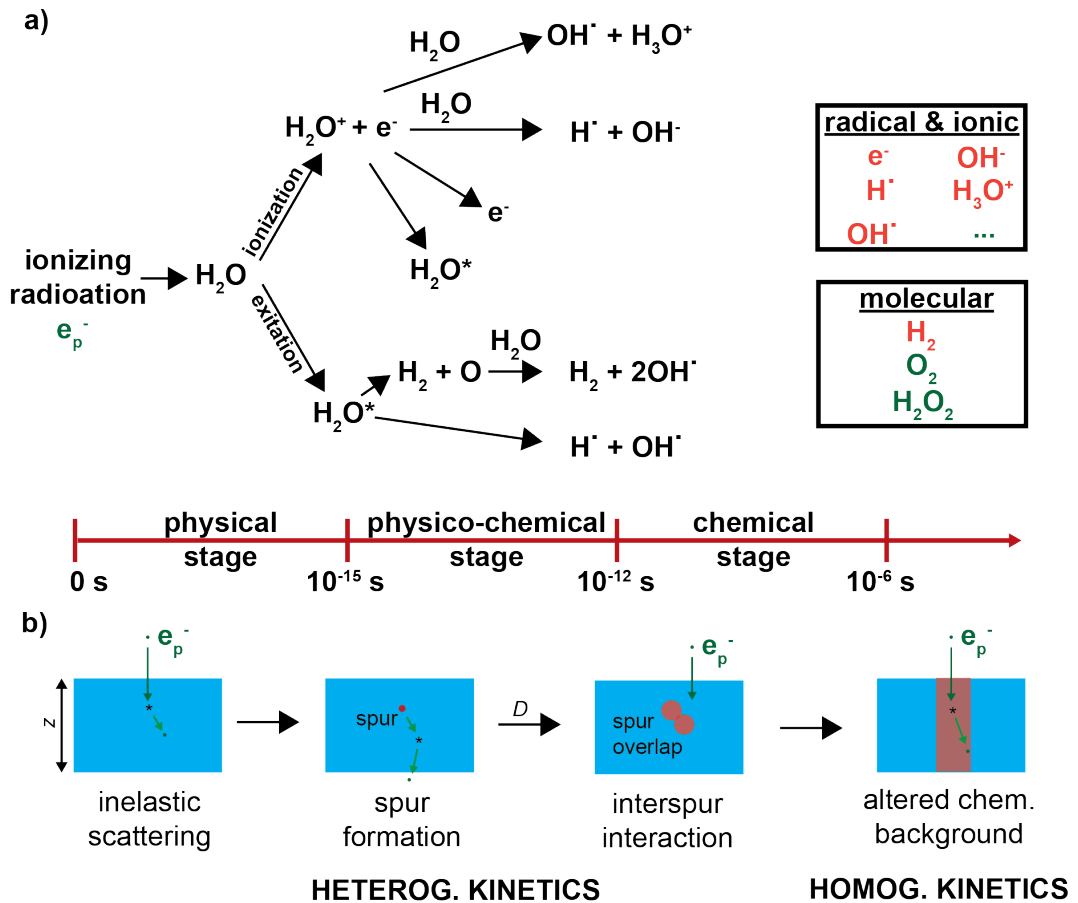
Figure 3.4: The Stages of Radiolysis in Water. a) Upon irradiation of water, excitation and ionization processes cause a complex chemical reaction network of radical, ionic and molecular species to unfold. **b)** At short time scales, radiolysis is spatially localized and the kinetics are strongly heterogeneous. After $t \sim 1$ µs of ongoing irradiation, it but transitions into a homogeneous regime. The figure was inspired by Le Caer.[110]

gen (O_2). To facilitate analyses of the reaction network, radiolytic species are categorized based on different properties.[37] In the context of chemical experiments, the classification according to their oxidizing or reducing capabilities, their reactivity with other species or functional groups or tendency to condensate in gas bubbles appears most useful. For more fundamental spatio-temporal analysis, the categories *primary* (e_h^-, H^+, OH^-, OH^-, H^-, H_2, H_2O_2) and *secondary* (O_2, O_3, *etc.*) species are more beneficial. *Primaries* are those species

formed directly in the relaxation process of radiolysis, *i.e*, those present at $t = 10^{-6}$ s, while *secondaries* result solely from chemical reactions between other species thereafter.

3.2.3.2   Radiolysis in LP-TEM

Radiolysis recently experienced regrowing interest by the LP-TEM community. Approaches to radiolytic effects are twofold. On one side, a deep theoretic understanding & description of radiolytic processes in irradiated reaction media is aspired to explain experimental observations. On the other side, mitigation strategies are evaluated to diminish the effects of radiolytic species on the imaged chemical process. Both aspects are revised below.

Modelling of Radiolysis

Several theoretic models were presented for the theoretic analysis of radiolytic reaction networks.[38, 78, 112, 113, 111] Numerical modelling of radiolysis in the context of LP-TEM was propelled by works of Schneider *et al.*,[37] who adapted previous works of Elliot *et al.*[38] The authors introduced a zero dimensional, time-dependent model that describes the homogeneous phase ($t > 10^{-6}$ s) of radiolysis reaction kinetics in pristine water upon continuous electron beam irradiation. In neat water alone, the chemical model considers 79 reactions between a total of 15 species upon the radiolytic generation of 8 primary species (e_h^-, $H^.$, $OH^.$, H_2, H_2O_2, H^+, $HO_2^.$, OH^-). Radiolytic generation of primary species was implemented based on their so-called G-values. G-values are generation values reflecting the number of molecules created per 100 eV of energy absorbed and were adopted from nuclear reactor research.[37, 78]

The model of Schneider and co-workers was solved in a zero dimensional geometry,[37] corresponding to a homogeneously irradiated media. For dose rates representative for LP-TEM irradiation, concentrations of radiolytic species reach steady-state values of up to a few millimol and within a millisecond in time (compare **Fig. 3.5a**). Steady-state concentrations were further found to increase with dose rate of the incident electron beam (**Fig. 3.5b**). The numerical model was exploited to understand experimental observations and improve experimental conditions reducing beam effects. However, the limited spatial and chemical complexity restricts the success of the 0D model for *realistic* LP-TEM scenarios with its main application being GLCs imaged in TEM mode.[104]

The implementation of the reaction-kinetic model in a spatially heterogeneous 1D radially symmetric geometry enabled a more realistic representation of the experimental situation
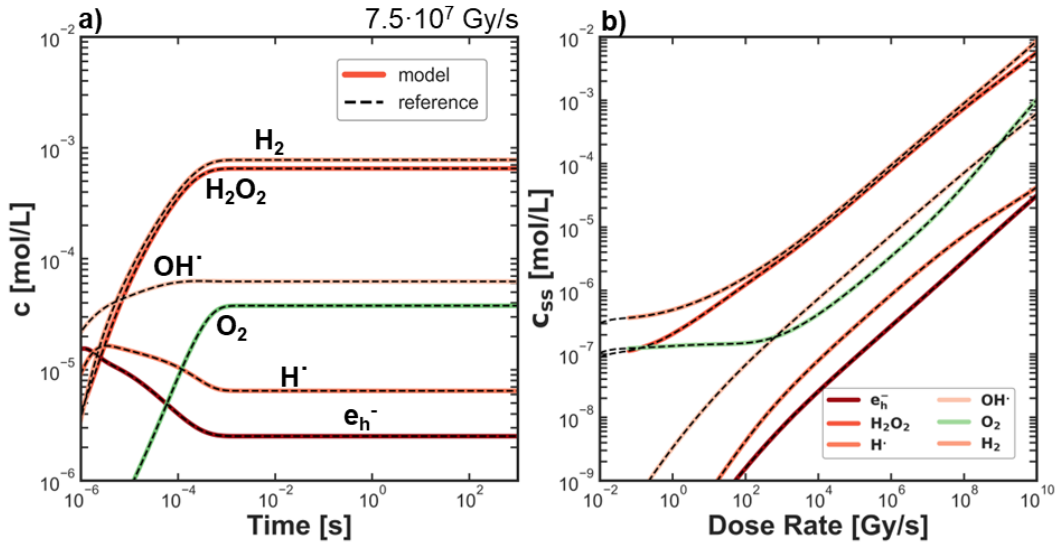
Figure 3.5: Homogeneous Modelling of Radiolysis (0D). Finite element (FE) modelling provides insights into the kinetics of the radiolysis reaction network; steady-state concentrations ($\leq$mM) are reached within microseconds (**a**).[37] The chemical reaction network shows non-linear behaviour with respect to various parameter. For instance, **b)** depicts the steady-state concentrations, c_{ss}, with respect to dose rate. Data of the reference model[37] was reproduced from literature as *dashed black lines* for a selection of species. The dose rate in **a)** was $7.5 \cdot 10^7$ Gy/s, representative for LP-TEM experiments.

comprising larger MEMS-based LCs.[37] In the simulations, the radiolytic generation of primary species was restricted to a small region with radius $r = 1$ µm, and diffusion of all species was modelled within the entire geometry ($r = 50$ µm). Due to diffusion, time-dependent behaviour and steady-state of the concentration are significantly altered depending on the position within the geometry as well as the reactivity of the species (compare **Fig. 3.6**). While more reactive species, *i.e.*, radicals & ions (*e.g.*, e_h^-), tend to exist predominantly within the irradiated region, less reactive, *i.e.*, molecular, species (*e.g.*, H_2) rather accumulate across extended regions over time.[37]

The initial model[37] has undergone continuous improvement and extension by the developers and was adapted by various other research groups, always aiming at better reflecting the complex experimental realities. For instance, more advanced models address aspects including experimental parameters such as temperature,[114] geometrical considerations,[115]
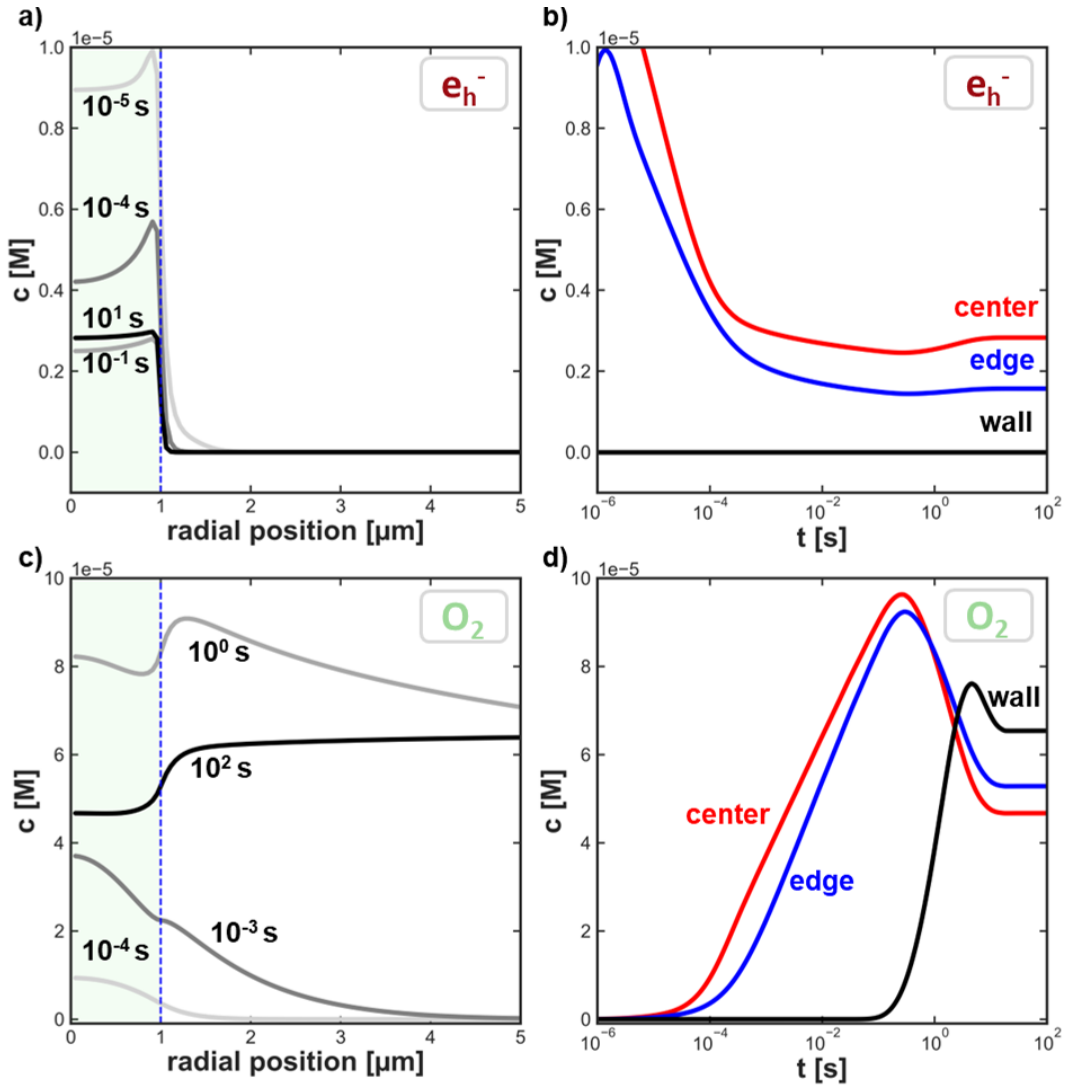
Figure 3.6: Heterogeneous Modelling of Radiolysis. a-d) In heterogeneous scenarios, the kinetics and steady-state values of the concentration of radiolytic species are strongly altered with respect to homogeneous models (compare **Fig. 3.5a**). The spatio-temporal characteristics of concentration profiles depend on the reactivity of the species, *i.e.* radical & ionic (*e.g.* e_h^-, **a** & **b**) or molecular (*e.g.* O_2, **c** & **d**), as well as the location with respect to the irradiating beam. Results are depicted for a beam radius $r = 1$ µm (*green background* in **a** & **c**). Data is reproduced from literature;[37] note that minor divergence from the reference plot (not shown) is due to typos in ref. [37] and improved time-stepping of the here presented computation.

extensions of the chemical reaction systems (beyond pure water) by considering additional species[116] and spatially inhomogeneous energy deposition due to backscattering from metallic nanoparticle.[109]

All these implementations expose several unresolved shortcomings. Foremost, the theoretical understanding was rather uncritically transferred from nuclear reactor science to LP-TEM research, despite the significant differnce in dose rate regimes. Quantitative input parameters of the model, *e.g.,* G-values, have not been validated through experiment, and eventually require adaptation.[117] Moreover, available models lack to precisely represent experimental realities. Irradiation geometries and time regimes tend to be over-simplified; neither three dimensional geometries nor the heterogeneous time regime ($t < 10^{-6}$ s) were considered. Aditionally, a discrepancy between experimentally applied and theoretically modelled imaging modes can be identified (STEM *vs.* TEM). Finally, the effect of applied stimuli on the radiolysis reaction network has been widely overlooked. The coupling of the reaction kinetics to additional physics was non-existing at the moment this thesis was conducted. Physics of particular interest in the context of LP-TEM experiments are mass transport under flow and in electrochemistry scenarios. The implementation of more accurate models is challenging due to the complexity and high computational costs.

In the theoretic description of complex systems with sets of coupled differential equations, non-linearities are a commonly observed phenomenon.[118] In non-linear systems, changing the input does not necessarily cause proportional changes in the obtained output; rather small adjustments to the former may result in significant changes to the latter. The reaction network of radiolysis appears to be such a complex system. In fact, non-linearities of the concentration of radiolytic species were depicted with respect to various input parameters, such as time and dose rate (see **Fig. 3.5a** & **b**), but not further analyzed.[37]

Mitigation Strategies

The development of general concepts for the mitigation of radiolytic effects is less advanced than the modelling of radiolysis. Low dose imaging is currently the most relevant mitigation strategy.[119] By reducing the beam current the local and accumulated dose are drastically reduced, thus also decreasing the amount of radiolytic species that may interfere with the applied stimulus (**Fig. 3.5b**). Low dose imaging was proven particularly useful for samples with high sensitivity to chemical changes and ionizing radiation. At the hypothetical limit

of zero dose irradiation, beam-induced artefacts would entirely vanish. Evidently, this limit remains out of reach since no information could be acquired, when the beam is switched off. Even though technological developments, such as direct electron cameras, led to significant improvements of low dose imaging, further efforts are required.

Another widely discussed mitigation concept involves additives, called scavenger. Scavengers are intentionally added to the reaction solution to themselves react with the radiolytic species forming less reactive species, thereby presumably protecting the investigated process from the impact of the beam. This approach is time-consuming and cannot be generalized since the peculiarities of each irradiated chemical system must be considered individually before adapting its chemical composition to the imaging conditions.[120, 121] In very few cases, experimental efforts were supported with theoretic modelling of radiolysis in engineered reaction networks.[106]

Recently, a more general approach to mitigate accumulation of radiolytic species in the imaged/irradiated volume was postulated in LP-TEM community: applying continuous flow conditions (see Ch. 3.3) to continuously renew the reaction media during the imaging process.[42, 48, 122] To best knowledge, neither systematic experimental nor theoretical works to evaluate this concept were reported by the time this thesis was developed.

3.2.4 State-of-the-Art in LP-TEM Experiments

The recent development of LP-TEM was influenced by the aspects discussed above, including available experimental setups, their limitations, intrinsic beam-induced artifacts, and confinement effects. Collectively, these factors have shaped the range of samples and processes that were investigated, the applicable stimuli, and the established methods for experimental procedures and data analysis. A concise outline of the state-of-the-art unfolds below.

3.2.4.1 Samples, Processes and Stimuli

The investigated nanomaterials exhibit a broad variety in terms of composition (metallic, semi-conductors, bio- and soft matter), shape (isotropic, radially symmetric and asymmetric), surface functionalization (organic, bio-chemical, inorganic molecules), the solvent (aqueous, organic), and their field of application (biomedicine, catalysis, energy storage) demonstrating the versatility of LP-TEM.[21, 48, 123, 124, 125, 126]

Historically, the beam-mediated formation of reactive species (see Ch. 3.2.3.2) has been the only mean to induce processes in LP-TEM scenarios. The electron beam itself was hence

a well-appreciated stimulus to induce dynamics such as the nucleation, growth and clustering of nanoparticles. However, experimental observations started to be deliberately discussed in the context of beam damage just recently. In a meta study, Ou *et al.* demonstrated the relevance of beam damage for a wide range of operation conditions.[31] With the integration of a growing number of stimuli into LC setups, radiolytic effects were increasingly perceived as obstructive artefacts making their thorough consideration, *via* numerical modelling and chemical scavenging strategies (Ch. 3.2.3.2), essential for reliable interpretation.[127, 128] One particularly illustrative example was presented by Korpanty and co-workers. The authors demonstrated the enhancing, respectively mitigating, effect of gold nanoparticles and isopropanol on the beam-mediated degradation of polyethylene glycol molecules in aqueous solution.[129]

Works comprising external stimuli such as heating, electric biasing and solution exchange are growing.[41, 42, 124] Temperature is a fundamental parameter in thermodynamics and kinetics. Thus, heating could provide access to a broad range of self-organization phenomena on the nanoscale.[130, 131] Lee *et al.* succeeded to derive temperature-dependent growth kinetics of nanoparticles from LP-TEM image sequences.[115] Moreover, Ambrozic and co-workers investigated the temperature dependence of beam-mediated precipitation and dissociation of plasmonic nanoparticles.[116]

One of the first examples of electric biasing was presented by Williamson and co-workers who tracked the electro-deposition of copper in customized static LCs in 2003.[89] Since then, electric biasing has developed into the most relevant stimulus being now widely applied for the study of energy materials and electro-catalysts in the context of green energy transformation.[123, 125] Electric biasing experiments are conveniently performed under continuous flow conditions to control the solution composition. In fact, solution renewal aims at refreshing reagents and/or removing reaction products, including radiolytic byproducts.[48] Typical experimental scenarios aim at observing structural modifications during electrochemical potential cycling, *i.e.*, cyclic voltammetry (CV), and dis/charging under constant potential, *i.e.*, chronoamperometry (CA).[26, 132]

In addition to electrochemistry (EC) scenarios, flow conditions were further applied to replicated mixing experiments *in situ*. Multi-inlet setups are used to exchange the reaction media inside the LFC to induce nanoscale processes relevant for material engineering, *e.g.*, nucleation, growth and self-assembly. Until now, convenient examples are rare.[133, 134] For instance, Ou and co-workers successfully revealed the crystallization pathways of nanocubes

induced by altering the buffer concentration by altering the flow conditions.[135]

In conclusion, and for the scope of this thesis, it is crucial to recognize that there are two main scenarios for the application of flow conditions in LP-TEM: continuous solution renewal is mostly required in the context of electrochemistry, while solution mixing/replacement is valuable to study fundamental questions of material engineering. Both scenarios rely on significantly different mass transport dynamics which is addressed in Ch. 3.3.3.

3.2.4.2 From Qualitative Observations to Quantitative Understanding

In the beginnings of LP-TEM, efforts were predominantly conducted to prove the feasibility of TEM imaging in liquid phase and to qualitatively describe observed processes and obtained products.[48] The term *in situ* was established to reflect successful preservation of *native* liquid environment, emphasizing the material's structure. In contrast, the term *operando* refers to scenarios in which the material's functionality is preserved and observed at adequate temporal resolution with no (detectable) beam damage.[125, 136]

Beyond qualitative studies, comprehensive quantitative works are rare and recent. Quantitative approaches exploit image analysis procedures to interpret observations based on quantitative characteristic numbers.[49] Such efforts were supported by theoretic methods providing additional information either through analytical,[137, 138] kinetic,[113, 139, 140, 141, 142] or numerical[137, 143] modelling, eventually combining various.[144] The existing approaches can be classified into two categories. In the first case, independent theoretic approaches only support the interpretation of experimental observations; while in the second case, quantitative experimental numbers directly serve as input parameters for physical models.[113, 139, 145, 146, 147, 148] A common use case of the latter approach comprises the direct calculation of the pairwise interparticle interaction potential from the tracking of nanoparticles in dimerization processes in steady-state and time-dependent scenarios.[139, 146, 147, 148] Thereby, the contributions of fundamental interaction mechanisms, such as electrostatic, van der Waals and steric forces, to the overall interaction could be estimated.[113, 145, 149]

Correlating experimental results from different techniques is a core concept of scientific methodology. Two approaches are possible, *i.e.*, *in situ* studies can be either 1) compared to macroscopic *ex situ* setups, or 2) combined with different *in situ* techniques to measure complementary properties in the very same LC setup.[150] In LP-TEM research, only a few manuscripts stand out currently meeting correlative standards. Kim *et al.* reported

in situ experiments of the 1D self-assembly of triangular gold nanoprisms together with *ex situ* SAXS measurements.[151] The steady-state interparticle spacing was found to be different in both experiments which was assigned to radiolytic effects on the solution's ionic strength altering the equilibrium of electrostatic and van der Waals forces governing the self-assembly process.[151] In another example, Mirsaidov and co-workers were able to enrich the understanding of linker-mediated self-assembly of cysteamine-functionalized, cetyltrimethy-lammonium bromide (CTAB)-capped gold nanorods. LP-TEM imaging revealed different parallel reaction pathways that were previously inaccessible by UV-vis spectroscopy.[152] Representative examples of correlative experiments in similar LC setups was presented by Yang and co-workers.[125, 153] The authors obtained comprehensive insights into structural transformations during CO_2 reduction by combining *in situ* LP-TEM imaging of copper catalysts under electrochemical conditions with operando resonant soft X-ray scattering studies.[154] The revised examples represent valuable groundwork directing the evolution of LP-TEM towards the validated characterization of nanomaterials under *realistic* conditions.

3.2.4.3 Current Limitations

Several bottlenecks define the current state of LP-TEM.[155] Many limitations arise directly from constraints of the experimental scenarios: Spatial and temporal resolutions of LP-TEM is currently limited to a few nanometers and tens of milliseconds under ideal conditions. At these timescales, nanoparticles could easily leave the field of view over the scope of an experiment assuming free Brownian motion. Thus, immobilizing the sample at the window surface is a convenient approach explaining why (electro-)catalysts deposited on electrodes have been heavily investigated.[125] Beyond that, the study of solvent-induced dynamics is strongly limited to processes mediated by the solid-liquid-interface;[156] sub-diffusive behaviour is a commonly observed phenomenon.[149, 157, 158] Beyond that, examples for the observation of freely moving particles in 3D are rare.[159] Those of more complex processes, *e.g.*, self-assembly in *free* solution, remain nonexistent. Developments in hard- and software evolution, *e.g.*, direct electron detectors & machine learning, are promising candidates to improve spatio-temporal resolution and thus to extend the range of accessible processes.[31]

The accumulation of gaseous species in the IA is problematic, particularly during biasing experiments. Gas molecules tend to condensate into bubbles, thereby expelling enclosed liquid from the IA and disrupting *in situ* measurements.[160] The main effort to prevent bubble formation has focused on the design of high flux setups, but their success has been

limited so far.[42, 43] Yang *et al* discussed a distinct perspective on gas enclosures, exploiting the reduced water content for high resolution imaging of the final product.[154]

Further limitations of LP-TEM arise from inadequate methodology. Analysis of raw experimental data, *i.e.*, image sequences, is often insufficient. This is rather surprising given that corresponding post-processing routines have been widely applied in light microscopy for decades.[161] A few authors defined quantitative parameters and demonstrated their benefits for positional and orientational tracking of particle dynamics.[137, 138, 152] For instance, the interparticle distance and relative alignment angles were shown useful to quantify reaction pathways of nanoparticle self-assembly.

Given that LP-TEM is a single particle imaging technique, stochastic methods are needed to ensure adequate interpretation of experimental results.[135, 149, 162, 163] An illustrative example was provided by Tan *et al.*, who observed up to 4 different attachment modes for the pairwise interaction of Au nanocubes.[137] Statistical analysis of the entire data set identified a dominant mode following the *prealigned attachment* pathway.[137] To further extend such routines establishing LP-TEM as reliable and credible sample characterization technique is crucial.

The most relevant limitation in the context of this thesis is the limited understanding of the stimuli integrated in LP-TEM setups, namely electric biasing, heating as well as solution mixing and replacement. It is crucial to calibrate the applied stimuli, especially against the background of radiolytic effects potentially interfering. Only a few examples exist that investigated the integrated stimuli. For instance, van Omme *et al.* presented heat transfer simulations providing a validated illustration of the homogeneity of heating in LC setups.[41] In addition, Fritsch *et al.* developed an experimental approach using diffraction patterns of crystalline gold nanoparticles (AuNPs) and their thermal variation to locally access temperature changes with an accuracy below 3 K,[114] thereby testing the numerical results of van Omme *et al.*[41] In the context of electrochemistry measurements, the successful determination of the potential of the reference electrode was a crucial advancement. In fact, the potential landscape was determined to be shifted by 0.8 V *vs* platinum reference electrodes in *ex situ* setups.[164] At the moment this thesis was elaborated, the understanding of mass transport dynamics in LFCs was limited to fundamental physical intuition with no quantitative data available.[42, 62] The hydrodynamic aspects have hardly played a role in the selection of the *adequate* flow system for LP-TEM experiments. This issue is further accompanied by inadequate methodology. Flow control is barely automatized and occa-

sionally literally left in the hand of the experimenters.[133] These observations are rather surprising considering the well-advanced and standardized methodology of flow experiments in the field of microfluidics (see Ch. 3.3).[51, 52, 165]

3.3   Microfluidics

3.3.1   Principles of Fluid Flow

3.3.1.1   Pressure-Driven Flow

Together with electroosmotic flow, pressure-driven flow is beyond the most relevant flow types in microfluidic devices, constituting approximately 90% of all use cases.[166] In pressure-driven flow, fluid convection results from the difference, Δp, between the pressures applied to the inlet, p_{in}, and the outlet, p_{out}, of a flow channel (Eq. 3.6). The resulting mean flow velocity, $\overline{v}$, is proportional to Δp with the proportionality factor being the product of the cross-section, A, of the flow channel and its flow resistance, R. R itself strongly depends on the channel geometry, *i.e.*, A (see Ch. 3.3.1.4). The product of A and $\overline{v}$ defines the mean volumetric flow rate, Q, which describes the volumetric transport rate (in m^3/s, Eq. 3.7).

$$\Delta p = p_{\mathrm{out}} - p_{\mathrm{in}} = RA\overline{v} \tag{3.6}$$

$$Q = \overline{v}A \tag{3.7}$$

Experimental flow control is achieved through control units such as syringe- or pressure-driven pumping systems. In syringe pumps, the volumetric inflow rate is directly defined according to the injection rate of the syringe; whereas in pressure-driven pumping systems, the inlet and outlet reservoirs of the hermetically sealed setup are individually pressurized so that the requested Q is achieved through a feedback loop. While syringe pumps are the best characterized and most easy to operate, pressure-driven systems benefit from the flexibility to adjust p_{out}, especially in the regime of negative pressures with respect to ambient conditions ($p_{\mathrm{out}} < p_0 = 1$ bar), and higher accuracy.[166] The latter is relevant in the context of window bulging of LFCs. Most flow control units are programmable which enables (semi-)automatic flow control.

3.3.1.2   Laminar & Turbulent Flow Types

When fluids are forced through a channel, their behavior inside the flow channels is complex. The complexity arises due to the interplay of various forces, including viscous, inertia and gravitational forces.[54, 167] These forces, and therefore their importance, scale differently with the channel dimension. Different flow types can thus be defined based on the governing forces. In large (millimeter-sized) flow channels, fluid physics are determined by inertial effects introducing flow instabilities such as turbulences (compare **Fig. 3.7b**). In (sub-)micrometer-sized channels, however, transport is usually determined by viscous dissipation; flow lines are thus barely perturbed and proceed in parallel (**Fig. 3.7a**). Additionally, gravity can be neglected with decreasing channel size. At intermediate conditions, a transitional regime is present where inertia and viscous forces arise to the same order, *i.e.*, laminar flow is increasingly perturbed by evolving instabilities.[54]

Characteristic numbers are crucial to estimate the hydrodynamic properties of flow setups.[51, 167] The Reynolds number, Re, is a dimensionless number to estimate the flow type in a channel. Re is defined as the ratio of inertia to viscous forces in a fluid (Eq. 3.8):

$$Re = \frac{\phi \overline{v} D_{\mathrm{H}}}{\mu},$$ (3.8)

where ϕ, μ and $\overline{v}$ are the density, the dynamic viscosity, and the mean velocity of the fluid, respectively. D_{H} describes a characteristic length of the the hydrodynamic system. For cylindrical flow channels it corresponds to the channel radius r.[167] $Re^* \sim 2000$ denotes the critical Reynolds number at which flow conditions transition from laminar ($Re < Re^*$) to turbulent ($Re > Re^*$). LP-TEM flow systems consist of (sub-)micrometer-sized channels and are operated at moderate flow rates resulting in $Re < 1$. Flow is therefore assumed to fall into the laminar regime.

3.3.1.3   Mean *vs.* Local Flow Velocity in Laminar Flow

Viscous forces determine the interaction between the moving fluid and the fixed channel walls.[51, 167] At the channel wall, the fluid is forced to zero velocity (no-slip condition), while it is free to move in the centre of the channel. In the laminar flow regime, a parabolic velocity profile is thus established along the channel cross-section with maximum velocity (v_{max}) at the radial center and zero at the wall (compare **Fig. 3.7a**). In other words,
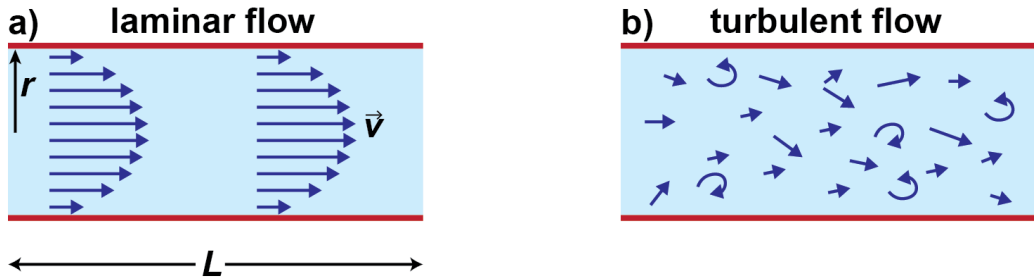
Figure 3.7: Laminar and Turbulent Flow Types. The interplay of forces acting in fluids changes with the channel dimensions which leads to different flow types. In laminar flow, the fluid proceeds on parallel flow lines (**a**), while turbulent flow is characterized by strong instabilities & fluctuations (**b**).

a volumetric flow rate applied can result in drastic differences in the local flow velocity depending on the channel geometry (refer to **Fig. 3.8**).

The mathematical expression of the parabolic velocity profile in channels with circular cross-section is defined by Eq. 3.9, where r defines the radial distance from the center of the channel with radius r:

$$\mathbf{v}(\mathbf{r}) = v_{\max}\left(1 - \left(\frac{\mathbf{r}}{r}\right)^2\right). \tag{3.9}$$

In channels with rectangular cross-section (**Fig. 3.8b**), parabolic velocity profiles in horizontal and vertical direction are superimposed. The velocity gradient in each direction is defined by the width, w, and height, h, of the channel, respectively, requiring adaptation of Eq. 3.9.[167, 168] For channels with rectangular cross-section of extremely high aspect ratios, AR ($AR>1/1000$; Poiseuille plane), the velocity can be assumed constant along the horizontal axis. The parabolic velocity gradient, $\mathbf{v}(y)$, is hence only relevant along the short vertical y-axis (parallel to h). In Poiseuille plane flow, the mean ($\overline{v}$) and maximum ($v_{\max}$) velocities are interconnected: $v_{\max} = 3\overline{v}/2$.[168]

3.3.1.4 Flow Channel Resistance

The flow channel resistance, R, correlates the applied flow rate, Q, with the required pressure difference, Δp, based on the internal geometry of the flow channel (compare Ch. 3.3.1.1). For flow channels with circular cross-section, the flow resistance, R_{circ}, can be calculated

a)

b)

c)
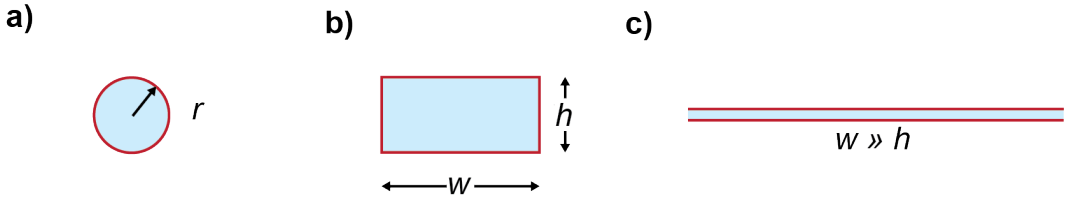
Figure 3.8: Cross-sections of Flow Channels. Illustration of circular (**a**) and rectangular (**b** & **c**) channel cross-sections. The shape of compartments in microfluidic devices can vary significantly affecting their hydrodynamic properties, *i.e.*, different local flow velocities at given volumetric flow rate.

from the kinematic viscosity, η, of the fluid, as well as the length, L, and radius, r, of the channel (Eq. 3.10).

$$R_{\text{circ}} = \frac{8\eta L}{\pi r^4} \tag{3.10}$$

For single flow channels with rectangular cross-section, the flow resistance, R_{rect}, follows Eq. 3.11.[169]

$$R_{\text{rect}} = \frac{4\eta L}{w^2 h^2 F_{\text{i}}} \tag{3.11}$$

In Eq. 3.11, w and h are the width and height of the channel (with $w > h$), respectively. F is a form factor that considers the rectangular cross-section of the channel:[170]

$$F = \frac{w}{3h} - \frac{64w^2}{\pi^5 h^2} \sum_{n=0}^{\infty} \frac{\tanh\left(\frac{(2n+1)\pi h}{2w}\right)}{(2n+1)^5}. \tag{3.12}$$

Various polynomial expressions were developed to approximate F in different ranges of the flow channel's aspect ratio ($AR = h/w$).[170, 171] The expression reported by Bao & Harrison approaches F in the range from AR=0.5 down to 0.05 with a relative standard deviation of <0.5% with respect to the numerical solution of Eq. 3.12.[170] All approximations of the form factor F fail in the range of aspect ratios relevant in LP-TEM with the AR in the LC being in the range of $10^{-3} - 10^{-4}$. Nevertheless, it is crucial to note that the resistance is scaling inversely with the channel cross-section (Eq. 3.10 and 3.11), narrow channels require drastically increased pressures to reach equivalent volumetric flow rates.

3.3.2 Flow in complex Channel Geometries

Microfluidic devices are typically designed by combining different flow channel compartments. To describe the hydrodynamic properties of such setups, the fundamental concepts discussed in Ch. 3.3.1 must be extended. The obtained expressions strongly depend on the relative assembly of the individual channel compartments. The most trivial multi-channel assembly combines two compartments either in series or in parallel as illustrated by R_1 & R_2 in **Fig. 3.9a** & **b**.

The total flow channel resistance of an assembly of channel compartments is defined in analogy to electrical resistance in electrical circuits. When channel compartments are aligned in series, the total flow resistance, $R_{\text{line,total}}$, follows from the sum of the individual flow resistances of all compartments (Eq. 3.13). When aligned in parallel, the total flow resistance, $R_{\text{parallel,total}}$, follows from the inverted sum of the individual flow resistances of all channel compartments (Eq. 3.14):[62]

$$R_{\text{line,total}} = \sum_{i}^{\text{channels}} R_i \tag{3.13}$$

$$R_{\text{parallel,total}} = \left(\sum_{i}^{\text{channels}} \frac{1}{R_i} \right)^{-1}. \tag{3.14}$$

In the scenario of two compartments with different resistances ($R_1 < R_2$) in series, the overall resistance is determined by the compartment with larger resistance: $R_{\text{line,total}} \approx R_2$. In contrast, the overall resistance is determined by the compartment with the smaller individual resistance when aligned in parallel: $R_{\text{parallel,total}}^{-1} \approx R_1^{-1}$. Connecting compartments in series requires higher pressures to reach the same overall volumetric flow rate and occasionally results in higher local flow rates, especially in compartments with narrow cross-sections, *e.g.*, R_2 in **Fig. 3.9c**. In parallel setups, large channels with small resistance, *e.g.*, R_1 in **Fig. 3.9d**, act as bypass (BP) channel for compartments of high flow resistance, drastically reducing the flow rate in the narrow main channel (R_2). Given the proportionality stated in Eq. 3.7, together with Eq. 3.6, the two sentences above are valid for both the overall volumetric flow rate and local linear flow velocity.

The fundamental concepts discussed are useful to estimate hydrodynamic properties, such as preferential flow paths, of flow setups of arbitrary complexity. In practice, this relies on the correct identification of flow channel segments in the microfluidic device.
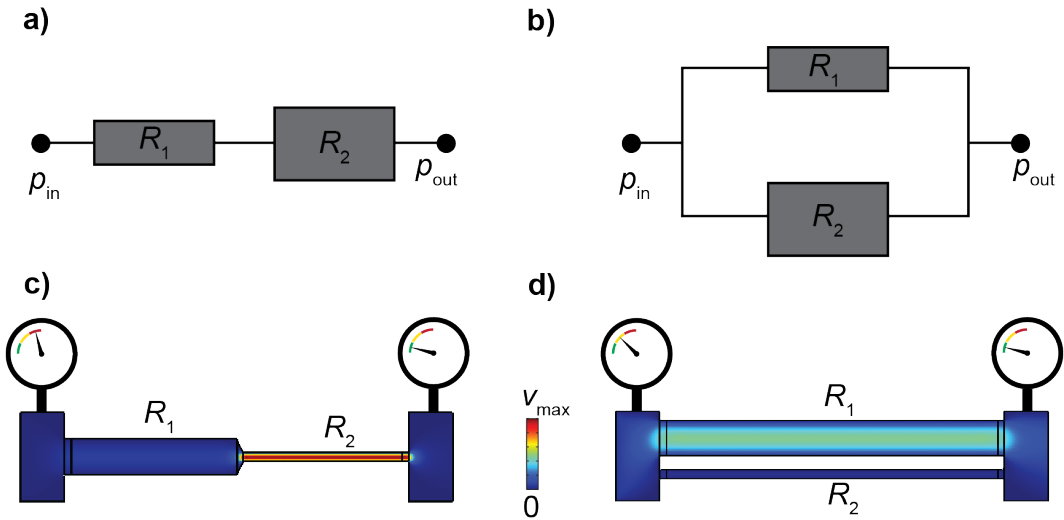
Figure 3.9: Complex Flow Channel Geometries. a), b) Schematic representation of two connected flow channel compartments with flow resistances, R_1 and R_2 ($R_1 < R_2$), that are connected in series (**a**) and in parallel (**b**), respectively. **c), d)** Flow velocity field in setups corresponding to **a** and **b**. The pressure difference, Δp, that is required to achieve the same mean volumetric flow rate in both setups is larger when assembled in series (**c**) than in parallel (**d**).

3.3.3 Mass Transport in Flow Scenarios

When microfluidic channels host chemical reactions, they are often referred to as flow reactors. Microfluidic reactors find broad application in fields ranging from the fabrication of materials to the investigation of fundamental physico-chemical concepts underlying structural dynamics.[52] In the latter case, flow systems can be perceived as model reactor for *ex situ* setups. For said applications, controlling mass transport is crucial to drive reactions and eventually replicate solution exchange properties of the reference systems.

Microfluidic reactors provide a versatile platform for flow experiments. The variability of applied concepts is immense;[172, 173] those most relevant in the context of this thesis are illustrated in **Fig. 3.10**. A sample of interest can be either moving through the flow channel with the final product leaving at the outlet, or remain localized at a fixed position inside the channel during the entire experiment. Depending on the use case, flow reactors can be operated in different modes with continuous flow being the most common. Solution exchange under continuous flow comprises both solution renewal and (*in situ*) mixing (**Fig. 3.10a**
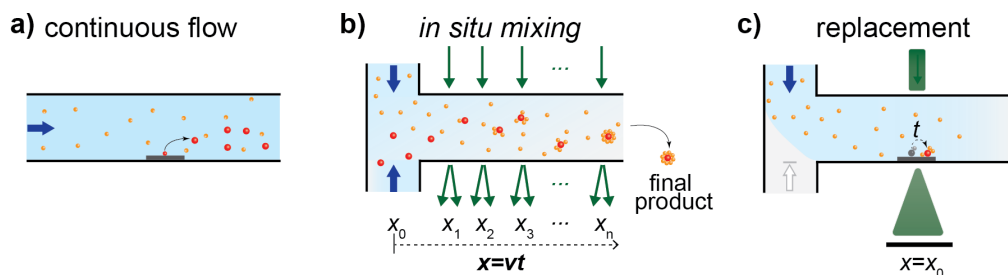
Figure 3.10: Mass Transport & Time-resolved Sample Characterization in Flow Channels. a) Continuous flow supplies fresh fluid and/or flushes locally generated species. **b & c)** Multi-inlet setups, can be used to mix fluids *in situ* (**b**) or replace one fluid with another (**c**). *In situ* mixing converts the temporal axis of the mixing experiment onto the spatial channel position (quasi-stationarity) enabling tracking dynamics by probing different locations (x_0-x_n) along the mixing channel in one experiment (**b**). Localized characterization methods such as LP-TEM require fixation of the sample within the restricted field of view (x_0), and thus solution replacement to induce mixing-like dynamics (**c**).

& **b**). In scenarios, where the sample is/must be fixed, mixing is replicated by replacing the background solution (**Fig. 3.10c**). In all scenarios, mass transport properties are determined by the interplay of solute diffusion and fluid convection inside the microfluidic reactors.

The complexity of flow reactor designs, and therefore mass transport, is determined by experimental requirements posed by the sample & dynamics under consideration.[52] Single-inlet setups are suited for continuous solution renewal, while multi-inlet setups additionally enable for control over the composition of the reaction media *via* mixing & replacement. The internal channel geometry is conveniently designed to control mass transport. *In situ* characterization methods can be integrated in microfluidic reactors. This results in additional restrictions for device fabrication, mainly due to compatibility issues.[58] While some devices are accessible for data acquisition across the entire flow device (compare **Fig. 3.10b**), others feature strongly localized measurements regions (**Fig. 3.10c**).[16] Convenient *in situ* characterization methods comprise light scattering, *e.g.,* X-ray scattering, UV-vis spectroscopy, and real-space imaging, *i.e.,* light & electron microscopy, but also electric and electrochemical sensing.[52]

LP-TEM is a strongly localized imaging technique, especially when operated at high

resolution, thus, requires samples to be confined inside the field of view.[22] LP-TEM flow reactors are predominantly operated under continuous flow; mixing hence is replicated by solution replacement. Ch. 3.3.3.1 to Ch. 3.3.3.3 contemplate the relevant aspects of mass transport in more detail.

3.3.3.1   Diffusion

Diffusion describes the passive and random motion of objects, *e.g.*, atoms, molecules and nanoparticles, in a medium. In the presence of a concentration gradient of the diffusive species, diffusion leads to a net movement from regions of high to regions of low concentration. Macroscopically, this net movement is expressed as a flux, *J*, based on Fick's law:[167]

$$J = -D\frac{dc}{d\boldsymbol{r}}.$$

(3.15)

In Eq. 3.15, D and c denote the diffusion coefficient and the concentration of a solute. In the regime of low Reynolds numbers, D follows from the Stokes-Einstein equation (Eq. 3.16):

$$D = \frac{k_{\mathrm{B}}T}{6\pi\eta R},$$

(3.16)

where k_{B}, T and R are the Boltzmann constant, the temperature and the radius of the diffusing species. Diffusive motion is inversely proportional to the solute's radius; relatively large nanoparticles tend to diffuse orders of magnitude slower than molecules and ions.[167]

3.3.3.2   Solution Renewal

Solution renewal describes the continuous supply of fresh reagent and/or removal of unwanted species.[167] Solution renewal typically aims at ensuring the *local* composition of the reaction solution, thus depends on *local* mass transport properties, *i.e.*, convective and diffusive flux. While the latter results from intrinsic solute properties and is negligibly small in the majority of setups, convective flux is proportional to the local flow velocity. Convective flux can thus be well defined through rational design of flow channel geometries, as illustrated by **Fig. 3.9c** & **d**, and selection of experimental parameters, *i.e.*, *Q*. Most common examples comprise the supply of cells in flow cytometry, supply of electrolyte in electrochemistry and flushing of gaseous species to suppress bubble formation in single and

multichannel setups.[174, 175, 176] Diffusion has been rarely exploited as it is outperformed by convective transport in most scenarios.

3.3.3.3 *In situ* Mixing & Solution Replacement

In batch chemistry experiments, solution mixing describes the abrupt introduction of new reagents to stimulate physical and/or chemical dynamics. The timescales of the mixing are strongly affecting the reaction pathway of the triggered physical and/or chemical process. Hence, controlling the mixing process is crucial to control the nanoscale dynamics. In nanoscience, the solute-induced nucleation, growth and self-assembly of particles are typical examples of mixing experiments.[11, 177]

The realization of mixing in microfluidic reactors requires multi-inlet setups.[178] Compositional changes can be achieved in two ways: either through *in situ* mixing or *via* solution replacement, depending on if the sample of interest is reliably fixed, or not (see below). In both cases, and in contrast to solution renewal (see above), the interplay of diffusion and convection must be considered along the *entire* mixing channel to control the mass transport dynamics. If the flow system serves as model reactor, replicating the mixing timescales of the *ex situ* setup is crucial to ensure correlatability of the results.[179, 180]

In situ mixing
In situ mixing is a well-known microfluidic concept for precise control over solute concentration directly inside a microfluidic multi-inlet mixing channel.[178] *In situ* mixing is achieved by simultaneously providing different reaction solution through the available inlets as illustrated in **Fig. 3.11**. Eq. 3.17 defines the partial flow ratio, *PFR*, of a solution:[167]

$$PFR = Q_{\text{solution}}/Q_{\text{total}}, \tag{3.17}$$

where Q_{solution} denotes the flow rate of a solution containing the solute of interest and Q_{total} denotes the total flow rate of all inlets. Given that the solute of interest is provided through one of the inlets at concentration c_{solution}, the resulting solute concentration, c_{mix}, assuming complete mixing at a given channel position (indicated by x in **Fig. 3.11a-c**), is expressed by Eq. 3.18. c_{mix} ranges between 0 and 100% of c_{solution}.

$$c_{\text{mix}} = PFR \cdot c_{\text{solution}} \tag{3.18}$$
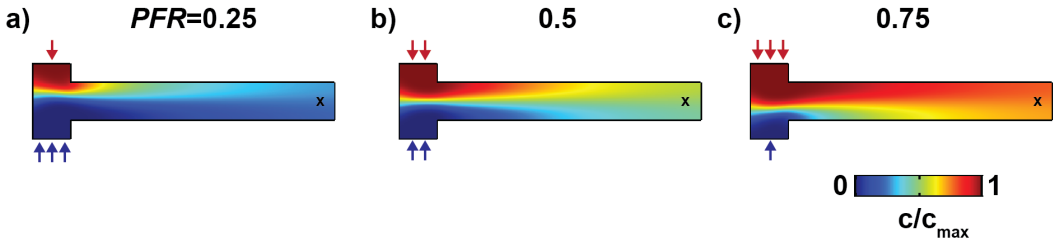
Figure 3.11: *In Situ* **Mixing. a-c)** 2D concentration profiles visualizing the mixing of two solutions (*red* and *blue*) in a double-inlet flow channel under different flow conditions with partial flow ratios, *PFR*, between 0.25 and 0.75. While in proximity to the mixing region the stationary concentration depends on the position, the concentration of the fully mixed solution close to the channel outlet (at x) is well defined *via* the *PFR*. Time-dependent composition gradients experienced by a sample are defined by the path along which it travels through the quasi-stationary concentration profiles inside the mixing channel. The total flow, Q_{total}, is identical in **a-c**.

Fig. 3.11a-c illustrate how c_{mix} at the end of the channel, *i.e.,* at x, changes with the *PFR*. Complete mixing is achieved in significant distance behind the mixing region, *i.e.,* the location where inflow channels merge, and the solution composition further upstream depends strongly on the exact location within the channel as well as the flow conditions applied, *i.e.*, *PFR* and Q_{total}.

The solution mixing dynamics experienced by a sample moving through the mixing channel thus result from the composition along its path;[179] in other words, the temporal axis of the mixing process is projected on the spatial axis defined by the channel length. The flow velocity, v, is the conversion factor as indicated in **Fig. 3.10b**. Note that locally the average composition is constant, *i.e.*, quasi-stationary. In microfluidic reactors, the local composition and thus the gradients experienced by a sample along the channel are precisely controllable, in particular under laminar flow conditions where intermixing occurs solely due to diffusion (no turbulences).[167] Thereby, customized mixing scenarios can be designed under continuous flow conditions. Notably, the compatibility of *in situ* mixing with localized characterization methods such as LP-TEM is limited.[62]

Solution Replacement

In scenarios where the sample must be fixed, and/or the field of view is constrained, mixing must be replicated by replacing the surrounding solution.[178] This implies that the individual flow rates at the inlets supplying different solutions must change in time, usually while keeping the overall flow rate, Q_{total}, constant. With respect to initial switches of the applied inflow rates, changes to the solution composition at a location of interest occur after a time delay, Δt. This delay corresponds to the travel time from the region where inlets merge to the location of interest. With increasing retention time, local solution replacement occurs increasingly gradual due to diffusive mass transport superimposed to convective fluid movement blurring the initially sharp concentration interface (Taylor dispersion).[179] In **Fig. 3.12a**, time-dependent compositional changes during solution replacement are illustrated for a simple double-inlet setup with t_0 defining the time point at which the inflow conditions are changed. **Fig. 3.12b** tracks compositional changes at two distinct location in proximity to the mixing region and further downstream. As apparent, delay time and concentration gradient depend strongly on the location within the channel setup and the applied flow conditions. With increased influence of diffusion, in the example depicted in **Fig. 3.12** due to the longer travel time required to reach channel outlet (*grey circles*), concentration gradients become more gradual with respect to scenarios governed by convection.

For simple channel geometries, the timescales of solution replacement can be estimated from fundamental considerations on convective and diffusive mass transport. The timescale, Δt_F, of solution replacement due to fluid flow, can be derived from the common definition of mean velocity, $\overline{v}$ (Eq. 3.19):

$$\Delta t_F = l/\overline{v}. \tag{3.19}$$

The timescale, Δt_D, of solution replacement due to solute diffusion, within a channel with identical expansion, l, as above (assuming zero flow), can be estimated from the mean square displacement time (Eq. 3.20):[179]

$$\Delta t_D = l^2/8D, \tag{3.20}$$

where D denotes the diffusion coefficient of the solute (Ch. 3.3.3.1). Notably, convective transport scales linear with the channel length, l (and reciprocally with flow velocity), while its contribution to diffusive transport is squared, l^2. Based on concepts displayed in Ch. 3.3.1
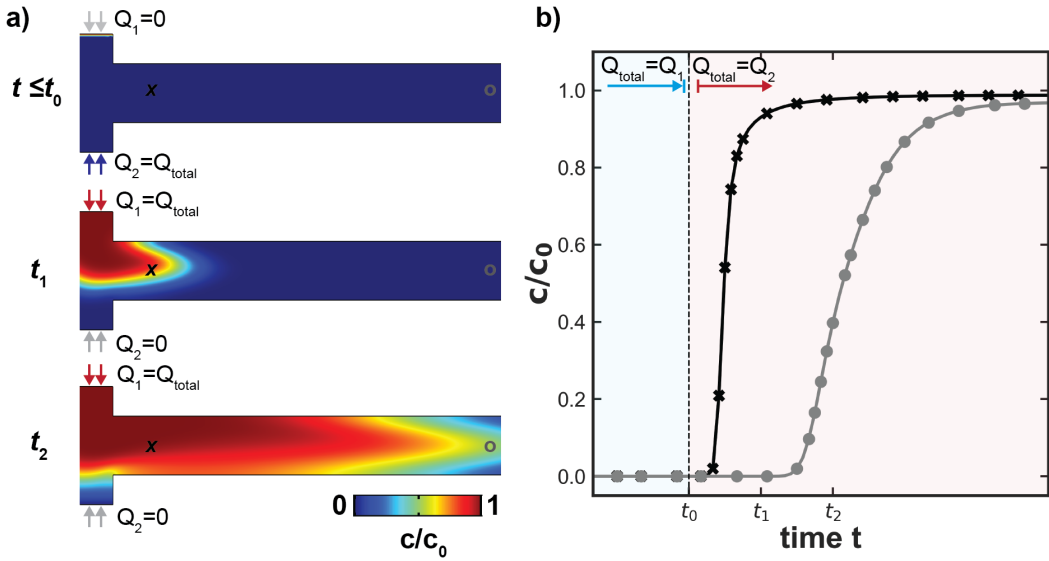
Figure 3.12: Solution Replacement Dynamics. a) Time-dependent 2D concentration maps illustrating the solution replacement in a double-inlet flow system with t_0 indicating the time point when the active inlet is changed from inlet #2 to inlet #1, each characterized by flow rates Q_2 and Q_1, respectively. **b)** The replacement dynamics are governed by the interplay of convection & diffusion of solutes *along* the channel strongly depending on the channel geometry and the position within the flow channel. Two locations close to the in- (*black crosses* in **a** & **b**) and outlet (*grey circles*) are compared. The total flow rate, $Q_\text{total} = Q_1 + Q_2$, is constant.

& 3.3.2, the relative assembly of channel compartments strongly affects the local replacement dynamics in more complex setups such as LP-TEM flow reactors.

3.3.4   Computational Fluid Dynamics Modelling

Theoretic mathematical modelling has always been a discipline in physical science supporting practical efforts of experimentalists. While some problems can be solved analytically, others cannot, and require numerical approaches. Recently, *in-silico* methods have become extremely powerful thanks to advances in hard- and software. The continuous increase in computing power of microprocessors has drastically accelerated numerical computations and reduced their costs, making this approach economically favorable. Sophisticated software environments have been developed to facilitate model implementation also for researchers with intermediate coding experience thanks to user-friendly interfaces.[181] COMSOL Mul-

tiphysics (COMSOL Inc., USA) is one of the most commonly used software environments, in particular for computational fluid dynamics.[182]

Models of different complexity and accuracy can be generated. Simplified implementations mark the starting point as hey are realized easily and solved rapidly; however, they typically enable qualitative evaluation of multiphysics phenomena only. More accurate models enable for quantitative description of realistic scenarios and even drive innovation through predictive prototyping procedures, yet come with increased computational costs. The following sub-chapters revise these concepts (Ch. 3.3.4.1 & 3.3.4.2) and provide selected examples (Ch. 3.3.4.3 & 3.3.4.4) relevant in the context of this thesis.

3.3.4.1   Correlative and Predictive Modelling

Numerical modelling approaches are typically categorized based on correlative and predictive aspects.[183] Correlative modelling is applied to test and explain experimental results; whereas predictive modelling permits rapid and resource saving screening of relevant parameters, thereby helping to identify worthwhile directions of scientific and technological developments, *e.g.*, in device fabrication. In fact, predictive modelling plays a crucial role in rapid prototyping procedures as it reduces the costly fabrication of physical prototypes (see Ch. 3.3.4.2). A prerequisite for powerful predictive models is the profound understanding of underlying physics inside the model geometry. This understanding can solely be gained *via* correlative modelling, *i.e.*, by validating the model against experimental observations.

3.3.4.2   Rapid Prototyping Procedure

Rapid prototyping describes the fabrication of a scale model of a physical part or their assembly based on three-dimensional computer-aided design (CAD) data using additive or subtractive manufacturing techniques.[184] During the predictive modelling step, the digital prototype (CAD file) serves as basis for rational design optimization of the physical prototype. Such combination of virtual and physical prototyping steps accelerated the design and fabrication of the final products and reduced costs.

As depicted in **Fig. 3.13**, the steps from an initial idea to the *final* product during rapid prototyping comprise *i*) the creation of a virtual prototype, *ii*) the refinement of its properties *via* numerical modelling of the governing physics, which enables *iii*) the manufacturing of a physical prototype that is finally *iv*) used to experimentally calibrate & refine the virtual model. The workflow is repeated iteratively until the product design is finalized.[183]
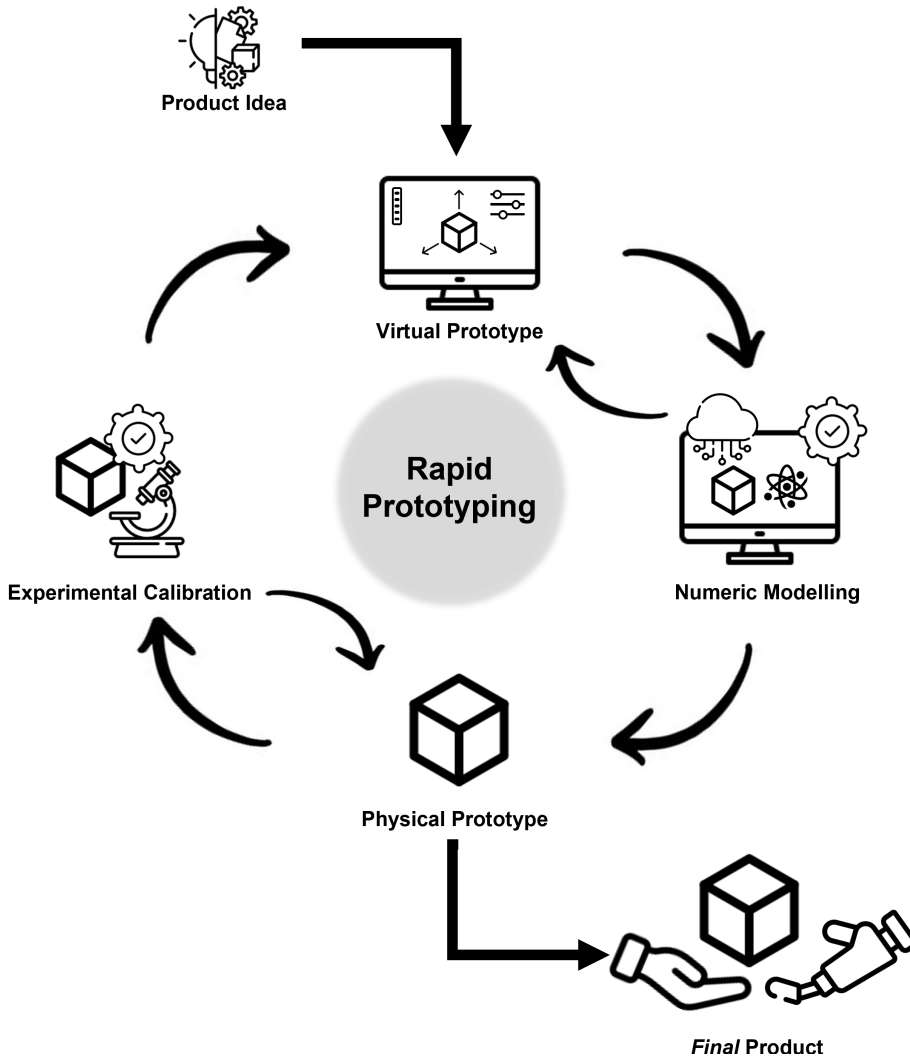
Figure 3.13: Rapid Prototyping Procedure. The combination of virtual and physical prototyping methods enables the efficient development of an initial idea into a product.

3.3.4.3 Modelling of Mass Transport in Microfluidic Systems

Numerical modelling plays an important role in simulating mass transport in microfluidic systems. The broad field of microfluidic applications has led to a vast variety of channel designs, and thus models of varying complexity ranging from simple correlative models of multiphysics problems to predictive applications in prototyping. The field is well summarized in comprehensive review articles and textbooks;[53, 167, 185, 186] here, only a selection of

relevant examples is outlined.

State-of-the-art modelling of laminar flow mixing reactors combines convective and diffusive mass transport applied to realistic flow channel geometries. Models of multi-inlet mixing devices were reported in simplified 2D and accurate 3D designs. Trebbin and coworkers, for instance, established a numerical description of the interdiffusion of two solvents in microfluidic mixing devices.[16, 179] The authors correlated the computed solution composition to time-resolved structural dynamics of nanomaterials probed *via in situ* SAXS and UV-vis spectroscopy. More advanced examples additionally consider chemical reaction kinetics. Panariello *et al.* reported simulations of silica nanoparticle synthesis in flow reactors revealing effects of the residence time distribution and diffusion-induced effects on the evolution of particle size distribution.[187] Prominent examples of predictive modelling comprise the prototyping of advanced flow channel geometries with fine-tuned fluid-structure interactions.[188]

In electrochemical modelling, drift of charged particles in electric fields must be considered in addition to convection and diffusion. Thus, solving Nernst-Planck-Poisson equation is a well-established task providing useful insights into complex electrochemical problems.[181, 189] Numerous customized models were implemented and solved relying on common simplifications, but also comprehensive examples which precisely consider the realistic geometry of the EC setups and governing physics were reported.[190, 191, 192, 193] Advanced models enabled the rational design of battery setups. Virtual prototyping contributed to the improvement of electrode and device geometries as well as electrolyte materials, beyond others.[175, 194] The current focus of electrochemical mass transport models clearly lies on systems relevant for green energy transition with a strong emphasis on flow battery systems.[175, 194] These systems exhibit strong conceptual similarities to electrochemical LP-TEM setups which are typically operated in flow conditions (compare Ch. 3.2.4).

3.3.4.4   Modelling of Mass Transport in Liquid-Phase TEM Setups

During recent years, the role of numerical modelling has been continuously growing in LP-TEM research; however, there is still very little literature available on mass transport simulations. Theoretical approaches mostly targeted the description of local diffusion of reactive species arising from radiolysis as extensively discussed in Ch. 3.2.3.2. Beyond that, Kröger & Verch reported two-dimensional stationary diffusion-reaction simulations to explain qualitatively the effects of confinement in LCs on ion transport during mineralization processes.[28]

The only theoretical description of fluid flow in a realistic multi-scale channel geometry was performed by Allen *et al.*[195] The author modelled Stokes flow through a nanoconfined channel; yet, could not obtain correlative experimental data to confirm estimated flow velocities.

Quantitative and experimentally validated models are barely existing and examples of implementations with predictive capabilities are scarce. Notably, Binggeli and co-workers presented a model that led to improved electrode setups for electrochemical applications.[196] Works of Petruk and colleagues accelerated the development of flow channel geometries with high volumetric flow rate.[43] Overall, there is a strong necessity for (correlative) modelling in LP-TEM research to increase basic understanding of mass transport and to enable more predictive approaches to design experiments and optimize setups. This need is growing with the number of stimuli integrated in experimental setups.

Chapter 4

Material & Methods

4.1 Experimental Techniques

4.1.1 Material & Equipment

4.1.1.1 Chemicals

Milli-Q water with resistivity of 18.2 MΩ·cm at 25 °C was used in all experiments. Phosphotungstic acid (PTA) (99.995%) and potassium permanganate ($KMnO_4$, > 99.0%) were purchased from Sigma-Aldrich and used as contrast agent for hydrodynamic quantification of LP-TEM flow systems by TEM and optical means. AuNP samples were obtained in collaboration with the Colloidal Systems Chemistry group at the CFM. Electrocatalysts were prepared by Advanced Materials for Sustainable Future Technologies at IIT.

4.1.1.2 Sample Characterization Tools

TEM was the central sample characterization technique used. TEM imaging was performed on a Titan 60-300 TEM/STEM transmission electron microscope (FEI, Netherlands) at CIC nanoGUNE, San Sebastian (Spain). A photograph of the machine is shown in **Fig. 4.1a**. The microscope is equipped with a high-intensity monochromated electron source (x-FEG), Lorentz lenses, image corrector, bi-prism for holography, spectrometers for EDX & EELS and bright & dark field STEM detectors. The demonstrated lateral resolution is 0.07 nm at 300 kV in conventional TEM, and 0.134 nm at 300 kV in STEM mode.

The TEM was operated in different imaging modes according to specific experimental
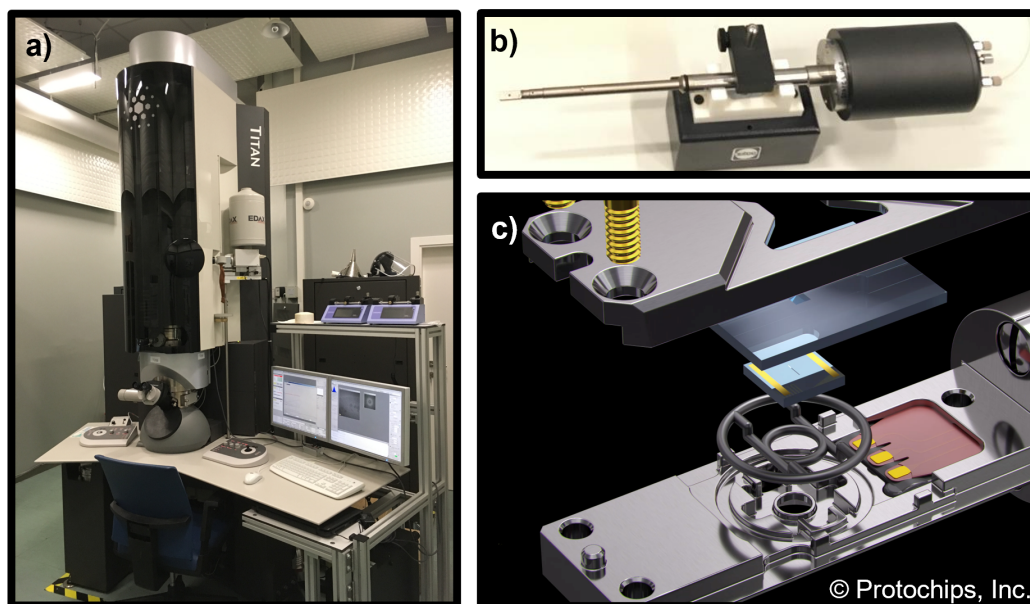
Figure 4.1: LP-TEM Infrastructure at CIC nanoGUNE. Photograph of **a)** the Titan TEM at CIC nanoGUNE in San Sebastian, Spain and **b)** a LP-TEM sample holder. **c)** Rendering of the expanded tip of a LP-TEM sample holder (Poseidon Select, Protochips Inc.) depicting the components forming the LC. Figure **c** was obtained from Protochips.

requirements. Hydrodynamic characterization of LP-TEM flow systems was performed in TEM Lorentz mode to image the complete window area ($\sim$20 x 20 um^2) in low magnification (500x). Nanoscale dynamics were imaged at higher resolution (typically >30.000x), both under continuous irradiation and in scanning mode depending on the resolution and beam sensitivity determined by the sample imaged.

Occasionally, correlative UV-vis measurements for hydrodynamic characterization of LP-TEM flow systems were performed on a Cary UV-Vis-NIR 3500 spectrometer (Agilent Technologies, Inc.) in the spectral range $400 < \lambda < 800$ nm.

4.1.1.3   LP-TEM Flow Systems

LP-TEM flow systems were set up by assembling LCs in the tip of dedicated sample holders. A photograph of the Poseidon holder series is depicted in **Fig. 4.1b** and an illustrative

representation of its tip is depicted in **Fig. 4.1c**. Both holder differ in respect to the flow channel geometry (refer to ref. [197] for details). Two types of double-inlet microfluidic LP-TEM sample holders were used for the experiments, namely Poseidon 200 and Poseidon Select (both Protochips, Inc.). LCs were assembled from MEMS-based chips. Small and large chips were obtained from Protochips company (EPT and EPB series).[198] The chips are made from Silicon (Si, 0.3 mm height) on which a 50 nm thin SiN membrane is deposited and therefore allows the electron beam to pass in its center (window cross-section: 20 x 550 µm^2, if not stated differently). The lateral expansion of the small and large chips are 2 x 2 mm^2 and 4.5 x 6 mm^2, respectively. On the small chips, so-called flow spacers are located in each corner. The lateral expansion of the spacers is 0.1 x 0.1 mm^2 and the height was chosen to be either 150 or 500 nm.

4.1.2 Setting up & Operating Microfluidic Systems

4.1.2.1 Assemblage of LP-TEM Sample Holder

Before assembling the LC, E-chips were cleaned with methanol and acetone and wettability was increased by gentle oxygen plasma treatment (10% O$_2$, 1 min) according to standard procedures.[198] Subsequently, the small E-chip was rapidly allocated in the tip of the microfluidic sample holder and ∼1 µL of sample solution was dispensed on top. The large E-chip was positioned on top carefully squeezing out protruding liquid. SiN membranes, which form the viewing window, were aligned in cross-configuration. Screws were finger tightened to close the lid, which was sealed either by a gasket (Poseidon Select) or two O-rings (Poseidon 200). Prior to inserting a holder into the microscope, optical and vacuum checks ($<10^{-5}$ mbar) were conducted to validate the assembly.

4.1.2.2 Flow Control *via* Syringe Pumps

To independently control the applied flow through the microfluidic LP-TEM systems, two syringe pumps (11 Elite Programmable Syringe Pumps, Havard Apparatus) were set up. Communication between the pumps was enabled *via* a RS-485 cable for synchronized execution of previously programmed flow profiles. Each pump was equipped with a 5 mL gas-tight syringe (1700 series Hamilton) which were connected to the inlets of the LP-TEM sample holder *via* associated PEEK tubings (length l = 0.5 m; the inner diameter for Poseidon Select and Poseidon 200 setup were ID_{select} = 127 µm and ID_{200} =100 µm, respectively). A

similar PEEK tubing (length $l = 6$ cm; inner diameters: $ID_{\text{select}} = 178$ µm & $ID_{200} = 150$ µm) was connected to the holder's outlet and immersed into a liquid reservoir to release the solution without pressure variation upon droplet formation. All tubing lengths were minimized to reduce the internal pressure built up. Prior to incorporating the LC in the holder tip, all inlet channels were thoroughly primed with aqueous solution to rinse gas bubbles.

Syringes were loaded with different solutions according to the requirements of experiments. For image contrast variation measurements, one syringe was filled with aqueous solution of the contrast agent ($c_{\text{PTA}} = 40$ mmol/L), whereas the other syringe contained pure water as reference.

4.1.2.3 Flow and Pressure Control *via* pressure-driven Pumps

An integrated pressure-driven pumping systems was used to measure the flow resistance of the microfluidic LP-TEM setup and to control the internal pressure. A pressure controller unit (OB1 MK3 Flow controller system, Elveflow by Elvesys) was operated to adjust pressures in both inlet and outlet reservoirs. Inlet and outlet reservoirs were connected through PEEK tubings (two each: $l_1 = 0.285$ m, $r_1 = 178$ µm; $l_2 = 0.77$ m, $r_2 = 127$ µm) to the LP-TEM holder. Flow meters (MFS2 flow sensor, Elveflow by Elvesys) were integrated in the inlet and outlet tubing to measure the volumetric flow rate resulting from the difference between the applied pressures up- and downstream with respect to the sample holder.

4.1.2.4 Flow Profiles

Solution replacement and *in situ* mixing were performed through previously programmed flow profiles. Two types of flow profiles were predominantly used in this thesis: 1) a stepwise abrupt switch of the total flow from one syringe to the other served to induce solution replacement in the flow channel system; 2) gradual change of the local solution composition and *in situ* mixing was realized by adjusting relative flow rates between the two syringes. The typical duration of experiments ranged from some minutes up to 2 h.

4.1.3 TEM Data Acquisition and Post-Processing

4.1.3.1 General Image Acquisition

Images were acquired on a Gatan Ultrascan 1000P 2K*2K CCD camera (GATAN, USA). Imaging parameters such as beam current density, exposition/dwell times and intervals be-

tween frames varied for different experiments and were dependent on the imaging mode. Image acquisition was manually synchronized with the pump's micro controller. Semi-automatized workflows were applied for processing and plotting of the data acquired. Acquired image sequences were aligned for drift in Digital Micrograph. Post-processing routines were developed in Python-2.7 software (numpy, scipy, matplotlib) to analyse and visualize results.[199]

4.1.3.2 Image Contrast Variation Method

Image contrast variation was exploited to visualize, characterize and quantify the hydrodynamic properties of microfluidic multi-inlet LP-TEM setups. The methodology relies on image contrast variation in dependence on changing the thickness and/or composition of the liquid inside the LC. Both concentration changes during solution replacement of an electronically dense contrast agent and the variation of window bulging upon pressure variations were tracked. Compositional changes were induced by syringe pumps, while a pressure-driven pumping system was used to alter bulging. In both cases, contrast changes were initiated through pre-defined flow profiles (Ch. 4.1.2.4) selectively altering one parameter.

Based on Eq. 3.5, the normalized transmitted intensity, I_{norm}, can be approximated by Eq. 4.1., where ρ_w, z and c_{CA} are the scattering power of water, the thickness of the liquid layer and the contrast agent concentration, respectively.[197]

$$I_{norm}(t) \approx 1 - \rho_w \cdot z \cdot c_{CA}(t) = 1 - K \cdot c_{CA}(t) \qquad (4.1)$$

In solution replacement experiments, the transmitted intensity values were converted into contrast agent concentration upon concentration calibration using linear multi-point interpolation. Based on the time-dependent variation, the effect of several experimental (total and relative flow rate) and structural (flow channel geometry) parameters on the hydrodynamic properties were quantified.

The selection criteria for the contrast agent were high average atomic number, good solubility in water, chemical inertness in respect to the components of the hardware and non-toxicity. One of a few such compounds is PTA, which is a well-known contrast agent for staining of biological specimen in conventional TEM and LP-TEM experiments.[22] PTA was used at a maximum concentration of 40 mM (about 10 wt%), which provided intensity variation well above the noise level at an electron dose rate of $0.3\,e^-/nm^2/s$.

4.2   Finite Element (FE) Simulations

Four steps were followed during FE modelling comprising 1) the creation of the geometric model (Ch. 4.2.1), 2) the definition of the physical model, *i.e.*, assembly of the partial differential equation system (Ch. 4.2.2), 3) the discretization of the model through meshing (Ch. 4.2.4) and 4) solving the discretized model (Ch. 4.2.5). Two main models were created in the scope of this thesis: the first model aimed at resolving convection & diffusion in *realistic* 3D LP-TEM flow channel geometries; the second model focused on beam-induced chemical reactions under the effect of flow and diffusion in simpler 2D geometry. Both numeric models were implemented in COMSOL Multiphysics software (version 5.3).[182]

4.2.1   Geometric Modelling

4.2.1.1   Virtual Imprinting

A detailed geometric representation of the *real* flow channel structure was a prerequisite to accurately simulate the hydrodynamic properties of microfluidic LP-TEM sample holder. Therefore, a virtual model of the tip of the Poseidon sample holder series was obtained from Protochips company. The schematic representation in **Fig. 4.2a** depicts the sample holder (*grey*) with internal tubings (not visible) and the small E-chip (*orange*) that is immersed into an oversized groove (*bathtub*). The small chip, together with the large chip (not shown), form the LFC which is sealed by a gasket (*black*). The flow channel geometry (**Fig. 4.2b**) was obtained from the geometric model of the sample holder (**Fig. 4.2a**) through virtual imprinting.

Geometrical refinements and simplifications of the base model were inevitable for successful creation of the model. These included the removal of tiny and malformed dead volumes, chamfering of sharp edges and reducing the length of in- and outlet. Said modifications were reduced to a minimum to obtain the most realistic structure. In addition, (re-)compartmentalization, *i.e.,* the creation of *artificial* sub-domains in the flow channel geometry, was especially relevant for subsequent meshing (compare Ch. 4.2.4). A representation of the final geometric model of the flow channel system is exemplary depicted for Poseidon Select in **Fig. 4.2b**. The figure reveals three sub-domains, *i.e.,* the large premixing channel (*grey*), the µm-sized BP channel (*orange*) with large pockets (*grey*) and the central nanochannel (NC) (*red*).
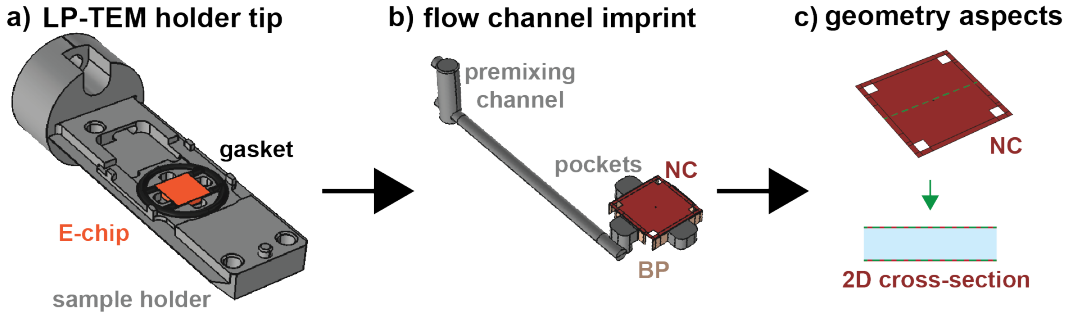
Figure 4.2: Virtual Imprinting and Symmetry Aspects. a) Virtual model of the most relevant components that form the tip of a microfluidic LP-TEM sample holder, *i.e.,* sample holder, gasket and MEMS-based E-chips. **b)** The flow channel geometry that is obtained through virtual imprinting of **a**. **c)** Schematic representation of the simplification of geometric models based on symmetry considerations, *i.e.*, the vertical cross-section of the central NC.

4.2.1.2   Symmetry Aspects

For most numeric applications, the complexity of a geometric model can be reduced by symmetry considerations. This allows lowering the computational costs without significantly reducing the model's accuracy (**Fig. 4.2c**). For instance, in a flow channel with rectangular cross-sections of extremely high aspect ratios like the NC (compare Ch. 3.3 on Poiseuille plane), the flow profile can be approximated through a 2D cross-section along the vertical channel axis where strong velocity gradients are expected. Such symmetry considerations were beneficial for the creation of an archetype model that calculates radiolysis under flow conditions.

4.2.2   Physics' Modelling

4.2.2.1   Convection and Diffusion

The general Navier-Stokes equation of incompressible fluids was implemented for stationary ($\partial \boldsymbol{v}/\partial t = 0$) and time-dependent conditions to describe convection and diffusion:

$$\rho\frac{\partial \boldsymbol{v}}{\partial t} + \rho(\nabla \boldsymbol{v})\boldsymbol{v} = \nabla[-p\boldsymbol{I} + \mu(\nabla \boldsymbol{v} + (\nabla \boldsymbol{v})^T)] + \mathbf{F} \tag{4.2}$$

$$\rho\nabla \cdot \boldsymbol{v} = 0, \tag{4.3}$$

where μ is the dynamic viscosity, $\boldsymbol{v}$ is the velocity vector, ρ is the (constant) solvent density, $\boldsymbol{I}$ is an identity matrix. All applied body forces $\boldsymbol{F}$, such as gravity, were set 0. The so-called Cauchy stress tensor $\boldsymbol{P} = [-p\boldsymbol{I} + \mu(\nabla\boldsymbol{v} + (\nabla\boldsymbol{v})^T)]$ represents viscous and pressure stresses. The transport of solute i *via* convection and diffusion was coupled according to Eq. 4.4:

$$\frac{\partial c_i}{\partial t} + \nabla \cdot (D_i \nabla c_i) + \boldsymbol{v}\nabla c_i = 0, \tag{4.4}$$

where D_i is the diffusion coefficient and c_i the concentration of the solute.

4.2.2.2   Radiolysis

Radiolytic Creation

In the area irradiated by the beam, the radiolytic creation of primary species (e_h^-, H·, H_2, OH·,H_2O_2, HO_2, H^+, OH^-) was calculated based on their G-values (Eq. 4.5):[37]

$$\frac{dc_i}{dt} = \frac{\rho \Psi G_i}{F}, \tag{4.5}$$

where ρ, Ψ and F are the density of the irradiated liquid, the absorbed dose rate and Faraday constant. The G_i values used for the modelling of radiolysis in pristine water were taken from Schneider *et al.*[37] and are listed in Tab. B.1 (Appendix B, p. 180).

Chemical Reactions

The created species initialize a complex chemical reaction network, that in neat water alone consists of 73 reactions and comprises 15 radiolytic species (8 primaries & 7 secondaries) and H_2O. The network was implemented as a set of first- and second-order reactions. Examples of bimolecular reaction rate equations are denoted in Eq. 4.6 and 4.7:

$$\frac{dc_i}{dt} = k_{jk} c_j c_k, \tag{4.6}$$

$$\frac{dc_i}{dt} = -k_{ij} c_i c_j, \tag{4.7}$$

where positive and negative signs denote production and consumption, respectively. k_{jk} and k_{ij} are the rate constants of the corresponding reactions. All reactions and rate constants

are listed in Tab. B.2 (Appendix B, p. 181).[37] Water was considered a solvent with much higher concentration.

4.2.3 Initial & Boundary Conditions

4.2.3.1 Convection and Diffusion

No slip, *i.e.*, zero fluid velocity at all channel walls (Eq. 4.8), and no-penetration (Eq. 4.9) boundary conditions were implemented:

$$\boldsymbol{v} = 0, \tag{4.8}$$

$$-\boldsymbol{n} \cdot [(D_i \nabla c_i) + c_i \boldsymbol{v}] = 0. \tag{4.9}$$

In Eq. 4.9, $\boldsymbol{n}$ denotes the unit normal vector of the walls. The inflow in each of the two inlets was implemented based on Eq. 4.10:

$$L_{\text{entr}} \nabla_t [p\boldsymbol{I} + \mu(\nabla \boldsymbol{v} + (\nabla \boldsymbol{v})^T)] = -p_{\text{entr}} \boldsymbol{n}, \tag{4.10}$$

where p_{entr} denotes the inlet pressure and L_{entr} the entrance length, which describes the distance after which the profile of entering flow is fully developed. The inlet flow velocities v_{water} and v_{CA} were fixed for both stationary and time-dependent simulations. Their values resulted from absolute (Q) and relative (PFR) mean volumetric flow rates which were varied in a range between 0 to 3000 µL/h and 0 to 1, respectively. Exceptionally, zero flow in the stationary case was considered based on inlet pressure $\hat{p}_0$. The outlet was defined by zero pressure $p_0 = 0$.

$$\boldsymbol{n}^T [p\boldsymbol{I} + (\nabla \boldsymbol{v} + (\nabla \boldsymbol{v})^T)]\boldsymbol{n} = -\hat{p}_0 \tag{4.11}$$

$$\hat{p}_0 \geq p_0, \boldsymbol{v} \cdot t = 0 \tag{4.12}$$

The inflow of contrast agent in time-dependent simulations was implemented through step functions ($0 \rightarrow 1$, width of transition zone: 0.1 min) of the contrast agent concentration,

where $c_0 = 40$ mM was the maximum inlet concentration. The onset of the increase was defined at 1 min relative to the beginning of the simulation.

4.2.3.2 Radiolysis

To represent neat water (pH 7), the initial concentration of all species, except from H_2O ($c_0 = 55.5$M), H^+ ($c_0 = 10^{-7}$M) and OH⁻ ($c_0 = 10^{-7}$M), were zero in all domains and at the inlet boundary. The inlet concentration of O_2 was altered to account for aerated solutions.

4.2.4 Meshing

4.2.4.1 General Design Concepts

In FE modelling, solving the differential equations of the physical models requires the discretization of the created geometric model. The process in which discrete elements are created is called meshing. The more elements are contributing to a mesh the more accurate solutions to the physical model can be calculated; however, more computational resources are required with increasing mesh size. The *optimal* mesh hence compromises the accuracy of the solution and the computational cost to obtain it. Fundamental design rules helped to optimize the mesh. The core idea behind all meshing concepts is to strategically accumulate mesh elements in regions where they are most useful. Thus, locally high mesh densities are required in regions of strong gradients. The applied meshing procedures are strongly dependent on the geometric complexity of the model and the implemented physics.

The efficiency of rational physics-based mesh design is demonstrated in **Fig. 4.3**. For the trivial case of laminar flow in a 2D model of a sub-µm-sized flow channel, the meshing rules can be derived from the no-slip boundary conditions at the channel wall. These resulted in a parabolic flow profile with an increasingly strong flow velocity gradient in proximity to the channel wall. Locally increased mesh density close to the channel walls resulted in precise computations at moderate mesh density. Equally precise solutions could be achieved when ignoring underlying physics, yet at significantly higher computational costs (see **Fig. 4.3c**).

In the more complex scenario of convection & diffusion in 3D models of LP-TEM flow systems, meshing of the entire flow channel geometry was a multi-step process. Up to ∼40 subsequent steps were required due to the geometric complexity and the underlying physics. As consequence of the geometric complexity, the computational cost was intrinsically high, which required meticulous rational design of the underlying mesh based on advanced con-
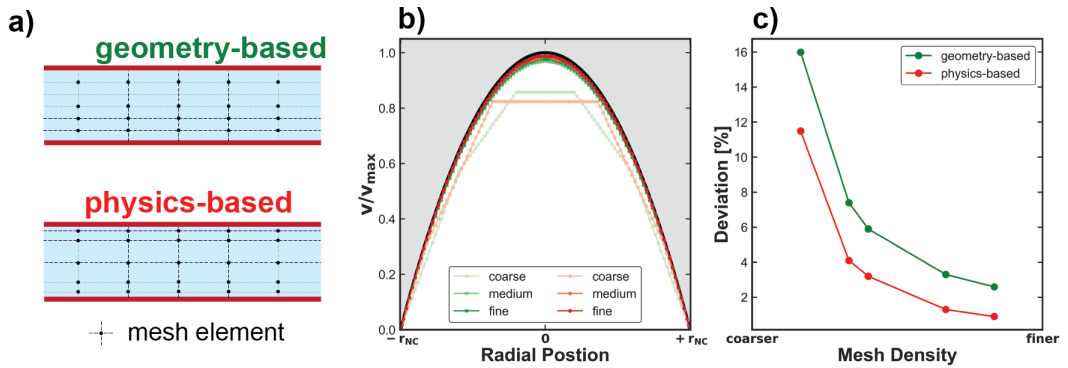
Figure 4.3: Rational Mesh Design Concepts. a) Schematic representation of geometry- and physics-based meshes for laminar flow models. **b)** Representative flow velocity fields that were calculated from geometry- and physics-based meshes with different radial mean mesh densities (coarse, medium, fine). *Black line* depicts the theoretic velocity profile for laminar flow in channels with radius r (compare Eq. 3.9). **c)** Deviations of geometry- and physics-based meshes from the theoretic solution. Physics-based meshes can result in more accurate solution at lower computational costs.

cepts. It turned out that for computing physically reasonable solutions, highly accurate meshing of the transition from the large premixing to the tiny NC was indispensable. An up-to-scale geometric representation of the transition zone is depicted in **Fig. 4.4a**. The 5 steps of the process solely dedicated to create a mesh for this zone are depicted in **Fig. 4.4b-f**. The procedure encompasses gradual and sweep meshing strategies which were applied to edges, faces and volumes of artificial sub-compartments.

4.2.4.2   Convergence Study

Convergence studies were performed to track the mesh optimization process. In flow models, the accuracy of the solution can be improved by increasing the mean vertical mesh density (compare vertical flow velocity profile in **Fig. 4.3c**). Computational resources were limiting the size of models that could be solved. However, gained accuracy decreased with increasing mesh resolution. In the context of this thesis, 2% deviation was conveniently defined as threshold in convergence studies.
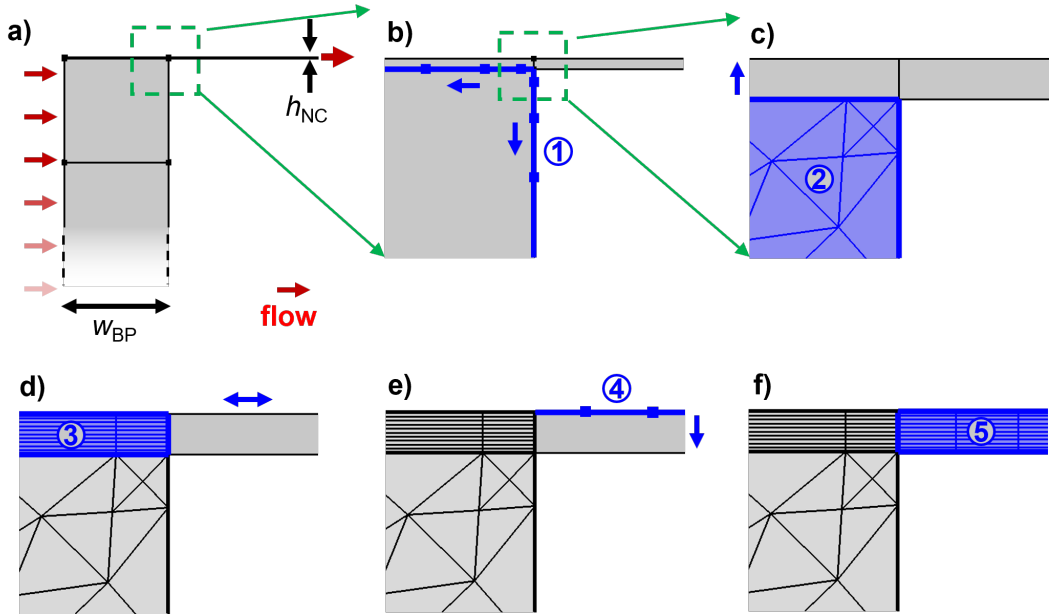
Figure 4.4: Flow Channel Geometry-derived Mesh Generation. a) To-scale geometric representation of the cross-section of the transition from the mm-sized BP to the sub-µm-sized NC compartment. The width of the large BP channel compartment is $w_{BP} = 25\,\mu m$ and the height of the NC is $h_{NC} = 150\,nm$. *Red arrows* indicate direction of fluid flow. The $25x25\,\mu m^2$ quadratic sub-compartment was created in re-compartmentalization process to support the meshing. **b-f)** Schematic representation of the 5-step process which was applied to mesh the transition region. First, **(1)** the two edges of the quadratic sub-compartment in proximity to the NC were meshed with in-creasing distance between the mesh points (25 points; 0.1 element ratio, **b**). They then **(2)** served as boundary condition for the meshing of the quadratic face (triangular ele-ments, maximum mesh element size: 60 µm, **c**). Subsequently, **(3)** the upper edge mesh was transferred into the BP sub-compartment of height h_{NC} through sweeping (10 lay-ers, **d**). Thereafter, **(4)** the NC surface was meshed (**e**) and **(5)** the corresponding mesh was transferred into the NC volume and connected to the BP sub-compartment (**(3)**, **d**) by choosing the same sweeping specifications (10 layers, **f**). The sweep mechanism was applied to extend the transition mesh over the full width of the NC, considering its local peculiarities. Note that **b** depicts the parts within the green box in **a** and **c** depicts the parts within the green box in **b**; **d-f** are depicting the same part of the geometry as **c**. Adapted from [197].

4.2.5   Numeric Solvers

COMSOL Multiphysics software provides a broad solver infrastructure for solving FE models. The solvers employ algorithms to numerically solve the discretized equations for the physical quantity of interest. Different solver methods were applied to calculate solutions. The suitability of these methods varied strongly between the implemented scenarios and was greatly affected by the complexity of the model (see above).

For most scenarios, a direct solver (*i.e.,* MUltifrontal Massively Parallel Sparse; MUMPS) was chosen. Direct solvers perform computationally intensive matrix factorization, resulting in higher accuracy generally obtained after longer computation times compared to iterative solvers. Direct solvers demonstrated increased robustness compared to iterative solvers.

Fully-coupled solver architectures were typically applied to solve multi-physics problems. Unlike segregated architectures, where the different physics are decoupled and equations are solved separately, fully-coupled solvers handle the interconnected equations in a single step. Within the COMSOL infrastructure, the *Automatic Newton* method was chosen as it combines the advantages of the *Newton-Raphson* method for iteratively solving nonlinear equations with the automatic adjustment of the solver's step size.[182]

Where appropriate, multi-physics problems were divided into two successive calculation steps. One illustrative example is the superposition of convective and diffusive mass transport in solution replacement and mixing scenarios. Assuming that the velocity profile is constant, it could first be solved in a stationary step before the superimposed time-varying concentration distribution was solved in a subsequent time-dependent solver step. This strategy notably reduced computation time, however, it was only carefully applied after ensuring negligible effect of the simplified boundary conditions on the model accuracy.

Chapter 5

Summary of Results

5.1   Introduction

This doctoral project started with a bitter lesson. The solute-induced clustering of AuNPs should have been studied using a LP-TEM flow reactor (Poseidon 200, Protochips Inc., USA). In preceding works, it was demonstrated that such samples show interesting properties, in particular for information storage in dynamic systems (Kruse, Merkens *et al.*, *ACS Appl. Nano Mater.*, 2020 & Mezzasalma, Kruse, Merkens *et al.*, *Adv. Mater.*, 2023).[200, 201] The sample further seemed a promising model system for LP-TEM experiments because AuNPs were supported in an agarose gel matrix potentially facilitating confinement of the sample in the IA.

To stimulate the clustering during the *in situ* experiment, the composition of the reaction solution, *i.e.*, NaCl salt concentration, was changed by adjusting the flow rates at the two inlets. Even though droplets of the reaction solution were immediately dripping from the outlet, no dynamics could be identified in the acquired images. The sample appeared stable for ∼1 h, before presumably beam-mediated degradation dynamics became visible as illustrated by **Fig. 5.1**. While initially high NaCl concentration seemed to stabilize the sample against the effect of the beam (**Fig. 5.1a-b**),[120] lowering the concentration led to crucially increased radiolytic damage dominating possible solute-induced AuNP dynamics (**Fig. 5.1c-e**). Further details on the *in situ* experiments are provided in Merkens *et al.*, *Imaging & Microscopy*, 2021.[202]

Despite that unexpected outcome, failure is not a scientific category. Several general
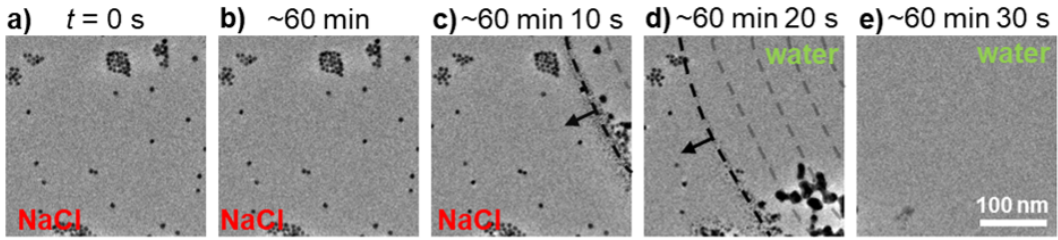
Figure 5.1: Solute-induced Dynamics in LP-TEM Flow Experiments. Insufficient calibration of mass transport and beam effects prohibit to distinguish between solute-induced and beam-mediated dynamics. *Black dashed line* indicates reaction front. Note the long delay in respect to the short degradation timescale. Adapted from [202].

insights could still be gained from the experiment. Foremost, surprisingly long delay times indicated a poor understanding of mass transport in LP-TEM flow reactors. These time scales exceed those relevant for many samples and corresponding *ex situ* setups, typically in the range of a few seconds.[200] They further prohibit disregarding accumulative beam effects in the interpretation of experimental observations.[95, 133]

These aspects motivated a systematic study of mass transport properties of LP-TEM flow reactors and beam effects which is discussed in Ch. 5.2, Ch. 5.3 and Ch. 5.4. Thereafter, Ch. 5.5 outlines the impact of the gathered knowledge for the design of flow reactors with optimized properties. Finally, in Ch. 5.6, several model experiments are reported to illustrate the impact of the knowledge acquired and the methodology developed for LP-TEM research.

5.2 Development of numerical Mass Transport Models

To investigate mass transport in different LP-TEM scenarios, various numerical models were implemented following standard FE modelling routines. The routines comprise 4 steps: 1) generation of the geometric model, 2) definition of relevant physics, initial and boundary conditions, 3) meshing of the geometry considering physical aspects, and finally 4) computing solutions under either stationary or time-dependent conditions. Refer to Ch. 4 for more details on each step. COMSOL Multiphysics (COMSOL, USA)[182] software was used as modelling environment given its friendliness for users with limited coding skills. *Optimal* models resulted as a trade off between accuracy and computational cost. Different requirements determined the implementation of each model (see Ch. 5.2.1 & 5.2.2).

5.2.1   Mass Transport in *realistic* Flow Channel Geometry

The core achievement of this doctoral thesis was to implement numerical models describing the convective and diffusive mass transport in *realistic* 3D channel geometries of commercial LP-TEM flow reactors (refer to Merkens *et al.*, *Ultramicroscopy*, 2023; Appendix A, p. 125).[197] The correct representation of the channel geometry was crucial for the success. Therefore, a virtual model of the flow channel system was generated from the virtual model of the LP-TEM device *via* virtual imprinting. CAD files of the setup were obtained from Protochips company and converted into 3D channel structures. In fact, geometric models of two different LP-TEM systems were generated, namely the Poseidon 200 and Poseidon Select (both Protochips Inc.). The two setups were chosen as they reflect two different types of flow reactors (compare Ch. 5.4.1).

Adequate meshing of the entire 3D geometry was essential for successful modelling of mass transport. Issues resulted from the sheer size of the 3D model as well as the 4 orders of magnitude difference in spatial dimensions between different compartments of the channel. Successful meshing relied on various tricks aiming to strategically accumulate mesh elements where they were most useful, both in space and time. Thus, individual meshes were developed for each mass transport mechanism and *artificial* channel compartments were created to increase control over the meshing process. The optimal meshes were determined in refinement studies (Ch. 4).[197]

Both, stationary and time-dependent solutions of the model were calculated. Stationary solutions were obtained for the characterization of fluid convection through the different flow channel geometries, thereby identifying preferential flow paths. Time-dependent description of the replacement of two reaction solutions were conducted to gain insights on the relevance of convective and diffusive transport for solution exchange dynamics. Below, this model is referred to as convection & diffusion (C&D) model.

5.2.2   Beam-induced Reaction Kinetics under Flow Conditions

Whether continuous flow can be applied to effectively rinse radiolytic species from the irradiated volume has been a long-standing question in LP-TEM postulated in various occasions.[42, 48, 122] By the time this thesis was conducted, only simple reaction-diffusion models existed;[37] no efforts had been reported to investigate the effect of flow.

In this thesis, a comprehensive numerical model describing the effect of flow on beam-induced chemical reactions was implemented. The model combined radiolytic reaction ki-

netics with diffusive and convective mass transport. Selective irradiation was reflected by generating initial species through source terms acting in a channel domain representing typical TEM conditions. The unfolding reaction network for neat water consisted 73 reactions between 15 species and was adapted from literature.[37] Notably, the vast amount of reactions drastically increase the computational costs, in particular due to the spatially heterogeneous irradiation scenario. The implementation thus relied on simplifications of the model geometry. 2D geometric representations, both horizontal and vertical, were generated to best reflect experimental realities, making use of symmetries. The models allowed to calculate stationary solutions providing steady-state concentration maps of all radiolytic species under different flow and irradiation conditions (compare Ch. 5.4.3). Below, the model is referred to as radiolysis & flow (R&F) model. Details on the implementation are provided in <u>Merkens</u> *et al.*, *Nano Express*, 2023 (Appendix A, p. 166).[203]

5.3   Model Validation

Numerical models are a practical tool in scientific research. However, they have to be interpreted carefully, since experimental reality can only be approximated. Therefore, it is essential to validate novel models against existing knowledge. Ideally, this knowledge is obtained through experiments; however, reference models provide an important alternative to validate novel models in scenarios where experimental data are hardly accessible. In the context of this thesis, both approaches were exploited: While existing methods to measure mass transport properties of microfluidic setups could be used to experimentally validate the C&D model, the R&F model could only be validated against existing reference models. The limitation in the latter scenario stems from the extremely difficult detection of radiolytic species, particularly in LP-TEM setups,[117, 204] which exceeded the resources within the scope of this thesis.

5.3.1   Evaluation *vs* Experiments

Flow experiments were crucial to validate the C&D model developed in this thesis. Convection in the C&D model was implemented by applying a forced volumetric flow. The pressure gradient, Δp, that was required for the requested volumetric flow rate, Q_{total}, was estimated by solving the stationary model. <u>Merkens</u> *et al.*, *Ultramicroscopy*, 2023 describes how a pressure-driven pumping system was used to measure the Δp-Q_{total}-dependence

experimentally.[203] A calibration curve enabled to calculate the overall flow resistance (Eq. 3.6), which was used to guide the geometrical model refinement, in particular to determine BP segments.

Moreover, an image contrast variation method was developed for experimental evaluation of solution exchange (see **Fig. 5.2**). The concept relies on the dependence of the transmitted intensity of a probe beam on the composition of the sample which it is passing through (see Ch. 4 for details).[197] In double-inlet flow reactors, the composition, and therefore contrast,
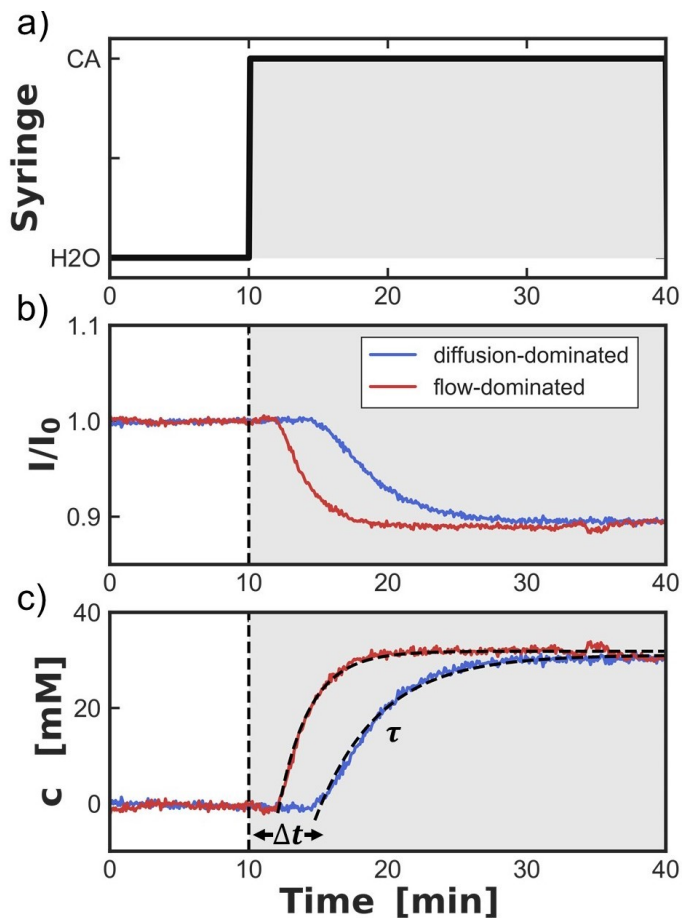
**Figure 5.2: Image Contrast Variation Method.** Changes to the flow conditions (**a**) lead to changes in the measured transmitted intensity (**b**) and can be converted into contrast agent concentration *via* concentration calibration (**c**). Characteristic numbers, *i.e.,* delay time Δt and exponential decay time constant τ serve for comprehensive hydrodynamic characterization of microfluidic LP-TEM setups.

in the IA can be altered by alternating the flow between solutions entering through the two available inlets: through one inlet pure solvent, here water, was provided, while a contrast agent (PTA) was provided through the other. The measured image contrast was converted into solute concentration through multi-point calibration. Thereby obtained experimental concentration curves were in good agreement with simulated curves evidencing successful implementation of the C&D models. The accuracy of the models was further confirmed by characteristic parameters defined to quantify solution replacement dynamics (see Ch. 5.4).

Image contrast variations were induced by both optical and electron-scattering dyes and tracked *via* UV-vis spectroscopy and electron microscopy, respectively.[197, 205] Each approach had advantages and disadvantages. While the optical method was more accessible (cheaper & faster) than the EM-based method, finding adequate optical dyes turned out more challenging due to limited compatibility with the setup (low extinction coefficients & chemical degradation). Note that the image contrast variation method is intrinsically limited to the IA defined by the narrow SiN windows in the LC. In contrast, the numerical modelling approach provides access to the entire flow reactor geometry.

5.3.2 Evaluation *vs* Reference Models

The R&F model implemented in this thesis was carefully evaluated against a reference model of diffusion & reaction in simpler 0D & 1D scenarios to support its validity.[37] Details thereon are provided in <u>Merkens</u>, *Nano Express*, 2023 (Appendix A, p. 166).[203] Moreover, the preliminary results initiated a follow up doctoral project partially dedicated to developing experimental strategies to validate radiolysis models in LP-TEM scenarios currently developed by Giuseppe De Salvo in the Electron Microscopy group at CIC nanoGUNE.

5.4 Central Findings

The bimodal approach combining theoretical and experimental methods developed in this thesis (compare Ch. 5.2) has evoked a deeper understanding of mass transport in LP-TEM scenarios which is outlined in the following. In Ch. 5.4.1, a classification scheme for microfluidic LP-TEM setups is provided with regards to the effects of their channel geometry on mass transport. Based on this, a profound analysis of mass transport in different holder configurations is carried out in Ch. 5.4.2. Finally, in Ch. 5.4.3, the effect of diffusive and, in particular, convective mass transport mechanisms on radiolysis is investigated.

5.4.1   Classification of LP-TEM Flow Reactor Setups

Many LP-TEM flow reactors have been introduced either in scientific literature or made available commercially.[43, 44, 45, 46, 47] As outlined in Ch. 3.2, the ideal LP-TEM flow reactor design depends on the specific application. Since currently available flow reactors do not combine the full range of features required for chemical flow reactors, selecting appropriate setups for LP-TEM flow experiments involves a trade-off between the multiple desired properties. This thesis has made substantial contributions to the development of criteria to classify LP-TEM flow reactors and thus facilitate the selection of appropriate setups for experiments.

In general, LP-TEM flow reactors are modular systems in which external flow control units are used to supply fluids through macroscopic supply channels to a sub-micrometre-sized LC where imaging is performed. The macroscopic supply lines are integrated into special TEM sample holders typically measuring some tens of centimetres in length and hundreds of micrometres in diameter. The LC is formed by two E-chips in the tip of the sample holder with channel heights of only a few hundreds of nanometres and lateral extension of a few millimetres. The IA is usually located in the center of the LC.

In <u>Merkens</u> *et al.*, *Ultramicroscopy*, 2023,[197] two *flow concepts* were identified which differ in respect to various aspects, most importantly the preferential flow path through the microfluidic LP-TEM systems. In *direct flow* setups, most of the flow is forced into the NC located in the LC by applying rather high operating pressures. As a consequence, mass transport is convection-dominated with high flow velocities established in the IA. In *bathtub* setups, micrometer-sized (off-chip) BP channels significantly reduce the operating pressure and substantially redirect the flow around the LC. This leads to diffusion-dominated mass transport in the IA due to very low flow velocities in the NC.

In multi-inlet setups, various characteristic locations can be identified to differentiate between systems as illustrated in **Fig. 5.3**. At the interface point (IP), the macroscopic channel compartment transitions into the NC located in the LC. The IA denotes the limited field of view defined by electron beam-transparent membranes, typically in the very centre of that NC. In multi-inlet flow reactors, the mixing point (MP) defines the location where (all) inlet channels merge. The channel segment between MP and IP is typically referred to as premixing channel.

In <u>Merkens</u> *et al.*, *Nature Communications*, *in review*, two *mixing concepts* were identified
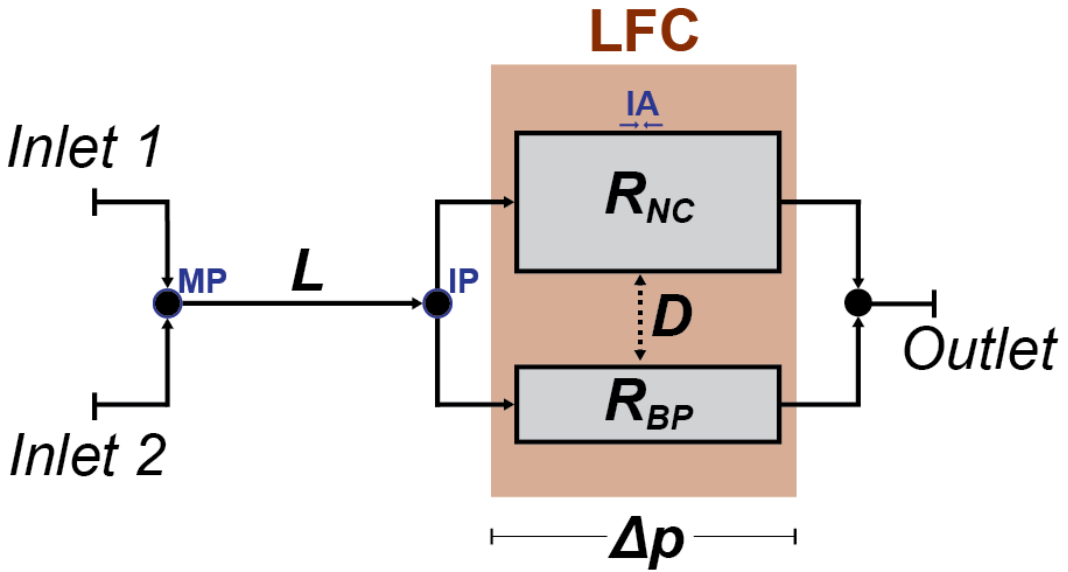
Figure 5.3: General Schematics of Double Inlet LP-TEM Flow Reactors. The internal geometry of the flow reactor defines its mass transport properties. Refer to the text or <u>Merkens</u> *et al.*, *Nature Communications*, *in review* for details on the depicted schematics (Appendix A, p. 140).[205]

for LP-TEM flow reactors.[205] In *premixing* setups, fluids are supplied through channels that merge far before the IP. In *onsite mixing* setups, the supply channels reach the LC separately so that the IP and the MP coincide. By combining the presented design concepts (*premixing vs. onsite mixing* and *direct flow vs. bathtub*), 4 different (in terms of mass transport dynamics) holder configurations, all with different IP, IA and MP locations, can be envisioned. Specific implementations of such systems may comprise a negligible premixing channel ($L = 0$) and either non-existent ($1/R_{\mathrm{BP}} = 0$) or multiple ($1/R_{\mathrm{BP}} = \sum(1/R_i)$) BPs, amongst others, without violating the generality of the description and **Fig. 5.3**.

5.4.2   Solution Exchange in LP-TEM Flow Reactors

As illustrated in Ch. 5.1, a qualitative understanding and quantitative knowledge of solution exchange dynamics in flow reactors is crucial to induce nanoscale dynamics and interpret the observations from LP-TEM experiments. Considering the large number of commercially available setups,[44, 47, 46, 45] it is rather surprising that hardly any information thereon is available, or at least publicly accessible. In this sub-chapter, the mass transport dynamics for

different holder configurations are first described qualitatively and thereafter characteristic numbers are introduced to quantify them. The two holder configurations which were used for experiments can best be characterized as *premixing/direct flow* and *onsite mixing/bathtub* design; compare previous sub-chapter. Further, refer to Ch. 4 for the specifications of both sample holders. The corresponding sample holders (Poseidon 200 and Poseidon Select; both Protochips Inc.)[44] are extensively used in numerous areas of LP-TEM research.[197]

5.4.2.1 Qualitative Description of Mass Transport Mechanisms

According to fundamental microfluidic knowledge outlined in Ch. 3.3, exchange dynamics result from the superposition of convection and diffusion. Their interplay in LP-TEM setups was found to be strongly affected by the flow channel geometry as illustrated by **Fig. 5.4**. In idealized *direct flow* setups (no BP), solution exchange is substantially governed by convection. The extremely thin central NC in the LC leads to high local velocities, v_c, that outperform diffusive transport, but requires extremely high operating pressures to push fluids through due to its high flow resistance. The C&D model which was developed in <u>Merkens *et al.*</u>, *Ultramicroscopy*, 2023, enabled the estimation of the flow resistance of such idealized *direct flow* configurations to be in the range of $R_{\text{total}} \sim 1$ bar·h/µL. This value corresponds to 4000 bar required to reach typical flow rates of 300 µL/h. Notably, this drastically exceeds experimentally realistic values (compare Ch. 5.3).[197]

Incorporating BP compartments around the NC decreases the overall flow resistance and promotes the relevance of diffusion on mass transport in the LC. In <u>Merkens *et al.*</u>, *Ultramicroscopy*, 2023, the initial model was refined by including tiny, yet relevant, BP compartments around the LC to realistically describe the Poseidon Select setup (**Fig. 5.4a**).[197] The thereby unlocked flow paths were preferred over the thin NC segments, reducing the flow velocity therein. More importantly, the overall flow resistance dropped significantly, *i.e.*, by 5 orders of magnitude as compared to the idealized configuration, such that the experimentally obtained values ($R_{\text{total}} \sim 0.3$ bar·h/µL) could be fitted.

The relevance of diffusion was dependent on present concentration gradients and the extend to which flow can bypass the NC. *Bathtub* configurations represent the extreme case with huge BP channels. Therein, the majority of flow bypasses the LC, rendering diffusion the predominant mass transport mechanism in the NC (**Fig. 5.4b**). This, for instance, applies for the Poseidon 200 sample holder.
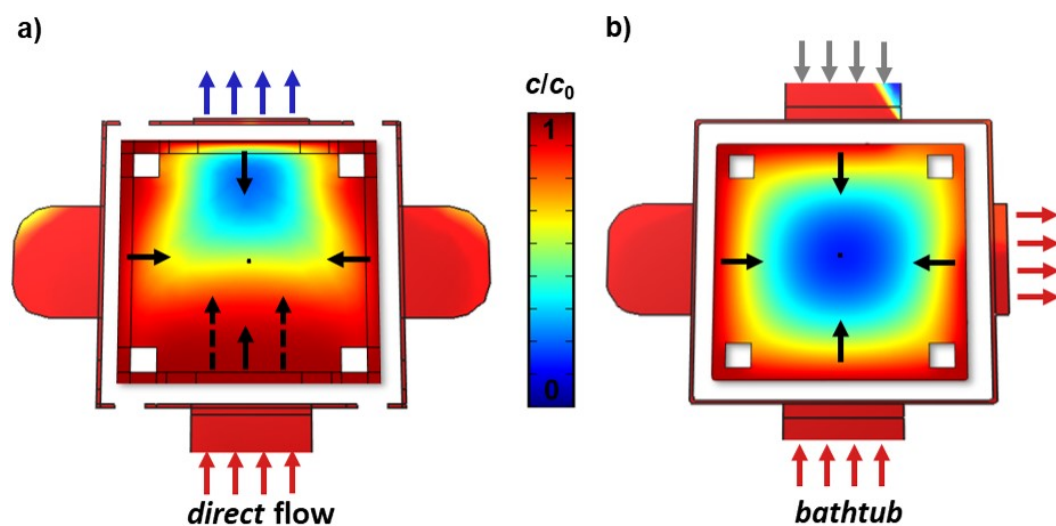
Figure 5.4: Mass Transport Mechanisms governing Solution Replacement.
Solution Replacement in *direct flow* (**a**) and *bathtub* (**b**) setups is governed by convection (*black arrows*) and diffusion (*dashed black arrows*), respectively. The solute concentration (c/c_0) distribution is depicted 200 s after the replacement was induced by changing the flow applied to the inlets. Mirror and radial symmetry of the concentration profiles indicate convection & diffusion as dominant mass transport mechanism, respectively. Depicted schematics were adapted from Merkens *et al.*, *Ultramicroscopy*, 2023.[197]

Both, convection- and diffusion-dominated setups are suited to continuously supply reactants to and/or remove them from the IA. While convective renewal relies on movement of the entire fluid, diffusive processes depend on the self-motion of solutes. In scenarios where the sample cannot be fixed inside the IA, diffusion-dominated setups should thus significantly reduce the risk of flushing the sample during the experiment. However, Merkens *et al.*, *Ultramicroscopy*, 2023 demonstrated that convection-based strategies provide superior control over the transport rate through the applied flow rate, supposedly reaching higher overall fluxes.[197] That may explain why they have found wider application, *e.g.*, for (electro-)chemical experiments, in which fluid flow is used to refresh reagents, *e.g.,* electrolytes, and/or remove liquid or gaseous reaction products.[42, 125] Groundbreaking research examples of energy materials were emphasized in Yang, Feijóo, Briega, Li, Krumov, Merkens *et al.*, *Current Opinion in Electrochemistry*, 2023.[206] Additionally, the potential to flush radiolytic species from the IA was proposed in various occasions,[48, 122] but never supported by systematic studies to the date this doctoral project was conducted (see Ch. 5.4.3).

Multiple inlets provide control over the composition of the liquid inside the microfluidic LP-TEM system. Experimentally, solution replacement was achieved by adjusting the flow rates at each of the inlets (compare Ch. 4.1.2 on operating flow systems). Although the flow was switched sharply, *i.e.*, within less than a seconds, between the two syringes, it was found that the concentration changes in the IA occurred with a significant time delay and proceeded rather gradually until a steady-state was reached (compare **Fig. 5.2**). Ch. 5.4.2.2 provides a quantitative analysis of the according time regimes for both convection- and diffusion-controlled setups.

More important to mention here are the qualitative differences in the two setups studied. In *premixing* setups with negligible BP channels (like Poseidon Select), the delay time was found to be largely determined by the retention time in the premixing channel compartment. In *onsite mixing* setups featuring extensive BP channels (Poseidon 200), time delay resulted predominantly from diffusion through the NC, *i.e.*, from the IP to the IA. Diffusion, superimposed on convection, was further the main cause for initially sharp concentration gradients becoming blurred (Taylor dispersion);[207] the retention time defined the time frame for this effect to evolve.

A notable conclusion of these findings is that the mass transport dynamics can be controlled by both experimental and structural parameters. In convection-controlled setups, the retention time, and therefore mass transport dynamics, can be altered through the applied flow rate. However, in diffusion-controlled setups, it is predetermined through the length of the diffusion path, *i.e.*, the width of the NC, and the solute's diffusion coefficient.

As outlined in Ch. 3.2, both setups have been used to induce solution exchange in different scenarios, predominantly to replicate mixing experiments. The interpretation of acquired image sequences was often limited, as beam effects could rarely be discarded from the observed dynamics;[208] most likely due to the elongated time regimes of solution replacement as also illustrated in **Fig. 5.1**. Further information on the qualitative aspects of mass transport is provided in <u>Merkens *et al.*</u>, *Ultramicroscopy*, 2023.[197]

5.4.2.2   Quantitative Characterization based on Hydrodynamic Parameters

Quantitative parameters were defined for the characterization and comparison of different LP-TEM flow reactors. Key numbers were the total flow channel resistance, R_{total}, the flow velocity in the center of the NC, v_{c}, the delay time, Δt, and the decay time constant, τ of

solution replacement. R_{total} is proportional to the pressure gradient, Δp, required to reach a given flow rate, Q_{total} (Eq. 3.6). It was obtained from both experiment & simulation and allowed the evaluation of modelled channel geometries and conclusions about bulging. v_{c} was obtained from numerical models only and served to estimate the relevance of convective flux in solution exchange, as well as evaluating the risk of flushing (by-)products and poorly immobilized samples. Δt and τ were obtained from experimental & simulated concentration curves *via* exponential fitting and applied to parameterize solution replacement dynamics.

The flow channel resistance, R_{total}, was determined to be in the range of a few hundreds of bar·h/mL for the convection-controlled Poseidon Select system (C.C. in **Fig. 5.5**); this corresponds to a pressure gradient of several hundred millibar along the channel at maximum applicable flow rates of 300 µL/h.[198] The resistance of the diffusion-controlled Poseidon 200 (D.C. in **Fig. 5.5**) was found 2 orders of magnitude smaller due to the larger BP available. The same overall flow rates can thus be achieved at drastically lower operating pressures (a few millibar for 300 µL/h). Experimentally measured flow resistances were crucial to validate the C&D model (Ch. 5.3);[197] in particular, they provided valuable hints on the geometric peculiarities of flow channel setup, *e.g.,* presence of BP channels. The developed bimodal approach will thus enable verification of ambiguous channel geometries of other LP-TEM flow setups, *e.g.,* ref. [41].
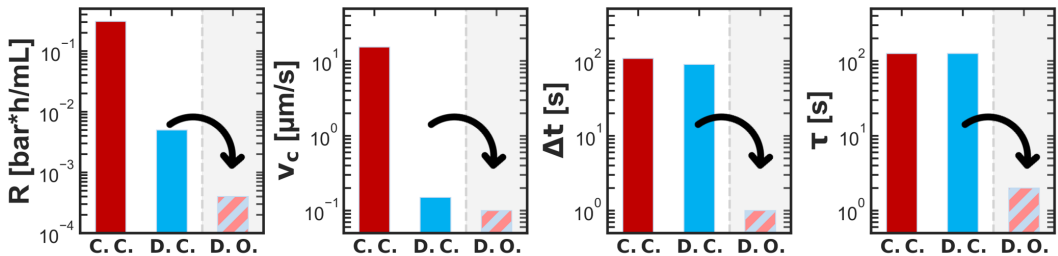
Figure 5.5: Quantitative Parameters characterizing Mass Transport. a) Total flow resistance, R_{total}; **b)** flow velocity in the center, v_{c}; **c)** delay time, Δt; decay time constant, τ, for convection- (C.C.) and diffusion-controlled (D.C.) as well as customized diffusion-optimized (D.O. $\triangleq$ *diffusion cell* in **Fig. 5.8**) LP-TEM flow reactors. Data from Merkens *et al.*, *Ultramicroscopy*, 2023 (*white background*) & Merkens *et al.*, *Nature Communications*, *in review* (*grey*) are combined for comparative purposes using the same color code (Appendix A, p. 126 & p. 140).[197, 205] *Black arrows* illustrate the by ~2 orders improved hydrodynamic properties of D.O. setups (see Ch. 5.5).

The operating pressure, Δp, is the experimentally relevant parameter that follows from the flow resistance according to Eq. 3.6. The significantly lower operating pressure in diffusion-controlled setups, *e.g.*, Poseidon 200, can be beneficial to improve image contrast. However, bulging is expected to still be determined by the pressure difference between the microscope's column ($\sim 10^{-8}$ mbar) and the high outlet pressure (typically ambient pressure, $p_{amb} \sim 1$ bar). Pressure-driven pumping systems are promising as they enable negative outlet pressures thereby reducing the overall pressure (below p_{amb}), and bulging.[209, 210] Indeed, this approach led to first promising results reported in literature.[42] In this thesis, preliminary results obtained with moderate negative outlet pressures ($p_{out} \approx$ -600 mbar) indicated contrast improvements of up to 15% (*unpublished*). However, this strategy is intrinsically limited due to the underlying working principle. In fact, the liquid is saturated with the gas used to force it through the channel. Consequently, the gas is likely to condensate into bubbles blocking segments of the channel.[176, 197] The condensation of gas bubbles is further facilitated by the decreasing pressure along the flow channel as well as sharp edges present in the flow channel.[211] Two major drawbacks are associated with the accumulating gaseous species: 1) they affect mass transport through the channel, and 2) may interfere with the radiolysis reaction network altering beam-mediated chemistry (see Ch. 5.4.3.3).[39]

Flow velocities in the IA of a few 10 µm/s and 0.1 µm/s were obtained for the convection-(Poseidon Select) and the diffusion-controlled setup (Poseidon 200) at maximum volumetric flow rate of Q_{total}=300 µL/h, respectively (see **Fig. 5.5b**). Note that since window bulging was neglected in the model, the results may overestimate the real values.[197] However, the obtained results are in agreement with flow velocities estimations for various setups reported elsewhere. For instance, Petruk *et al.* mentioned flow velocities as high as 50 mm/s for convection-optimized flow reactors, *i.e.*, no BP available.[43] The values were obtained from FE models and could not be validated in experiment. For the Stream system by DENSsolutions,[47] similar flow velocities, $v_c \sim 10$ mm/s, would be expected at comparable overall flow rates and NC heights of 200 nm relying on the *direct flow* design claimed.[41, 42] However, when we estimated the regime of required working pressures based on available information,[47] highly unrealistic working pressures ($\Delta p \sim 1000$ bar) were obtained. By adapting the model geometry (primitive models with channel heights of 1-2 µm, *i.e.*, larger than the nominal spacer size), more reasonable working pressures ($\Delta p \sim 7$ bar) were achieved leading to flow velocities $v_c \leq 1$ mm/s. These values are supported by recent experiments,

where the authors applied particle image velocimetry and measured the channel flow speed to be of a few µm/s for nominal spacer thickness of 500 nm (Q_{total}=300 µL/h).[212] Overall, the extended discussion highlights the importance of flow velocity calibration which is crucial to understand & control solution exchange dynamics, particularly the effect of convective transport on beam-induced chemistry. An in-depth discussion thereof follows in Ch. 5.4.3.

Finally, the timescale of solution replacement was determined to be in the range of (tens of) minutes with $\Delta t \approx \tau \approx 100$ s (**Fig. 5.5c** & **d**). There is no quantitative data available to compare the values to other multi-inlet LP-TEM flow reactors. Based on geometrical similarity, it is reasonable to assume that most other setups have similar characteristic timescales.[46] Recently, Insight Chips company (Insight Chips, Frederiksberg, Denmark)[45] provided qualitative data indicating the capability to fill the NC within seconds; however, the setup is strongly limited regarding the deposition of the sample prior to the experiment due to the monolithic LC design.[213]

The timescales of solution replacement in LP-TEM setups must be evaluated in the context of the nanoscale process of interest as well as mixing in *ex situ* reference setups. Both timescales are typically much shorter: nanoscale dynamics tend to occur on the (sub-)second timescale and mixing in batch reactors is completed within seconds.[16] Hence, the mixing timescales achievable with currently available microfluidic LP-TEM setups largely exceed the required range. This issue explains why mixing experiments are barely reported in literature and was further the main driving force for the prototyping of customized LP-TEM flow reactors described in Ch. 5.5. In depth discussion of all characteristic parameters, for instance their dependence on flow rate, is provided in Merkens *et al.*, *Ultramicroscopy*, 2023.[197]

5.4.3 Effect of Flow on Radiolysis

After the dynamics of convective and diffusive mass transport in LP-TEM flow reactors had been revealed (see above), the next challenge was to evaluate their impact on radiochemical processes, which are known to be of crucial importance in many LP-TEM scenarios.[31] Given the difficulty to measure radiolytic species in LP-TEM setups,[117] FE models offer a convenient environment to better understand radiolysis in such scenarios. Due to the complexity of the subject, the implementations available in literature are of limited accuracy. As outlined in Ch. 3.2.3, efforts had been concentrated on the reaction kinetics of beam-generated species and only recently was diffusion included as pertinent mass

transport mechanism.[37] The reported model geometries are strongly simplified,[37] which complicates transferring the results to *realistic* scenarios. Below, the effect of continuous flow on the radiolytic reaction network based on the R&F model are discussed (Ch. 5.4.3.1 & 5.4.3.2). Thereafter, in Ch. 5.4.3.3, the implications for scavenging strategies are revised.

5.4.3.1 Radiolytic Reaction Network under Continuous Flow

Based on simulations performed with the R&F model described in Ch. 5.2, continuous flow was found to have counter intuitive effects on the radiolytic reaction network in the irradiated volume of the modelled NC. A strong non-linear dependence of the steady-state concentration of radiolytic species on the flow velocity was revealed: only for a limited number of species did the steady-state concentration decrease with increasing flow rate; for a considerable number of chemically relevant species, an increase compared to zero flow was observed in an intermediate flow velocity regime. Mostly (gaseous) secondary (H_2 & O_2) and many less relevant primary species were eliminated efficiently; whereas several primaries experienced a significant increase in concentration, in particular $H^.$ & e_h^-.

The results were analysed in-depth considering reactant's lifetimes, spatial separation and self-scavenging of the reaction network. Refer to Merkens *et al*, *Nano Express*, 2023 for details (Appendix A, p. 166).[203] In brief, the concentration increase was traced back to a suppressed consumption of highly reactive species due to the removal of secondary radiolytic species which act as self-scavengers in the zero flow scenario. In **Fig. 5.6**, the mechanism
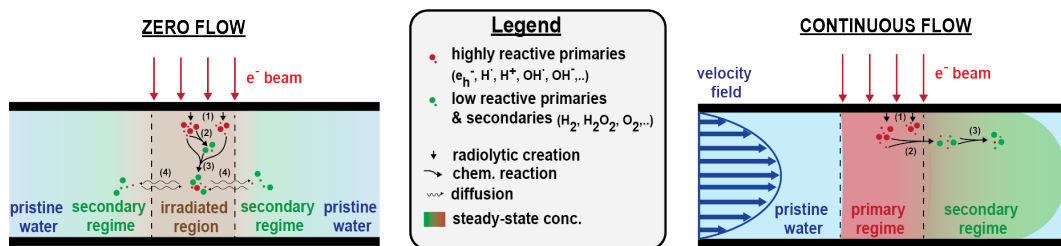
Figure 5.6: The Effect of Flow on Radiolysis. The radiolytic reaction network unfolds differently under zero (*left*) and continuous (*right*) flow conditions: (1) radiolytic generation of primary species; (2) creation of secondary species; (3) consumption of primaries; (4) diffusive coupling. Flow prohibits the accumulation of secondary species in proximity to the irradiated region and thus self-scavenging of the reaction network. Refer to Merkens *et al.*, *Nano Express*, 2023 for details (Appendix A, p. 166).[203]

is illustrated comparing the regime of continuous flow conditions (*right*) to the zero flow case (*left*). Diffusion-mediated self-scavenging is outperformed in the flow scenario. Similar trends were already evidenced but left unnoticed by Schneider *et al.* who reported high concentration of primaries about 10^{-5} s after irradiation started, which decreased later when the concentration of secondaries, and thus consumption rates, increased.[37]

5.4.3.2 Response to Flow Velocity & Composition of Influent Solution

The radiolysis reaction network was found to be highly sensitive to changes in the applied flow velocity as well as the composition of the solution entering through the inlet. **Fig. 5.7a & b** depict the steady-state concentration of all species in the reaction network for pristine water entering at mean flow velocities $\overline{v} \leq 1$ m/s. The concentration values were averaged across the IA. The absolute values are depicted in **5.7a** and were normalized to the zero flow values in **Fig. 5.7b**. The increase in concentration of H· and e_h^- was quantified to be 5- respectively 6-fold compared to zero flow (depicted at $\overline{v}=10^{-9}$ m/s due to logarithmic scale of x-axis).

When the composition of the entering solution was altered, the steady-state of the reaction network was found to be affected as well. **Fig. 5.7c** reflects the normalized concen-
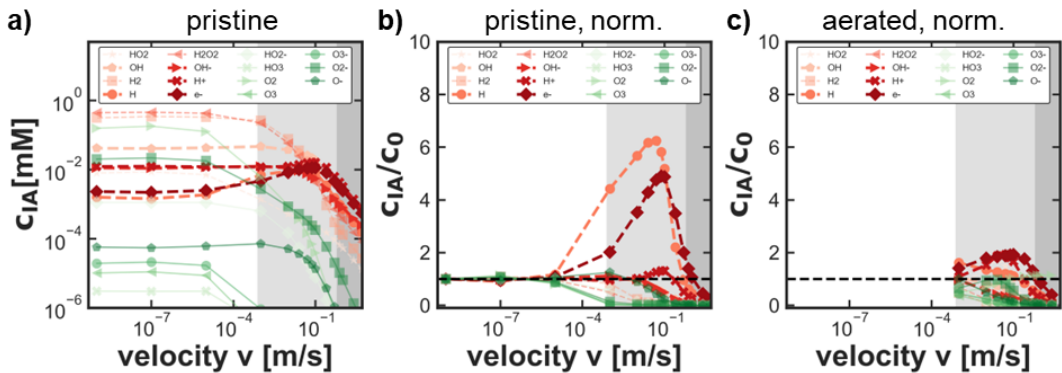
Figure 5.7: Steady-State Concentration of Radiolytic Species under Flow. The steady state concentration of all radiolytic species averaged over the IA is shown at different flow velocities. **a)** & **b)** Absolute concentration and normalized to zero flow for pristine water, respectively. **c)** Normalized concentration for aerated water (0.18 mM O_2). *Light grey* and *grey* background indicate the flow velocity regimes that lead to non-linear increase and effective flushing, *i.e.*, all $c_{IA}/c_0 < 1$. Refer to Merkens *et al.*, *Nano Express*, 2023 for details (Appendix A, p. 166).[203]

tration values for the flow of aerated solution (0.18 mM O_2) in the relevant velocity range. While the relative increase of e_h^- and particularly $H^{\cdot}$, was substantially suppressed ($<2x$), other species experienced concentration increase, *e.g.,* H^+.

5.4.3.3 Scavenging Strategies for Flow Experiments

Based on the understanding gained on the effect of convective transport on reaction networks (Ch. 5.4.3.1 & 5.4.3.2), its applicability for scavenging radiolytic species was evaluated. Therefore, the results in **Fig. 5.7** must be discussed in the context of existing LP-TEM flow reactors. In Ch. 5.4.2, the range of currently achievable local flow velocities was determined to be $v_c \leq 10^{-2}$ m/s. In this range, the concentration of many relevant species increases drastically, implying that fluid flow alone is not a suited general scavenging method.

Fortunately, flow is predestined to be combined with chemical scavenging strategies as reactants can be continuously provided through the inlets.[39, 120] Flow setups can thus ensure selective scavenging at long experimental timescales, contrary to closed LCs where scavengers are to be consumed within seconds.[91] The intrinsic challenge with chemical scavenging strategies is that the peculiarities of each chemical system must be considered separately and appropriate scavengers must be found for every process individually. Therefore, targeted literature research on reaction kinetics and the development of specific models must be pursued. Such task exceeded the scope of this doctoral project. Yet, the Electron Microscopy group of CIC nanoGUNE established fruitful collaborations with international institutions (Woehl group, University of Maryland, Baltimore, USA & Hutzler group, FZ Jülich, Germany) to further developing the knowledge acquired in this direction.

Nevertheless, the strong dependence of both selectivity and efficiency on $\overline{v}$ (compare **Fig. 5.7**), may potentially limit the success of flow-based scavenging strategies. Experimentalists might be forced to commit to a fixed flow rate in order to optimize other aspects of the multi-parameter problem. These aspects raised the question if scavenging approaches that rely on diffusion as flow velocity-independent mass transport mechanism may be more promising. However, diffusion-dominated solution exchange had demonstrated to be insufficient due to the long diffusion length in currently available *bathtub* setups (compare Ch. 5.4.2.1). As predicted from theory and as demonstrated in closed cell mixing setups,[91, 179] diffusion can lead to rapid solution exchange when it occurs over distances significantly shorter than the millimeter range. These considerations additionally motivated the development of diffusion-optimized LP-TEM flow reactors as outlined in Ch. 5.5.

5.5   Prototyping of customized LP-TEM Flow Reactors

5.5.1   Rapid Prototyping

A rapid prototyping process combining virtual and physical steps (compare Ch. 3.3.4.2) was established to develop optimized LP-TEM setups. The virtual prototyping step relied on validated C&D models (Ch. 5.2 & 5.3). Therein, the flow channel geometry was optimized numerically aiming at improving the solution exchange dynamics at low flow velocities in the IA. During the geometric modelling, limitations expected in the fabrication process were anticipated to best knowledge. In the physical step, prototypes were fabricated relying on top-down manufacturing. Workflows to process commercial E-chips (Protochips, Inc.) based on lithography methods and were developed under the guidance of Dr. Christopher Tollan. Experimental details of the workflow are intellectual property of CIC nanoGUNE & Protochips company.

5.5.2   The *Diffusion Cell* Concept

Optimized LP-TEM setups were designed emphasizing the role of diffusive mass transport. The concept of such *diffusion cells* is illustrated in **Fig. 5.8b**: micrometer-sized flow chan-
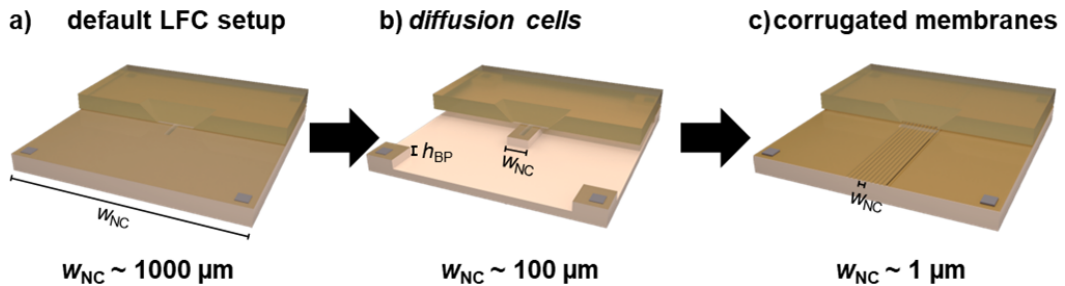

Figure 5.8: LC Designs for Diffusion-Optimized Mass Transport. a) In default setups, the lateral expansion of central NC is in the millimeter-range, resulting in extremely slow diffusion-controlled mass transport when off-chip BPs are present. **b)** *Diffusion cells* were developed to reduce the expansion of the central NC by 1 order, thereby accelerating diffusive transport by 2 orders of magnitude. Intrinsic limitations result from the window size. **c)** Further shrinking of the NC down to $w_{Nc} \sim 1$ µm may be obtained through corrugated membranes which results in NC and BP channels being present *across* the window. Note that corrugation in **c** is not depicted to scale.

nels were incorporated to guide the flow into the LC and around the central NC of reduced lateral extension comprising the IA. The diffusion-optimized design aimed at combining the following desired characteristics: 1) low overall flow resistance/pressure build-up, 2) possibility of large volumetric flow rates, 3) fast (units of seconds) solution exchange dynamics in the absence of flow in the IA, and 4) possibility to mount the sample before the experiment. Another intrinsic benefit of the concept is 5) its compatibility with existing holders as the external dimensions of the chips were kept standard. *Diffusion cells* can be operated in *premixing*- and *onsite mixing*-type sample holders. Details of both configurations are discussed in <u>Merkens</u> *et al.*, *Nature Communications*, *in review* (Appendix A, p. 140).[205]

Said manuscript reports in-depth on the development, fabrication and testing of physical prototypes.[205] Manufactured *diffusion cells* exhibited widths of the central NC in the order of $w_{NC} \approx 100$ µm - one order of magnitude less than the default setup.[198] The height of the incorporated on-chip BP channel was in the order of $h_{NC} \approx 10$ µm.

5.5.3 Improved Quantitative Parameters

In **Fig. 5.5**, the key parameters characterizing the diffusion-optimized setup (D.O.; data shown for modified *diffusion cell* used in Poseidon Select holder only) are summarized alongside with the default convection- and diffusion-controlled setups (Poseidon Select & Poseidon 200 operated with unprocessed flat chips). All parameters were found to be decreased significantly, by up to 2 orders of magnitude, reflecting a drastic improvement with respect to the unmodified designs, which additionally was in good agreement with predictions (compare Eq. 3.20).[179] Lower R_{total} enables for higher overall flow rates; or to operate at identical flow rates, but at lower pressure gradients, *i.e.*, potentially less bulging. This eventually revives the use of pressure-driven pumping strategies to reach negative pressure inside the setup ($p < p_{ambient}$; compare Ch. 5.4.2.2). By reducing v_c the relevance of diffusive mass transport is increased, unleashing new diffusion-based mechanisms to control solution renewal in the IA. Short mixing time constants ($\Delta t \approx \tau \approx$ 1-2 s) indicate drastically accelerated replacement dynamics leading to more realistically replicated mixing experiments inside the TEM. Refer to <u>Merkens</u> *et al.*, *Nature Communications*, *in review* (Appendix A, p. 140) for in-depth discussion of all quantitative parameters.[205]

Characteristic parameters, in particular, mixing time constants decrease with decreasing diffusion length, *i.e.*, the width of the NC.[205] In the evaluated approach, the regime of achievable mixing time constants was limited by structural constraints, *i.e.*, the viewing

windows (nominal width $\sim$50 µm) restricted the extension of the NC to $\sim$100 µm. Further potential for optimization & transferability of the concept to other LP-TEM systems were elucidated in <u>Merkens</u> *et al.*, *Nature Communications*, *in review* (Appendix A, p. 140).[205]

Thereafter, an alternative approach was evaluated to potentially overcome the outlined limitations of *diffusion cells*. The idea is a further development of diffusion-optimized setups (**Fig. 5.8b**) and relies on corrugated membranes as illustrated in **Fig. 5.8c**. Thereby, large BP channels are integrated directly into the viewing window leaving a central NC of drastically reduced lateral expansion. Numerical C&D models were implemented to estimate solution exchange dynamics in such setups. Mixing time constants as short as $\Delta t \approx \tau \approx$ 600-700 ms were obtained for w_{NC}=1 µm as promising preliminary result representing an improvement by $\sim$1 order of magnitude compared to *diffusion cells*. Consequently, the idea was presented as a patent application to the European Patent Office[1] and a project to fabricate first prototypes was initiated at CIC nanoGUNE.

5.6 Model Experiments

The acquired knowledge and the innovative *diffusion cells* constructed in the previous chapters enable quantitative LP-TEM flow experiments. Potential experimental scenarios span across various (electro-)chemical applications. Their realization, however, would demand significant efforts considering the standards this thesis aims to establish. At that point, this thesis encountered a *fortunate* dilemma, as it was impossible to address all improved aspects comprehensively. To give at least a preview, two pivotal model experiments are reported below. Ch. 5.6.1 discusses aspects related to scenarios replicating fast mixing dynamics, while Ch. 5.6.2 aims to demonstrate advances towards in-operando EC experiments.

5.6.1 Solvent-induced Dynamics of confined Nanoparticles

As a first model experiment, the project on solvent-induced dynamics of AuNPs confined in agarose gel introduced in Ch. 5.1 was re-accessed to demonstrate the benefits of improved mass transport in LP-TEM flow reactors. To unambiguously showcase the improvements and reduce beam-induced artefacts, the sample preparation was refocused. First, a reliable

---

[1]The patent application was filed on 24 July 2023 entitled *Flow Cells for Liquid-Phase Transmission Electron Microscopy and Methods* with the application number EP23382771. The designated inventors are A. Chuvilin, <u>S. Merkens</u>, C. Tollan and M. Grzelczak.

sample deposition procedure was developed in collaboration with Dr. Maiara Iriarte from the Self-Assembly group of CIC nanoGUNE and Dr. Joscha Kruse from the Donostia International Physics Center. The agarose solution was spin coated on one of the chips before assembling the LC. The thickness of the obtained thin-films of agarose gel was determined *via* atomic force microscopy (AFM) under 100% humidity. A topographic AFM image is shown in **Fig. 5.9a**. The gel height was measured along the *red dashed line* perpendicular across the step scratched into the sample. For gels with 1w/v% agarose, the optimal spinning speed was determined to be ∼70 rotations per second (r.p.s., during 15 s) leading to a gel thickness meeting the nominal spacer thickness of ∼150 nm (indicated by *black arrow* in **Fig. 5.9b**).

Second, the solution composition was simplified. The organic ligand bis(p-sulfonatophenyl) phenylphosphine (BSPP) was removed from the reaction solutions, to lower the amount of organic molecules thus reducing beam-induced damage. However, BSPP is crucial to control interparticle interactions due to its capability to screen surface charges of the AuNPs.[200] Therefore, attractive interactions between particles are expected to be reduced in the simplified scenario when altering the solution composition between aqueous NaCl solution and pure water (without BSPP). However, random Brownian-like motion of the AuNPs were expected to be maintained. In fact, previous studies reported that surface-mediated diffusion of nanoparticles in LC depends on various parameters comprising the charge of the SiN window, the charge of nanoparticles as well as the ionic strength of the solution, all being affected by the properties of the incident beam.[214] Low ionic strength was observed to substantially suppress particle motion, while an increased ionic strength led to longer hopping distances. Thus, two regimes of particle movement were postulated for providing pure water and NaCl in LP-TEM experiments, respectively.

LP-TEM experiments were prepared by spin coating 1%w/v agarose gel with nominal thickness of 150 nm on a big chip (70 r.p.s., 15 s; compare above) matching the selected spacer height. Together with modified small chips, a *diffusion cell* was assembled in the tip of a *bathtub/onsite mixing*-type sample holder (Poseidon 200, compare 5.5). The relevant geometric parameters of the flow setup comprised the height of the on-chip BP (10 µm) and the extension of the central NC (120 x 650 µm^2) rendering diffusion the dominant mass transport mechanism in the NC due to its nominal height of 150 nm. TEM imaging at a magnification of ∼27000x was applied to image particle movement in changing liquid environment with a temporal resolution of 2 s. During the 8 min of experiment, the flow of
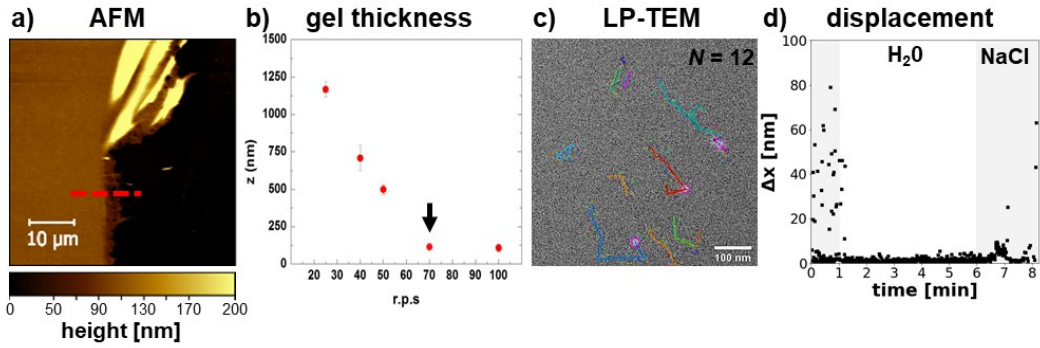
Figure 5.9: Rapid Nanoscale Dynamics induced by Solution Replacement.
a) Topographic AFM image of a spin-coated thin film of agarose gel (1%w/v) on SiN
membrane under 100% humidity. **b)** Dependence of the gel thickness on the spinning
speed (rotations per second, r.p.s.; duration: 15 s) measured across scratches as indi-
cated in **a** (*red dashed line*). **c)** Representative LP-TEM image of AuNPs in agarose gel
(nominal thickness: 150 nm; compare *black arrow* in **b**. The position of particles in the
IA ($N = 12$) was tracked during 8 min of experiment. **d)** Time-dependent displacement
of all tracked particles during the solution replacement experiment depicted in **c**. Two
mobility regimes are revealed; grey and white background indicate active water and
NaCl solution ($c=100$ mM) flow ($Q_{\text{total}}=500$ µL/h). Note the drastically reduced delay
time compared to **Fig. 5.1**.

aqueous NaCl ($c=100$ mM) solution was interrupted by pure water for 5 min starting 1 min
after the image acquisition was initiated.

The acquired image sequences were analysed after the experiment. Therefore, the par-
ticle motions were tracked using ImageJ software (TrackMate plugin). **Fig. 5.9c** depicts
exemplary one image of the acquired sequence, which was overlayed with the tracked paths
of 12 particles present in the IA. The displacement Δx of these particles *vs.* time is depicted
in **Fig. 5.9d**. Two mobility regimes are clearly distinguishable: while in pure water (*white
background*), mobility is strongly suppressed to displacements $0 < \Delta x < 5$ nm, an additional
mode is observed in NaCl solution (*grey*) which is characterized by hopping distances of sev-
eral tens of nanometers. While the hopping regime is in agreement with the hypothesis, the
non-zero displacement in pure water environment indicates beam-induced contraction of the
agarose gel. This interpretation is supported by the observation of various particles moving
in parallel during elongated time periods as illustrated by *blue*, *orange*, *red* and *turquoise*

tracks in **Fig. 5.9c**, however requires further investigation.

More relevant in the context of this thesis, however, are the dynamic aspects of the transition between both mobility regimes since the delay after which transitions occur reflect the solution exchange dynamics. According to **Fig. 5.9d**, the time delay was as short as few tens of seconds. These values are in excellent agreement with experimentally & numerically determined time constants reported in <u>Merkens</u>, *Nature Communications, in review* (Appendix A, p. 140)[205] for comparable experimental scenarios. The displayed experiment thus represents the first ever example of mixing times in the regime of seconds observed on a sample deposited prior to the assembly of the LP-TEM flow reactor. The achieved mixing times are in the range of standard *ex situ* setups and therefore exciting for correlative studies.

Note that the displayed results are preliminary. The main purpose is to illustrate the unique control over mass transport in innovative *diffusion cells*. As the underlying data is part of ongoing unpublished work, the representation may appear incomplete. Different projects are currently being realized and planned to optimize experimental & imaging conditions and increase understanding on the investigated process.

5.6.2   *In-operando* Characterization of Electrocatalysts

Electrochemistry (EC) is a highly relevant field for solving some of the largest problems related to the global energy transition ranging from energy storage to catalysis.[10] LP-TEM has the potential to contribute to various aspects thereof comprising the understanding of morphological changes of battery materials and catalytic processes on the nanoscale.[125] EC LP-TEM systems can be perceived as microscopic model reactors of macroscopic devices.

As discussed in Ch. 3.2.4, various LP-TEM sample holders have been introduced covering the possibility to apply electric potentials and to study electrochemical reactions in liquid environment at the nanoscale,[22] however only little work has been dedicated to calibrate and optimize the setups.[196] Reported developments of electrochemical liquid cell (EC-LC) setups has been driven by design rules derived from macroscopic setups. Most advanced EC-LC setups contain three electrodes comprising working electrode (WE), counter electrode (CE) and reference electrode (RE) to enable advanced experimental control.[22] In designs compatible with the Poseidon Select holder, a WE of $\sim$25.000 µm^2 surface area (A_S) is located in the IA and surrounded by a much larger semicircular CE ($A_S \sim$0.3 mm^2; compare **Fig. 5.10a**) to ensure the accuracy of measurements and efficiency of charge transfer
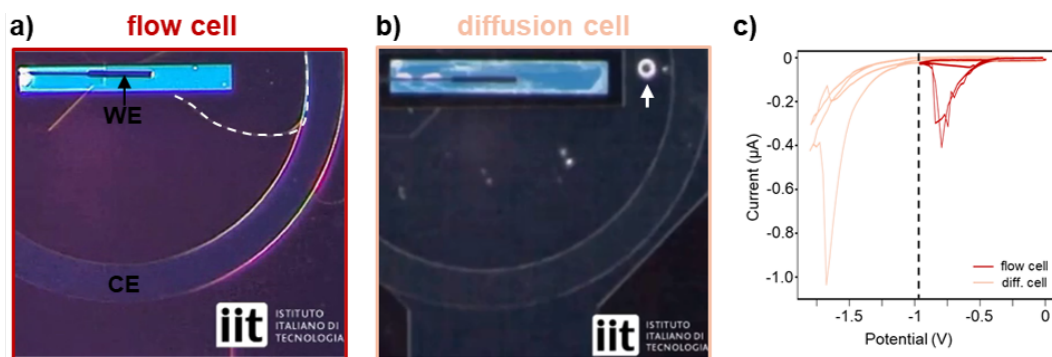
**Figure 5.10:** *In-operando* **Electrochemistry Experiments under** *Extreme* **Conditions. a, b)** Light microscopy images illustrating gas bubble formation during CV experiments in *flow* (C.C. in **Fig. 5.5**; **a**) and *diffusion cells* (D.O. in **Fig. 5.5**; **b**), respectively. Gas bubbles are indicated by *white dashed line* (**a**) and *white arrow* (**b**). The WE an CE are indicated in **a**. **c)** CVs obtained by operating default *flow* (*dark red curve*) and *diffusion cells* (*light red*) in Poseidon Select sample holder under flow conditions ($Q_{\text{total}} \sim$ 2000 µL/h). *Diffusion cell* setups sustain more negative potentials ($V \sim$ -1.6 V) and currents ($A \sim$ -1 µA) compared to *flow cells* for which accumulating gas bubbles restrict the *V*- and *A*-range to $\sim$ 1 V and $\sim$ -0.4 µA (*black dashed line*), respectively. Figures were adapted from Bejtka, Fontana, Gho, Merkens *et al.*, *Nature Communications, in submission.*[215]

from/to the electrolyte to maintain overall electric neutrality. The WE and CE are made from glassy carbon and platinum to image a sample *on* the electrode and to ensure excellent conductivity, respectively. All electrodes measure a few tens of nanometers in height to fit in the NC.

As outlined in the invited review Yang, Feijóo, Briega, Li, Krumov, Merkens *et al.*, *Current Opinion in Electrochemistry*, 2023,[206] such EC-LC setups have provided valuable insights into electrochemical materials and processes under moderate conditions of low potentials ($<$ 1 V) and currents (a few hundred nA). However, these setups encountered intrinsic limitations stemming from slow mass transport in the confined LC volume.[153] Particularly, when subjected to harsh conditions ($V > $1V), electrochemical water splitting generates gaseous species eventually leading to the formation of bubbles within the EC-LC. The effective removal of bubbles, or the prevention of their nucleation in the first place, is crucial to maintain stable conditions throughout the extended duration of EC experiments

and would enable *operando* conditions.

In macroscopic EC setups, flow is typically employed to efficiently avoid accumulation of adverse reaction products. Nevertheless, in LP-TEM flow setups operated with default LCs (flat chips without on-chip BP), rinsing bubbles appeared impossible, even at elevated flow rates of 2000 µL/h, as demonstrated by optical experiments described in Bejtka, Fontana, Gho, <u>Merkens</u> *et al.*, *Nature Communications*, *in submission*.[215]

The same manuscript discusses the advantages of enhanced diffusive mass transport in *diffusion cells* for EC experiments. Notably, the accumulation of gas bubbles on the WE was drastically reduced, as relatively small bubbles were continuously flushed away (indicated by *white arrow* in **Fig. 5.10b**). The improvements brought about by *diffusion cells* were quantified through CV and CA measurements. **Fig. 5.10c** illustrates a comparison between CVs obtained with *diffusion cells* (*light red curves*) and default *flow cell* setups (*dark red*). It reveals significantly, by factors of x2 and x3, extended ranges of stable potential respectively current. Even after applying strong electric potentials as big as $|V| \sim 1.8$ V, which led to dramatic bubble nucleation, initial conditions were efficiently restored within short periods of a few minutes in *diffusion cells* (not shown).

The drastic improvements illustrated in this chapter open the way for in-operando studies of electrochemical materials, particularly catalysts, enabling more correlative investigations. Further details will be shortly available in Bejtka, Fontana, Gho, <u>Merkens</u> *et al.*, *Nature Communications*, *in submission*.[215]

Chapter 6

General Conclusions

6.1   A Quantitative Approach to Mass Transport

This thesis establishes new quantitative standards regarding mass transport in LP-TEM scenarios. A bimodal approach of numeric models and flow experiments was developed enabling deep understanding of solution exchange in relevant LP-TEM flow reactors with widely accessible and restricted BP channels, respectively. Notably, the approach is easily transferable to characterize any LP-TEM flow reactor, potentially also those with less well-known channel geometries. Additionally, rapid prototyping procedures were implemented based on validated numeric models which enabled for the rational design of setups with defined mass transport properties. Further, understanding and control of the effect of convective transport on radiolysis reaction networks were achieved by merging a reaction diffusion model[37] with the physics of flow. The infrastructure presented in this thesis can be easily extended for increasingly realistic scenarios, both in terms of imaging conditions, *e.g.*, STEM irradiation, and considered stimuli, *e.g.*, electric biasing & heating.

In Merkens *et al.*, *Ultramicroscopy*, 2023 and Merkens *et al.*, *Nature Communications*, *in review*, the effect of different construction elements on transport characteristics was classified, which allowed for the categorization of LP-TEM flow reactors by channel geometry.[197, 205] The hydrodynamic properties of flow reactors were found to be determined by diffusion and convection and the interplay between both mechanisms varying strongly between different channel geometries. Two criteria are crucial to categorize multi-inlet setups: 1) the relative positioning of mixing *vs.* imaging location (*premixing vs onsite mixing*), and 2) the presence

of flow in the central NC (direct *vs* bypass flow). Moreover, characteristic numbers were defined to quantify solution exchange properties of LP-TEM flow reactors. Tab. 6.1 summarizes the range of the overall flow resistance (R_{total}), the local flow velocity (v_c) and the time constants of solution replacement (Δt & τ) for the investigated setups with restricted (Poseidon Select) and widely available BP (Poseidon 200).

Table 6.1: Comparison of calibrated LP-TEM flow reactors.

Holder	Config.	Mixing	Mass Transport	R_{total} [mbar·h/µL]*	v_c [µm/s]	τ [s]**
Poseidon Select	direct flow-like	premixing	convection	0.1-1	10	~100
Poseidon 200	bypass	onsite mixing	diffusion	0.01	0.1	≥100
diffusion cell	both	both	diffusion	0.0001	0.1	~1

* To convert R_{total} into required pressure (gradient), Δp, divide by flow rate, Q. Typical values are Q~100 µL/h.

** The delay time constant, Δt, was typically in the same order of magnitude as τ and was omitted for convenience.

6.2 Constraints of current Flow Reactors

The fact that access to LP-TEM sample holders and their hydrodynamic calibration had been limited led to insufficient consideration of their properties when selecting them for flow experiments.[79] Finally, the quantitative approach established here allows determining the possibilities and limitations of mass transport in LP-TEM flow reactors.

Merkens *et al.*, *Ultramicroscopy*, 2023 demonstrated that mass transport in setups with no or strongly limited BP is dominated by convection.[197] This results in high local flow velocities, and therefore convective renewal rates, in the IA, but requires high pressure gradients. This implies a significant risk to flush the sample and excessive window bulging degrading image contrast. Notably, applied flow rates provide certain control over the outlined properties. In conclusion, said distinctions can largely be extended to *direct flow* setups, such as ref. [47].

The manuscript further showed that mass transport in setups with substantial BP is determined by diffusion.[197] The low overall resistance allows for high overall flow rates through the setup, while local velocities in the IA remain low. As a result, samples are more likely to remain in the IA even without fixation. Renewal rates may result too low, as they are diffusion limited. In addition, applied flow rates have rather small impact on the outlined properties. In conclusion, said distinctions can largely be extended to *bathtub* setups, such as ref. [46].

In both LP-TEM setups investigated, the time constants of solution replacement were determined to be in the order of hundreds to thousands of seconds when operated using default LC designs. This is largely exceeding the timescale of nanoscale processes of interest as well as the mixing timescales of *ex situ* setups. Thus, mixing dynamics that can be replicated in existing LP-TEM setups are intrinsically limited to rather slow processes. The premixing channel was further found to cause an intrinsic delay as well as smearing of the observed concentration gradients. These properties are aggravated in *bathtub* setups with long diffusion length, *i.e.*, the extension of the NC, but result negligible in *onsite mixing* setups if direct flow can be ensured, *e.g.* , ref. [213].

Moreover, the effect of flow on the radiolysis reaction network was emphasized in Merkens *et al.*, *Nano Express*, 2023. The concentration of several highly reactive radiolytic species, *i.e.*, H$^{\cdot}$ & e$_{\mathrm{h}}^{-}$, were found to follow non-linear trends with increasing flow velocity which hampers the control over processes in the LC. Window bulging and the complex 3D channel structure add to the complexity.

6.3 Improving Methodology

To improve experimental methodology, the availability of adequate flow reactors is crucial. After having identified the constraints of existing equipment, a more suited flow reactor with superior mass transport properties was developed. The novel design is based on *diffusion cells* which were introduced in Merkens *et al.*, *Nature Communications*, *in review.*[205] The underlying concept combines various advantages which are summarized in Tab. 6.1. The versatility and integrity of *diffusion cells* allows overcoming the drawbacks associated with various established setups. Fast mass transport through the flow reactor and low risk of window breakage are achieved by enabling high total flow rates at low pressure build-up. The risk of flushing the sample from the IA is reduced by the negligible convective transport in the central NC. Enhanced diffusive transport drastically accelerates solution exchange in the IA. The dynamics of solution exchange were demonstrated within a few seconds, which is the fastest dynamics reported in literature. Ideas for further improving the performance of LP-TEM flow reactors were discussed in the context of a patent application.

This thesis explores various strategies for mitigating the effect of radiolytic species. In Merkens *et al.*, *Nano Express*, 2023,[203] the use of continuous flow as a general scavenging approach was ruled out due to the strong non-linear response of the radiolysis reaction

network. However, when combined with chemical scavenging strategies, continuous flow becomes powerful as it ensures a continuous supply of reagents. To achieve high scavenging selectivity and efficiency in the IA, precise control over the flow channel geometry and chemical reaction dynamics is essential. Merkens *et al.*, *Nature Communications, in review* points to an alternative scavenging mechanism in flow reactors based on diffusion in the central NC.[205] In diffusion-optimized setups, the NC can be seen as a liquid reservoir with minimal convective transport, allowing for control over the solution composition at the transition from the BP into the NC. This has the potential to simplify flow-mediated scavenging approaches to the precise control of reaction kinetics, which can be effectively simulated in diffusion-reaction models with simple 1D symmetry.[37]

6.4 Guidelines for Flow Experiments

Based on the adequate equipment and improved methodology developed in this thesis, practical guidelines for flow experiments can be derived. The knowledge gathered suggests to define specific *ideal* use cases for each LP-TEM flow reactor. This thesis proposes the following four main criteria to categorize LP-TEM flow experiments: 1) efficient solution renewal in the IA, 2) rapid solution mixing/replacement, 3) imaging of beam-sensitive samples and 4) high resolution imaging. Rules to select suited flow reactors for each scenario were derived from the corresponding experimental requirements. Recent advances in the field, to which this thesis has contributed substantially, have led to the availability of suitable flow reactors for each category. A need for further improvement exists, for instance regarding numeric modelling, but has been identified and is being addressed by the LP-TEM community. Tab. 6.2 summarizes the complex situation and aims to assist experimentalists in selecting the *ideal* flow reactor for their specific use case. As partially pointed out in the invited review Yang, Feijóo, Li, Krumov, Merkens *et al.*, *Current Opinion in Electrochemistry*, 2023, numerous research fields, including electrochemistry, biochemistry, nanotechnology will benefit from proper selection of experimental setups.[206]

6.5 Extending Frontiers

The results of this thesis are expected to substantially contribute to the development of LP-TEM by extending frontiers in existing areas. In fact, calibrated mass transport al-

Table 6.2: Guidelines for LP-TEM flow experiments.

Main Criteria	Requirement	Drawbacks	Design Requirements	Availability	Field of Application
efficient renewal in imaging area	high flux (locally): convective; diffusive	altered radiolysis chemistry, sample eventually flushed	depend on concept: high local flow velocity, short diffusion length	YES flow-controlled[43] diffusion-controlled[205]	electrochemistry & -catalysis
solution mixing/ replacement	correlative mixing dynamics, avoid flushing of sample	difficult to control (geometric complexity)	multiple inlets mixing region (convection vs diffusion)	YES within minutes[197] within seconds[205]	solute-induced nucleation, growth and SA
sensitive samples	controlled liquid environment effective scanning	precise preparation precise control	flow vs composition	in parts flow reactor yes, modelling needs development	biological & -chemical
high resolution imaging	minimized bulging	flow-induced pressure, thin channel -> high pressure	low hydrodyn. pressure, window integrity	in parts integrated windows,[213] pressure-driven flow[42]	atomic imaging of nucleation, growth & morphology changes

lows to select adequate flow setups for solution exchange experiments and paves the way to unequivocally disentangle flow-induced processes from beam-induced artefacts. Better understanding and control of radio-chemistry under flow conditions, helps clearing the view on the evolving chemistry under desired stimuli. By overcoming these long-standing bottlenecks, more reliable & quantitative analysis is enabled which will provide insights into a wide range of samples & processes.[49] In particular, studies of (electro-)chemically active materials, *e.g.*, catalysts, are often limited by excessive generation of gaseous species causing bubble nucleation. Diffusion-optimized setups have demonstrated improved solution renewal properties ensuring stable imaging conditions at long (tens of minutes) timescales and high (∼1.8 V) applied voltages enabling *in-operando* experiments (compare Bejtka, Merkens *et al*, *Nature Communications*, *in submission*).

In addition, the reported findings have the potential to initiate entirely new sub-areas of LP-TEM. Since previously, the timescale of solution replacement in state-of-the-art LP-TEM flow reactors has been limited to several minutes, the mixing process was strongly interfering with the nanoscale process under investigation. The rationally-designed flow reactors introduced in this thesis demonstrated unprecedentedly fast replacement dynamics,[205] which will open entirely new areas of materials research that were previously inaccessible *via* LP-TEM. The immense potential of *diffusion cells* was showcased through the solute-induced stimulation dynamics of metallic nanoparticle (compare Ch. 5.6.1), but is far from being exhausted. In general, diffusion-optimized LP-TEM flow reactors are expected to facilitate intriguing insights across numerous fields in very near future, in particular the new *diffusion cell* design given its compatibility with existing LP-TEM setups.

6.6   The Future of LP-TEM

LP-TEM is a rapidly evolving field. In a wider scope, the achievements of this thesis must be seen in the context of other groundbreaking developments reported recently. For instance, improved hard- and software provide data sets with ever increasing quality.[31] Direct electron detectors promise the acquisition of high contrast images at lowest possible dose rates drastically reducing beam damage.[18] Movie-mode dynamic TEM leads the way to sub-microsecond temporal resolution imaging.[216] Adaptation of image processing protocols from well-established light microscopy as well as newly introduced machine learning approaches extend the accessible information and enrich their interpretation.[31, 50] *Con-*

nected lab approaches point the way to the automation of experiments and facilitate handling of real-time data, *e.g.*, AXON Dose by Protochips company.[217]

In the near future, calibrated stimuli and established methodology, to which this thesis has made significant contributions, will hence be crucial to conduct more quantitative experiments under *in situ* & *in-operando* conditions. Moreover, optimised experimental setups will combine multiple stimuli so that results can be better correlated with reference experiments. Finally, samples and processes observed with high spatial and temporal resolution and with suppressed or deciphered beam effects will provide unprecedented insights into the *nanoworld.*

Bibliography

[1] Enoch, J.; McDonald, L.; Jones, L. Evaluating Whether Sight Is the Most Valued Sense. *JAMA Ophthalmol.* **2019**, *137*, 1317–1320.

[2] Heritage, A. Dictionary of the English Language. 2011; `https://www.thefreedictionary.com/observable`.

[3] Land, M. F.; Fernald, R. D. The evolution of eyes. *Annu. Rev. Neurosci.* **1992**, *15*, 1–29.

[4] Wollman, A. J. M.; Nudd, R.; Hedlund, E. G.; Leake, M. C.; Leake, M. C. From Animaculum to single molecules: 300 years of the light microscope. *Open Biology* **2015**, *5*, 150019.

[5] Knoll, M.; Ruska, E. Das Elektronenmikroskop. *Zeitschrift für Physik* **1933**, *78*, 318–339.

[6] Freundlich, M. M. Origin of the electron microscope. *Science* **1963**, *142*, 185–188.

[7] Grzelczak, M.; Pérez-Juste, J.; Mulvaney, P.; Liz-Marzán, L. M. Shape control in gold nanoparticle synthesis. *Chemical Society Reviews* **2008**, *37*, 1783–1791.

[8] Weller, H. Self-Organized Superlattices of Nanoparticles. *Angewandte Chemie (International Edition in English)* **1996**, *35*, 1079–1081.

[9] Araujo, T. P.; Quiroz, J.; Barbosa, E. C.; Camargo, P. H. Understanding plasmonic catalysis with controlled nanomaterials based on catalytic and plasmonic metals. *Current Opinion in Colloid and Interface Science* **2019**, *39*, 110–122.

[10] Cheng, H. N.; Doemeny, L. J.; Geraci, C. L.; Schmidt, D. G. Nanotechnology Overview: Opportunities and Challenges. *ACS Symposium Series* **2016**, *1220*, 1–12.

[11] Grzelczak, M.; Vermant, J.; Furst, E. M.; Liz-marza, L. M. Directed Self-Assembly of Nanoparticles. *ACS nano* **2010**, *4*, 3591–3605.

[12] Grzelczak, M.; Liz-Marzán, L. M.; Klajn, R. Stimuli-responsive self-assembly of nanoparticles. *Chemical Society Reviews* **2019**, *48*, 1342–1361.

[13] Taheri, M. L.; Stach, E. A.; Arslan, I.; Crozier, P. A.; Kabius, B. C.; LaGrange, T.; Minor, A. M.; Takeda, S.; Tanase, M.; Wagner, J. B.; Sharma, R. Current status and future directions for in situ transmission electron microscopy. *Ultramicroscopy* **2016**, *170*, 86–95.

[14] Dubochet, J.; Lepault, J.; Freeman, R.; Berriman, J. A.; Homo, J. . *Journal of Microscopy* **1982**, *128*, 219–237.

[15] De Yoreo, J. J.; Sommerdijk, N. A. Investigating materials formation with liquid-phase and cryogenic TEM. *Nature Reviews Materials* **2016**, *1*, 16035.

[16] Merkens, S.; Vakili, M.; Sánchez-Iglesias, A.; Litti, L.; Gao, Y.; Gwozdz, P. V.; Sharpnack, L.; Blick, R. H.; Liz-Marzán, L. M.; Grzelczak, M.; Trebbin, M. Time-Resolved Analysis of the Structural Dynamics of Assembling Gold Nanoparticles. *ACS Nano* **2019**, *13*, 6596–6604.

[17] Stewart, P. L. Cryo-electron microscopy and cryo-electron tomography of nanoparticles. *Wiley Interdisciplinary Reviews: Nanomedicine and Nanobiotechnology* **2017**, *9*, e1417.

[18] Nakane, T. et al. Single-particle cryo-EM at atomic resolution. *Nature* **2020**, *587*, 152–156.

[19] Klein, K. L.; Anderson, I. M.; De Jonge, N. Transmission electron microscopy with a liquid flow cell. *Journal of Microscopy* **2011**, *242*, 117–123.

[20] Jonge, N. D.; Ross, F. M. Electron microscopy of specimens in liquid. *Nature nanotechnology* **2011**, *6*, 695–704.

[21] Copois, V. et al. Imaging of soft materials using in-situ liquid-cell TEM. *International Journal of Pharmaceutics* **2007**, *127*, 549–59.

[22] de Jonge, N.; Ross, F. M. In *Liquid Cell Electron Microscopy*, 1st ed.; Ross, F. M., Ed.; Cambridge University Press: New York, 2016; Vol. 1; p 494.

[23] Grogan, J. M. The nanoaquarium: A platform for in situ transmission electron microscopy in liquid media. Ph.D. thesis, 2011.

[24] Abrams, I. M.; McBain, J. W. A closed cell for electron microscopy. *Journal of Applied Physics* **1944**, *15*, 607–609.

[25] Lutz, L.; Dachraoui, W.; Demortière, A.; Johnson, L. R.; Bruce, P. G.; Grimaud, A.; Tarascon, J. M. Operando Monitoring of the Solution-Mediated Discharge and Charge Processes in a Na-O$_2$ Battery Using Liquid-Electrochemical Transmission Electron Microscopy. *Nano Letters* **2018**, *18*, 1280–1289.

[26] Beermann, V.; Holtz, M. E.; Padgett, E.; De Araujo, J. F.; Muller, D. A.; Strasser, P. Real-time imaging of activation and degradation of carbon supported octahedral Pt-Ni alloy fuel cell catalysts at the nanoscale using: In situ electrochemical liquid cell STEM. *Energy and Environmental Science* **2019**, *12*, 2476–2485.

[27] Cameron Varano, A.; Rahimi, A.; Dukes, M. J.; Poelzing, S.; McDonald, S. M.; Kelly, D. F. Visualizing virus particle mobility in liquid at the nanoscale. *Chemical Communications* **2015**, *51*, 16176–16179.

[28] Kröger, R.; Verch, A. Liquid Cell Transmission Electron Microscopy and the Impact of Confinement on the Precipitation from Supersaturated Solutions. *Minerals* **2018**, *8*, 21.

[29] Chee, S. W.; Baraissov, Z.; Loh, N. D.; Matsudaira, P. T.; Mirsaidov, U. Desorption-mediated motion of nanoparticles at the liquid-solid interface. *Journal of Physical Chemistry C* **2016**, *120*, 20462–20470.

[30] Woehl, T. J.; Moser, T.; Evans, J. E.; Ross, F. M. Electron-beam-driven chemical processes during liquid phase transmission electron microscopy. **2020**, *45*, 746–753.

[31] Ou, Z.; Liu, C.; Yao, L.; Chen, Q. Nanoscale Cinematography of Soft Matter System under Liquid- Phase TEM. *Accounts of Material Research* **2020**, *1*, 41–52.

[32] Jonah, C. D. A Short History of the Radiation Chemistry of Water. *Radiation Research* **1995**, *144*, 141–147.

[33] Wang, C.; Shokuhfar, T.; Klie, R. F. Precise In Situ Modulation of Local Liquid Chemistry via Electron Irradiation in Nanoreactors Based on Graphene Liquid Cells. *Advanced Materials* **2016**, *28*, 7716–7722.

[34] Moser, T. H.; Mehta, H.; Park, C.; Kelly, R. T.; Shokuhfar, T.; Evans, J. E. The role of electron irradiation history in liquid cell transmission electron microscopy. *Science Advances* **2018**, *4*, eaaq1202.

[35] Meijerink, M. J.; Spiga, C.; Hansen, T. W.; Damsgaard, C. D.; de Jong, K. P.; Zečević, J. Degradation and Stabilization of Silica Nanospheres in Liquid Phase Transmission Electron Microscopy. *Particles & Particle System Characterization* **2018**, *36*, 1800374.

[36] Woehl, T. J.; Jungjohann, K. L.; Evans, J. E.; Arslan, I.; Ristenpart, W. D.; Browning, N. D. Experimental procedures to mitigate electron beam induced artifacts during in situ fluid imaging of nanomaterials. *Ultramicroscopy* **2013**, *127*, 53–63.

[37] Schneider, N. M.; Norton, M. M.; Mendel, B. J.; Grogan, J. M.; Ross, F. M.; Bau, H. H. Electron-Water interactions and implications for liquid cell electron microscopy. *Journal of Physical Chemistry C* **2014**, *118*, 22373–22382.

[38] Elliot, A. J.; McCracken, D. R. Computer modelling of the radiolysis in an aqueous lithium salt blanket: Suppression of radiolysis by addition of hydrogen. *Fusion Engineering and Design* **1990**, *13*, 21–27.

[39] Woehl, T. J.; Abellan, P. Defining the radiation chemistry during liquid cell electron microscopy to enable visualization of nanomaterial growth and degradation dynamics. *Journal of Microscopy* **2016**, *265*, 135–147.

[40] Kashin, A. S.; Ananikov, V. P. Monitoring chemical reactions in liquid media using electron microscopy. *Nature Reviews Chemistry* **2019**, *3*, 624–637.

[41] van Omme, J. T.; Wu, H.; Sun, H.; Beker, A. F.; Lemang, M.; Spruit, R. G.; Maddala, S. P.; Rakowski, A.; Friedrich, H.; Patterson, J. P.; Perrez Garza, H. H. Liquid phase transmission electron microscopy with flow and temperature control. *Journal of Material Chemistry C* **2020**, *8*, 10781–10790.

[42] Beker, A. F.; Sun, H.; Lemang, M.; van Omme, J.; Spruit, R. G.; Bremmer, M.; Basak, S.; Garza, H. P. In Situ Electrochemistry inside the TEM with Controlled Mass Transport. *Nanoscale* **2020**, *12*, 22192–22201.

[43] Petruk, A. A.; Allen, C.; Rivas, N.; Pichugin, K. High flow rate nanofluidics for in-liquid electron microscopy and diffraction. *Nanotechnology* **2019**, *30*, 395703.

[44] Protochips Inc,. 2023; `https://www.protochips.com/`.

[45] Insight Chips. 2023; `https://www.insightchips.com/contact`.

[46] Hummingbird Scientific. 2023; `https://hummingbirdscientific.com/`.

[47] DENSsolutions. 2023; `https://denssolutions.com/`.

[48] Pu, S.; Gong, C.; Robertson, A. W. Liquid cell transmission electron microscopy and its applications. *Royal Society Open Science 7*, 24.

[49] Woehl, T. Refocusing in Situ Electron Microscopy: Moving beyond Visualization of Nanoparticle Self-Assembly to Gain Practical Insights into Advanced Material Fabrication. *ACS Nano* **2019**, *13*, 12272–12279.

[50] Crocker, J. C.; Grier, D. G. Microscopic Measurement of the Pair Interaction Potential of Charge-Stabilized Colloid. *Physical Review Letters* **1994**, *73*, 352–356.

[51] Colinsk, A. In *Introduction to Microfluidics*, 2005th ed.; A. Colinsk„ Ed.; Oxford University Press: Oxford, 2007; pp 503–505.

[52] Whitesides, G. M. The origins and the future of microfluidics. *Nature* **2006**, *442*, 368–373.

[53] Bruus, H. *Theoretical microfluidics*; Oxford University Press: Oxford, 2008; Vol. 45; pp 45–5602–45–5602.

[54] Squires, T. M.; Quake, S. R. Microfluidics: Fluid physics at the nanoliter scale. *Reviews of Modern Physics* **2005**, *77*, 977–1026.

[55] Rapp, B. E. *Microfluidics: Modeling, Mechanics and Mathematics*; Elsevier, 2017.

[56] Ottino, J. M.; Wiggins, S. Introduction: mixing in microfluidics. *Philos. Trans. R. Soc. London A* **2004**, *362*, 923–935.

[57] Dou, Y.; Wang, B.; Jin, M.; Yu, Y.; Zhou, G.; Shui, L. A review on self-assembly in microfluidic devices. *Journal of Micromechanics and Microengineering* **2017**, *27*, 113002.

[58] Hiramoto, K.; Ino, K.; Nashimoto, Y.; Ito, K.; Shiku, H. Electric and electrochemical microfluidic devices for cell analysis. *Frontiers in Chemistry* **2019**, *4*, 396.

[59] Knauer, A.; Schneider, S.; Möller, F.; Csáki, A.; Fritzsche, W.; Köhler, J. M. Screening of plasmonic properties of composed metal nanoparticles by combinatorial synthesis in micro-fluid segment sequences. *Chemical Engineering Journal* **2013**, *227*, 80–89.

[60] Wang, L.; Sanchez, S. Self-assembly via microfluidics. *Lab on a Chip* **2015**, *15*, 4383–4386.

[61] Gerstner, D.; Kraus, T. Rapid nanoparticle self-assembly at elevated temperatures. *Nanoscale* **2018**, *10*, 8009–8013.

[62] Ring, E. A.; Jonge, N. D. Microfluidic system for transmission electron microscopy. *Microscopy and Microanalysis* **2010**, *16*, 622–629.

[63] Egerton, R. F. *Physical Principles of Electron Microscopy*, second edi ed.; Springer International Publishing: Edmonton, 2005; p 196.

[64] Abbe, E. Beiträge zur Theorie des Mikroskops und der mikroskopischen Wahrnehmung. *Archiv für mikroskopische Anatomie* **1873**, *9*, 418–440.

[65] Hell, S.; Wichmann, J. Breaking the diffraction resolution limit by stimulated emission: stimulated-emission-depletion fluorescence microscopy. *Optics Letters* **1994**, *19*, 780–782.

[66] Busch, H. Berechnung der Bahn von Kathodenstrahlen im axialsymmetrischen elektromagnetischen Felde. *Annalen der Physik* **1926**, *386*, 974–993.

[67] de Broglie, L. XXXV. A tentative theory of light quanta. *The London, Edinburgh, and Dublin Philosophical Magazine and Journal of Science* **1924**, *47*, 446–458.

[68] Thompson, G. P. Electron Optics. *Nature* **1932**, 81–83.

[69] Ruska, E. The Development of the Electron Microscope and of Electron Microscopy (Nobel Lecture). *Angewandte Chemie International Edition in English* **1987**, *26*, 595–605.

[70] Scherzer, O. The theoretical resolution limit of the electron microscope. *Journal of Applied Physics* **1949**, *20*, 20–29.

[71] Batson, P. E.; Dellby, N.; Krivanek, O. L. Sub-Angstrom Resolution using Aberration-corrected Electron Optics. *Nature* **2002**, *418*, 617–620.

[72] Reimer, L. In *Springer Series in Optical Sciences*, fourth edi ed.; Hawkes, P. W., Ed.; Springer Berlin Heidelberg: New York, 1997; p 595.

[73] Sawada, H.; Tanishiro, Y.; Ohashi, N.; Tomita, T.; Hosokawa, F.; Kaneyama, T.; Kondo, Y.; Takayanagi, K. STEM imaging of 47-pm-separated atomic columns by a spherical aberration-corrected electron microscope with a 300-kV cold field emission gun. *Journal of Electron Microscopy* **2009**, *58*, 357–361.

[74] Zhu, Y.; Dürr, H. The future of electron microscopy. *Physics Today* **2015**, *68*, 32–38.

[75] Williams, D. B.; Carter, C. B. *Transmission electron microscopy - A textbook for Materials Science*, 2nd ed.; Springer, 1996; p 779.

[76] Susi, T.; Meyer, J. C.; Kotakoski, J. Quantifying transmission electron microscopy irradiation effects using two-dimensional materials. *Nature Reviews Physics* **2019**, *1*, 397–405.

[77] Ottensmeyer, F. P. *Science*; 1982; Vol. 215; pp 461–466.

[78] Hill, M. A.; Smith, F. A. Calculation of initial and primary yields in the radiolysis of water. *Radiation Physics and Chemistry* **1994**, *43*, 265–280.

[79] Gong, P.; Yang, H.; Gao, H.; Zhang, B.; Xie, L. Scanning Near-field Fluorescence Microscopy Applied to ESEM. *IEEE Photonics Technology Letters* **2019**, *31*, 615 – 618.

[80] Novotný, F.; Wandrol, P.; Proška, J.; Šlouf, M. In situ WetSTEM observation of gold nanorod self-assembly dynamics in a drying colloidal droplet. *Microscopy and Microanalysis* **2014**, *20*, 385–393.

[81] Kunstmann-Olsen, C.; Belić, D.; Bradley, D. F.; Grzelczak, M. P.; Brust, M. Humidity-Dependent Reversible Transitions in Gold Nanoparticle Superlattices. *Chemistry of Materials* **2016**, *28*, 2970–2980.

[82] Londono-Calderon, A.; Wang, W.; Lawrence, J. J.; Bu, W.; Vaknin, D.; Prozorov, T. Salt-Induced Liquid Liquid Phase Separation and Interfacial Crystal Formation in Poly (N-isopropylacrylamide)-Capped Gold Nanoparticles. *Journal of Physical Chemistry C* **2021**, *125*, 5349–5362.

[83] Donald, A. M. The use of environmental scanning electron microscopy for imaging wet and insulating materials. *Nature Materials* **2003**, *2*, 511–516.

[84] Abrams, I. M.; McBain, J. W. A closed cell for electron microscopy. *Journal of Applied Physics* **1944**, *15*, 607–609.

[85] Textor, M.; De Jonge, N. Strategies for Preparing Graphene Liquid Cells for Transmission Electron Microscopy. *Nano Letters* **2018**, *18*, 3313–3321.

[86] van Deursen, P. M.; Koning, R. I.; Tudor, V.; Moradi, M. A.; Patterson, J. P.; Kros, A.; Sommerdijk, N. A.; Koster, A. J.; Schneider, G. F. Graphene Liquid Cells Assembled through Loop-Assisted Transfer Method and Located with Correlated Light-Electron Microscopy. *Advanced Functional Materials* **2020**, *30*, 1904468.

[87] Park, J.; Koo, K.; Noh, N.; Chang, J. H.; Cheong, J. Y.; Dae, K. S.; Park, J. S.; Ji, S.; Kim, I.-D.; Yuk, J. M. Graphene Liquid Cell Electron Microscopy: Progress, Applications, and Perspectives. *ACS Nano* **2021**, *15*, 288–308.

[88] Lim, K.; Bae, Y.; Jeon, S.; Kim, K.; Kim, B. H.; Kim, J.; Kang, S.; Heo, T.; Park, J.; Lee, W. C. A Large-Scale Array of Ordered Graphene-Sandwiched Chambers for Quantitative Liquid-Phase Transmission Electron Microscopy. *Advanced Materials* **2020**, *2002889*, 1–6.

[89] Williamson, M. J.; Tromp, R. M.; Vereecken, P. M.; Hull, R.; Ross, F. M. Dynamic microscopy of nanoscale cluster growth at the solid-liquid interface. *Nature Materials* **2003**, *2*, 532–536.

[90] Keskin, S.; Kunnas, P.; de Jonge, N. Liquid-Phase Electron Microscopy with Controllable Liquid Thickness. *Nano Letters* **2019**, *19*, 4608–4613.

[91] Kelly, D. J.; Clark, N.; Zhou, M.; Gebauer, D.; Gorbachev, R. V.; Haigh, S. J. In Situ TEM Imaging of Solution-Phase Chemical Reactions Using 2D-Heterostructure Mixing Cells. *Advanced Materials* **2021**, *33*, 2100668.

[92] Yamazaki, T.; Kimura, Y.; Vekilov, P. G.; Furukawa, E.; Shirai, M.; Matsumoto, H.; Van Driessche, A. E.; Tsukamoto, K. Two types of amorphous protein particles facilitate crystal nucleation. *Proceedings of the National Academy of Sciences of the United States of America* **2017**, *114*, 2154–2159.

[93] Cookman, J.; Hamilton, V.; Price, L. S.; Hall, S. R.; Bangert, U. Visualising early-stage liquid phase organic crystal growth via liquid cell electron microscopy. *Nanoscale* **2020**, *12*, 4636–4644.

[94] de Jonge, N.; Peckys, D. B.; Kremers, G. J.; Piston, D. W. Electron microscopy of whole cells in liquid with nanometer resolution. *Proceedings of the National Academy of Sciences of the United States of America* **2009**, *106*, 2159–64.

[95] Nielsen, M. H.; Aloni, S.; De Yoreo, J. J. In situ TEM imaging of CaCO3 nucleation reveals coexistence of direct and indirect pathways. *Science* **2014**, *345*, 1158–1162.

[96] Ercius, P.; Hachtel, J. A.; Klie, R. F. Chemical and bonding analysis of liquids using liquid cell electron microscopy. *MRS Bulletin* **2020**, *45*, 761–768.

[97] Dunn, G.; Adiga, V. P.; Pham, T.; Bryant, C.; Donez, J.; Belling, J. N.; Lafrance, B.; Jackson, J. A.; Barzegar, R.; Yuk, J. M.; Aloni, S.; Crommie, M. F.; Zettl, A. Graphene-Sealed Flow Cells for In Situ Transmission Electron Microscopy of Liquid Samples. **2020**, *14*, 9637–9643.

[98] Ring, E. A.; de Jonge, N. Video-frequency scanning transmission electron microscopy of moving gold nanoparticles in liquid. *Micron* **2012**, *43*, 1078–1084.

[99] Bychuk, O. V.; O'Shaughnessy, B. Anomalous diffusion at liquid surfaces. *Physical Review Letters* **1995**, *74*, 1795–1798.

[100] Jamali, V.; Hargus, C.; Ben-Moshe, A.; Aghazadeh, A.; Ha, H. D.; Mandadapu, K. K.; Alivisatos, A. P. Anomalous nanoparticle surface diffusion in LCTEM is revealed by deep learning-assisted analysis. *Proceedings of the National Academy of Sciences of the United States of America* **2021**, *118*, e2017616118.

[101] Verch, A.; Pfaff, M.; De Jonge, N. Exceptionally Slow Movement of Gold Nanoparticles at a Solid/Liquid Interface Investigated by Scanning Transmission Electron Microscopy. *Langmuir* **2015**, *31*, 6956–6964.

[102] Chee, S. W.; Anand, U.; Bisht, G.; Tan, S. F.; Mirsaidov, U. Direct Observations of the Rotation and Translation of Anisotropic Nanoparticles Adsorbed at a Liquid-Solid Interface. *Nano Letters* **2019**, *19*, 2871–2878.

[103] Pan, H.; Low, S.; Weerasuriya, N.; Wang, B.; Shon, Y.-S. Morphological transformation of gold nanoparticles on graphene oxide: effects of capping ligands and surface interactions. *Nano Convergence* **2019**, *6*, 11.

[104] Zhang, X.; Zhai, W.; Fan, L.; Kim, F.; Yu, Y. In Situ Electron Microscopy Study of the Dynamics of Liquid Flow in Confined Cells. *ACS Applied Materials & Interfaces* **2022**, *14*, 28882–28889.

[105] Grogan, J. M.; Schneider, N. M.; Ross, F. M.; Bau, H. H. Supporting Information: Bubble and pattern formation in liquid induced by an electron beam. *Nano Letters* **2014**, *14*, 359–364.

[106] Parent, L. R.; Gnanasekaran, K.; Korpanty, J.; Gianneschi, N. C. 100th Anniversary of Macromolecular Science Viewpoint: Polymeric Materials by In Situ Liquid-Phase Transmission Electron Microscopy. *ACS Macro Letters* **2021**, *10*, 14–380.

[107] R., M.; Hauwiller, UC Berkeley UC Berkeley Electronic Theses and Dissertations. Ph.D. thesis, University of California, Berkeley, 2015.

[108] Parent, L. R.; Vratsanos, M.; Jin, B.; Yoreo, J. J. D.; Gianneschi, N. C. Chemical and physical transformations of carbon-based nanomaterials observed by liquid phase transmission electron microscopy. **2020**, *45*, 727–737.

[109] Gupta, T.; Schneider, N. M.; Park, J. H.; Steingart, D.; Ross, F. M. Spatially dependent dose rate in liquid cell transmission electron microscopy. *Nanoscale* **2018**, *10*, 7702–7710.

[110] Le Caër, S. Water Radiolysis: Influence of Oxide Surfaces on H2 Production under Ionizing Radiation. *Water* **2011**, *3*, 235–253.

[111] Mozunder, A.; Magee, J. L. Model of Tracks of Ionizing Radiation Reaction Mechanisms. *Radiation Research* **1966**, *28*, 203–214.

[112] Elliot, A.; Bartels, D. The reaction Set, rate constants and g-values for the simulation of the radiolysis of light water. *Atomic Energy of Canada Limited Report* **2009**, p. 162.

[113] Tian, X.; Zheng, H.; Mirsaidov, U. Aggregation dynamics of nanoparticles at solid–liquid interfaces. *Nanoscale* **2017**, *9*, 10044–10050.

[114] Fritsch, B.; Hutzler, A.; Wu, M.; Khadivianazar, S.; Vogl, L.; Michael, P. M. Accessing local electron-beam induced temperature changes during in situ liquid-phase transmission electron microscopy. *Nanoscale Advances* **2021**, *3*, 2466–2474.

[115] Lee, S.; Schneider, N. M.; Tan, S. F.; Ross, F. M. Temperature Dependent Nanochemistry and Growth Kinetics Using Liquid Cell Transmission Electron Microscopy. *ACS nano* **2023**, *17*, 5609–5619.

[116] Ambrožič, B.; Prašnikar, A.; Hodnik, N.; Kostevšek, N.; Likozar, B.; Žužek Rožman, K.; Šturm, S. Controlling the radical-induced redox chemistry inside a liquid-cell TEM. *Chemical Science* **2019**, *10*, 8735–8743.

[117] Abellan, P.; Gautron, E.; Laverne, J. A. Radiolysis of Thin Water Ice in Electron Microscopy. *J. Phys. Chem. C.* **2023**, *127*, 15336–15345.

[118] Epstein, I. R.; Showalter, K. Nonlinear chemical dynamics: Oscillations, patterns, and chaos. *Journal of Physical Chemistry* **1996**, *100*, 13132–13147.

[119] Zhang, Y.; Keller, D.; Rossell, M. D.; Erni, R. Formation of Au Nanoparticles in Liquid Cell Transmission Electron Microscopy: From a Systematic Study to Engineered Nanostructures. *Chemistry of Materials* **2017**, *29*, 10518–10525.

[120] Abellan, P.; Parent, L. R.; Al Hasan, N.; Park, C.; Arslan, I.; Karim, A. M.; Evans, J. E.; Browning, N. D. Gaining Control over Radiolytic Synthesis of Uniform Sub-3-nanometer Palladium Nanoparticles: Use of Aromatic Liquids in the Electron Microscope. *Langmuir* **2016**, *32*, 1468–1477.

[121] Cho, H.; Jones, M. R.; Nguyen, S. C.; Hauwiller, M. R.; Zettl, A.; Alivisatos, A. P. The use of graphene and its derivatives for liquid-phase transmission electron microscopy of radiation-sensitive specimens. *Nano Letters* **2017**, *17*, 414–420.

[122] Koo, K.; Park, J.; Ji, S.; Toleukhanova, S.; Yuk, J. M. Liquid-Flowing Graphene Chip-Based High-Resolution Electron Microscopy. *Advanced Materials* **2020**, *7*, 2005468.

[123] Chao, H.-Y.; Venkatraman, K.; Moniri, S.; Jiang, Y.; Tang, X.; Dai, S.; Gao, W.; Miao, J.; Chi, M. In Situ and Emerging Transmission Electron Microscopy for Catalysis Research. *Chemical Reviews* **2023**, *123*, 8347–8394, PMID: 37327473.

[124] Wu, H.; Friedrich, H.; Patterson, J. P.; Sommerdijk, N. A.; de Jonge, N. Liquid-Phase Electron Microscopy for Soft Matter Science and Biology. *Advanced Materials* **2020**, *32*, 2001582.

[125] Yang, Y.; Xiong, Y.; Zeng, R.; Lu, X.; Krumov, M.; Huang, X.; Xu, W.; Wang, H.; Disalvo, F. J.; Brock, J. D.; Muller, D. A.; Abruña, H. D. Operando Methods in Electrocatalysis. *ACS Catalysis* **2021**, *11*, 1136–1178.

[126] Xu, Z.; Ou, Z. Direct Imaging of the Kinetic Crystallization Pathway: Simulation and Liquid-Phase Transmission Electron Microscopy Observations. *materials* **2023**, *16*, 26.

[127] Crook, M. F.; Laube, C.; Moreno-Hernandez, I. A.; Kahnt, A.; Zahn, S.; Ondry, J. C.; Liu, A.; Alivisatos, A. P. Elucidating the Role of Halides and Iron during Radiolysis-Driven Oxidative Etching of Gold Nanocrystals Using Liquid Cell Transmission Electron Microscopy and Pulse Radiolysis. *JACS* **2021**, *143*, 11703–11713.

[128] Crook, M. F.; Moreno-Hernandez, I. A.; Ondry, J. C.; Ciston, J.; Bustillo, K.; Alivisatos, A. P. EELS studies reveal in-situ oxidation of concentrated cerium electrolyte substantially influences the chemical environment in graphene liquid cells. *JACS* **2023**, *145*, 6648–6657.

[129] Korpanty, J.; Parent, L. R.; Gianneschi, N. C. Enhancing and Mitigating Radiolytic Damage to Soft Matter in Aqueous Phase Liquid-Cell Transmission Electron Microscopy in the Presence of Gold Nanoparticle Sensitizers or Isopropanol Scavengers. *Nano Letters* **2021**, *21*, 1141–1149.

[130] Korpanty, J.; Parent, L. R.; Hampu, N.; Weigand, S.; Gianneschi, N. C. Thermoresponsive polymer assemblies via variable temperature liquid-phase transmission electron microscopy and small angle X-ray scattering. *Nature Communications* **2021**, *12*, 6568.

[131] Bo, A.; Kraus, T.; Jonge, N. D. Temperature-Dependent Coalescence of Individual Nonpolar Gold Nanoparticles in Liquid. *ACS Applied Nano Materials* **2022**, *6*, 1146–1152.

[132] Holtz, M. E.; Yu, Y.; Gunceler, D.; Gao, J.; Sundararaman, R.; Schwarz, K. A.; Arias, T. A.; Abruña, H. D.; Muller, D. A. Nanoscale Imaging of Lithium Ion Distri-

bution During In Situ Operation of Battery Electrode and Electrolyte. *Nano Letters* **2014**, *14*, 1453–1459.

[133] Rizvi, A.; Mulvey, J. T.; Patterson, J. P. Observation of Liquid–Liquid-Phase Separation and Vesicle Spreading during Supported Bilayer Formation via Liquid-Phase Transmission Electron Microscopy. *Nano Letters* **2021**, *21*, 10325–10332.

[134] Stawski, T. M.; Roncal-Herrero, T.; Fernandez-Martinez, A.; Matamoros-Veloza, A.; Kröger, R.; Benning, L. G. "On demand" triggered crystallization of CaCO3 from solute precursor species stabilized by the water-in-oil microemulsion. *Phys. Chem. Chem. Phys.* **2018**, *20*, 13825–13835.

[135] Ou, Z.; Wang, Z.; Luo, B.; Luijten, E.; Chen, Q. Kinetic Pathways of Crystallisation on the Nanoscale. *Nature Materials* **2019**, *19*, 450–455.

[136] Gourdin, G.; Doan-Nguyen, V. In situ, operando characterization of materials for electrochemical devices. *Cell Reports Physical Science* **2021**, *2*, 100660.

[137] Tan, S. F.; Raj, S.; Bisht, G.; Annadata, H. V.; Nijhuis, C. A.; Král, P.; Mirsaidov, U. Nanoparticle Interactions Guided by Shape-Dependent Hydrophobic Forces. *Advanced Materials* **2018**, *30*, 1–8.

[138] Kim, B. H.; Yang, J.; Lee, D.; Choi, B. K.; Hyeon, T.; Park, J. Liquid-Phase Transmission Electron Microscopy for Studying Colloidal Inorganic Nanoparticles. *Advanced Materials* **2017**, *1703316*, 1–20.

[139] Yao, L.; Ou, Z.; Luo, B.; Xu, C.; Chen, Q. Machine Learning to Reveal Nanoparticle Dynamics from Liquid-Phase TEM Videos. *ACS Central Science* **2020**, *6*, 1421–1430.

[140] Woehl, T. J.; Park, C.; Evans, J. E.; Arslan, I.; Ristenpart, W. D.; Browning, N. D. Direct observation of aggregative nanoparticle growth: Kinetic modeling of the size distribution and growth rate. *Microscopy and Microanalysis* **2014**, *20*, 1612–1613.

[141] Grogan, J. M.; Rotkina, L.; Bau, H. H. In situ liquid-cell electron microscopy of colloid aggregation and growth dynamics. *Physical Review E - Statistical, Nonlinear, and Soft Matter Physics* **2011**, *83*, 1–5.

[142] Wu, J.; Gao, W.; Yang, H.; Zuo, J. M. Dissolution Kinetics of Oxidative Etching of Cubic and Icosahedral Platinum Nanoparticles Revealed by in Situ Liquid Transmission Electron Microscopy. *ACS Nano* **2017**, *11*, 1696–1703.

[143] Welch, D. A.; Woehl, T. J.; Park, C.; Faller, R.; Evans, J. E.; Browning, N. D. Understanding the Role of Solvation Forces on the Preferential Attachment of Nanoparticles in Liquid. *ACS Nano* **2015**, *10*, 181–187.

[144] Lin, G.; Chee, S. W.; Raj, S.; Král, P.; Mirsaidov, U. Linker-Mediated Self-Assembly Dynamics of Charged Nanoparticles. *ACS Nano* **2016**, *10*, 7443–7450.

[145] Anand, U.; Lu, J.; Loh, D.; Aabdin, Z.; Mirsaidov, U. Hydration Layer-Mediated Pairwise Interaction of Nanoparticles. *Nano Letters* **2016**, *16*, 786–790.

[146] Chen, Q.; Cho, H.; Manthiram, K.; Yoshida, M.; Ye, X.; Alivisatos, A. P. Interaction potentials of anisotropic nanocrystals from the trajectory sampling of particle motion using in situ liquid phase transmission electron microscopy. *ACS Central Science* **2015**, *1*, 33–39.

[147] Cho, H.; Moreno-Hernandez, I. A.; Jamali, V.; Oh, M. H.; Alivisatos, A. P. In Situ Quantification of Interactions between Charged Nanorods in a Predefined Potential Energy Landscape. *Nano Letters* **2021**, *21*, 628–633.

[148] Zhu, G.; Reiner, H.; Cölfen, H.; De Yoreo, J. Addressing some of the technical challenges associated with liquid phase S/TEM studies of particle, nucleation, growth and assembly. *Micron* **2019**, *119*, 35–42.

[149] Powers, A. S.; Liao, H. G.; Raja, S. N.; Bronstein, N. D.; Paul Alivisatos, A.; Zheng, H. Tracking Nanoparticle diffusion and interaction during self-assembly in a liquid cell. *Nano Letters* **2017**, *17*, 15–20.

[150] Yu, X. Y.; Liu, B.; Yang, L. Imaging liquids using microfluidic cells. *Microfluidics and Nanofluidics* **2013**, *15*, 725–744.

[151] Kim, J.; Jones, M. R.; Ou, Z.; Chen, Q. In Situ Electron Microscopy Imaging and Quantitative Structural Modulation of Nanoparticle Superlattices. *ACS Nano* **2016**, *10*, 9801–9808.

[152] Tan, S. F.; Chee, S. W.; Lin, G.; Mirsaidov, U. Direct Observation of Interactions between Nanoparticles and Nanoparticle Self-Assembly in Solution. *Accounts of Chemical Research* **2017**, *50*, 1303–1312.

[153] Yang, Y. et al. Operando studies reveal active Cu nanograins for CO_2 electroreduction. *Nature* **2023**, *614*, 262–269.

[154] Yang, Y.; Roh, I.; Louisia, S.; Chen, C.; Jin, J.; Yu, S.; Salmeron, M. B.; Wang, C.; Yang, P. Operando Resonant Soft X-ray Scattering Studies of Chemical Environment and Interparticle Dynamics of Cu Nanocatalysts for CO_2 Electroreduction. *Journal of the American Chemical Society* **2022**, *144*, 8927–8931.

[155] Ross, F. M. Opportunities and challenges in liquid cell electron microscopy. *Science* **2015**, *350*, aaa9886.

[156] Wang, M.; Dissanayake, T. U.; Park, C.; Gaskell, K. J.; Woehl, T. J. Nanoscale mapping of non-uniform heterogeneous nucleation kinetics mediated by surface chemistry. *Journal of the American Chemical Society* **2019**, *141*, 13516–13524.

[157] Bakalis, E.; Parent, L. R.; Vratsanos, M.; Park, C.; Gianneschi, N. C.; Zerbetto, F. Complex Nanoparticle Diffusional Motion in Liquid-Cell Transmission Electron Microscopy. *The Journal of Physical Chemistry C* **2020**, *124*, 14881–14890.

[158] Jamali, V.; Hargus, C.; Ben-moshe, A.; Aghazadeh, A.; Dong, H.; Mandadapu, K. K. Anomalous Nanoparticle Surface Diffusion in Liquid Cell TEM is Revealed by Deep Learning-Assisted Analysis. *Chem Rxiv* **2020**, 27.

[159] Welling, T. A. J.; Sadighikia, S.; Watanabe, K.; Grau-carbonell, A.; Bransen, M.; Nagao, D.; Blaaderen, A. V.; Huis, M. A. V. Observation of Undamped 3D Brownian Motion of Nanoparticles Using Liquid-Cell Scanning Transmission Electron Microscopy. *Particle & Particle Systems Characterization* **2020**, *2000003*, 2000003.

[160] Alam, S. B.; Yang, J.; Bustillo, K. C.; Ophus, C.; Ercius, P.; Zheng, H.; Chan, E. M. Hybrid nanocapsules for: In situ TEM imaging of gas evolution reactions in confined liquids. *Nanoscale* **2020**, *12*, 18606–18615.

[161] Crocker, J. C.; Grier, D. G. Methods of digital video microscopy for colloidal studies. *Journal of Colloid and Interface Science* **1996**, *179*, 298–310.

[162] Park, J.; Zheng, H.; Lee, W. C.; Geissler, P. L.; Rabani, E.; Alivisatos, A. P. Direct observation of nanoparticle superlattice formation by using liquid cell transmission electron microscopy. *ACS Nano* **2012**, *6*, 2078–2085.

[163] Lee, W. C.; Kim, B. H.; Choi, S.; Takeuchi, S.; Park, J. Liquid Cell Electron Microscopy of Nanoparticle Self-Assembly Driven by Solvent Drying. *Journal of Physical Chemistry Letters* **2017**, *8*, 647–654.

[164] Yang, Y.; tsun Shao, Y.; Jin, J.; Feij, J.; Roh, I.; Louisia, S.; Yu, S.; Guzman, M. V. F.; Chen, C.; Muller, D. A.; Abrun, D.; Yang, P. Operando Electrochemical Liquid-Cell Scanning Transmission Electron Microscopy (EC-STEM) Studies of Evolving Cu Nanocatalysts for CO 2 Electroreduction. *ACS Sustainable Chemistry Engineering* **2023**, *11*, 4119–4124.

[165] Luo, Y.; Qin, J.; Lin, B. Methods for pumping fluids on biomedical lab-on-a-chip. *Frontiers in Bioscience* **2009**, *14*, 3913–3924.

[166] Pennathur, S. Flow control in microfluidics: Are the workhorse flows adequate? *Lab on a Chip* **2008**, *8*, 383–387.

[167] Pozrikidis, C. *Hydrocarbon Engineering*, second edi ed.; Springer: New York, 2002; Vol. 7; p 791.

[168] Delplace, F. Laminar flow of Newtonian liquids in ducts of rectangular cross-section a model for both physics and mathematics. *Open Access Journal of Mathematical and Theoretical Physics* **2018**, *1*, 198–201.

[169] Longwell, P. A. In *Mechanics of Fluid Flow*; Hill, M. G., Ed.; 1966.

[170] Bao, J. B.; Harrison, D. J. Measurement of flow in microfluidic networks with micrometer-sized flow restrictors. *AIChE Journal* **2006**, *52*, 75–85.

[171] Easley, C. J. Development and application of microfluidic genetic analysis systems. Ph.D. thesis, University of Virginia, Charlottesville, 2006.

[172] Capretto, L.; Cheng, W.; Hill, M.; Zhang, X. Micromixing within Microfluidic devices. *Top Curr Chem* **201**, *304*, 27–68.

[173] Karniadakis, G.; Beskok, A.; Aluru, N. In *Microflows and Nanoflows*; Antman, S. S., Marsden, J. E., Sirovich, L., Eds.; Springer, 2005; p 824.

[174] Robinson, J. P. Flow cytometry: past and future. *BioTechniques* **2022**, *72*, 159–169.

[175] Alotto, P.; Guarnieri, M.; Moro, F. Redox flow batteries for the storage of renewable energy: A review. *Renewable and Sustainable Energy Reviews* **2014**, *29*, 325–335.

[176] Fu, T.; Ma, Y. Bubble formation and breakup dynamics in microfluidic devices: A review. *Chemical Engineering Science* **2015**, *135*, 343–372.

[177] Kruse, J.; Merkens, S.; Chuvilin, A.; Grzelczak, M. Kinetic and Thermodynamic Hysteresis in Clustering of Gold Nanoparticles: Implications for Nanotransducers and Information Storage in Dynamic Systems. *ACS Applied Nano Materials* **2020**, *3*, 9520–9527.

[178] Jahn, A.; Stavis, S. M.; Hong, J. S.; Vreeland, W. N.; Devoe, D. L.; Gaitan, M. Microfluidic mixing and the formation of nanoscale lipid vesicles. *ACS Nano* **2010**, *4*, 2077–2087.

[179] Vakili, M.; Merkens, S.; Gao, Y.; Gwozdz, P.; Vasireddi, R.; Sharpnack, L.; Meyer, A.; Blick, R.; Trebbin, M. 3D Micromachined Polyimide Mixing Devices for in Situ X-ray Imaging of Solution-Based Block Copolymer Phase Transitions. *Langmuir* **2019**, *35*, 10435–10445.

[180] Karnik, R.; Gu, F.; Basto, P.; Cannizaro, C.; Dean, L.; Kyei-Manu, W.; Langer, R.; Farokhzad, O. C. Microfluidic platform for controlled synthesis of polymeric nanoparticles. *Nano Letters* **2008**, *8*, 2906–2912.

[181] Dickinson, E. J.; Ekström, H.; Fontes, E. COMSOL Multiphysics®: Finite element software for electrochemical analysis. A mini-review. *Electrochemistry Communications* **2014**, *40*, 71–74.

[182] Multiphysics, C. COMSOL Multiphysics. 2023; `https://www.comsol.com/`.

[183] Yan, X.; Gu, P. A review of rapid prototyping technologies and systems. *Computer-Aided Design* **1996**, *28*, 307–318.

[184] Walsh, F. C.; Arenas, L. F.; Ponce de León, C. Developments in plane parallel flow channel cells. *Current Opinion in Electrochemistry* **2019**, *16*, 10–18.

[185] Boy, D. A.; Gibou, F.; Pennathur, S. Simulation tools for lab on a chip research: Advantages, challenges, and thoughts for the future. *Lab on a Chip* **2008**, *8*, 1424–1431.

[186] Termizi, S. N. A. A.; Shukor, S. R. A. Computational Fluid Dynamics of Mixing Performance in Microchanel. 2012; `http://dx.doi.org/10.1039/C7RA00172J%0Ahttps://www.intechopen.com/books/advanced-biometric-technologies/liveness-detection-in-biometrics%0Ahttp://dx.doi.org/10.1016/j.colsurfa.2011.12.014`.

[187] Panariello, L.; Mazzei, L.; Gavriilidis, A. Modelling the Synthesis of Nanoparticles in Continuous Microreactors: the Role of Diffusion and Residence Time Distribution on Nanoparticle Characteristics. *Chemical Engineering Journal* **2018**, *350*, 1144–1154.

[188] Bungartz, H.-J., Schäfer, M., Eds. *Fluid-Structure Interaction*; Springer Berlin Heidelberg, 2006; Vol. 53.

[189] Menon, S. H.; Mathew, J.; Anandapadmanabhan, E. N. Simulation techniques for predicting current and voltage distribution across electrode surface and electrolyte. *Journal of Solid State Electrochemistry* **2022**, *26*, 621–638.

[190] Zhu, M.; Wu, Q.; Chi, X.; Luo, Y. Simulation of all-vanadium redox flow batteries based on COMSOL. *Proceedings of the 29th Chinese Control and Decision Conference* **2017**, 6977–6982.

[191] Maghsoudy, S.; Rahimi, M.; Dehkordi, A. M. Investigation on various types of ion-exchange membranes in vanadium redox flow batteries: Experiment and modeling. *Journal of Energy Storage* **2022**, *54*, 105347.

[192] Gundlapalli, R.; Bhattarai, A.; Ranjan, R.; Ghimire, P. C.; Yeo, X. M.; Bin Zainudin, N. A.; Wai, N.; Mahlendorf, F.; Jasincuk, A.; Thorsten, H. Characterization and scale-up of serpentine and interdigitated flow fields for application in commercial vanadium redox flow batteries. *Journal of Power Sources* **2022**, *542*, 231812.

[193] Puleston, T.; Clemente, A.; Costa-Castelló, R.; Serra, M. Modelling and Estimation of Vanadium Redox Flow Batteries: A Review. *Batteries* **2022**, *8*, 121.

[194] Solyali, D.; Safaei, B.; Zargar, O.; Aytac, G. A comprehensive state-of-the-art review of electrochemical battery storage. *Int. Journal of Energy Research* **2022**, *46*, 17786–17812.

[195] Allen, C. R. Design and Fabrication of a Nanofluidic Cell System for High-Resolution Electron Microscopy of in-Liquid Samples. Ph.D. thesis, University of Waterloo, 2017.

[196] Binggeli, M.; Shen, T.-H.; Tileli, V. Simulating Current Distribution of Oxygen Evolution Reaction in Microcells Using Finite Element Method. *Journal of The Electrochemical Society* **2021**, *168*, 106508.

[197] Merkens, S.; Salvo, G. D.; Kruse, J.; Modin, E.; Tollan, C.; Grzelczak, M.; Chuvilin, A. Quantification of reagent mixing in liquid flow cells for Liquid Phase-TEM. *Ultramicroscopy* **2023**, *245*, 113654.

[198] Protochips, Poseidon Select - E-chips Ordering Guide. **2019**, 9.

[199] Oliphant, T. E. Python for Scientific Computing. *Computing in Science and Engineering* **2007**, *9*, 10.

[200] Kruse, J.; Merkens, S.; Chuvilin, A.; Grzelczak, M. Kinetic and Thermodynamic Hysteresis in Clustering of Gold Nanoparticles: Implications for Nanotransducers & Information Storage in Dynamic Systems. *ACS Appl. Nano Mater.* **2020**, *3*, 9520–9527.

[201] Mezzasalma, S. A.; Kruse, J.; Merkens, S.; Lopez, E.; Seifert, A.; Morandotti, R.; Grzelczak, M. Light-Driven Self-Oscillation of Thermoplasmonic Nanocolloids. *Advanced Materials 21*, e2302987.

[202] Merkens, S.; Salvo, G. D.; Kruse, J.; Dukes, M. J.; Modin, E.; Tollan, C.; Grzelczak, M.; Chuvilin, A. Fluidic liquid-phase TEM - towards flow-controlled composition of reaction media. *Wiley Analytical Science* **2021**, 6–12.

[203] Merkens, S.; Salvo, G. D.; Chuvilin, A. The Effect of Flow on Radiolysis in Liquid Phase-TEM flow cells. *Nano Express* **2023**, *3*, 045006.

[204] Robberstad Møller-Nilsen, R. E.; Canepa, S.; Jensen, E.; Sun, H.; Moreno-Hernandez, I. A.; Yesibolati, M. N.; Alivisatos, A. P.; Mølhave, K. S. Quantifying Aqueous Radiolytic Products in Liquid Phase Electron Microscopy. *The Journal of Physical Chemistry C* **2023**, *127*, 15512–15522.

[205] Merkens, S.; Tollan, C.; Salvo, G. D.; Bejtka, K.; Fontana, M.; Chiodoni, A.; Grzelczak, M.; Seifert, A.; Chuvilin, A. Towards sub-second Solution Exchange Dynamics in Liquid-Phase TEM Flow Reactors. *Nature Communications* **2023**, in review.

[206] Yang, Y.; Feijóo, J.; Briega Martos, V.; Li, Q.; Krumov, M.; Merkens, S.; De Salvo, G.; Chuvilin, A.; Jin, J.; Huang, H.; Pollock, C. J.; Salmeron, M. B.; Wang, C.; Muller, D. A.; Yang, P. Operando Methods: A New Era of Electrochemistry. *Current Opinion in Electrochemistry* **2023**, accepted.

[207] Wunderlich, B.; Nettels, D.; Schuler, B. Taylor dispersion and the position-to-time conversion in microfluidic mixing devices. *Lab on a Chip* **2014**, *14*, 219–228.

[208] Rizvi, A.; Mulvey, J. T.; Carpenter, B. P.; Talosig, R.; Patterson, J. P. A Close Look at Molecular Self-Assembly with the Transmission Electron Microscope. *Chemical Reviews* **2021**, *121*, 14232–14280.

[209] Merle, B.; Cassel, D.; Göken, M. Time-dependent deformation behavior of freestanding and SiN$_x$-supported gold thin films investigated by bulge tests. *Journal of Materials Research* **2015**, *30*, 2161–2169.

[210] Wu, H.; Su, H.; Joosten, R. R.; Keizer, A. D.; van Hazendonk, L. S.; Wirix, M. J.; Patterson, J. P.; Laven, J.; de With, G.; Friedrich, H. Mapping and Controlling Liquid Layer Thickness in Liquid-Phase (Scanning) Transmission Electron Microscopy. *Small Methods* **2021**, *5*, 2001287.

[211] Pereiro, I.; Khartchenko, A. F.; Petrini, L.; Kaigala, G. V. Nip the bubble in the bud: A guide to avoid gas nucleation in microfluidics. *Lab on a Chip* **2019**, *19*, 2296–2314.

[212] Shen, T.-h.; Girod, R.; Vavra, J.; Tileli, V. Considerations of Liquid-Phase Transmission Electron Microscopy Applied to Heterogeneous Electrocatalysis Considerations of Liquid-Phase Transmission Electron Microscopy Applied to Heterogeneous Electrocatalysis. *Journal of The Electrochemical Society* **2023**, *170*, 056502.

[213] Jensen, E.; Burrows, A.; Mølhave, K. Monolithic Chip System with a Microfluidic Channel for In Situ Electron Microscopy of Liquids. *Microscopy and Microanalysis* **2014**, *20*, 445–451.

[214] Woehl, T. J.; Prozorov, T. The Mechanisms for Nanoparticle Surface Diffusion and Chain Self-Assembly Determined from Real-Time Nanoscale Kinetics in Liquid. *Journal of Physical Chemistry C* **2015**, *119*, 21261–21269.

[215] Bejtka, K.; Fontana, M.; Gho, C.; Merkens, S.; Chuvilin, A.; Chiodoni, A. Electrochemical liquid phase TEM in aqueous electrolytes for energy applications: the role of liquid flow configuration. *Nature Communications, in submission*.

[216] Egan, G. C.; Lau, E. Y.; Schwegler, E. Multiframe Imaging of Micron and Nanoscale Bubble Dynamics. *Nano Letters* **2022**, *22*, 1053–1058.

[217] Damiano, J.; Walden, S.; Franks, A.; Marusak, K.; Larson, B.; Coy, M.; Nackashi, D. AXON Dose: A Solution for Measuring and Managing Electron Dose in the TEM. *Microscopy Today* **2022**, *30*, 22–25.

Appendix A

Publications as First Author

A.1 Quantification of Mass Transport in Flow Reactors

Stefan Merkens, Giuseppe De Salvo, Joscha Kruse, Evgenii Modin, Christopher Tollan, Marek Grzelczak, Andrey Chuvilin, **Quantification of reagent mixing in liquid flow cells for Liquid Phase-TEM**, *Ultramicroscopy*, 245, 113654, (**2023**).

The manuscript was cited as ref. [197]. It is accessible under

https://www.sciencedirect.com/science/article/pii/S0304399122001735?via%3Dihub.

Contents lists available at ScienceDirect

Ultramicroscopy

journal homepage: www.elsevier.com/locate/ultramic

Quantification of reagent mixing in liquid flow cells for Liquid Phase-TEM

Stefan Merkens [a,b,*], Giuseppe De Salvo [a,b], Joscha Kruse [a,c], Evgenii Modin [a],
Christopher Tollan [a], Marek Grzelczak [c,d], Andrey Chuvilin [a,e]

[a] Electron Microscopy Laboratory, CIC nanoGUNE BRTA, Tolosa Hiribidea 76, Donostia, San Sebastián 20018, Spain
[b] Department of Physics, Euskal Herriko Unibertsitatea (UPV/EHU), Donostia, San Sebastián 20018, Spain
[c] Donostia International Physics Center (DIPC), Paseo Manuel de Lardizabal 4, Donostia, San Sebastián 20018, Spain
[d] Centro de Física de Materiales CSIC-UPV/EHU, Paseo Manuel de Lardizabal 5, Donostia, San Sebastián 20018, Spain
[e] Ikerbasque, Basque Foundation for Science, 48013 Bilbao, Spain

ARTICLE INFO

ABSTRACT

Liquid-Phase Transmission Electron Microscopy (LP-TEM) offers the opportunity to study nanoscale dynamics of phenomena related to materials and life science in a native liquid environment and in real time. Until now, the opportunity to control/induce such dynamics by changing the chemical environment in the liquid flow cell (LFC) has rarely been exploited due to an incomplete understanding of hydrodynamic properties of LP-TEM flow systems. This manuscript introduces a method for hydrodynamic characterization of LP-TEM flow systems based on monitoring transmitted intensity while flowing a strongly electron scattering contrast agent solution. Key characteristic temporal indicators of solution replacement for various channel geometries were experimentally measured. A numerical physical model of solute transport based on realistic flow channel geometries was successfully implemented and validated against experiments. The model confirmed the impact of flow channel geometry on the importance of convective and diffusive solute transport, deduced by experiment, and could further extend understanding of hydrodynamics in LP-TEM flow systems. We emphasize that our approach can be applied to hydrodynamic characterization of any customized LP-TEM flow system. We foresee the implemented predictive model driving the future design of application-specific LP-TEM flow systems and, when combined with existing chemical reaction models, to a flourishing of the planning and interpretation of experimental observations.

1. Introduction

Triggering and observing dynamics of nanoscale objects in native liquid environments has always been a desired but challenging task in fields from bioscience to colloidal chemistry and crystal growth. Liquid-Phase Transmission Electron Microscopy (LP-TEM) is a fast developing electron microscopy technique addressing these challenges [1–4]. LP-TEM deals with tiny amounts of sample solution enclosed between two ultrathin electron transparent membranes forming a liquid cell (LC) integrated into TEM sample holders [4,5]. Though giving the opportunity to open new branches in nanoscience, [6] LP-TEM is still restrained by various unresolved issues such as transparency and bulging of membranes, [7,8] image deterioration due to liquid layer thickness, [9] theoretical description and mitigation of radiolytic effects, [10–14] and fast particle movement in liquids [15,16] to name a few. Various other technical issues are of key importance for establishing this technique as

a reliable and quantitative tool in nano-(bio-, electro-) chemistry: the development of standardized procedures for time-resolved experiments, application of external (*i.e.*, non-beam related) stimuli (electrical bias, temperature) and the description and control of chemical environment in the cell, among others [17].

Though the story of LP-TEM stems back to the middle of the last century, the current rise of this method was stimulated by the development of microfabrication techniques [18,19] and the breakthrough in TEM resolution due to aberration correction [20]. In 2003, Williamson et al. have introduced a concept of MEMS-based static LC, in which tiny amounts of liquid sample are fully sealed [21–24]. Their LC included electrodes, which allowed the observation of the initial growth of electrodeposited copper at a resolution of ~5 nm. Since then, such static LCs have been used to image a broad range of specimens from life [25,26] to material science [27] in their native liquid environment. The ultimate design of static LCs, utilizing graphene as the membrane material, was

---

introduced allowing for 3D imaging with atomic resolution [28].

An inherent shortcoming of static LCs is a lack of control over the chemical environment of the confined liquid layer inside the cell, *i.e.*, depletion of precursors and scavengers, [29,30] accumulation of reaction products including those of radiolysis, [11] and inability to trigger reactions by exchange of the reaction media. For the cases where such control is essential, LP-TEM flow systems have been introduced [31] and are now commercially available. Such systems consist of MEMS-based liquid flow cells (LFCs), which feature a discontinuous "flow" spacer, allowing for a liquid to enter the main channel and a special TEM holder embedding the LFC as well as supply and drain capillaries. Syringe- or pressure-controlled pumping systems are connected from the outside and used for liquid transport through the LP-TEM flow system. Single and dual inlet designs have been reported [32], allowing for supply [33–35] or replacement [36] of reaction solutions as well as elimination [1,25] of radiolysis products under interrupted [13] and continuous flow conditions. In combination with *in situ* electrodes [37] or embedded temperature control, [38] these systems find application in diverse research fields such as batteries, [37] (electro-) catalysis, [34] material synthesis, self-assembly and biology [39]. LP-TEM flow systems are intended to provide control over the composition of the reaction media in a reliable and reproducible manner [40,41]. In the "ideal" flow experiment, nanoscale dynamics would be stimulated by (fast) exchange of the solution accompanied by simultaneous imaging directly inside the LFC.

Upon a successful demonstration of the qualitative benefits of liquid flow cells, the next step would be extracting quantitative kinetic information from LP-TEM experiments and correlating these to bulk chemistry data, which, among others, might help understanding nanoscale mechanisms of colloidal reactions or initial stages of crystal growth [42]. As for now, this task is to a large extent suspended due to a lack of knowledge on the fluid dynamics inside multi-scale flow channel setups and thus the inability to predict the actual chemical composition of the reaction media and the dynamics of its replacement.

Actual LP-TEM flow systems are represented by two main concepts with supposedly different flow dynamics: 1) *bathtub* design, in which a MEMS-based LFC is embedded into an oversized cavity leaving space for the main fraction of the fluid to bypass the nanochannel inside the LFC or 2) *direct* flow systems, where the fluid flow is forced to enter the main flow channel (and pass across the imaging area) [43–45]. Both concepts have advantages and disadvantages. The *bathtub* design is more resilient to overpressure and allows for much higher flow rates, and hence a faster delivery of solution through the *whole* supply system, while the *direct* flow design requires a precise control of supply pressure yet promising a rapid solution replacement in the LFC *itself*. The characteristic length scales of the main flow channel range from (sub-) micrometer to a few tens of nanometers which indicates that the governing physics are predominantly based on microfluidics; [46,47] however, nanofluidic effects may be of increased importance in some setups [48]. Besides these general intuitive considerations, fluid dynamics in such complex systems remain barely explored.

To our knowledge, a hydrodynamic characterization of LP-TEM flow systems has been addressed only in a few experimental and theoretical works so far. Experimental works attempted to derive fluid dynamics in LP-TEM flow systems exclusively by imaging particle movement inside LFCs [31,45]. Thus, convective fluid flow was reported as a possible cause of directional particle movement superimposed on random particle diffusion [31]. Beyond a qualitative description, such particle tracking approaches do not provide a comprehensive hydrodynamic characterization of entire LP-TEM flow systems. Theoretical approaches have been mostly targeted to describe local diffusion of reaction species arising from radiolysis (in particular based on the works of Schneider *et al.*) [4,10,11]. Kröger & Verch reported simplified two-dimensional diffusion-reaction simulations to explain qualitatively the effects of nano-confinement in LCs on ion transport during mineralization processes under stationary conditions [29]. Yesibolati et al. introduced a

stationary solid mechanics model to estimate overall stress acting on the silicon nitride (SiN) membranes during the hydrodynamic filling of customized nanochannels assuming static pressure loads of 15 bar [49]. To our knowledge the only theoretical description of fluid flow was performed by Allen *et al.* who designed a LP-TEM sample holder for flow experiments based on numerical model simulation of Stokes flow through the nanoconfined channel of exact multi-scale channel geometry [7,43]. The limited literature in this area is rather surprising; especially in the view of the vast body of work which is available in microfluidics research where the spatio-temporal distribution of reactants is precisely controlled by experimental methods for concentration calibration [50] and numerical simulations of convection and diffusion in customized flow channels [40,41,51–53]. Implementation of such models for LP-TEM flow systems may be complicated owing to the complexity of the multi-scale flow channel geometry [36].

In this manuscript we present a method for experimental quantitative characterization of LP-TEM flow systems, as well as a comprehensive convection-diffusion model for the description of the fluid dynamics inside multi-scale flow channels. Experimental methodology and simulations are applied to characterize commercially available LP-TEM flow systems, representing both *bathtub* and *direct flow* concepts. Fundamental system characteristics are extracted and compared between the experiment and numerical model. Besides quantitative characterization through experiments, theoretical modeling provides a fundamental understanding of the fluid dynamics inside the channels of complex shape, revealing the bottlenecks of existing designs and provides ways for future improvement.

2. Methods

The here proposed method for experimental characterization of hydrodynamic properties of LP-TEM flow systems is schematically summarized in Fig. 1. The method utilizes variations in transmitted intensity due to different electron scattering properties of solutions with different composition. Programmable syringe pumps were used to alter the composition of the solution by independently controlling the flow rate in two inlets of the LP-TEM flow system. Clearly detectable intensity variations on the images were induced by replacing pure water with a strongly electron scattering contrast agent (CA) solution. The observed contrast variation was quantified and allowed characteristic time constants of solution replacement to be extracted.

2.1. Transmitted intensity in TEM

The proposed method for LP-TEM flow systems utilizes the dependence of the transmitted electron intensity on the concentration of the contrast agent in solution. Transmitted intensity in the general case can be expressed as:

$$I_t = I_0 exp(-\rho z) \tag{1}$$

Where I_0 is the incident intensity, I_t is the transmitted intensity, ρ is the combined elastic and inelastic scattering power ($\rho = 1/\lambda$ where λ is the mean free path) and z is the thickness of the irradiated sample. [54, 55] It is worth noting, that ρ depends on the electron energy, scattering angle and the composition of the material, but only the latter varies in our experiments. Assuming that the solution does not change its volume upon dissolution of contrast agent, which is a sound approximation at the maximum molar concentration of 40 mM used in this work, the transmission through an aqueous solution enclosed between e^--beam-transparent membranes can be denoted as I_w and I_s, respectively, depending on the presence of CA in the solution (Eq. (2) and Eq. (2a)):

$$I_w = I_0 exp(-[\rho_w \cdot z + \rho_m \cdot z_m]) \tag{2}$$

$$I_s = I_0 exp(-\{[\rho_w + c \cdot \rho_{CA}]z + \rho_m \cdot z_m\}) \tag{2a}$$

2
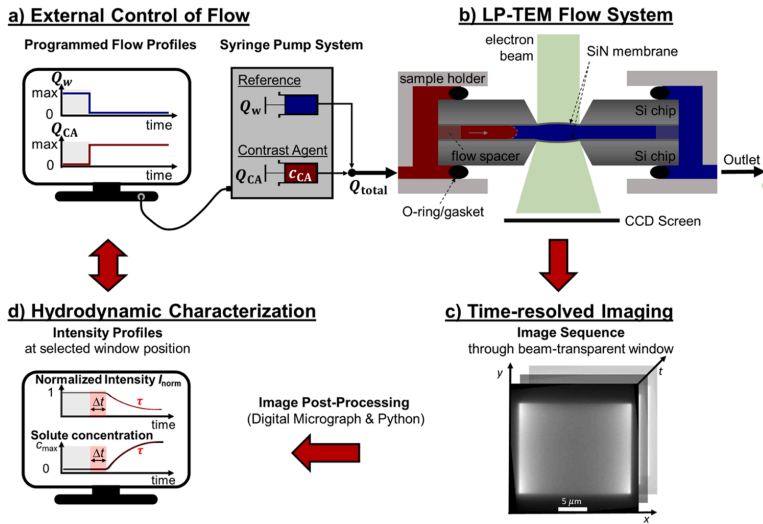
Fig. 1. Schematic representation of the image contrast variation method for hydrodynamic calibration of LP-TEM flow systems. a) A programmable double syringe pump system was used to control the liquid flow through two independent inlets of the LP-TEM flow system carrying pure water and an aqueous solution of a strongly electron scattering contrast agent (CA), respectively. **b)** A liquid flow cell (LFC) filled by flowing solution was monitored at particular time intervals (2 s as a rule) and **c)** recorded by pre-calibrated CCD camera. **d)** The acquired raw image sequences were post-processed to extract the time-dependent transmitted intensity and to correlate it to the flow profile of the supplying syringes.

where ρ_m and z_m are the scattering power and the thickness of the membranes, ρ_w and ρ_{CA} are scattering power for water and contrast agent respectively, z is the thickness of liquid layer and c is the solute concentration. From that, a relative (normalized) intensity can be written as:

$$I_{norm} = \frac{I_s}{I_w} = \exp(-\rho_{CA}\cdot c\cdot z) \approx 1 - \rho_{CA}\cdot z\cdot c = 1 - K\cdot c \qquad (3)$$

Based on Eq. (3), time-dependent variations of the liquid thickness (bulging) as well as contrast agent concentration may be tracked over time simply by measuring the transmitted intensity. Note that the experiments in this work were designed to study the latter case, *i.e.*, the local liquid thickness was kept constant by applying constant total flow rates (see below and *Supporting Information* section S1.3.3.). In independent experiments it was also shown that effect of the flow rate on the bulging can be neglected (see *Supporting Information* section S3.2.). Without making further assumptions about the absolute thickness of the liquid layer and the scattering power of the contrast agent, we will directly calibrate I_{norm} against the concentration c of contrast agent and show that this dependence is indeed linear to a very good accuracy.

The selection criteria for the contrast agent are high average atomic number, good solubility in water, chemical inertness in respect to the components of the hardware and non-toxicity. One of a few such compounds is phosphotungstic acid (PTA), which is a well-known contrast agent for staining of biological specimens in conventional TEM and LP-TEM experiments [4]. We have used PTA at a maximum concentration of 40 mM (about 10wt%), which provided an intensity variation well above the noise level at the electron dose rate in the incident beam of 0.3 $e^-/nm^2/s$.

2.2. Flow control

Controlled liquid flow through two inlet LP-TEM setups was realized by two electronically connected programmable syringe pumps (Pump 11 Pico Plus Elite, Harvard Apparatus, USA). One of the syringes contained pure demineralized water (MilliQ; resistivity: 18.2 MΩ·cm at 25 ºC), the other an aqueous solution of 40 mM PTA. Electronically interfaced pumps were programmed to supply a constant volumetric total flow rate (Q_{total}), yet changing the ratio of flow rates of the two channels. Further Q_{water} and Q_{CA} will be used for the flow rate of water and

contrast agent solution, respectively. Q_{total} was studied in a range from 25 to 1200 μL/h, defined by the minimum reasonable flow rate and maximum rate safe for the window membranes (determined empirically) [56].

We applied two types of flow profiles: 1) a stepwise abrupt switch of total flow from one syringe to the other was used for studying the dynamics of solute exchange in multi-scale flow channels of the holders; and 2) gradual change of the partial flow ratio ($PFR=Q_{CA}/Q_{total}$) of CA was used to evaluate the degree of control over the solute concentration in the window area (see also *Supporting Information* section S1.3.3., Fig. S1).

2.3. Flow channel geometry

Two types of double-inlet LP-TEM holders, namely Poseidon Select™ and Poseidon 200™ (Protochips, Inc., USA), were characterized. Poseidon Select features a few millimeters long premixing channel just before the LFC, so that the fluids from two inlets can mix before entering the nanochannel (NC, Fig. 2a). At the same time, it utilizes a rubber gasket of a complex shape which substantially blocks the bypass around the LFC, forcing more flow in between the chips. In the Poseidon 200-type holder, two inlet channels approach the MEMS-based LFC from two opposite sides, so that the mixing of the solutions takes place directly in the nanochannel (Fig. 2b). There is a substantial dead volume on all sides, which directs a major part of the flow around the LFC. The flow channel systems based on Poseidon Select™ and Poseidon 200™ holders are hereafter referred to as *premixing* and *on-site mixing*, respectively. (The term "setup" will explicitly refer to the real device only; while "configuration" in a similar context will be used to emphasize the conceptual differences, *i.e.*, it may comprise implemented numeric models (*vide infra*) of one or the other type.) Both configurations can be described as governed by microfluidic effects, since the central nanochannel was set up with flow spacers of a nominal thickness of 150 nm [48].

2.4. TEM data acquisition and post-processing

TEM imaging was performed on a Titan 60–300 TEM/STEM (FEI, Netherlands) in TEM Lorentz mode (used for the convenience of low magnification imaging) at 300 kV and x500 magnification. At this

3

*S. Merkens et al.*
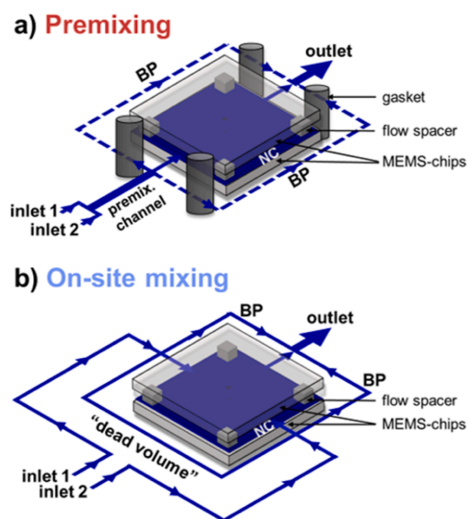
Fig. 2. Schematic representation of the LP-TEM flow systems in *premixing* and *on-site mixing* configurations. The nanochannel (**NC**) in the LFC is achieved by placing two MEMS-chips, separated by flow spacers, in an oversized bathtub (compare *Supporting Information* section S2.1., Fig. S2). Two inlet and one outlet capillaries provide independent solution supply (controlled *via* the pumping system) and drainage. **a)** In *premixing* configuration, inlet capillaries join together before entering the nanochannel and thus the solutions mixture must travel some distance inside the premixing channel before reaching the LFC. By design, such a setup has a rubber gasket eventually blocking the flow through the bathtub (bypass channel, **BP**). **b)** In the *on-site mixing* configuration two streams of solution from two inlet capillaries are supplied from two opposite sides directly to the nanochannel, however by design a large bypass along the sides of the MEMS-chips is opened for flow.

magnification, a complete 20×20 μm [2] window area (chips in cross-configuration, see *Supporting Information* section S1.3.1. for details) was imaged on a CCD screen. The beam intensity was adjusted by a gun lens to a dose rate of ~0.3 e^-/nm^2/s (without the sample) and was kept constant in all experiments. This dose rate was selected to achieve sufficient signal-to-noise ratio at a minimum possible dose rate to minimize potential beam effects. The dose rate was verified (without the sample) before and after experiments for intensity baseline correction. Images were acquired on a Gatan Ultrascan1000P 2K*2K CCD camera (GATAN, USA) at x4 binning, 2 s exposure time and 5 s intervals between frames. Image acquisition was manually synchronized with the pump's microcontroller. The typical duration of the experiments was 2 h (1440 images).

Acquired image sequences were aligned in Digital Micrograph for drift, and time dependent intensity profiles were averaged and extracted from selected regions: 10×10 pixel areas in all four corners, *c1 – c4,* and in the center, *ce,* of the window area. Extracted curves were processed and visualized with Python-2.7 workflow (numpy, scipy, matplotlib) [57] for further semi-automated processing and plotting.

2.5. Numerical modelling

Numerical modeling of the flow in multi-scale flow channels of the LP-TEM flow systems was performed in COMSOL Multiphysics software (version 5.3, COMSOL Inc., USA). Four key components defined a successful numerical model: selection of the appropriate hydrodynamic description; correct representation of the shape of the flow channels; their proper meshing; and accurate definition of boundary conditions.

In general, the flow type in a flow channel with a hydraulic diameter D_H is determined by the Reynolds number, *Re*, defined by: [58–60]

$$Re = \frac{\varphi \cdot v \cdot D_H}{\mu} \tag{4}$$

where φ, μ and v are the density, dynamic viscosity, and velocity of the fluid, respectively. At the flow rates accessible in LP-TEM flow systems, *Re* is very small (<1) in all compartments, which determines laminar flow through the entire setup (see a detailed discussion in *Supporting Information* section S2.2.). Therefore, the laminar flow module was used to solve the incompressible Navier-Stokes equation coupled with the equations for Fick's laws describing water as an incompressible fluid and the diffusion of solvated species (*Supporting Information* section S5.2.) therein [40]. Laminar flow is represented by flow lines proceeding in parallel through the channel, thus mixing between two separated phases is entirely determined by solute diffusion, *i.e.,* no turbulent mixing is expected [41,51,61]. The laminar flow defines a parabolic velocity profile across the channel [59]. The diffusion coefficient, D_{PTA}, of PTA in water was estimated as $6 \cdot 10^{-10}$ m^2/s based on Dynamic Light Scattering (DLS) measurements (*Supporting Information* section S4.1., Fig. S9). Put in perspective, PTA ions should diffuse slower in water than small inorganic salt ions, *e.g.,* NaCl ($D \approx 1 \cdot 10^{-9}$ m^2/s), but faster than nanoparticles ($D \approx 1 \cdot 10^{-11}$ m^2/s) [51]. It was assumed that a 40 mM solution of PTA has the same hydrodynamic properties as pure water (see *Supporting Information* section S5.2. and S7.2. for justification of this assumption). The contribution of gravitational force was neglected [61].

The geometry of the multi-scale flow channel system was derived from a geometric model of the entire LP-TEM setup consisting of the Poseidon sample holder, the gasket and the MEMS-chips *via* virtual imprinting (computer-aided design (CAD) file was provided by Protochips, Inc. under non-disclosure agreement, *Supporting Information* section S5.1.). The complexity of generating a proper mesh for the flow simulations stems mostly from the 4 orders of magnitude difference in spatial dimensions of the channels involved in the flow. This results in a corresponding difference in the mean node densities considered reasonable for different flow channel compartments (with orders of magnitude ranging from 10^4 in the premixing to 10^7 nodes/mm^3 in the nanochannels) and the necessity to link them at the interface. The details of the tricks and assumptions used for meshing can be found in *Supporting Information* section S5.4., and in Fig. S12.

The boundary conditions implemented to solve the numerical models were as follows: all channel walls including membranes were considered chemically inert and rigid (no membrane bulging was considered); no liquid slip along and no-penetration through the walls was permitted; inlets were transparent, and inflow was described by the volumetric flow rate; outlets were transparent and described by zero pressure (see also *Supporting Information* section S5.3.).

The two configurations of the LP-TEM flow system (Fig. 2) were modelled, and stationary as well as time-dependent solutions were calculated. Stationary solutions for the velocity field allowed the predominant flow lines through the channel setups to be determined. Time-dependent solutions simulated the abrupt switch of the applied flow from one inlet to the other and the PTA concentration at the window area was monitored in time and correlated with the experimental data. This computation allowed to verify the mass transport mechanisms involved in solute replacement and to evaluate the solution replacement dynamics for different channel configurations. Additionally, the stationary solution allowed verification of the peculiarities of mixing at different *PFRs*, *e.g.,* to determine the concentration distribution in the steady state when solution was supplied simultaneously from both inlets (*in situ* mixing).

4

3. Results and discussion

3.1. Experimental characterization of mixing dynamics

3.1.1. Quantification of solution replacement dynamics

Fig. 3a depicts typical normalized curves of transmitted intensity I_{norm} in the center (*red*) and the four corners (*blue*) of the imaging area that were obtained when repeatedly flowing contrast agent ($c_{initial,PTA} = 40$ mM) through a LP-TEM flow system for the *premixing* setup (Fig. 2a.) The applied flow was alternated every 30 min between contrast agent and water for 3 h, keeping the total flow constant at $Q_{total} = 300$ µL/h. The *gray* (water) and *white* (CA) background in Fig. 3a indicate the currently active syringe. As the total flow rate, beam energy and primary beam intensity are constant, contrast variations observed can be assigned uniquely to changes of CA concentration (see Section 2.1), influence of bulging effects can be neglected (see also *Supporting Information* section S3.2.). The periodicity of the measured intensity follows the periodicity of the inlets switching and thus demonstrates reproducibility of solution replacement in LP-TEM flow system as is typical for microfluidic mixing devices in general [41].

Intensity curves in Fig. 3a reveal that while the flow between two syringes was switched sharply, intensity changes occurred after a certain delay and proceeded rather gradually until a steady state was reached.

The time delay Δt between switching of the syringes and onset of the intensity change arises from the retention time of the solutions moving through the premixing channel towards the field of view. In Fig. 3b, Δt_1 and Δt_2, for in- and outflow of CA (consistently ~2 min) are depicted. Since no significant differences in delay time could be detected with respect to the lateral position across the imaged area (all 4 corners show the same value), the solution replacement can be considered to be uniform across the entire window (nominal window size: 20×20 µm^2) and is thus unaffected by window bulging (*Supporting Information* section S3, Fig. S5 and S6) [31].

The gradual intensity variation starting after the identified time delay reflects a gradual increase/decrease of CA concentration. This is defined by the interdiffusion at the interface between two solutions travelling along the premixing channel during Δt. Based on fundamental studies, this phenomenon can be qualitatively explained by the diffusion of CA which is superimposed with the parabolic flow velocity profile across the microfluidic channel (Taylor dispersion) [40].

The smooth intensity variation was quantified by exponential decay time constants, τ_1 and τ_2 for in- and outflow of the CA, respectively (Fig. 3c, also *Supporting Information* section S1.3.4., *Eq. S1* and *S2*). At high flow rates of 300 µL/h, consistently small values of ~2 min were obtained for the *premixing* setup (see further discussion on the dependence on flow rate and LP-TEM setup in Section 3.3). The slight difference in time constants for in- and out-flow is due to asymmetry by design of the premixing channel.

3.1.2. CA concentration calibration

As mentioned in relation to Eq. (3), we performed a direct calibration of the relative intensity drop *versus* concentration of the CA. The concentration of the solution in the syringe supplying CA was set to 0, 5, 10, 20 and 40 mM and replacement curves were measured for every
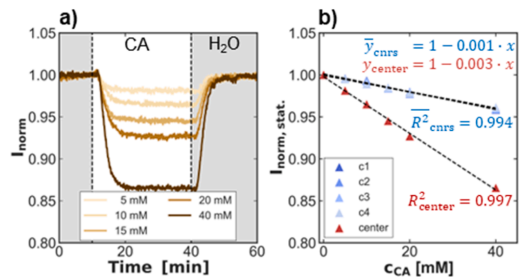
Fig. 4. Concentration calibration. a) Normalized transmitted intensity curves acquired for different initial concentrations $c_{initial}$ ($Q_{total} = 300$µL/h; *premixing* setup) obtained at the center of the imaging area. **b)** Transmitted intensity, $I_{norm,stat.}$, extracted from stationary timespan (25 – 40 min) for the curves in **a** for the center as well as for an average of 4 corners. Dashed lines represent linear regressions of $I_{norm,stat.}$ in the center (y_{center}; $R^2 = 0.997$) and corners ($\overline{y}_{cnrs}$, $\overline{R}^2 = 0.994$), respectively.
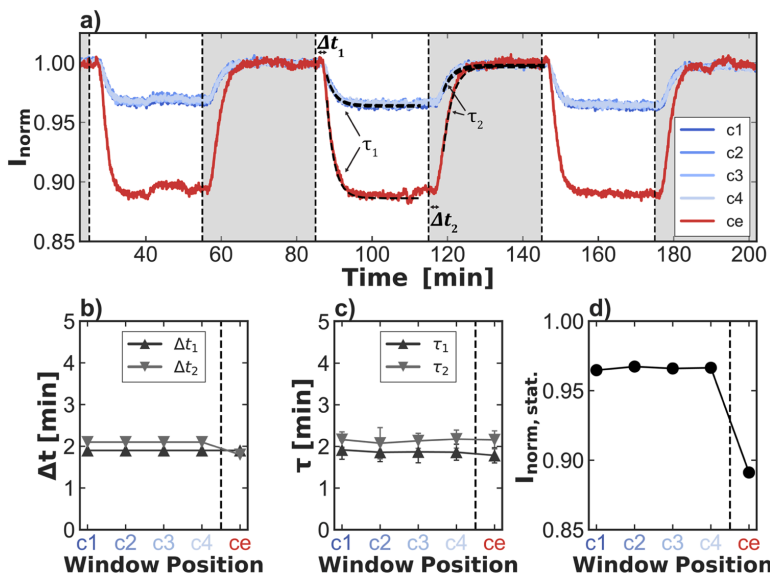
**Fig. 3. Reproducibility of flow experiments and extraction of characteristic parameters exemplarily shown for *premixing* setup at $Q_{total} = 300$ µL/h. a)** Normalized transmitted intensity curves acquired when applied flow was switched between water and contrast agent (CA) every 30 min for 3 h. *gray* (water) and *white* (CA) background illustrate currently active syringe. **b)-d)** Dependence of characteristic parameters, *i.e.,* **b)** delay times Δt, **c)** decay time constants τ and **d)** normalized stationary transmitted intensity, $I_{norm,stat.}$ on lateral position across imaged area (corners c1-c4 and center ce). In **b)-d)**, dashed lines are guides to the eyes. Error bars on **b)** and **d)** are smaller than the size of the markers and thus are not visible.

concentration as described in Section 3.1.1 (see Fig. 4a) and the steady state intensity was taken as characteristic for this concentration. The intensity variation is attributed solely to a varying concentration of the CA as the calibration was performed using the same assembly of the liquid flow cell and the same flow velocity of 300 μL/h, *i.e.,* with the same thickness of the liquid layer.

Fig. 4 shows measured intensity curves and linear regressions for the center and 4 corners of the imaged area, with the equations denoted in *red* and *blue*, respectively. Both regressions are explicitly accurate ($R^2 \geq$ 0.99) and intercepting the *y*-axis at 1 as expected (compare Eq. (3)). The (averaged) slope of the calibration line ($\sigma_{CA}\cdot z$) for the four corners allowed the molar scattering cross-section of PTA to be estimated as $\sigma_{PTA,m} = 6.9$ m$^{-2}\cdot$mol^{-1} at 300 keV, assuming the thickness of the liquid layer at the corners is equal to the spacer thickness ($z_{spacer} = 146$ nm, which was determined via SEM; compare *Supporting Information* section S4.2, Fig. S10). The slope ($\sigma_{CA}\cdot z$) in the center was three times larger when compared to the corners and reflects the window bulging (Fig. 3d) which has been quantitatively confirmed by Electron Energy Loss Spectroscopy (EELS) measurement (*Supporting Information* section S4.3, Fig. S11). These observations confirm the validity of linear approximation proposed by Eq. (3) and allow the CA concentration to be measured, assuming two points of a linear dependence are known, *i.e.,* steady-state intensities of pure water and CA solution flow, respectively.

Thus, we have introduced an experimental method for quantitative measurement of solution replacement in a mixing flow liquid cell. It should be noted that experimental data acquisition is restricted to a field of view defined by the electron beam-transparent SiN membranes, and thus does not give a complete picture of fluid dynamics. To achieve a more comprehensive hydrodynamic description of the flow in the entire LP-TEM flow system, a numeric physical model based on exact geometry of double inlet LP-TEM flow system was implemented, and the results were compared to experimental data.

3.2. Numeric simulation of solute replacement dynamics

3.2.1. Convection – stationary solution for flow velocity field

Stationary solutions of the incompressible Navier-Stokes equation were obtained with the initial aim of qualitative characterization of fluid convection through the different flow channel geometries. Focus was laid on discriminating principal flow pathways and potential bypass flows affecting the solution replacement in the field of view. To highlight the contribution of convection and diffusion to solution replacement, an initial model of the *premixing* configuration was constructed in an ideal way, *i.e.,* the rubber gasket was assumed to block completely the bypass channel, thus the flow is directed into and confined in the nanochannel

only. We will refer to this model as "*ideal*" *premixing* model. Further we will discuss the consequences of this assumption as well as will provide a more realistic model with adjusted geometry (see section 3.2.3).

Fig. 5 schematically illustrates solvent convection through two different configurations (**a**) "*ideal*" *premixing* and **b**) *on-site mixing* model, obtained from numeric simulations for a constant total flow rate: $Q_{total} = 300$ μL/h. Flow lines are shown in red, and the background color represents the magnitude of the flow velocity $|v|$. Three different channel compartments can be discriminated in these models contributing differently to the flow: the nanochannel (**NC**) - a broad (2 mm) and thin gap (150 nm here, defined by the spacer thickness) between two MEMS chips with a tiny viewing area in the middle; the bypass channel (**BP**) - a waste volume around LFC with a typical cross-section of a few thousands of μm^2; the side pockets (**SP**) - technological dead volumes of about 0.25 mm^3 connected to **BP**.

A principal difference of the flow between the *premixing* and *on-site mixing* configurations is the accessibility of the bypass channel. In the *premixing* model, the liquid is forced into the narrow gap between chips and thus the magnitude of flow velocity in simulation can reach values of the order of 1 m/s in some parts of **NC** for the volumetric flow of 300 μL/h. **BP** channel and **SP**s serve rather as dummy volumes "sucking" parts of the flow from the sides of **NC** which results in a lateral inhomogeneity of the flow velocity field. In the case of the *on-site mixing* model, the main flow is directed through the **BP** due to its much lower flow resistance (analytical description of the "multi-channel flow model" can be found in the literature [31] and in *Supporting Information* section S2.3.) limiting the flow velocity through the **NC** to a few hundred nm/s.

The flow velocity through the imaging area (indicated by *small black squares* at the lateral center of **NC** in Fig. 5) was determined to be $2.4\cdot10^{-2}$ and $1.5\cdot10^{-7}$ m/s for the *premixing* and *on-site mixing* models, respectively. Consequently, the flow travel time from the **NC** entrance to the viewing area could be estimated as 0.1 s and 10 min for the two configurations.

3.2.2. Diffusion

Due to the laminar flow, solution mixing in LP-TEM flow systems is dominated by solute diffusion driven by the concentration gradient [40]. The retention time of a fluid volume element flowing along its predetermined flow line defines the time frame for diffusion to occur and to smear out the initially sharp concentration profile in axial as well as radial direction due to parabolic velocity profile in the channel (Taylor dispersion) [41].

The diffusive flux, J_D, of a solute (in mol/m^2/s) can be calculated
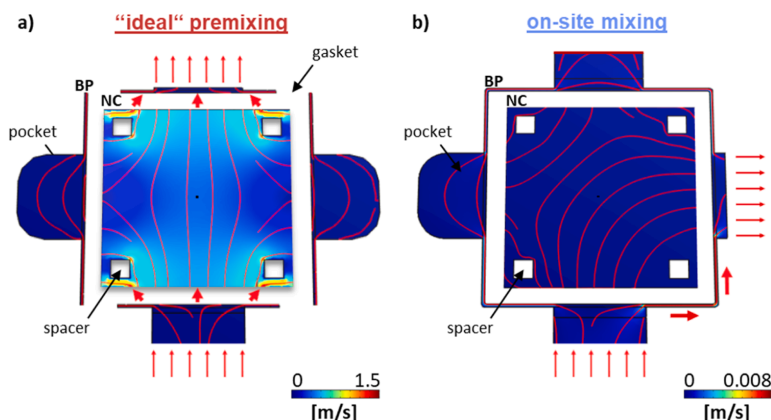
Fig. 5. Liquid flow through two LFC configurations as determined by numeric simulations: **a)** "*ideal*" *premixing* (*i.e.,* **BP** fully blocked) and **b)** *on-site mixing.* Red lines indicate direction and background color represents magnitude of flow velocity. Note that the velocity can vary by orders of magnitude within the **NC** and with respect to the surrounding **BP**. Note also the velocity scale difference between the two configurations. The **BP**s representation was enlarged with respect to the **NC** to improve visibility. Set of 6 *slim red arrows* indicate active in- and outlet flow, *bold short red arrows* indicate preferential flow. *Small black squares* in the center of **NC** mark imaging area in experiment (20×20 μm^2).

according to Fick's first law for one-dimensional diffusion $J_D = -D\frac{dc}{dx}$, where D and $\frac{dc}{dx}$ are the diffusion coefficient of a solute and a gradient of concentration, respectively [62]. For a **NC** with the dimensions as reported here, a maximum diffusive flux of the solute from the inlet to the membrane window can be estimated to be $J_D \approx 24$ μmol/m^2/s assuming a maximum gradient of $\Delta c = 40$ mM over $\Delta x = 1$ mm from the entrance to the center of the **NC** ($D_{PTA} = 6\cdot10^{-10}$ m^2/s, see *Supporting Information* section S4.1. for the discussion).

It is interesting to compare this value to the mass transport taking place via convection, which can be estimated as $J_C = v \cdot c$, where v is the linear flow velocity in the direction to the center and c is the solute concentration [63]. For the *on-site mixing* configuration, $J_C \approx 20$ μmol/m^2/s, which is comparable to the diffusion mass transport, meaning that diffusion contributes substantially to solution replacement. In the *"ideal" premixing* configuration with entirely blocked BPs, the convection transport, J_C, approaches 20 mol/m^2/s and thus the diffusion transport can be neglected.

3.2.3. Refinement of the premixing model

The simulations in Fig. 5 were performed by applying a forced volumetric flow. However, in reality the driving force for a fluid flowing through the channel system is the pressure difference between the inlet (s) and outlet. Inversing the problem, one can estimate from simulations a pressure built up due to the flow in the channel. For a moderate volumetric flow of 300 μL/h for the *on-site mixing* configuration, a pressure built up of ~2 mbar from out- to inlet of LC is required, which is a reasonable value. [64] The *"ideal" premixing* model (Fig. 5a) would require up to ~4000 bar pressure build up to ensure 300 μL/h flow through the nanochannel. This pressure is far from being achievable by the supply system, as well as far above the pressure that can be tolerated by the SiN membrane forming the imaging area. [64,65] The fact that flow rates of 300 μL/h can be experimentally applied in the *premixing* setup (yet being at the limit of membrane rigidity) therefore suggests that the **BP** are partially opened, and a substantial part of the flow is redirected. The resistance and thus the opening of this **BP** can be estimated by comparing simulations to experimental data as well as applying an analytical "multi-channel flow model" [31].

From the simulated data, the flow resistance of the *"ideal" premixing* model can be estimated as $R_{PR} = R_{NC} = \Delta p/Q = 4000/300$ bar/(μL/h) $\approx$ 13 bar/(μL/h) where R_{NC} is the flow resistance of the nanochannel, Δp is a pressure drop, and Q is a total flow. Assuming that the **BP** channel has the same geometry in *on-site* and *premixing* configurations, a flow resistance of one corner of **BP** channel can be calculated from the *on-site* model as $R_{BP} \approx (4/3)\cdot(2$ mbar/300 μL/h) ≈ 0.008 mbar/(μL/h); see *Supporting Information* section S2.4. for detailed discussion.

In an independent experiment, the pressure drop in a Poseidon Select holder with a 150 nm spacer and a volumetric flow rate of 300 μL/h was measured to be in the range of 100 mbar (see *Supporting Information* section S2.5.). This allows the flow resistance of the *premixing* setup to be estimated as: $R_{PR} \approx 100/300$ mbar/(μL/h) ≈ 0.3 mbar/(μL/h), which is almost 5 orders of magnitude lower than that of the *"ideal" premixing* model (with entirely blocked **BP**) yet 50 times higher than that of a configuration with fully opened **BP**s.

This low resistance can be ascribed to a leakage at the positions of the gasket (see arrow in Fig. 5a indicating one of 4 equivalent positions). The flow resistance of the *premixing* configuration can be described more accurately by an equivalent scheme as in Fig. S3a (*Supporting Information* section S2.4.) and thus can be expressed as:

$$\frac{1}{R_{PR}} = \left(\frac{1}{2R_G + 2R_{BP}} + \frac{1}{2R_G + 2R_{BP}} + \frac{1}{R_{NC}} \right) \qquad (5)$$

where R_G is the resistance of a leak channel at each individual gasket position (we assume all of them being equivalent). Provided that R_{BP} is low and thus can be neglected and R_{NC} is high and thus $1/R_{NC}$ can be neglected as well, we come to a relation $R_{PR} \approx R_G$. This defines the

opening, *i.e.,* cross-section, of the leakage channel to be of the order of a few percent of **BP** cross-section which can be easily due to the gaps at the corners of the gasket.

Though the resistance of the leak channel depends on a few parameters like length, opening and cross section, [66] only the value of resistance itself has an influence on the flow dynamics in the **NC**, which is what we are after. Thus, the leakage channel shape was approximated in the way most convenient for further flow simulations (rectangular cross-section; refer to *Supporting Information* sections S2.3. to S.2.5.). The opening of the channel was fit to reproduce the real experimentally observed dynamics and by fact was close to 2% of **BP** cross-section. Further we will refer to this model with adjusted geometry as *premixing (2% leakage)*, to distinguish from the initial *"ideal" premixing* model without leakage channel.

The linear flow velocity in the imaging area of the refined *premixing (2% leakage)* model was found to be $1.5\cdot10^{-5}$ m/s (for a 300 μL/h inflow rate) which is substantially lower than for the "ideal" *premixing* model ($2.4\cdot10^{-2}$ m/s), yet two orders of magnitude faster than for the *on-site mixing* configuration ($1.5\cdot10^{-7}$ m/s). This optimized model was further used for time-dependent simulations of the solution mixing dynamics.

3.2.4. Time dependent simulation of solution replacement

A time-dependent model was implemented and solved for the hydrodynamic replacement of water by the CA solution for both LP-TEM cell configurations, considering both convection and diffusion. Simulations started with the LFC entirely filled by water; at $t = 1$ min the flow of CA solution was ramped sharply at the corresponding inlet (which *for the on-site mixing* configuration is close to the entrance of the LFC, while for the *premixing* configuration it is the entrance to the premixing channel, not shown on the images). Fig. 6 shows the CA concentration in the LFC at different times (0.2, 0.5, 1 and 7 min) after enabling the CA flow (Q_{total}=300 μL/h). The 20×20 μm^2-sized viewing area in experiments is represented by the tiny *black square* in the center of **NC**.

The solution replacement mechanism is drastically sensitive to the flow channel configuration (compare Fig. 6a and b). In the *premixing* configuration, the time delay is constituted by the time necessary for the CA solution to travel through the premixing channel, after which the concentration of CA in the imaging area rapidly increases to maximum due to the high flow velocity in the **NC**. Thus, the replacement dynamics should show a strong dependence on the volumetric flow rate. On the contrary, in the *on-site* configuration, most of the flow is directed to the **BP**s and replacement dynamics are determined by the diffusion from these volumes to the imaging area. This process is substantially slower and should show relatively weak dependence on the volumetric flow rate.

To quantify the mentioned effects, we will apply the same processing to extract time constants as for the experimental data (compare Section 3.1.1 and Fig. 3) and will compare the outcome to experimental measurements.

3.3. Analysis of hydrodynamic properties of commercial LP-TEM flow systems

Below we analyze characteristics of solution replacement (Section 3.3.1) and *in situ* fluid mixing (3.3.2) of two commercially available LP-TEM flow systems (Poseidon 200 and Poseidon Select, Protochips Co, USA) and compare them to corresponding numerical models.

3.3.1. Solution replacement dynamics

Characteristic time constants of solution replacement (delay time Δt and decay constant τ) were experimentally measured as described in Section 3.1.1 for the flow velocities from 25 to 300 μL/h for the Poseidon Select (*premixing*) setup, and from 50 to 1200 μL/h for the Poseidon 200 (*on-site mixing*) setup. Fig. 7 represents the data obtained experimentally in comparison to numerical simulations of the corresponding models.

As discussed in Section 3.2.4, the *premixing* configuration (Poseidon
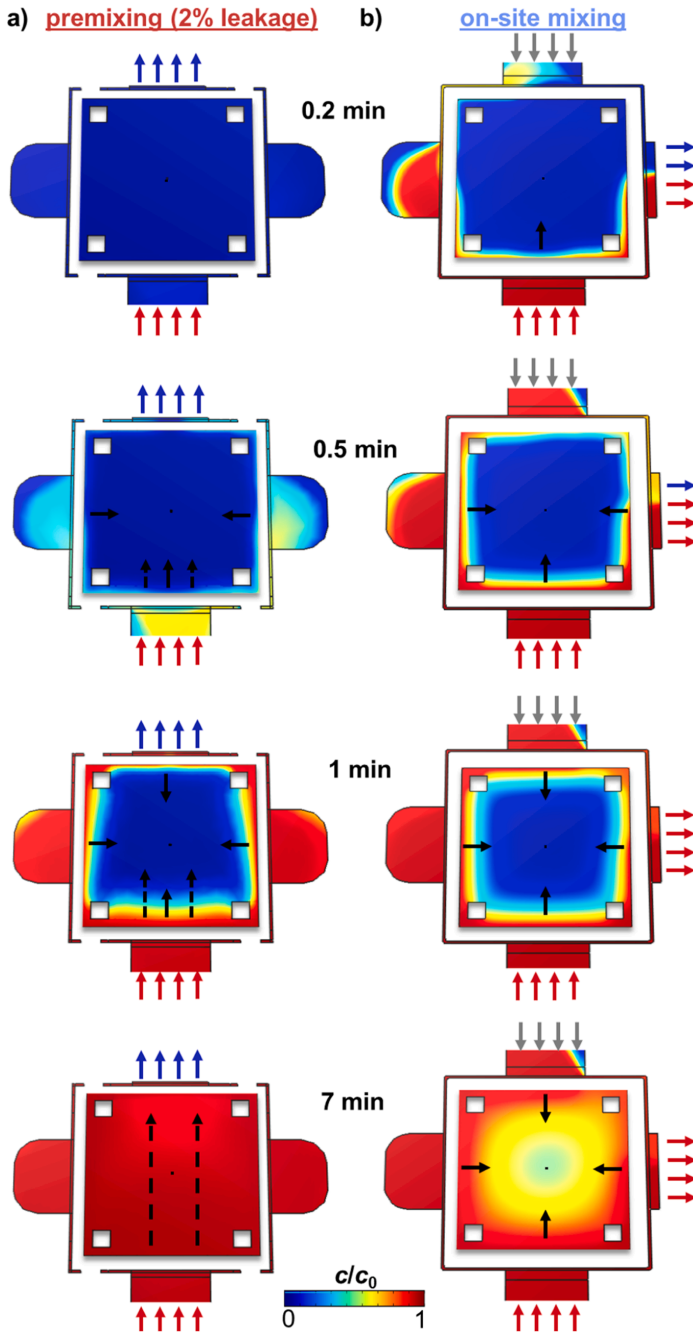
Fig. 6. Illustrative representation of solution replacement dynamics in two LP-TEM flow systems: *premixing (2% leakage)* configuration (column **a**) and *on-site mixing* configuration (column **b**) extracted from numeric simulations ($Q_{total} = 300$ μL/h). The solute (CA) concentration are shown for four different time points: 0.2, 0.5, 1 and 7 min after switching the inflow of the CA solution. The predominant directions of solute transport are indicated by *black arrows; dashed* and *continuous lines* indicating convective and diffusive flux respectively. The **BPs** representation was enlarged with respect to the **NC** to improve visibility. *Black squares* in the center of **NC** mark an area equivalent to the window imaged in experiment (20×20 μm^2). *gray arrows* indicate inactive water flow, Q_{water}=0. Note that in **a**) the **BP** appears discontinued because the concentration profile was taken at half-height, which differs from the location of the leakage channel (refer to **Fig. S13** for clarification).

8
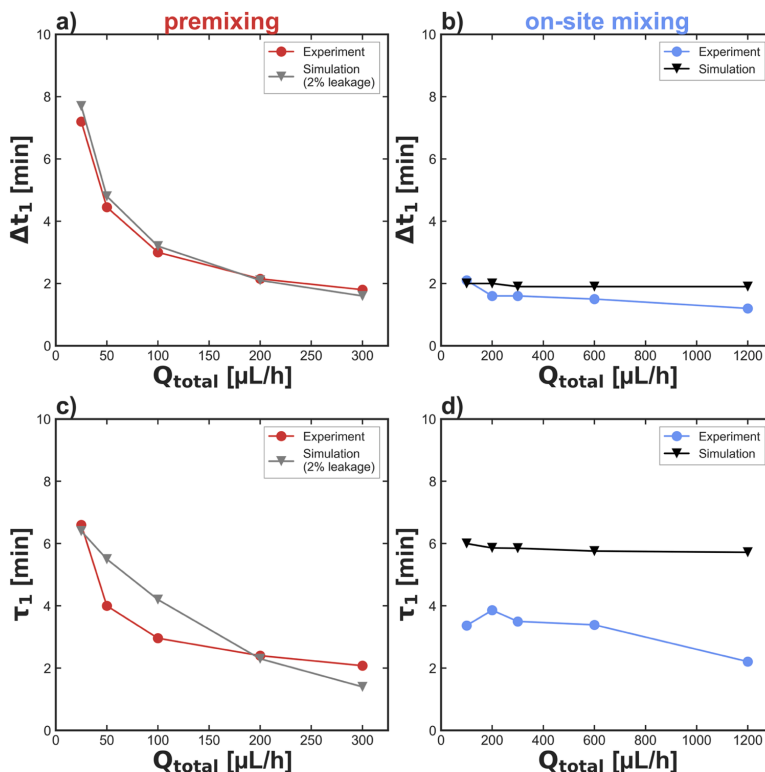
Fig. 7. Dependence of solution replacement dynamics on the volumetric flow rate in two types of LP-TEM flow systems. a) simulated and experimentally measured delay times for *premixing* configuration; **b)** simulated and experimentally measured delay times for *on-site mixing* configuration; **c)** simulated and experimentally measured decay constants for *premixing* configuration; **d)** simulated and experimentally measured decay constants for *on-site mixing* configuration.

Select) is characterized by convection driven solution replacement, even in the presence of a 2% **BP** opening. This determines the reciprocal dependence of the characteristic time constants on the flow velocity, which is clearly visible in Fig. 7a and c. Characteristic times for solution replacement in the imaging area range from 8 to 2 min. At the maximum flow velocity of 300 μL/h one can expect the onset of chemical composition change in the field of view within 2 min (Fig. 7a) and about 80% solution replacement within 5 min (following Fig. 7c and Eq. S1&2). Simulations reasonably predict the delay times for the *premixing* configuration, which is not surprising as this was achieved by fitting the degree of **BP** opening. At the same time, the shape of the curve for decay time is substantially different from experimental data, seemingly underestimating the dependence on the flow velocity. This discrepancy may be attributed to the fact that in the numeric model the nominal spacer thickness (*i.e.,* the height of the **NC**) of 150 nm was used, which is most probably an underestimation of the real height in experiments (see *Supporting Information* section S7 for in-depth discussion; section S7.1. in particular).

Time constants curves for *on-site mixing* setup (Poseidon 200) (Fig. 7b, d) show a nearly neglectable dependence on flow rate, which confirms diffusion driven solution replacement. It should be noted that the delay times are smaller as compared to *premixing* configuration, as the CA solution is delivered directly to the LFC and does not need to travel through the long premixing channel. However, solution exchange dynamics described by decay constant are substantially slower as compared to the *premixing* (2% *leakage*) configuration at

the same flow velocities due to diffusion limited replacement. Simulation substantially overestimates both time constants, and at the same time shows notably lower dependence on the flow rate. This may indicate that the actual **NC** thickness is larger than the nominal 150 nm and thus a convection mechanism contributes more to solution replacement than the simulation predicts. We should note here that not a single parameter was fitted to create geometric models for simulations of *on-site mixing* setup. The contribution of some of these parameters, *e.g.,* the diffusion coefficient and asymmetric (or mis-) alignment of LFC in the oversized bathtub, to the variability of simulated data are discussed in the *Supporting Information* section S7.

3.3.2. In situ fluid mixing

In situ fluid mixing is a well-known microfluidic concept for precise control over solute concentration directly inside a microfluidic multi-inlet mixing channel [41,51]. Here we validate the applicability of this approach for varying a solution composition in flow LP-TEM experiments. Alternatively to changing the solute concentration in the solution supplied by the pumping system (as we showed in Section 3.1.1), the chemical composition in the viewing area could be smoothly altered by changing the relative flow of the two connected syringes (carrying concentrated solution and pure water, respectively; compare Fig. S1b). Defining a partial flow ratio of the solution as $PFR=Q_{solution}/Q_{total}$, where $Q_{total}=Q_{solution}+Q_{water}$, the resulting solute concentration, c_{mix}, assuming complete mixing at given channel position can be expressed as:

$$c_{mix} = PFR \cdot c_{solution} \tag{6}$$

The established linear relation between CA concentration and transmitted intensity (compare Fig. 4) allows the experimental measurements to be interpreted directly in terms of concentration (see Fig. S7 for raw intensity curves). Fig. 8a and c show the dependence of the steady state CA concentration, c_{mix}, in the imaging area of liquid flow cell *vs. PFR* of CA solution for *premixing* (2% *leakage*) and *on-site* configuration, respectively.

For the *premixing* (2% *leakage*) configuration the experimental and simulated values of the steady state concentration of contrast agent *vs. PFR* ($Q_{total}=300$ μL/h) showed an excellent agreement and deviate only slightly from the expected concentration (Eq. (6), *dashed line* in Fig. 8a and c). Due to the laminar flow in the premixing channel, the mixing of the CA solution with pure water happens only by diffusion and thus a small discrepancy from the ideal concentration can be attributed to the lack of time for complete interdiffusion. In fact, simulation for $Q_{total}=25$ μL/h, *i.e.,* 12 times longer residence in premixing channel, shows a complete intermixing (*gray squares* in Fig. 8a). Color maps in Fig. 8b representing a concentration profile across **NC** in a steady state confirm nearly complete intermixing in the whole **NC** area at $Q_{total}=300$ μL/h and *PFR*s close to 0.5.

The *on-site mixing* configuration showed no linear dependence of concentration on the *PFR* (Fig. 8c). Both experiment and simulation follow a step-like curve with an abrupt jump. Concentration profiles extracted from simulations at *PFR*s close to 0.5 (Fig. 8d) reveal that the streams from two inlets compete for the **BP** channel (see Fig. S20), switching the extent of diffusion interface from bypass to nanochannel at *PFR*≈0.5. This directly results in the abrupt switching of the diffusion-controlled steady state concentration in the imaging area. Deviation of the simulated curve from the experimental one can be attributed to asymmetric positioning of the chip and thus inequivalent **BP** channels for the CA solution and water inlets, which is confirmed by the corresponding simulations (*gray squares* in Fig. 8c, refer to *Supporting Information* section S7.4. for more details).

In summary, the flow control over solute concentration in the viewing area can be readily achieved if two flows are mixed before

entering the **NC**, *i.e., premixing* setups like Poseidon Select holder featuring gasket technology.

4. Conclusions

We have proposed a method to characterize *in situ* the dynamics of flow and diffusion in LP-TEM flow systems. The method is based on tracking of the transmitted intensity variation determined by the concentration of electron dense solute. We have characterized the dynamics of solution replacement in two commercially available LP-TEM systems, finding that characteristic times for solution replacement are in the order of 5 min and depend differently on the total flow rate for the two systems. While in *direct* flow systems the total flow rate can be used to control the time constants, *bathtub* setups predominantly depend on intrinsic parameters such as solute-specific diffusion and nanochannel dimensions. It was also shown that the *premixing*-type Poseidon Select holder allows for a precise control over the solute concentration in the viewing area by adjusting the flow rates in two inlets.

A numerical model accounting for the real multi-scale channel geometry, liquid convection and solute diffusion was used to simulate steady and time-dependent scenarios and served to reveal the contribution of convection and diffusion in solution exchange dynamics. A purely convective solution replacement is not feasible in *direct* flow systems that is due to the high pressure in the nanochannel even at moderate flow rates. Thus, for fast replacement (*i.e.,* a large total volumetric flow rate), fluid should be redirected into a bypass for releasing the pressure, reducing thus convection in the nanochannel by orders of magnitude and rendering the diffusion as a primary parameter for the solute replacement.

We anticipate that the acquired dynamic characteristics of commercial LP-TEM flow systems will allow for better planning of *in situ* experiments involving concentration variations in the viewing area and thus a more reliable interpretation of the results. Understanding the role of convection and diffusion in solution exchange dynamics, as well as the implemented numerical model of the liquid flow cell will enable targeted and reliable development of future liquid flow cells with optimized hydrodynamic properties.
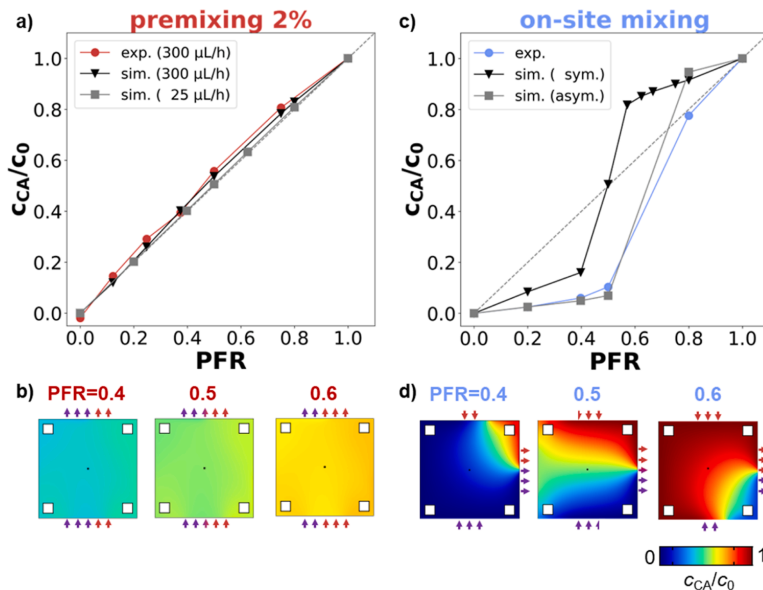

Fig. 8. Dependence of the solute concentration on the partial flow ratio (*PFR*) of the solution. A) Experimental and simulated points for the CA concentration in the viewing window area for the *premixing* configuration at $0<PFR<1$ at the total flow rate $Q_{total}=300$ μL/h; simulated points for $Q_{total}=25$ μL/h are also shown to illustrate completeness of mixing at longer retention time; **b)** simulated CA concentration maps in **NC** of *premixing* configuration at $Q_{total}=300$ μL/h and *PFR*s close to 0.5; **c)** experimental and simulated points for the CA concentration in the viewing window area for the *on-site mixing* configuration at $0<PFR<1$ at $Q_{total}=300$ μL/h; simulated points for asymmetrically assembled LFC (see *Supporting Information* section S7.4. for details) are also shown to illustrate the reason for asymmetry in the experimental profile. **d)** Simulated CA concentration maps in **NC** of *on-site mixing* configuration at $Q_{total}=300$ μL/h and *PFR*s close to 0.5.

10

Declaration of Competing Interest

The authors declare that they have no known competing financial interests or personal relationships that could have appeared to influence the work reported in this paper.

Data availability

Data will be made available on request.

Acknowledgements

Supplementary materials

Supplementary material associated with this article can be found, in the online version, at doi:10.1016/j.ultramic.2022.113654.

References

[1] K.L. Klein, I.M. Anderson, N. de Jonge, Transmission electron microscopy with a liquid flow cell, J. Microsc. 242 (2011) 117–123.
[2] N. de Jonge, F.M. Ross, Electron microscopy of specimens in liquid, Nat. Nanotechnol. 6 (2011) 695–704.
[3] V. Copois, et al., Imaging of soft materials using in-situ liquid-cell TEM, Int. J. Pharm. 127 (2007) 549–559.
[4] N. de Jonge, F.M. Ross, *Liquid Cell Electron Microscopy. Liquid Cell Electron Microscopy*, 1, Cambridge University Press, 2016.
[5] I.M. Abrams, J.W. McBain, A closed cell for electron microscopy, J. Appl. Phys. 15 (1944) 607–609.
[6] S. Pu, C. Gong, A.W. Robertson, Liquid cell transmission electron microscopy and its applications, R. Soc. Open Sci. 7 (2020) 24.
[7] C.R. Allen, Design and Fabrication of a Nanofluidic Cell System for High-Resolution Electron Microscopy of In-Liquid Samples, University of Waterloo, 2017.
[8] H. Wu, et al., Mapping and controlling liquid layer thickness in liquid-phase (scanning) transmission electron microscopy, Small Methods 5 (2021), 2001287.
[9] N. de Jonge, N. Poirier-Demers, H. Demers, D.B. Peckys, D. Drouin, Nanometer-resolution electron microscopy through micrometers-thick water layers, Ultramicroscopy 110 (2010) 1114–1119.
[10] T. Gupta, N.M. Schneider, J.H. Park, D. Steingart, F.M. Ross, Spatially dependent dose rate in liquid cell transmission electron microscopy, Nanoscale 10 (2018) 7702–7710.
[11] N. Schneider M., Michael Norton M., Brian Mendel J., Joseph Grogan M., Frances Ross M., Haim Bau H., Electron-water interactions and implications for liquid cell electron microscopy, J. Phys. Chem. C 118 (2014) 22373–22382.
[12] T.J. Woehl, P. Abellan, Defining the radiation chemistry during liquid cell electron microscopy to enable visualization of nanomaterial growth and degradation dynamics, J. Microsc. 265 (2017) 135–147.
[13] M. Wang, C. Park, T.J. Woehl, Quantifying the nucleation and growth kinetics of electron beam nanochemistry with liquid cell scanning transmission electron microscopy, Chem. Mater. 30 (2018) 7727–7736.
[14] B. Fritsch, et al., Radiolysis-driven evolution of gold nanostructures – model verification by scale bridging *in situ* liquid-phase transmission electron microscopy and x-ray diffraction, ChemRxiv (2022) 1–24.
[15] T.A.J. Welling, et al., Observation of undamped 3D brownian motion of nanoparticles using liquid-cell scanning transmission electron microscopy, Particle & Particle Systems Characterization 10 (2020), 2000003.
[16] M.N. Yesibolati, K.I. Mortensen, H. Sun, S. Tidemand-Lichtenberg, K. Mølhave, Unhindered brownian motion of individual nanoparticles in liquid phase scanning transmission electron microscopy, Nano Lett. 20 (2020) 7108–7115.

[17] G. Zhu, H. Reiner, H. Cölfen, J. de Yoreo, Addressing some of the technical challenges associated liquid phase S/TEM studies of particle, nucleation, growth and assembly, Micron (2018).
[18] J. Frenken, I. Groot, Research in Heterogeneous Catalysis, Springer International Publishing, 2017.
[19] X.Y. Yu, B. Liu, L. Yang, Imaging liquids using microfluidic cells, Microfluid Nanofluidics 15 (2013) 725–744.
[20] N. de Jonge, L. Houben, R.E. Dunin-Borkowski, F.M. Ross, Resolution and aberration correction in liquid cell transmission electron microscopy, Nat. Rev. Mater. 4 (2018) 61–78.
[21] M.J. Williamson, R.M. Tromp, P.M. Vereecken, R. Hull, F.M. Ross, Dynamic microscopy of nanoscale cluster growth at the solid-liquid interface, Nat. Mater. 2 (2003) 532–536.
[22] P.M.G. van Deursen, et al., Graphene liquid cells assembled through loop-assisted transfer method and located with correlated light-electron microscopy, Adv. Funct. Mater. 30 (2020), 1904468.
[23] M. Textor, N. de Jonge, Strategies for preparing graphene liquid cells for transmission electron microscopy, Nano Lett. 18 (2018) 3313–3321.
[24] C. Wadell, et al., Nanocuvette: a functional ultrathin liquid container for transmission electron microscopy, ACS Nano 11 (2017) 1264–1272.
[25] N. de Jonge, D.B. Peckys, G.J. Kremers, D.W Piston, Electron microscopy of whole cells in liquid with nanometer resolution, Proc. Natl. Acad. Sci. U. S. A. 106 (2009) 2159–2164.
[26] A. Cameron Varano, et al., Visualizing virus particle mobility in liquid at the nanoscale, Chem. Commun. 51 (2015) 16176–16179.
[27] D.J. Kelly, et al., Nanometer resolution elemental mapping in graphene-based TEM liquid cells, Nano Lett. 18 (2018) 1168–1174.
[28] M.R. Hauwiller, et al., Gold nanocrystal etching as a means of probing the dynamic chemical environment in graphene liquid cell electron microscopy, J. Am. Chem. Soc. 141 (2019) 4428–4437.
[29] R. Kröger, A. Verch, Liquid cell transmission electron microscopy and the impact of confinement on the precipitation from supersaturated solutions, Minerals 8 (2018) 21.
[30] D.J. Kelly, et al., Situ TEM imaging of solution-phase chemical reactions Using 2D-heterostructure mixing cells, Adv. Mater. 33 (2021), 2100668.
[31] E.A. Ring, N. de Jonge, Microfluidic system for transmission electron microscopy, Microsc. Microanal. 16 (2010) 622–629.
[32] G. Lin, S.W. Chee, S. Raj, P. Král, U. Mirsaidov, Linker-mediated self-assembly dynamics of charged nanoparticles, ACS Nano 10 (2016) 7443–7450.
[33] T. Yamazaki, et al., Two types of amorphous protein particles facilitate crystal nucleation, Proc. Natl. Acad. Sci. U. S. A. 114 (2017) 2154–2159.
[34] V. Beermann, et al., Real-time imaging of activation and degradation of carbon supported octahedral Pt-Ni alloy fuel cell catalysts at the nanoscale using: in situ electrochemical liquid cell STEM, Energy Environ. Sci. 12 (2019) 2476–2485.
[35] J. Cookman, V. Hamilton, L.S. Price, S.R. Hall, U. Bangert, Visualising early-stage liquid phase organic crystal growth via liquid cell electron microscopy, Nanoscale 12 (2020) 4636–4644.
[36] M.H. Nielsen, S. Aloni, J.J. de Yoreo, In situ TEM imaging of CaCO3 nucleation reveals coexistence of direct and indirect pathways, Science 345 (6201) (2014) 1158–1162.
[37] L. Lutz, et al., Operando monitoring of the solution-mediated discharge and charge processes in a Na-O2 battery using liquid-electrochemical transmission electron microscopy, Nano Lett. 18 (2018) 1280–1289.
[38] K. Aliyah, et al., Real-time *in situ* observations reveal a double role for ascorbic acid in the anisotropic growth of silver on gold, J. Phys. Chem. Lett. 11 (8) (2020) 2830–2837.
[39] C.T. Hendley, J. Tao, J.A.M.R. Kunitake, J.J. de Yoreo, L.A. Estroff, Microscopy techniques for investigating the control of organic constituents on biomineralization, MRS Bull. 40 (2015) 480–489.
[40] G. Karniadakis, A. Beskok, N. Aluru, *Microflows and Nanoflows. Microflows and Nanoflows*, Springer, 2005.
[41] S. Merkens, et al., Time-resolved analysis of the structural dynamics of assembling gold nanoparticles, ACS Nano 13 (2019) 6596–6604.
[42] Z. Ou, Z. Wang, B. Luo, E. Luijten, Q. Chen, Kinetic pathways of crystallisation on the nanoscale, Nat. Mater. 19 (2019) 450–455.
[43] A.A. Petruk, C. Allen, N. Rivas, K. Pichugin, High flow rate nanofluidics for in-liquid electron microscopy and diffraction, Nanotechnology 30 (2019) 8.
[44] J.M. Grogan, L. Rotkina, H.H. Bau, In situ liquid-cell electron microscopy of colloid aggregation and growth dynamics, Phys. Rev. E Stat. Nonlin. Soft Matter Phys. 83 (2011) 1–5.
[45] C. Mueller, M. Harb, J.R. Dwyer, R.J.D Miller, Nanofluidic cells with controlled path length and liquid flow for rapid, high-resolution *in situ* electron microscopy, Mater. Res. Soc. Symp. Proc. 1544 (2013) 1–9.
[46] H. Bruus, Theoretical Microfluidics, 45, Oxford University Press, 2008.
[47] A. Colinsk, Introduction to Microfluidics, Oxford University Press, 2007.
[48] L. Chen, et al., Milli-, micro- and nanofluidics: manipulating fluids at varying length scales, Mater. Today Nano (2020) 1–37.
[49] M.N. Yesibolati, S. Laganá, S. Kadkhodazadeh, N.J. Zaluzec, K. Mølhave, Electron inelastic mean free path in water, Nanoscale 12 (2020) 20649–20657.
[50] F. Togi, T. Kubota, K. Toyama, A. Ishida, S. Harada, Quantitative evaluation of solute dispersion in irregularly shaped micro-channels, Microfluid Nanofluidics 24 (2020) 1–8.
[51] M. Vakili, et al., 3D micromachined polyimide mixing devices for in situ X-ray imaging of solution-based block copolymer phase transitions, Langmuir 35 (32) (2019) 10435–10445.

[52] J. He, et al., Hydrodynamically driven self-assembly of giant vesicles of metal nanoparticles for remote-controlled release, Angew. Chem. Int. Ed Engl. 52 (2013) 2463–2468.

[53] D.A. Boy, F. Gibou, S. Pennathur, Simulation tools for lab on a chip research: advantages, challenges, and thoughts for the future, Lab Chip 8 (2008) 1424–1431.

[54] D.B. Williams, C.B. Carter, *Transmission Electron Microscopy - A textbook For Materials Science. Springer,* Springer, 1996.

[55] L. Reimer, Transmission electron microscopy - physics of image formation and microanalysis. Springer Series in Optical Sciences, Springer, Berlin Heidelberg, 1997.

[56] Protochips Inc. *Poseidon Select Workflow & Training Poseidon Select Version 1.3.* (2017).

[57] T.E. Oliphant, Python for Scientific Computing, Comput. Sci. Eng. 9 (2007) 10.

[58] C. Pozrikidis, *Fluid Dynamics - Theory, Computation and Numeric Simulation. Hydrocarbon Engineering,* 7, Springer, 2002.

[59] T.M. Squires, S.R. Quake, Microfluidics: fluid physics at the nanoliter scale, Rev. Mod. Phys. 77 (2005) 977–1026.

[60] J.E. Hesselgreaves, R. Law, D.A. Reay, *Compact Heat Exchangers. Compact Heat Exchangers,* Elsevier Ltd., 2017.

[61] B.E. Rapp, Microfluidics: Modeling, Mechanics and Mathematics, Elsevier, 2017.

[62] M.P. di Cagno, et al., Experimental determination of drug diffusion coefficients in unstirred aqueous environments by temporally resolved concentration measurements, Mol. Pharm. 15 (2018) 1488–1494.

[63] N. Kavokine, R.R. Netz, L. Bocquet, Fluids at the nanoscale: from continuum to subcontinuum transport, Ann. Rev. Fluid Mech. 53 (2021) 377–410.

[64] A.F. Beker, et al., In situ electrochemistry inside the TEM with controlled mass transport, Nanoscale 12 (2020) 22192–22201.

[65] K. Koo, J. Park, S. Ji, S. Toleukhanova, J.M. Yuk, Liquid-flowing graphene chip-based high-resolution electron microscopy, Adv. Mater. 2005468 (7) (2020).

[66] F. Delplace, Laminar flow of Newtonian liquids in ducts of rectangular cross-section a model for both physics and mathematics, Open Access J. Mathe. Theoretical Phys. 1 (2018) 198–201.

A.2   Optimization of Mass Transport in Flow Reactors

Stefan Merkens, Christopher Tollan, Giuseppe De Salvo, Katarzyna Bejtka, Marco Fontana, Angelica Chiodoni, Marek Grzelczak, Andreas Seifert, Andrey Chuvilin, **Towards sub-second Solution Exchange Dynamics in Liquid-Phase TEM Flow Reactors**, *Nature Communications*, *in review.*

The manuscript was cited as ref. [205]. A preprint is available under `https://doi.org/10.21203/rs.3.rs-3208774/v1`.

Towards sub-second Solution Exchange Dynamics in Liquid-Phase TEM Flow Reactors

Stefan Merkens (✉ s.merkens@nanogune.eu)

CIC nanoGUNE BRTA; Department of Physics, Euskal Herriko Unibertsitatea (UPV/EHU)
https://orcid.org/0000-0001-5635-8659

Christopher Tollan

CIC nanoGUNE BRTA

Giuseppe De Salvo

CIC nanoGUNE BRTA; Department of Physics, Euskal Herriko Unibertsitatea (UPV/EHU)

Katarzyna Bejtka

Center for Sustainable Future Technologies@Polito, Istituto Italiano di Tecnologia (IIT); Department of Applied Science and Technology (DISAT), Politecnico di Torino   https://orcid.org/0000-0003-1731-5861

Marco Fontana

Center for Sustainable Future Technologies@Polito, Istituto Italiano di Tecnologia (IIT); Department of Applied Science and Technology (DISAT), Politecnico di Torino

Angelica Chiodoni

Center for Sustainable Future Technologies@Polito, Istituto Italiano di Tecnologia (IIT)
https://orcid.org/0000-0002-4386-842X

Marek Grzelczak

Donostia International Physics Center (DIPC); Centro de Física de Materiales CSIC-UPV/EHU
https://orcid.org/0000-0002-3458-8450

Andreas Seifert

CIC nanoGUNE BRTA; IKERBASQUE   https://orcid.org/0000-0001-5849-4953

Andrey Chuvilin

CIC nanoGUNE BRTA; IKERBASQUE   https://orcid.org/0000-0002-3712-5638

Abstract

Liquid Phase-Transmission Electron Microscopy research increasingly relies on liquid flow reactors to monitor nanoscale dynamics. Current challenges comprise fast mass transport dynamics inside the central nanochannel of the liquid cell, typically *flow cells*, and reliable fixation of the specimen in the limited imaging area. In this work, we present a novel liquid cell concept, the *diffusion cell*, that satisfies these seemingly contradictory requirements by providing additional on-chip bypasses to allow high convective transport around the nanochannel in which the diffusive transport predominates. *Diffusion cell* prototypes were developed using numerical mass transport models and fabricated on the base of existing two-chip MEMS-setups. Important hydrodynamic parameters such as the total flow resistance, the flow velocity in the imaging area and the time constants of mixing were improved by ~2-3 orders of magnitude compared to existing setups. Obtained solution replacement dynamics within seconds already matches the mixing timescales of many *ex situ* scenarios, with further improvements possible. *Diffusion cells* can be easily integrated into existing Liquid Phase Transmission Electron Microscopy workflows, provide correlation of results with *ex-situ* experiments, and can create entirely new research directions for fast nanoscale processes in liquids.

INTRODUCTION

Liquid-Phase Transmission Electron Microscopy (LP-TEM) is an emerging experimental technique which permits the monitoring of processes in liquid samples with nanometer-scale resolution.[1,2] LP-TEM relies on liquid cells (LCs), which are enclosures of (sub-)micrometer thin liquid layers between electron-beam transparent membranes known as windows.[3] Sophisticated LC setups have been developed through micro-electromechanical system (MEMS) fabrication techniques which can incorporate various stimuli such as electrical biasing, heating, and solution exchange, enabling *in situ* and *in-operando* experiments.[4−9]

In LP-TEM flow reactors, the enclosed fluid is connected to external reservoirs, allowing for control over its composition inside the LC. Single and multi-inlet systems enable a broad range of flow experiments comprising continuous renewal and exchange of fluid. This versatility, combined with the ability to incorporate the stimuli mentioned above,[5] distinguishes flow systems from recently proposed static mixing cells.[10] In (electro)chemical LP-TEM experiments, fluid flow serves multiple purposes, including the renewal of reagents, removal of liquid or gaseous reaction products, including radiolytic byproducts and the triggering of nanoscale dynamics such as nucleation, crystal growth and dissolution as well as self-assembly of nanoparticles.[11,12] Recent studies have also demonstrated that flow conditions significantly disrupt the radiolytic reaction network,[13,14] providing additional control of the chemical environment in the area irradiated with the electron beam (IA).

The ideal flow reactor design depends on the specific application; however, certain characteristics are generally required. These include a thin, electron-transparent liquid layer in the imaging area, the ability to deposit samples prior to experimentation & their immobility under flow conditions, and precise control

over the liquid composition.[15,16] Additionally, eliminating gas bubbles is crucial to minimize artifacts, especially in electrochemistry experiments.[17] Moreover, for truly quantitative *in situ* experiments, it is essential to achieve fluid replenishment/mixing dynamics in the LC that are faster than the observed process.[18]

Numerous LP-TEM flow systems have been established in the scientific literature and commercialized,[19–24] and the understanding of their hydrodynamic properties is increasing.[25] Based on general microfluidic considerations, solution exchange in flow reactors results from superimposed diffusive and convective mass transport.[21–23] Solute diffusion is driven by a concentration gradient and fluid flow by a pressure gradient.[26] In (sub-)micrometer-sized channels, fluid flow is typically laminar, and the velocity profile is determined by the flow resistance and the relative alignment of individual channel compartments.[7,27]

According to recent studies, the Poseidon Select sample holder by Protochips Inc.[21] provides convective flow rates in the IA of $\sim 10^{-5}$ m/s at operating pressures of ~ 100 mbar.[25] These values were obtained from experimentally validated finite element simulations assuming a 150 nm thick liquid layer and the presence of a tiny bypass. Petruk *et al.* developed flow systems without bypass compartments leading to increased flow velocities up to $5 \cdot 10^{-2}$ m/s in the IA, and thus accelerated solution renewal.[24] This approach, however, comes at the cost of increased operating pressure (~ 300 mbar for 1 μm high channels), increased bulging and the risk of window rupture, and flushing of the sample. Various strategies were explored to counteract these effects, including microengineering to enforce window stiffness[28] and improved flow control based on pressure-driven pumping systems.[16] As far as we understand, the Stream holder from DENSsolutions[20] is a system with similar characteristics and limitations,[5,6] although quantitative hydrodynamic data is not available.

Recent studies have further demonstrated that the solution exchange dynamics in the IA of available LP-TEM flow reactors are much slower than most processes studied. This complicates reliable interpretation of triggered dynamics.[25] The characteristic timescales of solution exchange for the Poseidon Select and the Poseidon 200 sample holder (both Protochips Inc.[21]) were found to be limited to a few (tens) of minutes due to long feeding channels and excessive diffusion lengths depending on the specific setup and experimental conditions.[25] Similar values are expected for the Dual Flow Liquid System by Hummingbird Scientific due to geometric similarities.[22] Mølhave *et al.* achieved accelerated mixing dynamics and eliminated window bulging by miniaturizing the channel geometry, enabling a variety of flow and diffusion experiments and improved image quality.[23] However, a generic limitation of this recently commercialized concept (Insight Chips[19]) lays in the monolithic LC design, which restricts access to the interior of the nanochannel, thereby hindering *a-priori* sample deposition.

The flow systems presented cannot combine the full range of features required for chemical flow reactors within the stated needs. As a consequence, selecting appropriate setups for LP-TEM flow experiments involves a trade-off between the multiple desired properties. In fact, diffusion has been largely overlooked as a potential major mass transport mechanism despite the advantages it can provide (*i.e.*, slow velocity

in the IA achieved at low operating pressure), presumably due to its inefficiency at millimetre scale distances. LP-TEM flow systems with a negligible contribution of convective transport in the IA have been reported but have failed to sufficiently emphasize diffusion (*e.g.*, Poseidon 200 setup by Protochips[21] and Dual Flow Liquid System by Hummingbird Scientific[22]).[25,29]

In this manuscript, we propose a novel liquid cell concept, the *diffusion cell*, that relies on diffusive mass transport in proximity to the imaging area, tremendously improving all desirable characteristics of LP-TEM flow reactors, namely the possibility for large overall volumetric flow rates; low overall flow resistance, *i.e.*, low pressure build-up; fast (within seconds) solution exchange dynamics with negligible flow in the IA; flexibility to mount samples prior to experimentation; and compatibility with established holders. Several designs for various applications were developed by virtual prototyping on previously validated numerical models. Physical prototypes were fabricated, and their performance verified.

RESULTS AND DISCUSSION

The Diffusion Cell Concept

LP-TEM flow systems are set up by assembling MEMS-based LCs, typically *flow cells*, in the tip of dedicated sample holders exhibiting limitations outlined in the introduction.[22] Fig. 1a illustrates a novel LC concept, the *diffusion cell*, as a means to improve the hydrodynamic properties of such systems. A micrometer-sized flow channel (height h_{BP}) with expected low resistance (on-chip bypass, BP_{on}) aims at guiding flow into the *diffusion cell* and around the central nanochannel (NC, width w_{NC}) comprising the IA in which the higher flow resistance imposes diffusion as the dominant mass transport mechanism. Note that the proposed *diffusion cell* design is compatible with existing LP-TEM flow sample holders as the external dimensions of the chips remain unchanged. Below, the *diffusion cell* concept will be tested in commercially available LP-TEM flow setups with different mass transport characteristics and compared to default *flow cells* (w_{NC} = 2 mm).[25]

Direct Flow vs. Bathtub Configurations

Two flow concepts have been established for LP-TEM sample holders which differ regarding the preferential flow path through the LC.[25] In *direct flow* setups, most of the flow is forced into the NC inside the LC, resulting in convection-dominated mass transport and high velocities in the imaging area (usually located in the center of the LC) achieved at rather high operating pressures. In *bathtub* setups, micrometer-sized (off-chip) bypass channels substantially redirect the flow around the LC, and thus the NC, leading to diffusion-dominated mass transport in the IA due to very low flow velocities, and relatively low operating pressures (see also Fig. 5 in [25]).

In general, the overall pressure drop Δp developed along either of these flow systems can be expressed by Eq. 1:

$$\Delta p = Q_{\text{total}} R_{\text{total}} = Q_{\text{total}} \left(\frac{R_{\text{BP}} R_{\text{NC}}}{R_{\text{BP}} + R_{\text{NC}}} \right)$$

(1)

where Q_{total} is the overall volumetric flow rate, and R_{total}, R_{BP} & R_{NC} are the flow resistance of the entire flow system, available bypass(es) and the central nanochannel, respectively.

Convective mass transport through the NC is further defined by the ratio of the flow resistances of the NC and BP (Eq. 2):

$$Q_{\text{NC}} = \frac{R_{\text{BP}}}{R_{\text{NC}}} \bullet \frac{Q_{\text{total}}}{1 + \frac{R_{\text{BP}}}{R_{\text{NC}}}}$$

(2)

with $v_{\text{NC}} = Q_{\text{NC}}/A_{\text{NC}}$, where Q_{NC} and v_{NC} denote the volumetric flow rate and the mean flow velocity through the NC and A_{NC} being its cross-section (*Supporting Information* section 2 for details on the derivation of Eqs. 1 & 2).

Eqs. 1 & 2 indicate that additional on-chip bypass channels reduce the overall pressure drop (decreasing R_{BP} lowers R_{total}) as well as the convective mass transport through the NC. To validate the beneficial effect of *diffusion cells* operated in *direct flow* and *bathtub*-type configurations, we performed finite-element simulations of convective transport. Figure 1c & **d** illustrate the flow velocity profiles through channel geometries derived from the Poseidon Select and Poseidon 200 sample holders (both Protochips Inc.[21]), respectively. The width of the NC and the height of the BP_{on} were w_{NC} = 0.2 mm and h_{BP} = 10 µm, respectively. In both configurations, the *diffusion cell* design guides flow into the on-chip bypass channel (BP_{on}) yet restricts it in the central NC of reduced lateral dimensions. In particular for the *direct flow* configuration, the operating pressure (Δp) and the flow velocity in the center of the IA (v_{c}) are significantly decreased, from 100 to 6 mbar and from 15 to 1.5 µm/s, respectively (at Q_{total}=300 µL/h; see Fig. 1c).

Premixing vs. Onsite Mixing Configurations

Various characteristic locations can be defined to differentiate between multi-inlet systems as illustrated in Fig. 1b. At the interface point (IP), macroscopic capillary channels interface with the nanochannel located in the LC. The mixing point (MP) defines the merging point of (all) inflow channels. The channel compartment between the MP and the IP is usually referred to as the premixing channel with the length L.

Two mixing concepts have been established for LP-TEM flow reactors.[22] In *premixing* setups, fluids are fed through supply channels that merge far before the IP; whereas in *onsite mixing* setups, the supply channels reach the LC separately so that the IP and the MP coincide. By combining the presented design concepts (*premixing* vs. *onsite mixing* and *direct flow* vs. *bathtub*), 4 different (in terms of mass transport

dynamics) holder configurations, all with different IP, IA and MP locations, can be envisioned. Specific implementations of such systems can comprise a negligible premixing channel ($L = 0$) and either non-existent ($1/R_{BP} = 0$) or multiple ($1/R_{BP} = \sum 1/R_i$, compare *Supporting Information* section 2) bypasses (BP), amongst others, without violating the generality of the description and Fig. 1b. The two most relevant sample holders studied here, the Poseidon Select and Poseidon 200 (both Protochips Inc.),[21] correspond to a *direct flow* configuration with *premixing*, and a *bathtub* configuration with *onsite mixing*, respectively. [25]

The flow in the *diffusion cell* is split between the BP_{on} and the NC based on their respective flow resistances with convective mass transport through the NC being described by Eq. 2 (see above). A solute also reaches the IA by diffusion D from the BP_{on}.

For a general comparison of mass transport, the travel time is a suitable quantity.[30] The overall travel time, t, results from the respective travel times in the premixing channel, t_L, and in the NC, t_{NC}, according to $t = t_L + t_{NC}$. While t_L is determined mostly by convection along L (*Eq. 3*), t_{NC} is determined by both convection and diffusion in the NC (*Eq. 4*; compare *Supporting Information* section 2):

$$t_L = \frac{L}{(Q_{total}/A_L)} \text{ and } t_{NC} = \frac{t_D t_C}{t_D + t_C}. \text{ (3), (4)}$$

In *Eqs. 3 & 4*, A_L is the cross-section of the premixing channel and t_D & t_C are characteristic times of mass transport by diffusion and convection, respectively.

For simplicity, the NC is assumed to be symmetric regarding convection and diffusion (*i.e.*, travel distance and diffusion length being both equal to half the extent of the NC, $w_{NC}/2$). t_D and t_C can thus be expressed as:[30]

$$t_c = \frac{\left(\frac{w_{NC}}{2}\right)}{\left(\frac{Q_{NC}}{A_{NC}}\right)} \text{ and } t_D = \frac{\left(\frac{w_{NC}}{2}\right)^2}{8D}. \text{ (5), (6)}$$

In *Eq. 6*, D is the diffusion coefficient of the solute in the solvent.

Eq. 3−6 points to several possibilities for decreasing t. First, the mixing channel can be eliminated by supplying both solutions directly on chip ($L = 0$), which sets t_L to zero. This was realized in commercial holder setups, *e.g.*, the Poseidon 200 (Protochips Inc. [21]) and the Nano Channel Chip (Insight Chips[19]). Second, the volumetric flow can be increased, thereby decreasing t_C following Eqs. 3 & 5. However, this is accompanied by a proportional increase in the internal LC pressure (Eq. 1), which is intrinsically limited by the robustness of the membrane. Additionally, a high flow may influence the mobility of the sample and thus disturb the observation. Finally, both t_C and t_D can be reduced by reducing the lateral extension of the NC, w_{NC}. Note that the convective term t_C depends approximately linearly on w_{NC}, while the diffusive term t_D has a quadratic dependence on w_{NC} (compare Eqs. 3 & 5 & *Supporting Information* section 2).

We have simulated convective & diffusive transport in the above introduced models (w_{NC} = 0.2 mm, h_{BP} = 10 µm, Q_{total} = 300 µL/h) to evaluate the effect of BP_{on} on solution exchange in *diffusion type* LP-TEM flow reactors. The active inlet was abruptly changed from pure water to an aqueous solution of a solute (diffusion coefficient: D = 6·10^{-10} m^2/s, concentration at inlet: c_0 = 40 mM). Time-resolved concentration maps of the solute in *flow* and *diffusion cells* were compared for the *direct flow/premixing* (Fig. 2a & **b**) and for the *bathtub/onsite mixing* (Fig. 2c & **d**) configuration, respectively. Diffusion-controlled solution exchange in *diffusion cells* completes in ~ 20 s in both holder configurations (from 30 to 50 s in *direct flow/premixing* and 10 to 30 s in *bathtub/onsite mixing* configurations; compare Fig. 2e & **f**). The larger time delay (Δt) in the case of the *premixing* configuration is due to non-zero t_L. Interestingly, the concentration profiles in the NC are radially symmetric in both cases (snapshots at 30 s in Fig. 2e and 10s in Fig. 2f) indicating diffusion-controlled solution exchange. Figure 2g & **h** compare the time-dependent concentration profiles in the center of the NC ($\hat{=}$IA) for *direct flow/premixing* and *bathtub/onsite mixing* setups demonstrating that the on-chip bypass leads to drastically accelerated solution exchange in both cases with respect to the default setup (w_{NC} = 2 mm).[25]

Based on the analysis of Figs. 1 & 2, the positive effect of *diffusion cells* on the hydrodynamic properties of LP-TEM flow reactors is evident. Among the multiple benefits are 1) the reduction of t_D by already > 1 order of magnitude, and diffusion becoming the dominant mechanism of mass transport in the NC; 2) reduction of the overall flow resistance and, consequently, reduction of the developed pressure and/or the possibility to apply significantly higher flow rates; 3) negligible convective transport in the NC, which improves sample stability; and 4) compatibility with existing LP-TEM flow holders and sample deposition protocols.

Virtual Prototyping of Diffusion Cell Geometry

To evaluate the potential and limitations of the proposed *diffusion cell* design, the influence of relevant geometrical and experimental parameters on its hydrodynamic properties was screened by simulations. Starting from parameters used for Figs. 1 & 2, simulations were performed extending the tested range for the width of the nanochannel (2 mm < w_{NC} < 0.05 mm), the height of the on-chip BP channel (150 nm < h_{BP} < 50 µm) and the volumetric flow rate (300 µL/h < Q_{total} < 3000 µL/h). The monitored characteristic parameters were the pressure drop (Δp) between the in- and outlet, the linear flow velocity (v_c) at IA, the delay (Δt) and the decay time (τ) constants of solution replacement in the IA. Figure 3 summarizes the characteristic values obtained in simulations both for *direct flow/premixing* and *bathtub/onsite mixing* configurations.

A central finding of the virtual prototyping was that the lateral extension of the NC (w_{NC}) has no significant effect on the developed pressure (Fig. 3a) and flow velocity (Fig. 3d) in the NC (after the initial sharp drop) since the flow resistance in the NC decreases proportionally to the flow resistance of the BP_{on} maintaining a balanced flow distribution. Increasing the height of the BP_{on} (h_{BP}) decreases the pressure drop, Δp, to a negligible 0.1 mbar (Fig. 3b) and the flow velocity, v_c, to a few tens of nm/s (Fig. 3e). This is

a consequence of the drastically decreased flow resistance of the BP_{on}, which further allows for high overall volumetric flow rates up to 3000 µL/h, while maintaining pressure build-up below 100 mbar (Fig. 3c).

The achievable mixing times are characterized by Δt and τ, as introduced earlier[25] and illustrated in Fig. 2g & **h**. The delay time Δt (onset of solution replacement) decreases with decreasing w_{NC} reaching values as low as a few seconds for 100 µm wide NCs (Fig. 3g). Δt further decreases with increasing flow rate as expected from Eq. 2 (Fig. 3i). However, beyond the initial steep drop, Δt shows no further dependence on the height of the NC (Fig. 3h). The exponential decay constant τ depends even more strongly on the lateral extension of the NC (Fig. 3j). Moreover, it remains almost constant at different h_{BP} (Fig. 3k) and Q_{total} (Fig. 3l), particularly in the *bathtub/onsite mixing* configuration (*light blue curve*). This unambiguously points to diffusion as the main mass transport mechanism inside the NC in both *onsite mixing* and *premixing* configurations. Even for the relatively low diffusion coefficient used in the simulations ($D = 6 \cdot 10^{-10}$ m^2/s), τ can reach ~ 1 s for w_{NC}=100 µm. A further decrease in NC extension does not result in a further decrease in τ. This peculiar behaviour was associated with intermixing of the solutions at the inactive inlet. As we will show below, improved experimental methods can further accelerate solution exchange.

Further analysis of Fig. 3 allows for in-depth understanding of the hydrodynamic properties of the flow reactor geometries (for which we direct the reader to the *Supporting Information* section 4.2). Here, we rather emphasize the main conclusion of the virtual prototyping, namely that the inclusion of BP_{on} dramatically improves the main hydrodynamic characteristic of LP-TEM flow reactors, such as mixing time (<< 10 s), while allowing high total flow rates (up to 3000 µl/h), negligible convective transport in IA (v_c < 20 nm/s) and negligible pressure buildup (down to 0.1 mbar at Q_{total} = 300 µl/h).

Device Fabrication & Design Rules

To experimentally test the new design concept, physical prototypes of *diffusion cells* were fabricated. For simplicity, and to demonstrate the versatility of the design, commercially available E-chips (EPB-52DNF; Protochips, Inc.[21]) were used.[31] Micrometer-sized bypass channels were etched into existing chips using optical lithography, wet-chemical and reactive ion etching (see *Methods* for details). The specifications of the existing chips led to several geometric constraints ("Design Rules") that had to be met to ensure the structural integrity of the modified chips, which resulted in the final prototypes differing slightly from the designs modelled for Fig. 1−3. The E-chips are 2 x 2 x 0.3 mm^3 in size, have a rectangular viewing window (550 x 20 µm^2) with an inclined groove on the back side. Flow spacers (0.2 mm x 0.2 mm x 100 nm) are located in the 4 corners. The derived chip design, which meets all requirements, is shown in Fig. 4b. The extension of the central island forming the nanochannel was measured to be ~ 120 x 650 µm^2, and the bypass channel etched on the chip ($h_{BP} \approx 10$ µm) is formed between the four pentagonal plateaus at the corners, on which the spacers are located.

Experimental Testing of Diffusion Cells

To test the functionality of the prototypes and confirm the predictions of the numerical model, the modified E-chips were installed in commercial LP-TEM sample holders with well-known hydrodynamic properties (see above and [25]). Both *direct flow/premixing-* (Poseidon Select) and *bathtub/onsite mixing-* type (Poseidon 200; Protochips. Inc.[21]) configurations were tested. The orientation of the central island with respect to the flow direction was chosen to favor the flow, *e.g.*, provide linear flow around the rectangular NC in the Poseidon Select setup. Simulated velocity profiles for both setups are depicted in Fig. 4a & **c**, respectively.

To quantify the solution exchange dynamics of the fabricated prototypes, an established contrast variation method was applied.[25] Time-dependent concentration profiles were obtained by tracking changes in the intensity of the transmitted signal as a result of alternating the flow of a highly electron-scattering contrast agent (phosphotungstic acid, PTA) and pure water. Compared to previous works, the time resolution of the experiment was significantly increased (200 ms *vs.* 5 s).[25] Refer to *Methods* section for experimental details.

The obtained time-dependent concentration curves (Fig. 4d & **e**) show accelerated solution replacement dynamics compared to the default *flow chip* (w_{NC} = 2 mm) by nearly two orders of magnitude.[25] Flow rates were tested in an extended range ($300 \leq Q_{total} \leq 3000$ µl/h). The characteristic time constants (Δt and τ; Fig. 4f-i) were extracted to obtain comparable quantitative data. The minimum delay time and decay time constant were determined to be Δt = 12 s and τ = 9 s for the Poseidon Select and Δt = 13 s and τ = 3.7 s for the Poseidon 200 sample holder, as compared to previous experimental records $\Delta t \sim$ 110 s & $\tau \sim$ 120 s and $\Delta t \sim$ 86 s & $\tau \sim$ 156 s, respectively.[25] For both configurations, the experimentally measured time constants were larger than the predictions of the numerical models (*grey triangles* in Fig. 4f-i). This discrepancy comes from the simplifications of the model, in particular neglecting the window bulging. Refer to *Supporting Information* section 5 for detailed discussion.

The following aspects must be considered concerning the experimental results. First, the achieved mixing times depend on the diffusion coefficient of the contrast agent, as diffusion act as the dominant mass transport mechanism. With PTA being a relatively slow diffusive species ($D_{PTA} \sim 6 \cdot 10^{-10}$ m^2/s), even faster solution exchange dynamics are expected for solutes commonly encountered in (electro-)chemical processes (*e.g.*, sodium ions: $D_{Na+} \sim 1.3 \cdot 10^{-9}$ m^2/s), as demonstrated through newly developed optical methods (refer to *Supporting Information* section 6). Second, even though the *bathtub/onsite mixing* configuration can lead to faster mixing times compared to the *direct flow/premixing* configuration (both in simulation and experiments), the Poseidon 200 system is experimentally less reliable than the Poseidon Select system due to less control over the LC alignment in the holder tip (eventually reflected in the more pronounced deviation between simulated and modeled time constants; Fig. 4h, i).[25] Third, the main criteria for prototyping were versatility, ease of fabrication and compatibility with existing equipment, pointing to further improvement capacities.

General Guidelines

To further accelerate solution exchange, general guidelines can be concluded based on Eq. 1−6 and Fig. 3, potentially leading to sub-second dynamics:

- The premixing channel should be removed because the delay time Dt is half of the total mixing time;
- NC size should be as small as possible; for 20 μm-sized windows,[31] 50 μm wide NCs seem to be the technological limit;
- the overall flow rate should be as high as possible to minimize the solution's travel time from IP to IA;
- for the same purpose, the off-chip BP should be minimized;
- to reduce the pressure drop at high overall flow rates, the BP_{on} should be as deep as possible; simulations show that 50 μm is sufficient for the maximum feasible flow rate.

Thus, using the terminology established above, the ideal LP-TEM mixing reactor would rely on *onsite mixing* (no premixing channel) and *direct flow* (no or minimal off-chip BP). Structurally, only Insight Chips[19] offers such systems, which however is limited to pre-assembled LCs. DENSsolutions[20] has no multi-inlet systems so far, and Protochips[21] offers either *onsite mixing* or *direct flow*, but not a combination.

Improved Experimental Methodology

To challenge the limits of the *diffusion cell* concept, we evaluated a virtual LP-TEM configuration that meets the above criteria. The most obvious setup would be the Poseidon 200 configuration with limited off-chip BP, *i.e.*, with integrated gasket technology. To date, such setups are not available for LP-TEM but can be accessed through simulations and replicated in *ex situ* devices (refer to *Supporting Information* section 5 & 6 for details). Apart from the ideally designed channel geometry, sophisticated experimental methodology turned out to be even more crucial. As stated above (Fig. 3g, j), reducing w_{NC} below 100 μm did not further accelerate solution replacement in the IA due to intermixing of the solutions at the inactive inlet. It was, however, previously demonstrated that the *inactive* inlet can be operated at a negligibly small partial flow rate ($PFR < < 0.5$) to avoid intermixing at the inlet without affecting the concentration in the NC of *onsite mixing* setups since the negligible flow is guided around the IA at a sufficient distance.[25]

Figure 5a depicts time-dependent concentration maps inside the diffusion cell simulated for a flow channel geometry derived from Poseidon 200 holder featuring gasket technology, *i.e.*, representing a *direct flow/onsite mixing* configuration. The relevant model parameters were: lateral extension of NC: 0.05 mm x 0.65 mm; NC height: 150 nm (without considering the bulge); h_{BP} = 50 μm; and Q_{total} = 3000 μl/h (resulting in Δp = 2.5 mbar). Background flow was induced at the *inactive* inlet at the rate of $0.05 \cdot Q_{total}$. At a steady-state of 0.95 water flow, a solute is mainly passing through the off-chip BP, and nothing reaches the IA ("*steady-state (5%)*" on Fig. 5a). After enabling the solute flow at $0.95 \cdot Q_{total}$, the solution is completely replaced around the NC in < 0.5 s. About 90% of solute replacement in the IA is reached in ~ 0.7 s after the flow changeover. The characteristic time constants extracted from Fig. 5c are

significantly less than 1 s, namely Δt = 0.3 s & τ = 0.21 s. Note that in comparison to the above, the diffusion coefficient was adjusted to reflect more realistic scenarios of diffusing small molecules (D = 1.3•10^{-9} m^2/s; compare *Supporting Information* section 5). At steady state solute flow ("*steady-state (95%)*" on Fig. 5a), the relative concentration in the IA (c/c_0) rises to 1.0 because 5% flow of pure water is confined in the nearest off-chip BP and does not reach the IA.

Discussion - Further Scenarios

Beyond the Protochips ecosystem, a virtual double-inlet *diffusion cell* hypothetically compatible with the Stream system by DENSsolutions[20] was created based on the geometric characteristics available for the single-inlet setup.[6] Simulated solution replacement dynamics for such devices also pointed towards sub-second mixing times (with 90% solution replacement achieved in ~ 0.7 s; see *Supporting Information* section 7).

In addition to solution mixing, fluid renewal in the IA plays an important role in LP-TEM, in particular to remove radiolysis products and/or deliver scavengers.[13] Considering that the solution is completely renewed by diffusion in less than a second, it is in principle possible to select imaging conditions in which the influence of radiolytic species would be minimized.

Another important aspect of *in situ*/*in-operando* experiments in electrochemistry and catalysis is bubble formation in gas evolution reactions.[17,32] For example, in electrochemical LCs, gas bubbles often irreversibly block extended nanochannels and disrupt the normal conductivity of the electrolyte. The presence of a deep (tens of micrometers) on-chip BP channel with a strong fluid flow surrounding a significantly smaller nanochannel can not only prevent the formation of bubbles, but also remove already existing ones. However, the presence of electrodes imposes additional design rules for the on-chip BP geometry. In a following manuscript, we will describe the development, implementation and application of *diffusion cells* optimized for electrochemistry.

CONCLUSION

A new liquid cell concept for LP-TEM flow experiments relying on diffusion as the main mass transfer mechanism inside the nanochannel, the *diffusion cell*, is presented. Key advantages include 1) fast solution mixing/exchange dynamics - the fastest experimentally obtained mixing constants were ~ 2 s, which is ~ 2 orders of magnitude faster than previous results on default setups;[25] 2) about 2 orders reduced fluid flow velocities in the imaging region, which can be important for mechanical stability of samples; 3) about 3 orders reduced flow resistance, which positively affects window bulging and simultaneously increases the range of applicable flow rates (up to 3000 µL/h were tested); 4) the versatility of the proposed *diffusion cells* allows their use with existing LP-TEM holders applying established workflows and does not limit sample preparation. Simulations of optimized scenarios demonstrated the ability to achieve sub-second mixing/exchange dynamics when applying sophisticated experimental methodology. This paves the way for studying fast nanoscale kinetics and should allow the correlation of LP-TEM results with bulk *ex situ* experiments.

Declarations

AUTHOR CONTRIBUTIONS

S.M. − *diffusion cell* design idea (equal), conceptualization (equal), experiments (lead), simulations (lead), data curation and analysis (lead), writing original draft (lead), review and editing (supporting); C. T. − manufacturing of physical prototypes (lead), review and editing (supporting); G. D. − simulations (lead), data curation and analysis (lead), review and editing (supporting); K. B. − experiments (supporting), data curation and analysis (lead), review and editing (supporting); M. F. − experiments (supporting), data curation and analysis (lead), review and editing (supporting); A. Chi. − experiments (supporting), data curation and analysis (lead), review and editing (supporting), resources (equal); M. G. − experiments (supporting), data curation and analysis (lead), review and editing (supporting), resources (equal); A. S. − review and editing (supporting), resources (equal); A. Chu. − *diffusion cell* design idea (equal), conceptualization (equal), supervision (lead), data curation and analysis (supporting), writing original draft (lead), review and editing (supporting), resources (equal), funding (lead).

COMPETING INTEREST

The authors declare no competing interests.

Methods

Flow Reactor Systems: Two different LP-TEM sample holder setups, Poseidon select™ and Poseidon 200™ (both Protochips, Inc.[21]), were used for experiments. The assembly process of the flow reactors was identical for all setups and followed standard procedures (see previous work[25] and *Supporting Information* section 1).

Physical Prototyping of *Diffusion Cells*: Both chemical and reactive ion etching (RIE) strategies were applied to modify E-chips. To enable chemical etching, photolithography was applied to write the patterns defining on-chip bypass channel in the SiN surface layer using a picosecond laser (wavelength: 355 nm; power: 0.1 W; 1 pass; line spacing: 5 μm; speed: 15 mm/s). In a second step, KOH etching (KOH

concentration: 40 %w/v; temperature: 80 °C) was applied to selectively etch out silicon from the previously irradiated area. To obtain ~ 30 μm deep, the immersion times of ~ 30 min were required. In a final step, ion beam etching (30 kV; Ga source; FEI Helios Nanolab 600) was applied to remove overhanging material and smooth the edges, especially of the central nanochannel. Details of RIE methods are intellectual property of Protochips Inc.

Image Contrast Variation Method: The procedure for hydrodynamic quantification of flow reactors was adopted from (image) contrast variation method described in a previous manuscript.[25] In LP-TEM, the (normalized) transmitted intensity, , can be expressed based on *Eq*. 5:

$$I_{\text{norm}} = \frac{I}{I_0} = \approx 1 - \rho_{\text{CA}} \cdot z \cdot c = 1 - K \cdot c, \qquad (5)$$

where I_0 and I denote the transmitted intensity through a LC containing pure water and contrast agent solution, respectively. z is the thickness of liquid layer and ρ_{CA} as well as c are scattering power and concentration of the contrast agent, respectively.

Flow Control: Two electronically connected programmable syringe pumps (Pump 11 Pico Plus Elite, Harvard Apparatus, USA) were used to control liquid flow through the two-inlets reactor. One of the syringes contained pure demineralized water (MillliQ; resistivity: 18.2 M Ω•cm at 25 °C), the other an aqueous solution of contrast agents at concentrations to ensure ≥ 10% decrease of transmitted intensity of pure water solution – that was, 40 mM for phosphotungstic acid (PTA) LP-TEM flow experiments.[25] The electronically interfaced pumps were programmed to provide a constant volumetric total flow rate (Q_{total}), yet abruptly alternating the applied flow between the reference (water; Q_{water}) and contrast agent (Q_{CA}) solution at constant time intervals (usually every 5 min) to study the dynamics of solution exchange. Q_{total} was studied in an elevated range from 300 up to 3000 μL/h, by the minimum reasonable flow rate and maximum rate safe for the window membranes (representing a 10x increase in respect to previous study).[25]

Data Acquisition and Post-processing: TEM imaging was performed on a Tecnai G2 F20 S-twin microscope (FEI), operated at 200 kV. The same imaging conditions were used for all the experiments: parallel beam illumination, M2250*x* magnification, beam intensity adjusted to a dose rate of approximately 8 e/nm2/s (without the sample). Local image intensity (I) curves were averaged from a 1 x 1 μm^2 area in the center of the viewing window and acquired on a Gatan Orius 2K*2K CCD camera (GATAN, USA) at an interval of 0.2 s between data points.

Data acquisition was manually synchronized with the pump's microcontroller with an accuracy < 1 s. The typical duration of the experiments was 10 min (1 datapoint each 200 ms). raw intensity curves were loaded in customized Python-2.7 workflows (numpy, scipy, matplotlib) for further semi-automated processing and plotting.[33]

Convection Diffusion Model: An experimentally validated numeric model for convection and diffusion in realistic 3D LP-TEM flow reactor geometries was adopted from previous work[25] for virtual prototyping. The details of the model implementation (*i.e.,* underlying physics, geometric model refinement, meshing, definition of boundary conditions) and its validation for Poseidon 200 and Poseidon Select type sample holders (Protochips Inc.)[21] were described in previous study.[25] In brief, the laminar flow module was used to solve the incompressible Navier-Stokes equation coupled with the equations for Fick's laws describing water as an incompressible fluid and the diffusion of solvated species therein. For the boundary conditions, all channel walls including membranes were considered chemically inert and rigid (no membrane bulging was considered qualitatively for model refinement); no liquid slip along and no-penetration through the walls was permitted; inlets were transparent, and inflow was described by the volumetric flow rate; outlets were transparent and described by zero pressure. Stationary as well as time-dependent solutions were calculated to obtain stationary velocity and pressure maps as well as local time-dependent solute concentration profiles, respectively.

Due to the highly parametrized implementation of the initial model,[25] virtual prototyping was feasible through reasonable screening of model input parameters. Most relevant parameters were the lateral extension of the central nanochannel, w_{NC}, (defining the width of the on-chip bypass channel), the heigh of the on-chip bypass channel, h_{BP}, the diffusion coefficient D of the solute as well as the total volumetric flow rate, Q_{total}. Screening of geometric parameters was performed within the intrinsic limitations of the setup, *i.e.,* dimension of the small E-chip (2 mm x 2 mm x 0.2 mm), with w_{NC} and h_{BP} ranging from 0.05 to 2 mm and 150 nm to 50 µm, respectively. Q_{total} was screened in the range 300 µL/h $\leq Q_{total} \leq$ 3000 µL/h. Diffusion coefficients were selected in agreement with experiment (where appropriate) and ranged between 10^{-9} m^2/s and 10^{-11} m^2/s. For PTA, D was assumed as $D_{PTA} = 6 \cdot 10^{-10}$ m^2/s.[25]

References

1. Jonge, N. de & Ross, F. M. Electron microscopy of specimens in liquid. Nat Nanotechnol 6, 695–704 (2011).

2. Jonge, N. de & Ross, F. M. *Liquid Cell Electron Microscopy. Liquid Cell Electron Microscopy* vol. 1 (Cambridge University Press, 2016).

3. Abrams, I. M. & McBain, J. W. A closed cell for electron microscopy. J Appl Phys 15, 607–609 (1944).

4. Klein, K. L., Anderson, I. M. & de Jonge, N. Transmission electron microscopy with a liquid flow cell. J Microsc 242, 117–123 (2011).

5. Beker, A. F. *et al.* In situ electrochemistry inside a TEM with controlled mass transport. Nanoscale 12, 22192–22201 (2020).

6. van Omme, J. T. *et al.* Liquid phase transmission electron microscopy with flow and temperature control. Journal of Material Chemistry C 8, 10781–10790 (2020).

7. Ring, E. A. & De Jonge, N. Microfluidic system for transmission electron microscopy. Microscopy and Microanalysis 16, 622–629 (2010).

8. Korpanty, J., Parent, L. R., Hampu, N., Weigand, S. & Gianneschi, N. C. Thermoresponsive polymer assemblies via variable temperature liquid-phase transmission electron microscopy and small angle X-ray scattering. Nat Commun 12, (2021).

9. Lee, S., Schneider, N. M., Tan, S. F. & Ross, F. M. Temperature Dependent Nanochemistry and Growth Kinetics Using Liquid Cell Transmission Electron Microscopy. ACS Nano 17, 5609–5619 (2023).

10. Kelly, D. J. *et al.* In Situ TEM Imaging of Solution-Phase Chemical Reactions Using 2D-Heterostructure Mixing Cells. Advanced Materials 33, (2021).

11. Yang, Y. *et al.* Operando Methods in Electrocatalysis. ACS Catal 11, 1136–1178 (2021).

12. Nielsen, M. H. & Yoreo, J. J. De. Liquid Cell TEM for Studying Environmental and Biological Mineral Systems. Liquid Cell Electron Microscopy 316–333 (2017).

13. Merkens, S., De Salvo, G. & Chuvilin, A. The Effect of Flow on Radiolysis in Liquid Phase-TEM flow cells. Nano Express 3, 14 (2023).

14. Schneider, N. M. *et al.* Electron-Water interactions and implications for liquid cell electron microscopy. Journal of Physical Chemistry C 118, 22373–22382 (2014).

15. Cheng, N., Sun, H., Beker, A. F. & Omme, J. T. van. Nanoscale visualization of metallic electrodeposition in a well-controlled chemical environment. Nanotechnology (2022).

16. Wu, H. *et al.* Mapping and Controlling Liquid Layer Thickness in Liquid-Phase (Scanning) Transmission Electron Microscopy. Small Methods 5, 9 (2021).

17. Yang, Y. *et al.* Elucidating Cathodic Corrosion Mechanisms with Operando Electrochemical Transmission Electron Microscopy. J Am Chem Soc 144, 15698–15708 (2022).

18. Z Xu & Z Ou. Direct Imaging of the Kinetic Crystallization Pathway: Simulation and Liquid-Phase Transmission Electron. *materials* 16, (2023).

19. Insight Chips. Insight Chips. https://www.insightchips.com/ https://www.insightchips.com/contact (2023).

20. DENSsolution. DENSsolutions. https://denssolutions.com/ https://denssolutions.com/ (2023).

21. Protochips Inc. Protochips. https://www.protochips.com/ https://www.protochips.com/ (2023).

22. Hummingbird Scientific. Hummingbird Scientific. https://hummingbirdscientific.com/ https://hummingbirdscientific.com/ (2023).

23. Jensen, E., Burrows, A. & Mølhave, K. Monolithic Chip System with a Microfluidic Channel for *In Situ* Electron Microscopy of Liquids. Microscopy and Microanalysis 20, 445–451 (2014).

24. Petruk, A. A., Allen, C., Rivas, N. & Pichugin, K. High flow rate nanofluidics for in-liquid electron microscopy and diffraction. Nanotechnology 30, 8 (2019).

25. Merkens, S. *et al.* Quantification of reagent mixing in liquid flow cells for Liquid Phase-TEM. Ultramicroscopy 245, 113654 (2023).

26. Ottino, J. M. & Wiggins, S. Introduction: mixing in microfluidics. Philos. Trans. R. Soc. London A 362, 923–935 (2004).

27. Delplace, F. Laminar flow of Newtonian liquids in ducts of rectangular cross-section a model for both physics and mathematics. Open Access Journal of Mathematical and Theoretical Physics 1, 198–201 (2018).

28. Koo, K., Park, J., Ji, S., Toleukhanova, S. & Yuk, J. M. Liquid-Flowing Graphene Chip-Based High-Resolution Electron Microscopy. Advanced Materials 2005468, 7 (2020).

29. Nielsen, M. H., Aloni, S. & De Yoreo, J. J. In situ TEM imaging of CaCO3 nucleation reveals coexistence of direct and indirect pathways. Science (1979) 345, 1158–1162 (2014).

30. Vakili, M. *et al.* 3D Micromachined Polyimide Mixing Devices for in Situ X-ray Imaging of Solution-Based Block Copolymer Phase Transitions. *Langmuir* 35, (2019).

31. Protochips Inc. *Protochips' Guide to Poseidon E-chips Version 1.3 Copyright 2018 14.* https://academic.oup.com/toxsci/article/1676330/Table_of_Contents (2018).

32. Lu, Y. *et al.* Self-hydrogenated shell promoting photocatalytic H2 evolution on anatase TiO2. Nat Commun 9, 1–9 (2018).

33. Oliphant, T. E. Python for Scientific Computing. Comput Sci Eng 9, 10 (2007).

Figures
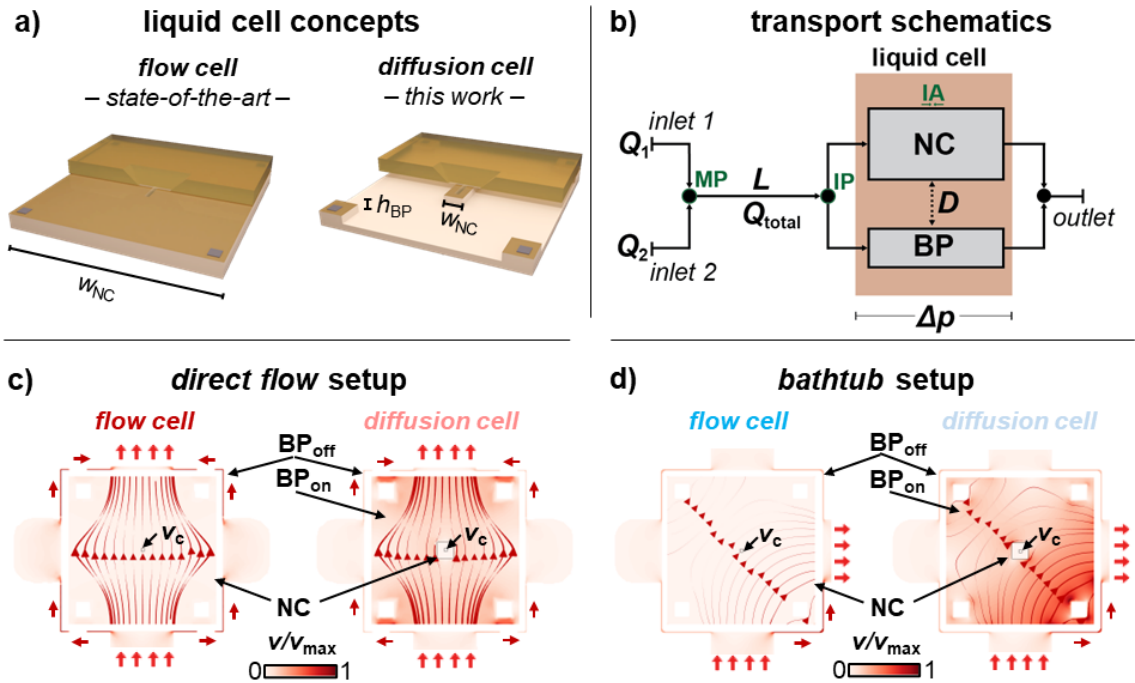
Figure 1

The Concept of *Diffusion Cells* for Liquid-Phase TEM Flow Systems. a) In *diffusion cells,* on-chip bypass channels (height, h_{BP}) are placed around a central nanochannel of drastically reduced width (w_{NC}) as compared to conventional *flow cells*. **b)** Schematic representation of mass transport in double inlet LP-TEM flow systems where Inlet 1, Inlet 2 – two inlet channels with flow rates Q_1 & Q_2; L – distance between mixing point (MP) and the interface point (IP) - entrance into the liquid flow cell (LC); NC & BP – central nanochannel where imaging is performed (IA) and micrometer-sized channel compartment bypassing the NC (on- or/and off-chip) with corresponding flow resistances R_{NC} and R_{BP}, respectively; D – diffusion transport between BP and NC; Q_{total} – total flow rate ($Q_{total} = Q_1 + Q_2$); Δp – pressure drop developed due to the flow through NC and BP. **c, d)** Flow velocity profiles in *flow* and *diffusion cells* for *direct flow* (**c**) and *bathtub* (**d**) setups, respectively. NC – central nanochannel; BP_{on} & BP_{off} – on- & off-chip bypass channels; v_c – flow velocity in the center of NC (*i.e.*, IA). Refer to for details of the simulations.
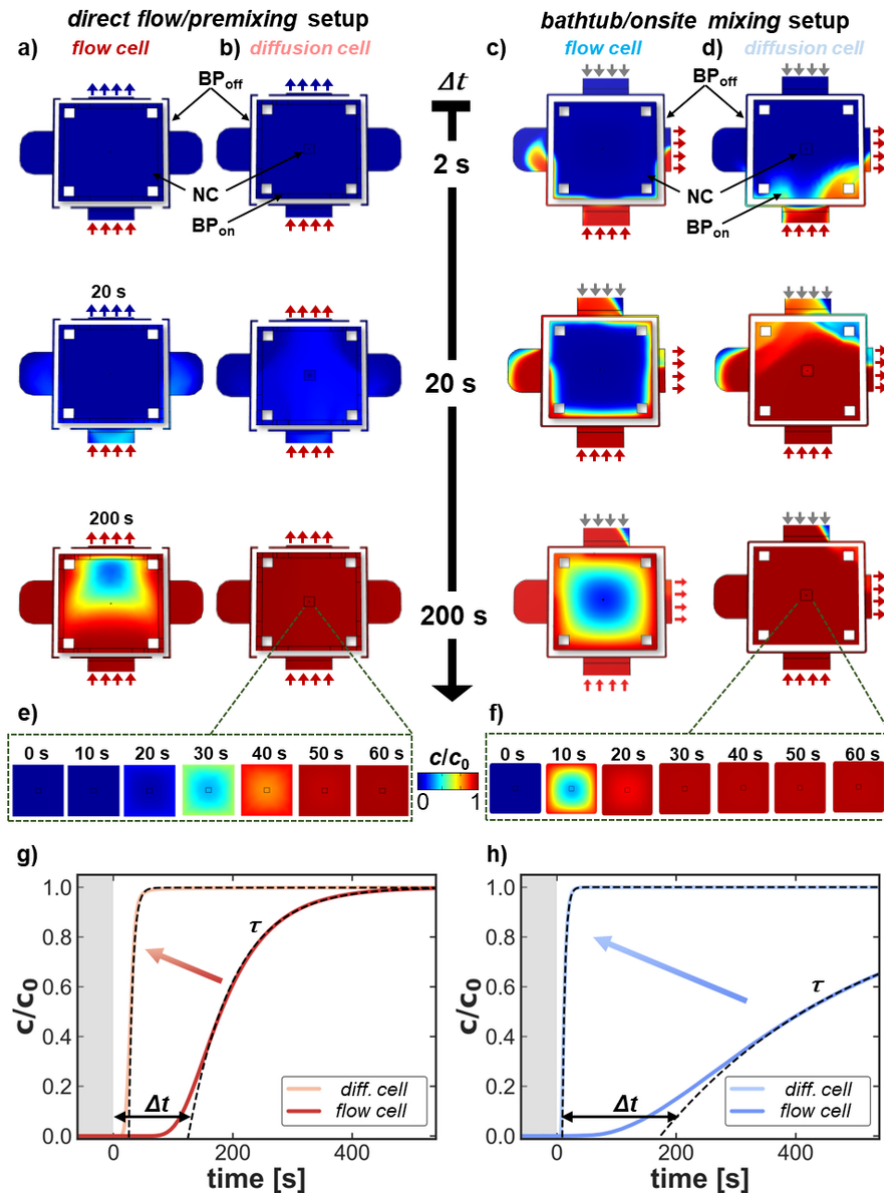
Figure 2

Accelerated Solution Replacement in LP-TEM Flow Reactors operated with *Diffusion Cells*. a -d) 2D concentration maps of the *direct flow/premixing* (**a**, **b**) and the *bathtub/onsite mixing* (**c**, **d**) setup operated with default *flow* (**a**, **c**) and *diffusion cells* (**b**, **d**) at 2, 20 and 200 s after externally initiated solution replacement. Color coding represents the degree of substitution of one solution by another after abrupt switching of the flow from one inlet to the other. The *flow cell* and the *diffusion cell* form a central

nanochannel with lateral expansion of 2 x 2 mm^2 (**a, c**) and 0.2 x 0.2 mm^2 (**b, d**), respectively. The latter is surrounded by an on-chip bypass channel of 10 µm height. **e, f)** Enlarged 2D concentration maps in the reduced central nanochannel (**b**) for the time range of strongest concentration variation for the configurations depicted in **b** and **d**, respectively. **g, h)** Time-dependent concentration curves extracted from the center of the imaged area for the four channel configurations depicted in **a-d**. *Gradient arrows* in **g** & **h** indicate accelerated solution replacement. Q_{total} and D were 300 µL/h and 6·10^{-10} m^2/s, respectively. Details of the simulation can be found elsewhere.
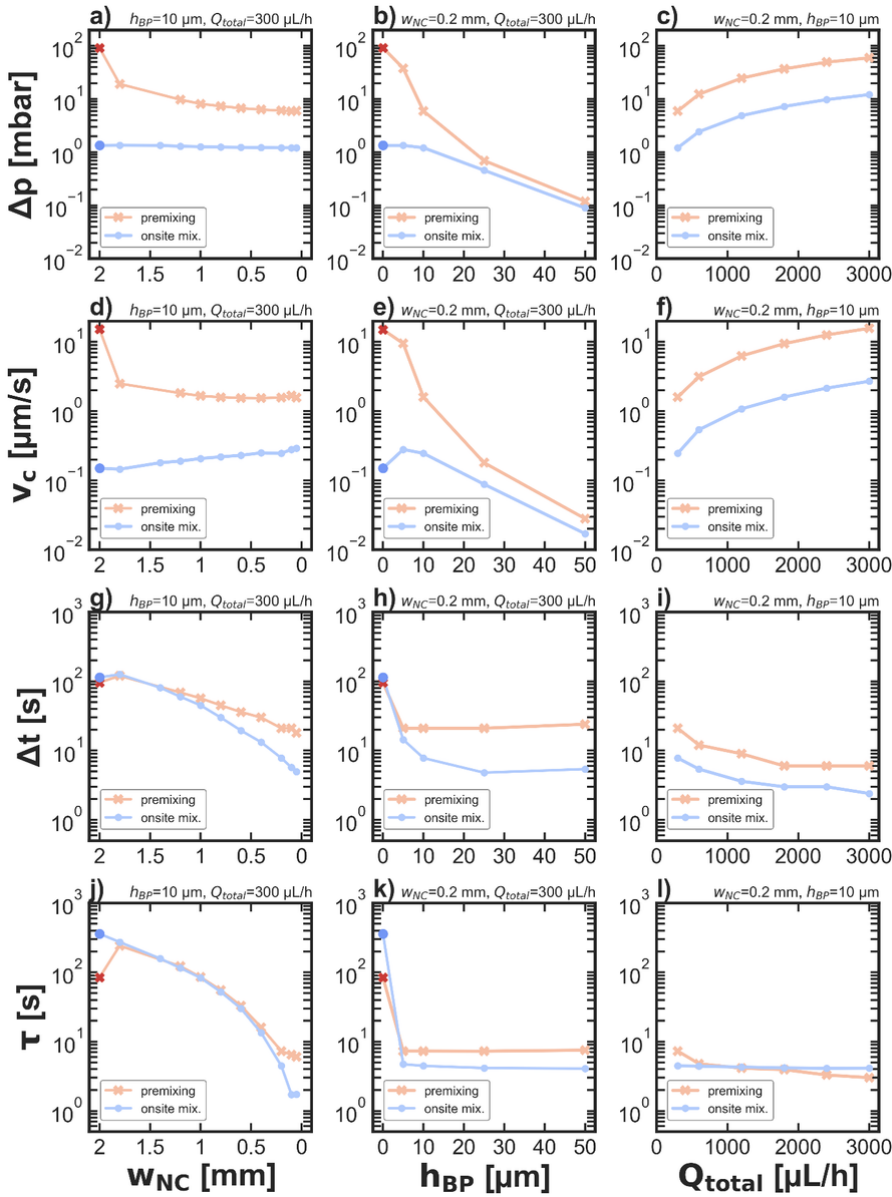
Figure 3

Virtual Prototyping of *Diffusion Cell* Geometry. The four characteristic hydrodynamic parameters, *i.e.,* the overall pressure drop, *Δp* (**a-c**), the velocity in the center of the imaged area, v_c (**d-f**), the delay, *Δt* (**g-i**), and the decay time, *τ* (**j-l**), constants of solution replacement, are depicted for *diffusion cells* operated in *direct flow/premixing* (*light red crosses*) and *bathtub/onsite mixing* (*light blue circles*) configuration, respectively. The *left column* (**a, d, g, j**) screens the width of the nanochannel for 2 mm > w_{NC} > 0.05 mm

(h_{BP} = 10 μm, Q_{total} = 300 μL/h). The *central column* (**b**, **e**, **h**, **k**) screens the height of the bypass channel for 150 nm < h_{BP} < 50 μm (w_{NC} = 0.2 mm, Q_{total} = 300 μL/h). The *right column* (**c**, **f**, **i**, **l**) screens the total flow rate for 300 μL/h < Q_{total} < 3000 μL/h (w_{NC} = 0.2 mm, h_{BP} = 10 μm). *Dark red* and *dark blue crosses* in the first two columns represent the default *flow cell* (w_{NC} = 2 mm; no BP_{on}) in *direct flow/premixing* and *bathtub/onsite mixing* configurations, respectively. The diffusion coefficient of the diffusive species was D = 6·10^{-10} m^2/s. An extended discussion of the data is provided in *Supporting Information* section 4.2.
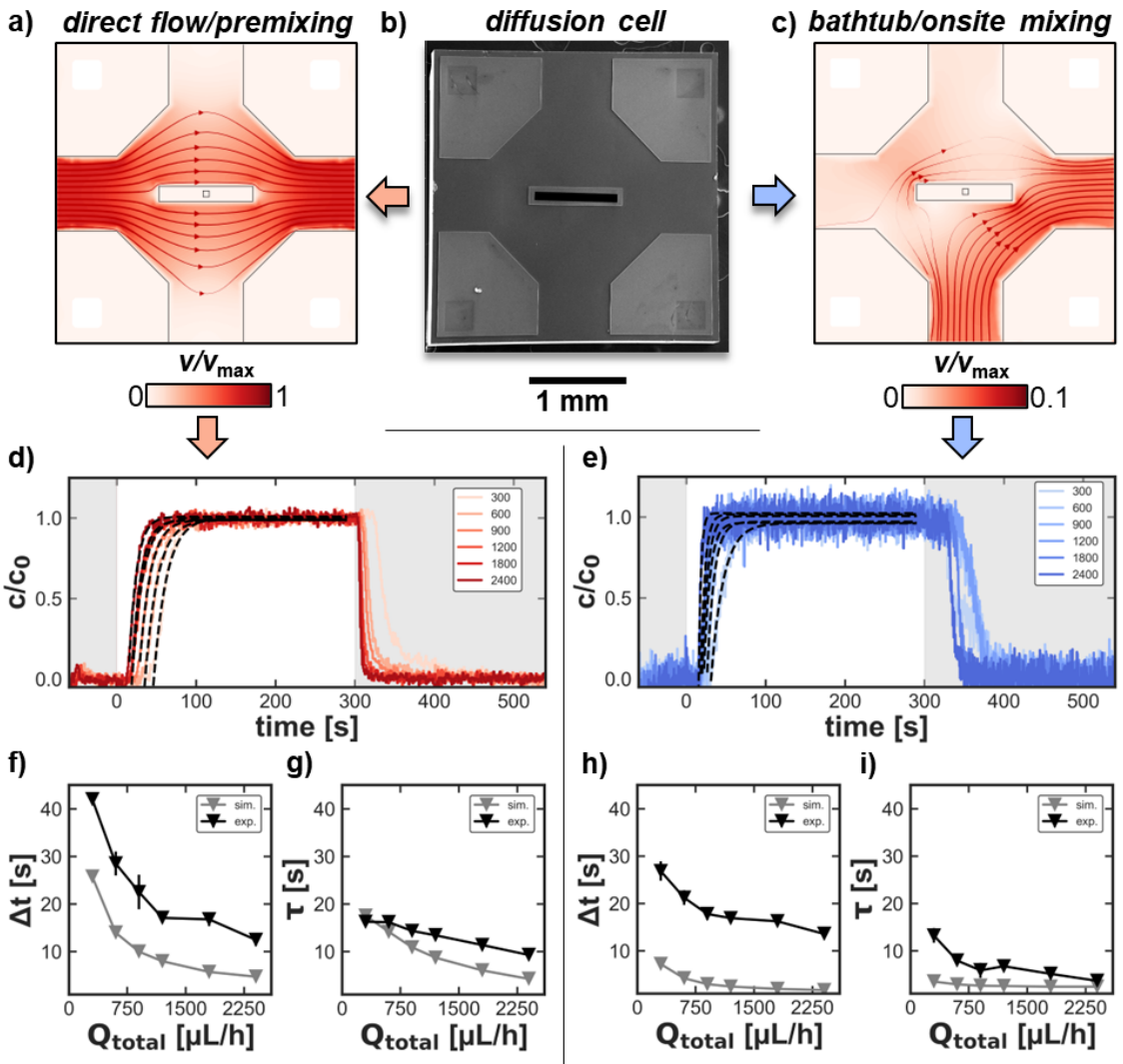

Figure 4

Experimental Quantification of Solution Replacement in *direct flow/premixing* **and** *bathtub/onsite mixing* **LP-TEM Flow Reactors operated with** *Diffusion Cells*. **a-c)** SEM image of the modified E-chip used to build *diffusion cells* (**b**) and simulated flow velocity fields illustrating transport through *direct flow/premixing* (*i.e.,* Poseidon Select) and *bathtub/onsite mixing* (*i.e.,* Poseidon 200) flow reactors, respectively. Flow is bypassing the central nanochannel where the diffusion is domination. Active inlets are at the left (**a**) and bottom (**c**) edge, respectively. *Red lines* indicate direction and *background color* and *line thickness* represent magnitude of flow velocity. For Q_{total} = 300 µL/h, the maximum velocity inside the LC is v_{max} = $7{\cdot}10^{-4}$ m/s. *Black squares* in **a** & **c** illustrate the imaging area resulting from perpendicular assembly of windows (*black rectangle* in **b**). **d, e)** Normalized curves of contrast agent concentration (*red*; phosphotungstic acid, PTA; $D_{PTA}{\sim}6{\cdot}10^{-10}$ m^2/s) reflecting solution replacement in Poseidon Select (**d**) and Poseidon 200 (**e**) setups measured at flow rates 300 < Q_{total} < 2400 µL/h. *Black dashed lines* represent exponential fits. Refer to *Methods* and previous manuscript for details on experiment and data processing. **f-i)** Simulated and experimentally measured delay times, Δt (**f**, **h**), and decay time constants, τ, (**g**, **i**) of solution replacement. In most cases, markers size exceeds error bars for experimental data in **f-i**.
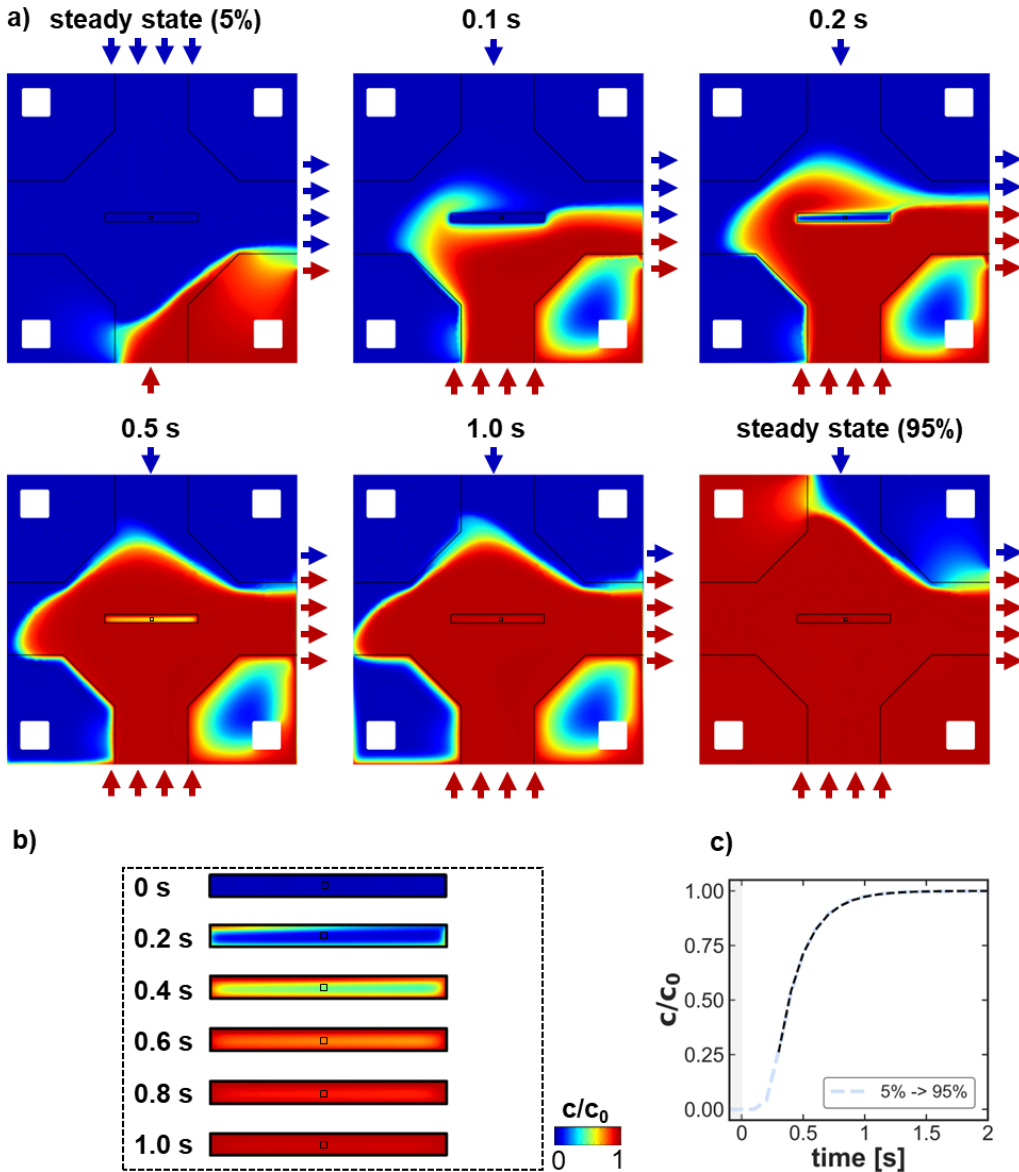
Figure 5

Sub-second solution replacement in virtual *direct flow/onsite mixing* setups operated with *diffusion cells* and under optimized experimental conditions. a) 2D concentration maps at different moments after swap of the inlets flow. $t = 0$ s represents a steady state at 0.05 flow from the bottom inlet (solute) and 0.95 flow from the top inlet (pure water); at this moment the flow has been changed to 0.95 solute solution and 0.05 of pure water, total flow Q was kept constant. The steady-state (*ss*) concentration maps for

Q_{CA} = 0.05•Q_{total} and Q_{CA} = 0.95•Q_{total} are denoted as *ss* (*5%*) and *ss* (*95%*), respectively. Q_{total} and D were 3000 μL/h and 1.3•10^{-9} m^2/s, respectively. Geometric parameters were w_{NC} = 0.05 mm, l_{NC} = 0.65 mm, h_{NC} = 150 nm (flat – no bulging assumed), h_{BP} = 50 μm, respectively. A gasket was assumed to block approximately 98% of the off-chip bypass. **b)** 2D concentration maps of the reduced central nanochannel (**a**) are depicted enlarged for the time range of the largest concentration variation. **c)** Time-dependent concentration profile (*blue curve*) in IA induced through optimized experimental methodology. Note that despite the non-zero flow at *inactive* inlets, the solute concentration varies between the two extrema, 0 and c_0 (refer to *in situ mixing* discussed in). Exponential fitting (*black dashed line*) resulted in Δt = 0.3 s and τ = 0.21 s.

Supplementary Files

This is a list of supplementary files associated with this preprint. Click to download.

- SupportingPrototypingfinal.docx

A.3 The Effect of Flow on Radiolysis

Stefan Merkens, Giuseppe De Salvo, Andrey Chuvilin, **The Effect of Flow on Radiolysis in Liquid Phase-TEM flow cells**, *Nano Express*, 3, 4, 045006, (**2023**).

The manuscript was cited as ref. [203]. It is is accessible under `https://iopscience.iop.org/article/10.1088/2632-959X/acad18`.

NANO EXPRESS

PAPER

The effect of flow on radiolysis in liquid phase-TEM flow cells

Stefan Merkens[1,2,4,*] [iD], **Giuseppe De Salvo**[1,2,4] **and Andrey Chuvilin**[3] [iD]

[1] Electron Microscopy Laboratory, CIC nanoGUNE BRTA, Tolosa Hiribidea 76, 20018 Donostia—San Sebastián, Spain
[2] Department of Physics, Euskal Herriko Unibertsitatea (UPV/EHU), 20018 Donostia—San Sebastián, Spain
[3] Ikerbasque, Basque Foundation for Science, 48013 Bilbao, Spain
[4] Equally contributing
[*] Author to whom any correspondence should be addressed.

E-mail: s.merkens@nanogune.eu

Abstract

Applying a continuous flow to rinse radiolytic species from the irradiated volume is a widely proposed strategy to reduce beam-related artefacts in Liquid-Phase Transmission Electron Microscopy (LP-TEM). However, this has not been verified either experimentally or theoretically to date. Here we explore an extended numerical model implementing radiolytic chemistry, diffusion and liquid convection to study the peculiarities of beam-induced chemistry in the presence of a flowing liquid within a heterogenously irradiated nanoconfined channel corresponding to a LP-TEM flow cell. Intriguingly, the concentration of some principal chemical species, predominantly hydrogen radicals and hydrated electrons, is found to grow significantly rather than to decrease in respect to zero-flow when moderate flow conditions are applied. This counterintuitive behaviour is discussed in terms of reactants' lifetimes, spatial separation of the reaction network and self-scavenging by secondary radiolytic species. In the presence of a flow the consumption of highly reactive species is suppressed due to removal of the self-scavengers, and as a result their concentration in the irradiated area increases. A proof of concept for the supply of scavengers by the flow is demonstrated. Unravelling the effect of flow on radiolysis spawns direct implications for LP-TEM flow experiments providing yet one more control parameter for adjusting the chemistry in the irradiated/imaging area, in particular for mitigation strategies by continuous supply of scavengers.

Introduction

Liquid-Phase TEM and radiolysis

Liquid-Phase Transmission Electron Microscopy (LP-TEM) has evolved into a convenient experimental technique for the imaging of dynamic processes (biological, chemical, electro-chemical, *etc.*) at the nano-meter scale in wet-chemical environments [1–3]. Besides the uncontested benefits, such as high spatial resolution of TEM [4], utilising electrons for imaging caused several challenges to arise [5–8]. The main issue of using high-energy electrons for imaging is the inevitable creation of radiation damage in the irradiated matter, with radiolysis of water molecules being the most relevant in LP-TEM [3].

Briefly, radiolysis describes the scission of molecules (most importantly water) upon high-energy ionizing irradiation resulting in the creation of molecular, ionic and radical species [9–12]. The latter ones are highly reactive, thus can interfere with the (bio-) chemical processes of interest [6, 13].

Since the early days of LP-TEM, radiolytic effects have been ambiguously discussed in the community: when the technique was limited to static liquid cells (LCs; e⁻-beam-transparent reservoirs entirely enclosing the sample solution, thus protecting it from the surrounding vacuum of the microscope), the e⁻-beam itself was the only (thus well-appreciated) stimulus to induce nanoscale dynamics [14–16]. With the evolution of LCs, a growing

number of stimuli (*e.g.,* temperature, electric bias, solution replacement and mixing) were incorporated thus enabling the reproduction of macroscopic (electro-)chemical experiments at the nanoscale within the TEM [17–20]. Consequently, radiolytic effects have been increasingly perceived as obstructive artefacts that require thorough consideration and mitigation [6, 20].

Strategies to account for radiolysis

The strategies developed to deal with radiolytic effects are twofold: (1) a profound theoretical understanding & description of the radiolytic processes in complex reaction media helping to explain experimental observations and (2) the mitigation of the radiolytic species in the irradiated volume and limiting their effects on physico-chemical processes under imaging [21].

The field of numeric modelling for theoretical description of radiolysis in LP-TEM was initiated predominantly by the work of Schneider and co-workers [13] who adopted existing knowledge [12] in radiation chemistry of water for TEM conditions by implementing a one-dimensional (1D) time-dependent reaction-diffusion model. The model comprises two types of species, namely primaries and secondaries, and describes the reaction kinetics in water upon continuous e⁻-beam irradiation [13]. Primaries are defined as those species predominantly generated directly by irradiation (*i.e.,* having non-zero generation cross-sections due to electron impact—*G*-values) [10], while secondaries are created through chemical reactions between primaries as well as other secondaries [13]. We refer the reader to other manuscripts for an in-depth description of both assumptions in the established radiolysis model (*e.g.,* *G*-value theory and early heterogeneous stage), and its physical background [10, 13, 22–24].

The initial model has been under continuous improvement and extension and has been adapted by several research groups aiming to better reflect the complex experimental realities. Existing implementations address aspects including the experimental parameters (*e.g.,* temperature) [7, 13, 25], geometrical considerations [26], extending the chemical reaction system (beyond pure water) [22, 27–30], spatial inhomogeneities of energy deposition due to inhomogeneities of the scattering matter [22, 26].

The development of general concepts for the mitigation of radiolytic effects is less advanced. One widely discussed concept involves additives, called scavengers, that are intentionally added to the reaction media and undergo fast reactions with the primary species decreasing their concentration [22, 31, 32]. By this means, the investigated process is expected to be less affected by radiochemistry—at least for a limited time span until the initial scavenger quantity is consumed. The main problem of this approach is that it is difficult to generalize since the peculiarities of each chemical system must be considered separately and appropriate scavengers must be found for every process individually [31, 32].

Flow in Liquid-Phase TEM

Recently, a more general approach to mitigate radiolytic species in the irradiated volume was proposed in the LP-TEM community, namely: application of flow in the liquid flow cell (LFC) for continuous renewal of the reaction media during the imaging process [7, 17, 33, 34]. To our knowledge, neither systematic experimental nor theoretical works were conducted so far to validate the approach. Thus, it remains unclear whether convective mass transport could serve for effective removal of the radiolytic species from the irradiated volume.

Various experimental LP-TEM setups supporting flow of the liquid in the imaging area are available nowadays [17, 18, 33, 35, 36]. All setups are based on microchips being allocated in the tip of a microfluidic TEM sample holder and can be categorised in two classes based on the way how the flow is directed. In the so-called 'bathtub' configuration, the microchips are immersed into an oversized flow channel and the liquid exchange in the LFC, and thus in the imaging area, is achieved mainly by diffusion [37, 38]. In the second setup which is often referred to as 'nanofluidic', all the flow is forced into the nanochannel and liquid exchange in the imaging area is dominated by convection [35, 38]. Recently it was shown that solution exchange (due to diffusion) in a 'bathtub' setup is very slow and thus can hardly be utilised for liquid replenishment in the imaging area [38]; in an ideal 'nanofluidic' configuration, however, the linear flow velocity in the nanochannel can reach 1 μm/μs (according to information provided by the manufacturer) which is promising for efficient flushing of radiolytic species [18].

In this manuscript, we theoretically evaluate the influence of liquid flow in the irradiated area on the kinetics of the radiolytic reaction network and as a result on the concentration of reactive species. For this purpose, an existing radiolysis model [13] was implemented in a finite element (FE) simulation environment and extended by the convection components. In the range of experimentally reasonable velocities, the flow was found to have counterintuitive effects on the radiolytic reaction network in the irradiated volume with intriguing implications for LP-TEM experiments.
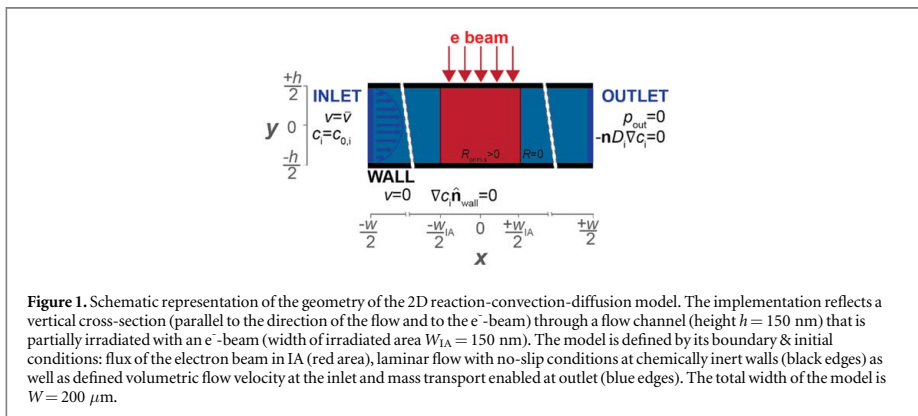
Figure 1. Schematic representation of the geometry of the 2D reaction-convection-diffusion model. The implementation reflects a vertical cross-section (parallel to the direction of the flow and to the e⁻-beam) through a flow channel (height $h = 150$ nm) that is partially irradiated with an e⁻-beam (width of irradiated area $W_{IA} = 150$ nm). The model is defined by its boundary & initial conditions: flux of the electron beam in IA (red area), laminar flow with no-slip conditions at chemically inert walls (black edges) as well as defined volumetric flow velocity at the inlet and mass transport enabled at outlet (blue edges). The total width of the model is $W = 200$ μm.

The Model

In the presented model, the well-established implementation for reaction-diffusion kinetics of radiolysis by Schneider *et al. was extended with the physics of laminar flow in 2D space* [13]. Equation 1 denotes the differential mathematical expression for calculating concentration fields, $c_i(x,y,t)$, of radiolytic species i in space, (x,y), and time, t.

$$\frac{dc_i}{dt} = \frac{\rho\psi G_i}{F} + \sum_{j,k\neq i} k_{jk} c_j c_k - \sum_j k_{ij} c_i c_j + D_i \nabla^2 c_i + \boldsymbol{v}\nabla c_i \tag{1}$$

The right-hand terms in equation 1 correspond to (1) the volumetric creation rate due to radiolysis, (2) production and (3) consumption due to chemical reactions, (4) diffusivity of a species i and (5) convection due to continuous flow. The variables ρ, ψ, G_i, F, k_{jk} & k_{ij}, D_i and $\boldsymbol{v}$ denote the density of the irradiated liquid, absorbed dose rate, generation rate of species i due to absorbed dose (note, that $G_i = 0$ for all but the 8 primary species; compare table S1 in *Supporting Information*), Faraday constant, rate constants of chemical reactions, diffusion coefficient of species i and the linear velocity of flowing liquid, respectively. ∇ and ∇^2 are 2D spatial gradient and Laplacian operators, respectively.

Geometrical description

The geometry of the model represents the nanochannel around the imaging area in the LP-TEM setup as a 2D cross-section in the plane along the flow direction and perpendicular to the beam path (refer to the *Supporting Information* section 3 and 6 for the justification of sufficiency of 2D simulations and related assumptions). All geometrical aspects of the model are defined in figure 1. The channel of length $W = 200$ μm and height $h = 150$ nm is entirely filled with water. The electron beam is uniformly and continuously irradiating the imaging area of width $W_{IA} = 150$ nm in the middle of the liquid flow cell ($x = 0$). The flow is directed from left to right at constant volumetric flow rate. The lateral extensions of the irradiated and non-irradiated sections were chosen to represent TEM-like imaging conditions and to eliminate artefacts arising from boundary conditions (see *Supporting Information* section 4 for justification).

Radiolysis and diffusion

The radiolytic creation rate of primary species (e_h^-, H˙H˙, OH˙, H₂, H₂O₂, H⁺, HO₂, OH⁻; 1ˢᵗ right-hand term in equation 1) within the irradiated region is calculated from constant non-zero G-values (≜ number of molecules created per 100 eV of absorbed energy, table S1) and an electron flux.

Upon creation, the species populate a complex chemical reaction network, that in neat water alone consists of 73 reactions and comprises 15 chemical species (8 primaries and 7 secondaries) and H₂O [13]. The reactions are implemented as a set of kinetic equations (compare table S2) considering water as a solvent with much higher constant concentration [13].

Diffusive flux is an inherent consequence of concentration gradients due to the heterogeneous irradiation. Diffusion is mathematically described by Fick's 2ⁿᵈ law (4ᵗʰ term in equation 1).

The model was first implemented in 0 (no diffusion) and 1D (heterogeneous irradiation and diffusion) and tested against the reference model [13] (see *Supporting Information* section 4), and only then combined with the physics of the flow in a 2D channel geometry.

Laminar flow

Flow of a liquid through a channel (neglecting gravitational and inertial forces) results from a pressure gradient along the flow channel and depends strongly on the internal channel geometry and applied flow conditions [39–42]. The flow type, either turbulent or laminar, can be estimated by the characteristic Reynold number, which when being below ∼2100 will indicate a laminar flow [43]. In typical microfluidic scenarios including LP-TEM cells, the Reynolds number is well below 1 [38], indicating laminar flow (see *Supporting Information* section 1 for details).

In laminar flow, the liquid travels on parallel flow lines following a pressure gradient between in- and outlet; transport between flow lines occurs by diffusion only [41, 44]. The flow velocity in the channel varies from the walls to the centre with maximum velocity at the centre and zero flow at the walls resulting from viscous forces (no-slip conditions) [39–41]. For laminar flow, the velocity profile between two infinitely long parallel plates separated by distance h is described by plane Poiseuille flow as [42]

$$\boldsymbol{v}(y) = 6\frac{Q}{h^3}\left(\left(\frac{h}{2}\right)^2 - y^2\right) = \frac{3}{2}\,\bar{v}\left(1 - \left(\frac{y}{h/2}\right)^2\right) \tag{2}$$

where h and y are as indicated in figure 1. Q is a volumetric flow rate; $\bar{v} = Q/A$ is an average flow velocity derived from the cross-section A of the flow channel. Equation 2 describes a parabolic velocity profile with the maximum flow velocity, v_{max}, in the middle of the channel equal to $3/2$ of the average velocity, $\bar{v}$. The relation between $\bar{v}$ and the experimental parameter Q can be established by 3D finite elements simulations based on the real geometry for every setup [38]. Since volumetric flow is obsolete for 2D geometry, we will focus on the more general parameter $\bar{v}$ at the inlet later in the text. Refer to *Supporting Information* section 1 for further details on fluid flow (in LP-TEM setups).

Boundary and initial conditions

The initial concentration of all species, except for H_2O, H^+ and OH^-, were zero in all domains, H^+ and OH^- concentrations corresponded to pH and pOH 7. The production rate of primary species in the IA (figure 1) was defined by corresponding G-values and an absorbed dose rate of $\psi = 7.5 \cdot 10^7 \frac{Gy}{s}$ (equivalent to 5.7 pA beam current assuming circular beam shape with the diameter W_{IA}).

The channel walls (*black lines* in figure 1) were considered impermeable and chemically inert (*i.e.,* neglecting the effect of reactive surface sites, $N_{s,i}$, on *bulk* solute concentration, $c_i = N_i/V$, which is reasonable since $N_{s,i} \ll N_i$) for all species and no interaction with the electrons of the beam were considered (*i.e.,* secondary electrons generated in the membranes were neglected which was demonstrated reasonable for materials with low electron scattering power such as SiN_x) [26]. No-slip conditions were assumed for the flow at the walls (*i.e.,* the flow velocity was zero at the walls). The flow velocity was implemented as uniform mean inflow velocity $\bar{v}$ at the inlet (*left edge* in figure 1) directed into the channel. The outlet (*right edge* on figure 1) was set as a drain for both convective and diffusive mass transport. From available literature, a reasonable $\bar{v}$ inside the nanochannel of LP-TEM flow devices was estimated to be in the range from 0 to 1 m/s [18]. Refer to the *Supporting Information* section 1 and 3 for the mathematical implementation of the model and justification of the flow velocity range.

Solving the model

The model was implemented in COMSOL Multiphysics® software and solved with a finite element method [45]. A rectangular mesh was generated, and the optimal element size (2 nm × 2 nm spatial resolution) was determined in a convergence study (refer to *Supporting Information* section 4 for details).

In this manuscript, the stationary solution of equation 1 (*i.e.,* $dc_i/dt = 0$), which reflects the chemical equilibrium of all radiolytic species under the influence of constant irradiation in IA and fluid flow, is analysed. The stationary state is achieved in the time scales of ∼1 s according to the reference 1D model [13] and the equivalent time dependent solution for the 2D in-plane model obtained in this work (*Supporting Information* section 6 for details).

Results and discussion

The steady-state spatial distribution of all radiolytic species was calculated under constant irradiation in the IA and constant flow at mean velocities ranging from 0 to 1 m/s.

Effect of flow on concentration of radiolytic species

In figure 2, obtained steady state 2D concentration fields ((**a**), (**b**), (**c**), (**d**)) are shown alongside the 1D concentration profiles (at $y = 0$; (**e**), (**f**), (**g**), (**h**)) for four representative species: chemically stable molecular hydrogen H_2 and oxygen O_2 as well as the highly reactive atomic hydrogen $H^.$ and hydrated electrons e_h^-. The
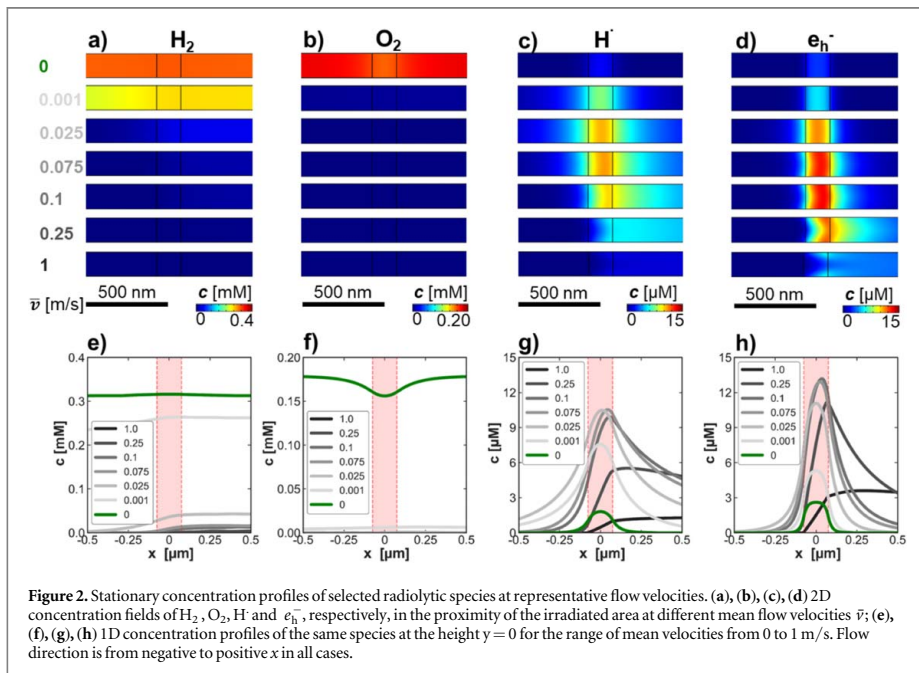
Figure 2. Stationary concentration profiles of selected radiolytic species at representative flow velocities. (**a**), (**b**), (**c**), (**d**) 2D concentration fields of H_2, O_2, H· and e_h^-, respectively, in the proximity of the irradiated area at different mean flow velocities $\bar{v}$; (**e**), (**f**), (**g**), (**h**) 1D concentration profiles of the same species at the height $y = 0$ for the range of mean velocities from 0 to 1 m/s. Flow direction is from negative to positive x in all cases.

behaviour of the concentration profiles of the species in respect to the flow is qualitatively different. H_2 concentration (figure 2(**a**), (**e**)) decreases with increasing flow velocity with a pronounced tail downstream, so this species is efficiently *washed away* from the IA already at moderate flow velocities, >0.001 m/s. Such behaviour was widely postulated in the literature [7, 17, 33, 34], however, this does not hold for all radiolytic species as is evident from the rest of the panels of figure 2. Molecular oxygen is completely *eliminated* in the proximity of IA already at minimal flow (figure 2(**b**), (**f**)), while concentration of atomic hydrogen (figure 2(**c**), (**g**)) and hydrated electrons (figure 2(**d**), (**h**)) substantially *increase* in the IA at moderate flow velocities. Only at water flow of ∼0.25 m/s the two latter species start to be rinsed effectively (compared to the zero-flow case). Concentration profiles in dependence of the flow velocity for all species can be found in figure **S11**.

Figure 3(**a**) summarises the dependence of the averaged concentration (c_{IA}) of all species in IA on flow velocity, while figure 3(**b**) shows concentrations *versus* flow velocity normalised to zero-flow values (c_{IA}/c_0). In both plots, data curves of primaries and secondaries are coloured in *shades of red* and *green*, respectively. Overall, an increase of concentration is observed for 5 species (neglecting those with concentration below 10^{-4} mM): atomic hydrogen H·, hydrated electrons e_h^-, protons H^+, hydroxyl ions OH^- and hydroxyl radicals OH·. The most significant increase is observed for H· and e_h^- (6 and 5 times respectively), while the concentrations of H^+, OH^- and OH·H· increase by 15%–30%.

Changes in the concentration start at 10^{-5} m/s and develop differently for different species with increasing velocity. All species experiencing significant increase of concentration are primaries, *i.e.*, those with non-zero *G*-values. It is interesting to note that concentrations of H^+ and OH^- do not change synchronously, pointing to the possibility of controlling acidity in the IA by flow velocity. As it was pointed out recently [46], H^+ and OH^- are out of equilibrium if water is irradiated, so radiolytic acidity π^* should be used instead of *p*H. Dependence of this value on the flow velocity is provided in *Supporting Information* section 5.

**Analysis of concentration increase**
Assuming that the production rate of H· and e_h^- in chemical reactions is relatively low as compared to radiolytic generation rate, the increase of concentration for the above discussed primary species is caused mostly by the decrease of the consumption rate. This decrease in consumption is the consequence of a reduced concentration of secondary reactants involved in the consumption reactions.

A potential reasoning to explain the increase of steady state concentration of certain species with an increase of flow velocity may be referred to as 'spatial reaction network separation'. In the presence of a flow, the spatio-temporal evolution of reaction networks is altered in respect to zero flow. Chemical reactions, which in the absence of the flow would occur at one and the same location inside the irradiated region (*i.e.*, in the IA), are

Figure 3. Average concentrations of radiolytic species in the IA in dependence of the flow velocity. Primary species are coloured in shades of red, secondary species are coloured in shades of green. Data points shown at 10^{-9} m/s on a log-scale corresponds to actual zero-flow simulation. (**a**) Raw averaged concentrations, c_{IA}, in the log-log-scale. (**b**) Concentrations in log-linear coordinates normalised to zero flow values, c_{IA}/c_0.

taking place *while* the solution is traveling along the channel once flow is present. The reaction time (Δt) of the occurring chemical reactions is transformed onto the lateral spatial axis (Δx) parallel to the flow [44]. The velocity, v, can be perceived as the conversion factor: $\Delta x = v \cdot \Delta t$ [44]. Thus, the slower the reaction, the further away on x-axis (on average) it will take place. At the same time, radiolytic generation of the primary

Figure 4. Comparison of the average lifetime, τ, of the species in the IA with the travel time of the flow through IA. The curves' colour scheme is the same as for figure 3. Note constant lifetimes for HO_2^- and O^- which are consumed only by first order reactions.
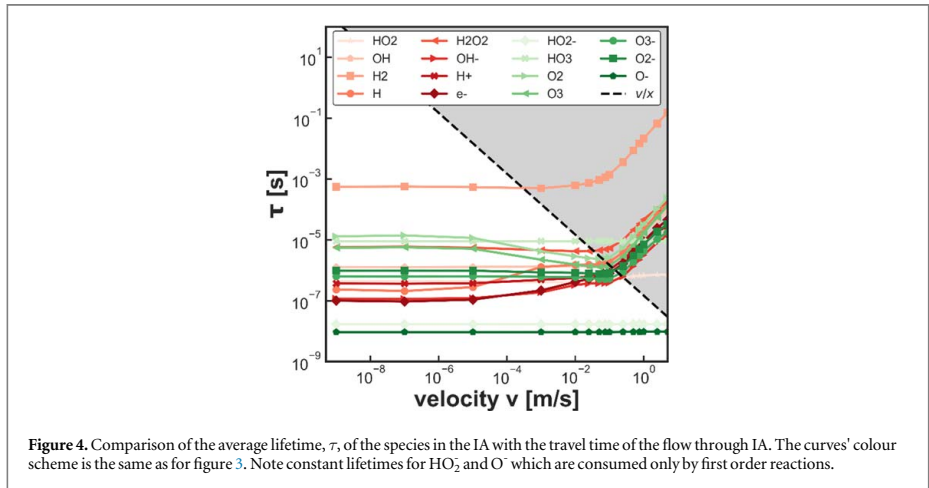
species is not affected by the flow and takes place within the IA only. Generation and consumption reactions may thus be separated spatially leading to an increase of the concentration of primaries in the IA.

To validate this scenario, one would need to compare the *lifetime*, τ, of the species to the travel time, Δt, of the liquid through IA: $\Delta t = W_{IA}/\bar{v}$. If $\tau_i > \Delta t$, the species has time to be rinsed from the IA and participates in the reaction network downstream; if $\tau_i < \Delta t$, this species will react inside the IA. Lifetimes of the species may be defined as the time necessary to decrease its concentration to zero assuming zero order consumption reaction:

$$\tau_i = \frac{c_i}{R_i^{cons}} \tag{3}$$

where R_i^{cons} is a sum of consumption rates for species i ($\hat{=}$ 3rd right-hand term of equation 1). It should be noted that equation 3 is equivalent to the definition of the half-life time for the zero, first and second order reactions up to the constant coefficient ½ for zero and ln2 for the 1st order reactions (see *Supporting Information* section 2 for detailed discussion) [47, 48].

Figure 4 shows the lifetime, τ_i, averaged over IA for all species in comparison to the solutions' travel time, Δt, through IA. The data is obtained following equation 3 from the steady state reaction rates and concentrations averaged over the IA (compare figure S11 and S15 in *Supporting Information* section 5 for illustrative representation). For all species, except H_2, the lifetime starts to exceed the travel time in the flow velocity range 0.01-0.1 m/s, *i.e.*, the spatial reaction network separation starts being effective above these velocities. However, an increase of concentrations of $H^{\cdot}$ and e_h^- has already onset at flow velocities as low as 10^{-5} m/s, where lifetimes are a few orders of magnitude lower than the travel time, *i.e.,* the reaction network is not disturbed at these velocities. Thus, another mechanism is likely to cause the drop in consumption of $H^{\cdot}$ and e_h^- in the flow velocity range from 10^{-5} to 10^{-2} m/s.

As can be seen from zero flow concentration profiles in figure S11, constant, *i.e.*, non-zero, steady state concentrations in the proximity of the IA are established for several species, namely H_2O_2, H_2, O_2, O_3 and O_2^-. These occur despite the opened boundary conditions at the edges of the model, *i.e.*, the diffusion of secondary products out of it. From our time dependent simulations and the work of Schneider *et al.* [13] follows that this steady state is established within units of seconds even for a 200 μm large model (see *Supporting Information* figure S21) and much faster for smaller closed volumes with limited outward-diffusion (steady state in the absence of diffusion occurs within ∼1 ms) [13]. It is interesting to compare qualitatively the diffusion fluxes of the species in the steady state at zero flow (see *Supporting Information* figure S10). Most of the species diffuse out of the IA, meaning that they are generated there in excess with respect to the surrounding. Only H_2O_2 and O_2 diffuse back towards the IA, indicating that they are preferentially generated in excess outside the IA and are consumed inside the IA. The fastest consumption reactions for H_2O_2 and O_2 are the reactions #20, #23, #36, #37 with $H^{\cdot}$ and e_h^- (see table S2 for the indices of reactions). In turn, the fastest consumption reaction for $H^{\cdot}$ is reaction #37 with O_2, while e_h^- is primarily consumed in reaction #20 with H_2O_2. Thus, the reason for the high consumption rate of $H^{\cdot}$ and e_h^- at zero flow is by reactions with H_2O_2 and O_2 which accumulated at high concentrations due to the limited (outward) diffusion.

When applying flow, the concentration of accumulated species dramatically drops at flow velocities as small as 10^{-5} m/s (see figure 3(**a**)), because even the minimal flow outperforms the diffusional mass transport, and the

Figure 5. Stationary concentration profiles of O_2 and $H \cdot H \cdot$ at representative velocities of the flow of water with 0.18 mM of dissolved O_2. Note, that zero flow concentration figures are from figure 2 for comparison. (**a**), (**b**) 2D concentration fields of O_2 and $H \cdot$ in the proximity of the irradiated area; (**c**), (**d**) 1D concentration profiles of the same species at the height $y = 0$ (at maximum flow velocity). Flow direction is from negative to positive x in all cases.

species are flushed away from the liquid flow cell and cannot accumulate. This leads to a substantial suppression of reactions #36, #37, #20, #23 and as a result to the growth of concentrations of $H \cdot$ and e_h^- in the IA.

It is peculiar to note, that such a trend has been evidenced already by Schneider *et al* [13] (see *e.g.,* figure 3 in referenced manuscript), who reported a high concentration of primaries at the timescales of 10^{-5} s after irradiation started, which decreased later, when the concentration of secondaries (and thus consumption reaction rates) increased.

To validate this scenario, simulations for the flow of aerated water with dissolved O_2 at a concentration corresponding to the steady-state value of the initial simulation at zero flow (0.18 mM) were performed. Figure 5 shows the steady-state concentrations of O_2 and $H \cdot$ in the presence of such flow (compare to figure 2(**b**), (**c**); the colour range is the same on both figures). A straightforward consequence of the presence of O_2 in water is the almost complete suppression of the $H \cdot$ concentration increase. Moreover, an expected drop of O_2 concentration is observed downstream upon passing through the IA, confirming O_2 consumption in the IA. At 0.001 m/s diffusion still plays a role in the mass transport and is affecting the solution upstream.

It should be noted here that scavenging is a selective process. Thus, decrease in $H \cdot$ and e_h^- concentrations by flowing O_2-saturated water is accompanied by the increase of concentrations of H^+, HO_2 and O_2^- (compare figure **S17**). In turn, application of H_2O_2 flow (figure **S14**) suppresses more efficiently e_h^- than $H \cdot H \cdot$ as compared to O_2 (see figure **S17** and **S18**).

General remarks

Our numeric study shows that radiolysis is represented by a complex and mutable reaction network and its steady state strongly depends not only on the dose rate as was pointed out previously [13], but also on the mass transport in the system. In the analysis of distinct irradiation scenarios, not only the dose rate and reaction set should be considered, but also a complete geometrical representation of the experiment defining the spatial distribution of the reactants.

The simulations show that accumulation of such species as O_2 and H_2O_2 in the liquid cell due to limited mass transport (*e.g.,* static cell) leads to a self-scavenging of highly reactive atomic hydrogen and hydrated electrons. In this respect, the main action of the flow is the suppression of the accumulation of *self-scavengers*,

which in turn leads to a substantial increase in concentration of the reactive radiolytic species in the IA when a pure water flow is applied.

As is illustrated by figure 4 the concept of 'flushing away' radiolytic species does not seem to work in a straightforward way. In TEM-like irradiation scenarios, the lifetime of all species in the IA is much shorter than the travel time of the solution through the IA for moderate flow velocities and thus the reaction network in the IA is not spatially disturbed—all the species have time to react at the place where they were generated. Spatial separation of the reaction network can be efficiently achieved only at linear flow velocities exceeding 0.1 m/s.

However, the flow can be used for the efficient supply of scavengers. Figure 5 shows that a continuous supply of O_2 at the zero-flow steady-state concentration upon application of the flow efficiently prevents an increase of $H^.$ concentration (figure 2). Moreover, if an O_2-saturated water solution (at 1.22 mM obtained at 1 bar pure O_2 pressure) [49] is supplied, the concentration of $H^.$ in the IA can be reduced by a factor of ~5 (see *Supporting Information* section 5; figure **S13** and **S17**) as compared to the zero-flow case. It should be noted that O_2, while providing a proof of concept for the applicability of flow-supplied scavenging, is not acting as a universal scavenger as it causes an increase of the concentration of several species (see *Supporting Information* figure **S17** and **S18**). More targeted and more efficient scavenging reagents may be found for specific applications. We would like to arbitrarily point out here that the implementation of any experimental methodology utilizing flow strongly relies on the immobilisation of nano-objects on the membrane [1].

The results of this work confirm observations already made by Schneider *et al* [13]. An approximately 5-fold increase of the $H^.$ H concentration between homogeneous (equivalent to a confined cell without outward diffusion) and heterogeneous (diffusion exhaust of the irradiated area) models was evidenced and back-diffusion of *self-scavengers, e.g.*, O_2, into the irradiated area was illustrated [13].

Conclusions

The influence of the flow on the radiolytic reaction network in the liquid cell of LP-TEM setups was studied by finite-elements simulation. A reaction diffusion model for radiolysis was extended with the physics of laminar flow in a sub-μm channel and the steady state concentration profiles of the radiolytic species upon e^--beam irradiation were calculated for a range of experimentally realistic liquid flow velocities.

A strong increase of the reactive radiolytic species $H^.$ H and e_h^- was observed in the IA upon application of the flow of pure water ($pH = pOH = 7$). This increase is attributed to the removal of *self-scavenging* species, *i.e.*, O_2 and H_2O_2, by the flow which would otherwise excessively accumulate in the whole volume of the liquid cell, diffuse back into the IA and support high consumption rates of $H H^.$ and e_h^-.

By analysis of the reactants' lifetimes, it was demonstrated that up to a 0.1 m/s linear flow velocity, the reaction network is not spatially disturbed and thus the concept of *flushing away* reactive species from the IA may not be straight forward. The main effect of the flow is thus considered as preventing the accumulation of reactants in the whole liquid cell.

It was further demonstrated that flow can be exploited for continuous supply of scavengers by showcasing the efficient scavenging of $H^.$ H by an O_2-saturated water flow. Contrary to the closed liquid cells where scavengers are to be consumed within seconds, flow setups can provide scavenging at long experimental timescales.

Acknowledgments

Data availability statement

The data generated and/or analysed during the current study are not publicly available for legal/ethical reasons but are available from the corresponding author on reasonable request.

ORCID iDs

Stefan Merkens ⓘ https://orcid.org/0000-0001-5635-8659
Andrey Chuvilin ⓘ https://orcid.org/0000-0002-3712-5638

References

[1] Klein K L, Anderson I M and de Jonge N 2011 Transmission electron microscopy with a liquid flow cell *J. Microsc.* **242** 117–23

[2] Jonge N de and Ross F M 2011 Electron microscopy of specimens in liquid *Nat. Nanotechnol.* **6** 695–704

[3] Ross F M 2016 *Liquid Cell Electron Microscopy* (Cambridge: Cambridge University Press) vol. 1 (https://doi.org/10.1017/9781316337455)

[4] Hauwiller M R *et al* 2019 Gold nanocrystal etching as a means of probing the dynamic chemical environment in graphene liquid cell electron microscopy *J. Am. Chem. Soc.* **141** 4428–37

[5] Abellan P *et al* 2014 Factors influencing quantitative liquid (scanning) transmission electron microscopy *Chem. Commun.* **50** 4873–80

[6] Ou Z, Liu C, Yao L and Chen Q 2020 Nanoscale Cinematography of Soft Matter System under Liquid- Phase TEM *Accounts of Material Research* **1** 41–52

[7] Fritsch B *et al* 2021 Accessing local electron-beam induced temperature changes during *in situ* liquid-phase transmission electron microscopy *Nanoscale Adv* **3** 2466–74

[8] Dissanayake T U, Wang M and Woehl T J 2021 Revealing reactions between the electron beam and nanoparticle capping ligands with correlative fluorescence and liquid-phase electron microscopy *ACS Appl. Mater. Interfaces* **13** 37553–62

[9] le Caër S W 2011 Radiolysis: influence of oxide surfaces on H_2 production under ionizing radiation *Water (Basel)* **3** 235–53

[10] Hill M A and Smith F A 1994 Calculation of initial and primary yields in the radiolysis of water *Radiat. Phys. Chem.* **43** 265–80

[11] Elliot A J and Bartels D M 2009 *The reaction Set, rate constants and g-values for the simulation of the radiolysis of light water over the range 20 deg to 350 deg C based on information available in 2008* (AECL–153-127160-450-001) Atomic Energy of Canada Limited 162

[12] Elliot A J and McCracken D R 1990 Computer modelling of the radiolysis in an aqueous lithium salt blanket: Suppression of radiolysis by addition of hydrogen *Fusion Eng. Des.* **13** 21–7

[13] Schneider N M *et al* 2014 Electron-water interactions and implications for liquid cell electron microscopy *J. Phys. Chem. C* **118** 22373–82

[14] Park J H *et al* 2015 Control of electron beam-induced Au nanocrystal growth kinetics through solution chemistry *Nano Lett.* **15** 5314–20

[15] Hermannsdörfer J, de Jonge N and Verch A 2015 Electron beam induced chemistry of gold nanoparticles in saline solution *Chem. Commun.* **51** 16393–6

[16] Zheng K *et al* 2010 Electron-beam-assisted superplastic shaping of nanoscale amorphous silica *Nat. Commun.* **1** 1–8

[17] Beker A F *et al* 2020 *In situ* electrochemistry inside the TEM with controlled mass transport *Nanoscale* **13** 22192–22201

[18] van Omme J T *et al* 2020 Liquid phase transmission electron microscopy with flow and temperature control *J. Mater. Chem. C* **8** 10781–90

[19] Fahrenkrug E, Alsem D H, Salmon N and Maldonado S 2017 Electrochemical measurements in *In Situ* TEM Experiments *J. Electrochem. Soc.* **164** H358–64

[20] Kashin A S and Ananikov V P 2019 Monitoring chemical reactions in liquid media using electron microscopy *Nat Rev Chem* **3** 624–37

[21] Woehl T J *et al* 2013 Experimental procedures to mitigate electron beam induced artifacts during *in situ* fluid imaging of nanomaterials *Ultramicroscopy* **127** 53–63

[22] Korpanty J, Parent L R and Gianneschi N C 2021 Enhancing and mitigating radiolytic damage to soft matter in aqueous phase liquid-cell transmission electron microscopy in the presence of gold nanoparticle sensitizers or isopropanol scavengers *Nano Lett.* **21** 1141–9

[23] Mozunder A and Magee J L 1966 Model of tracks of ionizing radiation reaction mechanisms *Radiat. Res.* **28** 203–14

[24] Buxton G V, Greenstock C L, Helman W P, Ross A B and Tsang W 1988 Critical review of rate constants for reactions of hydrated electrons, hydrogen atoms and hydroxyl radicals in aqueous solution *J. Phys. Chem. Ref. Data* **17** 513

[25] Ambrožič B *et al* 2019 Controlling the radical-induced redox chemistry inside a liquid-cell TEM *Chem. Sci.* **10** 8735–43

[26] Gupta T, Schneider N M, Park J H, Steingart D and Ross F M 2018 Spatially dependent dose rate in liquid cell transmission electron microscopy *Nanoscale* **10** 7702–10

[27] Hutzler A *et al* 2018 Unravelling the mechanisms of gold–silver core–shell nanostructure formation by *in Situ* TEM using an advanced liquid cell design *Nano Lett.* **18** 7222–9

[28] Crook M F *et al* 2021 Elucidating the role of halides and iron during radiolysis-driven oxidative etching of gold nanocrystals using liquid cell transmission electron microscopy and pulse radiolysis *J. Am. Chem. Soc.* **143** 11703–13

[29] Wang M, Park C and Woehl T J 2018 Quantifying the nucleation and growth kinetics of electron beam nanochemistry with liquid cell scanning transmission electron microscopy *Chem. Mater.* **30** 7727–36

[30] Fritsch B *et al* 2022 Evolution of gold nanostructures model verification by scale bridging *In Situ* liquid-phase transmission electron microscopy and x-ray diffraction *Adv. Sci.* **9** 2202803

[31] Woehl T J and Abellan P 2016 Defining the radiation chemistry during liquid cell electron microscopy to enable visualization of nanomaterial growth and degradation dynamics *J. Microsc.* **265** 135–47

[32] Cho H *et al* 2017 The use of graphene and its derivatives for liquid-phase transmission electron microscopy of radiation-sensitive specimens *Nano Lett.* **17** 414–20

[33] Koo K, Park J, Ji S, Toleukhanova S and Yuk J M 2020 olution electron microscopy *Adv. Mater.* **33** 2005468

[34] Pu S, Gong C and Robertson A W 2020 Liquid cell transmission electron microscopy and its applications *R Soc Open Sci* **7** 191204

[35] Petruk A A, Allen C, Rivas N and Pichugin K 2019 High flow rate nanofluidics for in-liquid electron microscopy and diffraction *Nanotechnol.* **30** 395703

[36] Dunn G *et al* 2020 Graphene-sealed flow cells for In Situ transmission electron microscopy of liquid samples *ACS Nano* **14** 9637–43

[37] Cheng N, Sun H, Beker A F, Omme J T *et al* 2022 van. Nanoscale visualization of metallic electrodeposition in a well-controlled chemical environment *Nanotechnology* **33** 445702

[38] Merkens S 2023 Quantification of reagent mixing in liquid flow cells for Liquid Phase-TEM *Ultramicroscopy* **245** 113654

[39] Colinsk A 2007 *Introduction to Microfluidics* (Oxford: Oxford University Press)

[40] Squires T M and Quake S R 2005 Microfluidics: fluid physics at the nanoliter scale *Rev. Mod. Phys.* **77** 977–1026

[41] Ottino J M and Wiggins S 2004 Introduction: mixing in microfluidics *Philos. Trans. R. Soc. London A* **362** 923–35

[42] Delplace F 2018 Laminar flow of Newtonian liquids in ducts of rectangular cross-section a model for both physics and mathematics *Open Access J. Math. Theor. Phys.* **1** 198–201

[43] Pozrikidis C 2002 *Fluid dynamics - Theory, Computation and Numeric Simulation. Hydrocarbon Engineering* (New York: Springer) 2nd edn (https://doi.org/10.1007/978-0-387-95871-2)

[44] Vakili M *et al* 2019 3D micromachined polyimide mixing devices for *in situ* x-ray imaging of solution-based block copolymer phase transitions *Langmuir* **35** 10435–445

[45] COMSOL Multiphysics v. 5.3. COMSOL AB, Stockholm, Sweden (www.comsol.com)

[46] Fritsch B *et al* 2022 Tailoring the acidity of liquid media with ionizing radiation - rethinking the acid-base correlation beyond pH arXiv: 2209.05331

[47] IUPAC 1997 *Compendium of Chemical Terminology.* ed A D D McNaught and A Wilkinson (Oxford: Blackwell Scientific Publication) 2nd edn (the "Gold Book") (https://doi.org/10.1351/goldbook)

[48] Atkins P W, de Paula J and Keeler J 2017 *Atkins' Physical Chemistry.* (London: Oxford University Press) 11th edn

[49] National Institute of Standards and Technology 2021 NIST Chemistry WebBook, SRD 69 - Oxygen (https://webbook.nist.gov/cgi/cbook.cgi?ID=C7782447&Mask=10#Refs)

Appendix B

Radiolysis Model

Table B.1: G-values for 300 keV-electron irradiation of liquid water from Hill & Smith.[78]

Species	G value (molecules/100 eV)
e_h^-	3.47
H^*	1.00
H_2	0.17
OH^*	3.63
H_2O_2	0.47
HO_2	0.08
H^+	4.42
OH^-	0.95

Table B.2: Implemented reactions and rate constants of the radiolysis model for water.

#	reaction	rate constant $k_\#$ (25°C)	unit
1	$H^+ + OH^- \rightarrow H_2O$	1.40E+11	$M^{-1}s^{-1}$
2	$H_2O \rightarrow H^+ + OH^-$	1.40E-03	s^{-1}
3	$H_2O_2 \rightarrow H^+ + HO_2^-$	5.00E+10	$M^{-1}s^{-1}$
4	$H^+ + HO_2^- \rightarrow H_2O_2$	1.12E-01	s^{-1}
5	$H_2O_2 + OH^- \rightarrow HO_2^- + H_2O$	1.30E+10	$M^{-1}s^{-1}$
6	$HO_2^- + H_2O \rightarrow H_2O_2 + OH^-$	5.82E+07	$M^{-1}s^{-1}$
7	$e_h^- + H_2O \rightarrow H + OH^-$	1.90E+01	$M^{-1}s^{-1}$
8	$H + OH^- \rightarrow e_h^- + H_2O$	2.20E+07	$M^{-1}s^{-1}$
9	$e_h^- + H^+ \rightarrow H$	2.30E+10	$M^{-1}s^{-1}$
10	$H \rightarrow e_h^- + H^+$	3.91	s^{-1}
11	$OH + OH^- \rightarrow H_2O + O^-$	1.30E+10	$M^{-1}s^{-1}$
12	$O- + H_2O \rightarrow OH + OH^-$	1.04E+08	$M^{-1}s^{-1}$
13	$O- + H^+ \rightarrow OH$	1.00E+11	$M^{-1}s^{-1}$
14	$OH \rightarrow O^- + H^+$	1.26E-01	s^{-1}
15	$O_2^- + H^+ \rightarrow HO_2$	5.00E+10	$M^{-1}s^{-1}$
16	$HO_2 \rightarrow O_2^- + H^+$	1.35E+06	s^{-1}
17	$HO_2 + OH^- \rightarrow O_2^- + H_2O$	5.00E+10	$M^{-1}s^{-1}$
18	$O_2^- + H_2O \rightarrow HO_2 + OH^-$	1.86E+01	$M^{-1}s^{-1}$
19	$e_h^- + OH \rightarrow OH^-$	3.00E+10	$M^{-1}s^{-1}$
20	$e_h^- + H_2O_2 \rightarrow OH + OH^-$	1.10E+10	$M^{-1}s^{-1}$
21	$e_h^- + O_2^- + H_2O \rightarrow HO_2^- + OH^-$	1.30E+10	$M^{-2}s^{-1}$
22	$e_h^- + HO_2 \rightarrow HO_2^-$	2.00E+10	$M^{-1}s^{-1}$
23	$e_h^- + O_2 \rightarrow O_2^-$	1.90E+10	$M^{-1}s^{-1}$
24	$e_h^- + e_h^- + 2\,H_2O \rightarrow H_2 + 2\,OH^-$	5.50E+09	$M^{-3}s^{-1}$
25	$e_h^- + H + H_2O \rightarrow H_2 + OH^-$	2.50E+10	$M^{-2}s^{-1}$
26	$e_h^- + HO_2^- \rightarrow O^- + OH^-$	3.50E+09	$M^{-1}s^{-1}$
27	$e_h^- + O^- + H_2O \rightarrow OH^- + OH^-$	2.20E+10	$M^{-2}s^{-1}$
28	$e_h^- + O_3^- + H_2O \rightarrow OH^- + OH^- + O_2$	1.60E+10	$M^{-2}s^{-1}$
29	$e_h^- + O_3 \rightarrow O_3^-$	3.60E+10	$M^{-1}s^{-1}$
30	$H + H_2O \rightarrow H_2 + OH$	1.10E+01	$M^{-1}s^{-1}$

(Continued on next page)

#	reaction	rate constant $k_{\#}$ (25°C)	unit
31	$H + O^- \rightarrow OH^-$	1.00E+10	$M^{-1}s^{-1}$
32	$H + HO_2^- \rightarrow OH + OH^-$	9.00E+07	$M^{-1}s^{-1}$
33	$H + O_3^- \rightarrow OH^- + O_2$	1.00E+10	$M^{-1}s^{-1}$
34	$H + H \rightarrow H_2$	7.80E+09	$M^{-1}s^{-1}$
35	$H + OH \rightarrow H_2O$	7.00E+09	$M^{-1}s^{-1}$
36	$H + H_2O_2 \rightarrow OH + H_2O$	9.00E+07	$M^{-1}s^{-1}$
37	$H + O_2 \rightarrow HO_2$	2.10E+10	$M^{-1}s^{-1}$
38	$H + HO_2 \rightarrow H_2O_2$	1.80E+10	$M^{-1}s^{-1}$
39	$H + O_2^- \rightarrow HO_2^-$	1.80E+10	$M^{-1}s^{-1}$
40	$H + O_3 \rightarrow HO_3$	3.80E+10	$M^{-1}s^{-1}$
41	$OH + OH \rightarrow H_2O_2$	3.60E+09	$M^{-1}s^{-1}$
42	$OH + HO_2 \rightarrow H_2O + O_2$	6.00E+09	$M^{-1}s^{-1}$
43	$OH + O_2^- \rightarrow OH^- + O_2$	8.20E+09	$M^{-1}s^{-1}$
44	$OH + H_2 \rightarrow H + H_2O$	4.30E+07	$M^{-1}s^{-1}$
45	$OH + H_2O_2 \rightarrow HO_2 + H_2O$	2.70E+07	$M^{-1}s^{-1}$
46	$OH + O- \rightarrow HO_2^-$	2.50E+10	$M^{-1}s^{-1}$
47	$OH + HO_2^- \rightarrow HO_2 + OH^-$	7.50E+09	$M^{-1}s^{-1}$
48	$OH + O_3^- \rightarrow O_3 + OH^-$	2.60E+09	$M^{-1}s^{-1}$
49	$OH + O_3^- \rightarrow O_2 + O_2 + H^+$	6.00E+09	$M^{-1}s^{-1}$
50	$OH + O_3 \rightarrow HO_2 + O_2$	1.10E+08	$M^{-1}s^{-1}$
51	$HO_2 + O_2^- \rightarrow HO_2^- + O_2$	8.00E+07	$M^{-1}s^{-1}$
52	$HO_2 + HO_2 \rightarrow H_2O_2 + O_2$	7.00E+05	$M^{-1}s^{-1}$
53	$HO_2 + O^- \rightarrow O_2 + OH^-$	6.00E+09	$M^{-1}s^{-1}$
54	$HO_2 + H_2O_2 \rightarrow OH + O_2 + H_2O$	5.00E-01	$M^{-1}s^{-1}$
55	$HO_2 + HO_2^- \rightarrow OH + O_2 + OH^-$	5.00E-01	$M^{-1}s^{-1}$
56	$HO_2 + O_3^- \rightarrow O_2 + O_2 + OH^-$	6.00E+09	$M^{-1}s^{-1}$
57	$HO_2 + O_3 \rightarrow HO_3 + O_2$	5.00E+08	$M^{-1}s^{-1}$
58	$O_2^- + O_2^- + 2H_2O \rightarrow H_2O_2 + O_2 + 2OH^-$	1.00E+02	$M^{-1}s^{-1}$
59	$O_2^- + O^- + H_2O \rightarrow O_2 + 2OH^-$	6.00E+08	$M^{-1}s^{-1}$
60	$O_2^- + H_2O_2 \rightarrow OH + O_2 + OH^-$	1.30E-01	$M^{-1}s^{-1}$
61	$O_2^- + HO_2^- \rightarrow OH + O_2 + OH^-$	1.30E-01	$M^{-1}s^{-1}$
62	$O_2^- + O_3^- + H_2O \rightarrow O_2 + O_2 + 2OH^-$	1.00E+04	$M^{-1}s^{-1}$

(Continued on next page)

#	reaction	rate constant $k_\#$ (25°C)	unit
63	$O_2^- + O_3 \rightarrow O_3^- + O_2$	1.50E+09	$M^{-1}s^{-1}$
64	$O^- + O^- + H2O \rightarrow O_2 + O_2 + 2OH^-$	1.00E+09	$M^{-1}s^{-1}$
65	$O^- + O_2 \rightarrow O_3^-$	3.60E+09	$M^{-1}s^{-1}$
66	$O^- + H_2 \rightarrow H + OH^-$	8.00E+07	$M^{-1}s^{-1}$
67	$O^- + H_2O_2 \rightarrow O_2^- + H_2O$	5.00E+08	$M^{-1}s^{-1}$
68	$O^- + HO_2^- \rightarrow O_2^- + OH^-$	4.00E+08	$M^{-1}s^{-1}$
69	$O^- + O_3^- \rightarrow O_2^- + O_2^-$	7.00E+08	$M^{-1}s^{-1}$
70	$O^- + O_3 \rightarrow O_2^- + O_2$	5.00E+09	$M^{-1}s^{-1}$
71	$O_3^- \rightarrow O_2 + O^-$	3.30E+03	s^{-1}
72	$O_3^- + H^+ \rightarrow O_2 + OH$	9.00E+10	$M^{-1}s^{-1}$
73	$HO_3 \rightarrow O_2 + OH$	1.10E+05	s^{-1}

This doctoral thesis was realized at the frontier between liquid-phase transmission electron microscopy (LP-TEM) and microfluidics. It contributes to the elevation of LP-TEM to a quantitative experimental technique for the study of nanoscale dynamics in liquid environments by applying concepts established in microfluidics.

A workflow combining numeric modelling and flow experiments was elaborated. The workflow reveals and quantifies the effect of structural elements of microfluidic LP-TEM reactors on mass transport. Moreover, the effect of flow on the radiolysis reaction network was analysed. The acquired knowledge led to the development of customized LP-TEM mixing reactors with optimized mass transport.

This manuscript derives general guidelines for LP-TEM flow experiments and showcases model experiments to demonstrate the progress towards quantitative LP-TEM studies.

supervised by

Andrey Chuvilin

Marek Grzelczak

eman ta zabal zazu

UPV   EHU